Lanthanide and Transition Metal Ions Activated Advanced Phosphors for Optical and Radiation Dosimetry Applications

by

Sitakanta Panda

Enrolment No: CHEM 02 2015 04 006
Indira Gandhi Centre for Atomic Research,
Kalpakkam, Tamil Nadu, India

A thesis
Submitted to
The Board of Studies in Chemical Sciences

In partial fulfillment of requirements for the Degree of
DOCTOR OF PHILOSOPHY
of
HOMI BHABHA NATIONAL INSTITUTE

December 2020

Homi Bhabha National Institute

Recommendations of the Viva Voce Committee

As members of the Viva Voce Committee, we certify that we have read the dissertation prepared by **Sitakanta Panda** **"Lanthanide and transition metal ions activated advanced phosphors for optical and radiation dosimetry applications"** and recommend that it may be accepted as fulfilling the thesis requirement for the award of Degree of Doctor of Philosophy.

Chairman: **Dr.** K. Ananthasivan	Date: 07/05/21
Guide/ Convener: **Dr.** B. S. Panigrahi Panigrahi	Date: 07.05.2021
External Examiner: **Dr.** Venkataramanan Mahalingam	Date: 07.05.2021
Member 1: **Dr.** T. R. Ravindran TRRavindran	Date: 7.5.2021
Member 2: **Dr.** K. I. Gnanasekar Gnanasekar	Date: 7/5/21

Final approval and acceptance of this thesis is contingent upon the candidate's submission of the final copies of the thesis to HBNI.

I hereby certify that, I have read this thesis prepared under my direction and recommend that it may be accepted as fulfilling the thesis requirement.

Date: 07.05.2021
Place: Panigrahi

Panigrahi
Dr. B.S. Panigrahi

Statement by Author

This dissertation has been submitted in partial fulfillment of requirements for an advanced degree at Homi Bhabha National Institute (HBNI) and is deposited in the Library to be made available to borrowers under rules of the HBNI.

Brief quotations from this dissertation are allowable without special permission, provided that accurate acknowledgement of source is made. Requests for permission for extended quotation from or reproduction of this manuscript in whole or in part may be granted by the Competent Authority of HBNI when in his or her judgment the proposed use of the material is in the interests of scholarship. In all other instances, however, permission must be obtained from the author.

Sitakanta Panda

Sitakanta Panda

Declaration

I, hereby declare that the investigation presented in the thesis has been carried out by me. The work is original and has not been submitted earlier as a whole or in part for a degree / diploma at this or any other Institution / University.

Sitakanta Panda

Sitakanta Panda

List of Publications arising from Thesis

Journal

1. Probing the site occupancy of dopants in deep red-NIR emitting $LiAl_5O_8$: Eu^{3+}, Cr^{3+} and Fe^{3+} nano phosphors using photoluminescence and X-ray absorption spectroscopy. **Sitakanta Panda**, P. Vinodkumar, Madhusmita Sahoo, U. Madhusoodanan, B.S. Panigrahi. *J. Alloys Compd.* 2021, 857, 157615-157623. **[I.F=4.650]**
2. Effect of gadolinium on europium luminescence and its in-situ valence conversion in $SrBPO_5$ host. **Sitakanta Panda**, P. Vinodkumar, Satendra Kumar, U. Madhusoodanan, N. Suriyamurthy, B.S. Panigrahi. *J. Lumin*. 2020, 225, 117349-117357. **[I.F=3.280]**
3. Synthesis, characterization and optical properties of $BaCeO_3$: Eu – An efficient red phosphor for w-LED applications. **Sitakanta Panda**, P. Vinodkumar, U. Madhusoodanan, R. Ramachandran, V. Shridharan, B.S. Panigrahi. *J. Lumin*. 2019, 214, 116538-116545. **[I.F=3.280]**
4. Probing the optical properties and luminescence mechanism of a UV-emitting $SrBPO_5$: Ce^{3+} phosphor. **Sitakanta Panda**, P. Vinodkumar, U. Madhusoodanan, B.S. Panigrahi. *Luminecence* 2019, 34, 8, 887-894. **[I.F=1.885]**

Manuscript under Preparation

1. A comparative study of Ce^{3+} luminescence in $CaBPO_5$, $SrBPO_5$ and $BaBPO_5$ hosts. **Sitakanta Panda,** B.S. Panigrahi et al.
2. Effect of Gd^{3+} codoping on Eu^{3+} and Eu^{2+} luminescence in $MBPO_5$: Eu, Gd phosphors. **Sitakanta Panda,** B.S. Panigrahi et al.

Conference Presentation

1. Photoluminescence study of Europium and Samarium doped $SrBPO_5$. **Sitakanta Panda et al.**, National conference on Luminescence and its Application (NCLA), CSIR-IICT, Hyderabad, India, 9-11th Jan 2017: **Poster Presentation**.
2. $SrBPO_5$: Eu, Gd as a new TL material for radiation dosimetry. **Sitakanta Panda et al.**, National Conference on Thermophysical Properties, IGCAR, Kalpakkam, India, 6-8th Nov 2017: **Young Scientist Award for Outstanding Oral Presentation**.

3. Optical properties of $SrBPO_5$: Ln^{3+} [Dy^{3+}/Sm^{3+}/Gd^{3+}] nano phosphors. **Sitakanta Panda et al.**, NCLA, CSIR-NIIST, Trivandrum, India, 14-16th Feb 2018: **Best Poster Presentation**.
4. Luminescence properties of $BaCeO_3$: Eu^{3+} phosphors. **Sitakanta Panda et al.**, International Conference on Luminescence and its Applications, PRS University, Raipur, India, 7-10th Jan 2019: **Oral Presentation**.
5. Lanthanide-activated $CaBPO_5$ phosphors for phototherapy and LEDs applications. **Sitakanta Panda et al.**, National Conference on Advanced Materials & Environmental Science, (NCAMES), Kalinga University, Naya Raipur, India, 14-15th Oct 2019: **Oral Presentation**.

Other Journal Publications (Not Included in Thesis)

1. Thermoluminescence properties of strontium borophosphate doped with praseodymium and enhancement with uranyl codoping. P. Vinodkumar, **Sitakanta Panda**, U. Madhusoodanan, B.S. Panigrahi. Radiat. Phys. Chem. 2020, 174, 108914-108920. **[I.F=2.110]**.
2. Structural and optical properties of Ce-doped strontium borophosphate glasses. P. Ramakrishna, **Sitakanta Panda**, P. Vinodkumar, D.K. Mohapatra, H. Jena, B.S. Panigrahi. *Indian J. Phys.* https://doi.org/10.1007/s12648-020-01910-4. **[I.F=1.407]**.
3. $SrBPO_5$: Ce^{3+}, Dy^{3+}–A cold white-light emitting phosphor. P. Vinodkumar, **Sitakanta Panda**, G. Jaiganesh, R. Padhi, U. Madhusoodanan, B.S. Panigrahi, Spectrochimica Acta Part A: Molecular and Biomolecular Spectroscopy 2021, 253, 119560. **[I.F=3.232].**
4. Color tuning from green to orange-red in $SrBPO_5$: UO_2^{2+}/Pr^{3+} phosphor via energy transfer for solid-state lighting applications. P. Vinodkumar, G. Jaiganesh, **Sitakanta Panda**, R. Padhi, U. Madhusoodanan, B.S. Panigrahi, Results in Physics 2021, 21, 103757. **[I.F=4.019].**
5. Structural and Optical Properties of Cerium and Dysprosium Coactivated Borophosphate Glasses for Cool White Light Application. P. Ramakrishna, **Sitakanta Panda**, P. Vinodkumar, R.K. Padhi, H. Jena, B.S. Panigrahi. Journal of Non-Crystalline Solids: In Press. **[I.F=2.929].**

Dedicated to

My Grandparents, Parents & Brother

Acknowledgements

First and foremost, I express my sincere gratitude to **Dr. B.S. Panigrahi**, my Research Supervisor, for his insightful guidance and lively discussions all the way leading to the completion of my Ph.D. Especially, his skill of solving various critical problems in a simpler way persuade me a lot during my research.

I am extremely grateful to my doctoral committee members, **Dr. K. Ananthasivan, Dr. T. R. Ravindran and Dr. K. I. Gnanasekar**, for their careful evaluation and insightful suggestions during the review meetings.

I would like to express my gratitude to **Dr. A. K. Bhaduri**, Director, IGCAR, for providing the opportunity to continue the research work at IGCAR. I would like to thank **Dr. B Venkatraman**, Director, SQRMG, IGCAR, for providing a pleasant atmosphere for my smooth research.

I am thankful to **Dr. N. Sivaraman and Dr. Brahmananda Rao**, former and present Dean Chemical Sciences, HBNI, IGCAR, for their support and being friendly during all the procedure throughout the tenure.

I am thankful to **Dr. Vidya Sundararajan, Dr. T.S. Lakshmi Narasimhan and Dr. M. Saibaba**, present and former Dean SA, for the wonderful hospitality during my stay at JRF Enclave.

I would like to acknowledge the **Dept. of Atomic Energy, Govt. of India** for research fellowship. I am also thankful to all reviewers and the examiner for their notable time and careful evaluation.

I express my heartfelt gratitude to **Dr. U. Madhusoodanan** for all his timely and ever-willing help in carrying out this research work.

I would like to express my special thanks of gratitude to **Dr. R. Ananthanarayanan** for his constant motivation and help in writing the thesis.

I also take this opportunity to thanks **Dr. S. Amrithapandian, Dr. V. Shridharan, Dr. Arindam Das, Dr. Satendra Kumar, Dr. H.N. Jena, Mr. Sanjit Parida, Mr. Biranchi Mohapatra,** for their help during various experiments and useful discussions. I am further thankful to **Dr. S.N. Jha**, RRCAT, Indore, for providing synchrotron facility.

I deeply express my thanks to my beloved friends **Santanu, Prasant, Sudarsana, Ramaswamy, Binaya, Anil, Vikas, Vidyasagar, Darpan, Suman, Rahul, Pavan, Bijaya, Sachin, Chandrakumar, Bolasankar, Mahimakumar, Sindhuja, Nandini, Harimohan, Dinesh, Chavan, Revanth, Soumya, Dillip, Abhisekh, Subhranshu and Nirod.**

I take this opportunity to thank **P. Vinodkumar, P. Ramakrishna, Dr. R.K. Padhi, Dr. A. Rout, Mr. Devdas and Mrs. Chitra**, for providing a cordial atmosphere in the lab.

On this occasion, I will express my heartiest gratitude and respect to my ideal teachers **Dr. Prakash Mohanty**, Utkal University and **Dr. Shreelekha Bhatta Mishra**, Berhampur University, for introducing me to the mysterious universe of Chemistry.

I would like to express my heartiest gratitude and honor to **my Grandparents, Parents, Brother and Sister-in-law**, for their unconditional love, care and support.

Finally, I thank my nephew **Devansh** for the pleasant and delightful leisure I enjoy with him.

Sitakanta Panda

Sitakanta Panda

Abstract

Solid-state luminescent materials, commonly called phosphors, have drawn the attention of the research community owing to their wide applications in solid-state lighting (SSL), biomedical imaging and radiation dosimetry. Many of such phosphors have borate, phosphate, borophosphate, oxides of silicate and aluminate, and oxysulfide as host materials. Most importantly, phosphors based on oxysulfide, halide, phosphate and borate hosts have not been paid much attention owing to their hygroscopic nature, poor chemical and thermal stability. In this context, the silicate hosts pose excellent thermochemical stability and are non-hygroscopic, though they require a very high calcination temperature (≥1250 °C) for their synthesis. However, the alkaline earth borophosphate ($MBPO_5$; M=Ca/Sr/Ba) hosts possess good thermochemical stability as well as non-hygroscopicity. Unlike silicates, $MBPO_5$ can be prepared by the conventional solid-state reaction (SSR) route at lower calcination temperature (900-1000 °C). Synthesis at low temperature effectively reduces the volatilization of the structural component and thereby, the defect formation is reduced leading to efficient luminescence from the phosphor. Moreover, an advanced phosphor must have multi photonic applications with improved color quality, high longevity, high radiation stability, environmental sustainability and low cost. In addition to these properties, the phosphor must have a large band gap (>3.2 eV), as in semiconductors and insulators, to avoid the reabsorption of the emission by the host. To keep pace with the recent demand for advanced lighting technology, the synthesis of Ln and TM ions doped phosphors is in active research to develop highly efficient phosphors that meet the industrial standards. An efficient phosphor must have a befitting combination of activator(s) and host.

In this context, Ln and TM ions activated stillwellite-structured $MBPO_5$, perovskite-structured $BaCeO_3$ and cubic-structured $LiAl_5O_8$ phosphors are preferred for various lighting applications as they exhibit good structural integrity, high thermochemical stability

and are non-hygroscopic. Based on these favorable structural and optical properties, it was decided to synthesize and characterize the structural, morphological and optical properties of certain Ln and TM ions in $MBPO_5$, $BaCeO_3$ and $LiAl_5O_8$ hosts. The present thesis deals with the synthesis and extensive optical and dosimetric characterization of $MBPO_5$: Ce/Eu/Gd, $BaCeO_3$: Eu and $LiAl_5O_8$: Eu/Cr/Fe phosphors. In the course of the work, the following areas are explored in detail.

$SrBPO_5$: Ce phosphors are synthesized by the solid-state reaction route at 1000 °C. From the powder X-ray diffraction (XRD) patterns, the phase purity and the structure of the samples are ascertained. For band gap measurements, diffuse reflectance spectroscopy (DRS) is utilized. Photoluminescence (PL) studies establish the intense UV-blue emission, characterized by two short lifetimes with 14 and 36 ns, from $SrBPO_5$: $Ce_{0.01}$ that finds application in solid-state lighting and scintillation. For the first time, we investigated and explained the site occupancy of Ce^{3+} in $SrBPO_5$ and the nature of defects using time-resolved emission spectroscopy (TRES) and positron annihilation lifetime spectroscopy (PALS), respectively. TRES corroborated the presence of two site occupancies for Ce^{3+} in this host. PL of γ-irradiated and bleached phosphor confirmed the absence of valence conversion of cerium ($Ce^{3+} \leftrightarrow Ce^{4+}$) demonstrating its reusability in scintillation applications. The mechanism of thermally stimulated luminescence (TSL) of the γ-irradiated $SrBPO_5$: Ce is also demonstrated. Finally, a comparative luminescence study of $MBPO_5$: Ce^{3+} phosphors is presented.

Once again, $SrBPO_5$: Eu/Gd phosphors are synthesized through the solid-state reaction route at 1000 °C. PL of $SrBPO_5$: $Gd_{0.075}$ displays intense and narrow emission at 313 nm (UV-*B*) and therefore suggesting its potential application in phototherapy. The effect of Gd codoping on the PL and TSL of $SrBPO_5$: Eu is explored due to the possible energy transfer between Gd^{3+} and Eu^{3+}. Remarkably, the orange-red emission of Eu^{3+} got enhanced in $SrBPO_5$: $Eu_{0.01}$, $Gd_{0.075}$ due to energy transfer from Gd^{3+} to Eu^{3+}. In addition to energy transfer, Gd^{3+} facilitates unusual in-situ valency conversion ($Eu^{2+} \rightarrow Eu^{3+}$) enhancing Eu^{3+} emission furthermore and the same is reported here for the first time. A comparative study of the luminescence properties of Gd^{3+}, Eu^{3+} and Eu^{2+} in $MBPO_5$ hosts is also investigated to arrive at a potential light-emitting diodes (LEDs) phosphor. The color purity of orange-red emitting Eu^{3+} in $CaBPO_5$: $Eu_{0.01}$, $Gd_{0.10}$, $SrBPO_5$: $Eu_{0.01}$, $Gd_{0.075}$ and $BaBPO_5$: $Eu_{0.01}$, $Gd_{0.05}$ is determined to be 97%, 94% and 97%, respectively. This study is relevant towards making efficient orange-red (Eu^{3+}), blue (Eu^{2+}) and UV-*B* (Gd^{3+}) LEDs. The mechanism of TSL and calculation of trap parameters in SBP: Eu/Gd phosphors are studied. The work highlights the favorable TSL characteristics of SBP: Eu, Gd phosphor with linear dose-response in the range of 100 mGy-10 Gy.

Perovskite structured $BaCeO_3$: Eu phosphors are successfully prepared through a facile solution combustion synthesis route at different calcination temperatures (1000-1300 °C). The influence of calcination temperature on the morphology and PL, and the variation of asymmetric ratio as a function of dopant concentration, excitation wavelength and temperature (77 and 300 K) of $BaCeO_3$: Eu phosphor are explored in detail. The $BaCeO_3$: $Eu_{0.09}$ phosphor calcined at 1200 °C exhibits intense red emission with 100% color purity and a higher color coordinates than that of the existing commercial red phosphors. Two different site occupancies of Eu^{3+} in $BaCeO_3$ are established by TRES analysis. PALS investigation revealed oxygen and metal-oxygen vacancy defects in the pristine and Eu doped samples. The usefulness of $BaCeO_3$: Eu for high-dose radiation dosimetry is established through TSL studies. $BaCeO_3$: Eu gave a linear dose-response (0-1000 Gy) and exhibited suitable trap parameters. It is interesting to note that the linear dose-response up to 1000 Gy suggests its potential use in high-energy radiation dosimetry

A single-step solution combustion synthesis route is used to successfully synthesize LiAl$_5$O$_8$: Eu/Cr/Fe nano phosphors with an average particle size of 60 nm at low synthesis temperature (600 °C). The powder XRD patterns confirm the single phase and inverse spinel crystal structure of cubic LiAl$_5$O$_8$. In LiAl$_5$O$_8$, Li$^+$ has octahedral (O$_h$) coordination whereas Al^{3+} has both tetrahedral (T$_d$) and O$_h$ coordination. Extensive studies are carried out to clarify the prevailing ambiguity in the preference of the activator for Li$^+$/Al^{3+} sites. For the first time, X-ray absorption spectroscopy studies confirmed the presence of Eu^{3+} at Li$^+$-O$_h$ site only whereas Fe^{3+} at Li$^+$-O$_h$, Al^{3+}-O$_h$ and Al^{3+}-T$_d$ sites with reduced coordination number indicating the presence of oxygen defects. The cause of the broad emission (620-830 nm) of Fe^{3+} and the sharp emission of Cr^{3+} (713 nm) and intense emission of Eu^{3+} in the deep red-NIR region are discussed in detail. All three activators exhibit intense red-NIR emission with 100% color purity suggesting them as potential phosphors for solid-state lighting, laser and biomedical applications.

Table of contents

List of Figures

List of tables

Table of Contents

Friday, May 14, 2021

Chapter 7

Summary and Future work

7.1. Summary

In the present thesis, emerging phosphors based on alkaline earth borophosphate, barium cerate and lithium aluminate hosts are synthesized and characterized for potential applications spanning from UV-*B*, UV-*A*, red, deep red-NIR LEDs to radiation dosimetry. The synthesis and extensive optical characterization of $MBPO_5$: Ce/Eu/Gd, $BaCeO_3$: Eu and $LiAl_5O_8$: Eu/Cr/Fe phosphors are explored in detail. A brief chapter wise summary of the thesis along with the scope for future study is outlined as follows.

A brief literature review about the importance of synthesis routes, host materials, luminescent centers, the structural and optical properties, and the challenging issues are presented in chapter 1. The motivation and objective of the research work are also briefed in this chapter.

The experimental techniques carried out for material synthesis and characterization are briefly outlined in chapter 2, with the basic principle of operation and major components of the instruments. The synthesis of $MBPO_5$: Ce/Eu/Gd phosphors through a modified SSR route while $BaCeO_3$: Eu and $LiAl_5O_8$: Eu/Cr/Fe phosphors through the SCS route are presented.

In chapter 3, the structure, morphology, band gap and luminescence properties of $MBPO_5$: Ce phosphors are investigated. PL of Ce^{3+} exhibits intense UV-Blue (320-420 nm) emission with nanosecond lifetime (10-36 ns) whose utility is exploited in security industry, fluorescent sensing levels and scintillators. PL lifetime and TRES measurements confirm the presence of Ce^{3+} in two different sites in $MBPO_5$ hosts. PALS study suggests two types of defects present in undoped and Ce doped SBP that influence its luminescence properties. The mechanism of the TSL glow curve of γ-irradiated SBP: Ce phosphor is established from its TSL emission spectrum. A comparative luminescence study of Ce^{3+} among $SrBPO_5$, $CaBPO_5$ and $BaBPO_5$ hosts is also presented.

Chapter 4 focuses on the optical properties of Gd doped and Eu-Gd codoped $MBPO_5$ phosphors. Gd^{3+} exhibits intense and narrow UV-*B* emission at 313 nm in $MBPO_5$: $Gd_{0.075}$ phosphors. Here, the effect of Gd codoping on the PL and TSL properties of $SrBPO_5$: Eu phosphors is explored. In the Eu-Gd codoped $MBPO_5$, Eu^{3+} luminescence gets significantly enhanced due to the energy transfer from Gd^{3+} to Eu^{3+}. In addition to the energy transfer, surprisingly, Gd^{3+} facilitates the valency conversion from Eu^{2+} to Eu^{3+} which enhances the efficiency of Eu^{3+} luminescence furthermore. This has not been reported so far to the best of our knowledge and is addressed in the present work. The comparative study shows intense orange-red emission from Eu^{3+} in $CaBPO_5$: $Eu_{0.01}$, $Gd_{0.10}$, $SrBPO_5$: $Eu_{0.01}$, $Gd_{0.075}$ and $BaBPO_5$: $Eu_{0.01}$, $Gd_{0.05}$ with 97%, 94% and 97% color purity suggesting them as potential candidates for SSL applications. This study is relevant towards making efficient orange-red (Eu^{3+}), blue (Eu^{2+}) and UV-B (Gd^{3+}) LEDs. In addition to PL, TSL investigations on SBP: Eu/Gd are reported in detail for the first time. The mechanism of TSL and calculation of trap parameters in SBP: Eu, SBP: Gd and SBP: Eu, Gd phosphors are presented. The chapter highlights the favorable TSL characteristics of SBP: Eu, Gd phosphor that has shown a linear dose-response covering two orders of magnitude in the dose range of 100 mGy to 10Gy and useful trap parameters for radiation dosimetry.

Chapter 5 presents the PL and TSL properties of perovskite structured $BaCeO_3$: Eu prepared through the SCS route. The SEM image analysis ascertains high agglomeration above 1200 °C. Optimization of calcination temperature (1000-1300 °C) and Eu-concentration (1-10 mol%) reveal intense red color from $BaCeO_3$: $Eu_{0.09}$ phosphors calcined at 1200 °C. PL study corroborates that the asymmetric ratio of Eu^{3+} is as a function of dopant concentration, excitation wavelength and temperature. The color purity of Eu^{3+} in $BaCeO_3$:

$Eu_{0.09}$ is found to be 100% with excellent color coordinate suggesting it as a suitable candidate for red phosphor. PL lifetime and TRES analysis confirm two site occupancies for Eu^{3+} in this host. The defect studies using PALS reveal the presence of oxygen vacancy and barium-oxygen vacancy complex in this host for the first time. TSL glow curves of γ-irradiated $BaCeO_3$: Eu exhibit multiple traps and a linear dose-response in the range of 0-1000 Gy suggesting it as a high-energy radiation dosimetry phosphor.

Chapter 6 presents the single-step synthesis of in $LiAl_5O_8$: $Fe^{3+}/Cr^{3+}/Eu^{3+}$ nano phosphors through the SCS route at 600 ^oC. The powder XRD patterns confirm the single phase and inverse spinel structured cubic lattice of $LiAl_5O_8$. The morphology of synthesized phosphors shows the formation of spherical and compacted nano particles with an average size of 60 nm. The XAS investigations reveal the exact local coordination environment of dopants for the first time. The study confirms the presence of Eu^{3+} in Li^+-O_h site whereas Fe^{3+} in Li^+-O_h, Al^{3+}-O_h and Al^{3+}-T_d sites with a reduction in coordination number. The reduction in the coordination number indicates a lower symmetry and the presence of oxygen vacancy around the activators in this host resulting in intense deep red-NIR emission. The cause of the observed unusual broad emission of Fe^{3+} (620-830 nm) is due to its presence in multiple sites experiencing a different magnitude of CFS. TRES studies also corroborate the site occupancy of Fe^{3+} showing a blue-shift in different time domains. PL of $LiAl_5O_8$: Eu (0.5 mol%), $LiAl_5O_8$: Fe (500 ppm) and $LiAl_5O_8$: Cr (100 ppm) exhibits intense deep red-NIR emission with 100% color purity and improved color coordinates than that of the National Television Standard Committee recommendations suggesting them as potential nano phosphors for SSL, laser and biomedical applications.

7.2. Future work

In the future, the following work can be carried out.

- Quantification of Eu^{2+} to Eu^{3+} conversion

- Leaching studies with respect to different site occupancy
- Field study of $SrBPO_5$: Gd, Eu and $BaCeO_3$: Eu phosphors for radiation dosimetry applications
- Development of LEDs based on $SrBPO_5$, $BaCeO_3$ and $LiAl_5O_8$ phosphors for solid-state lighting and biomedical applications
- Development of nano phosphors for optical thermometry and long afterglow phosphors for noninvasive temperature sensing and emergency security applications.

Summary

In the present thesis, emerging phosphors based on alkaline earth borophosphate, barium cerate and lithium aluminate hosts are synthesized and characterized for potential applications spanning from UV-*B*, UV-*A*, red, deep red-NIR LEDs to radiation dosimetry. The synthesis and extensive optical characterization of $MBPO_5$: Ce/Eu/Gd, $BaCeO_3$: Eu and $LiAl_5O_8$: Eu/Cr/Fe phosphors are explored in detail. A brief chapter wise summary of the thesis along with the scope for future study is outlined as follows.

A brief literature review about the importance of synthesis routes, host materials, luminescent centers, the structural and optical properties, and the challenging issues are presented in chapter 1. The motivation and objective of the research work are also briefed in this chapter.

The experimental techniques carried out for material synthesis and characterization are briefly outlined in chapter 2, with the basic principle of operation and major components of the instruments. The synthesis of $MBPO_5$: Ce/Eu/Gd phosphors through a modified SSR route while $BaCeO_3$: Eu and $LiAl_5O_8$: Eu/Cr/Fe phosphors through the SCS route are presented.

In chapter 3, the structure, morphology, band gap and luminescence properties of $MBPO_5$: Ce phosphors are investigated. PL of Ce^{3+} exhibits intense UV-Blue (320-420 nm) emission with nanosecond lifetime (10-36 ns) whose utility is exploited in security industry, fluorescent sensing levels and scintillators. PL lifetime and TRES measurements confirm the presence of Ce^{3+} in two different sites in $MBPO_5$ hosts. PALS study suggests two types of defects present in undoped and Ce doped SBP that influence its luminescence properties. The mechanism of the TSL glow curve of γ-irradiated SBP: Ce phosphor is established from its TSL emission spectrum. A comparative luminescence study of Ce^{3+} among $SrBPO_5$, $CaBPO_5$ and $BaBPO_5$ hosts is also presented.

Chapter 4 focuses on the optical properties of Gd doped and Eu-Gd codoped $MBPO_5$ phosphors. Gd^{3+} exhibits intense and narrow UV-*B* emission at 313 nm in $MBPO_5$: $Gd_{0.075}$

phosphors. Here, the effect of Gd codoping on the PL and TSL properties of $SrBPO_5$: Eu phosphors is explored. In the Eu-Gd codoped $MBPO_5$, Eu^{3+} luminescence gets significantly enhanced due to the energy transfer from Gd^{3+} to Eu^{3+}. In addition to the energy transfer, surprisingly, Gd^{3+} facilitates the valency conversion from Eu^{2+} to Eu^{3+} which enhances the efficiency of Eu^{3+} luminescence furthermore. This has not been reported so far to the best of our knowledge and is addressed in the present work. The comparative study shows intense orange-red emission from Eu^{3+} in $CaBPO_5$: $Eu_{0.01}$, $Gd_{0.10}$, $SrBPO_5$: $Eu_{0.01}$, $Gd_{0.075}$ and $BaBPO_5$: $Eu_{0.01}$, $Gd_{0.05}$ with 97%, 94% and 97% color purity suggesting them as potential candidates for SSL applications. This study is relevant towards making efficient orange-red (Eu^{3+}), blue (Eu^{2+}) and UV-B (Gd^{3+}) LEDs. In addition to PL, TSL investigations on SBP: Eu/Gd are reported in detail for the first time. The mechanism of TSL and calculation of trap parameters in SBP: Eu, SBP: Gd and SBP: Eu, Gd phosphors are presented. The chapter highlights the favorable TSL characteristics of SBP: Eu, Gd phosphor that has shown a linear dose-response covering two orders of magnitude in the dose range of 100 mGy to 10Gy and useful trap parameters for radiation dosimetry.

Chapter 5 presents the PL and TSL properties of perovskite structured $BaCeO_3$: Eu prepared through the SCS route. The SEM image analysis ascertains high agglomeration above 1200 °C. Optimization of calcination temperature (1000-1300 °C) and Eu-concentration (1-10 mol%) reveal intense red color from $BaCeO_3$: $Eu_{0.09}$ phosphors calcined at 1200 °C. PL study corroborates that the asymmetric ratio of Eu^{3+} is as a function of dopant concentration, excitation wavelength and temperature. The color purity of Eu^{3+} in $BaCeO_3$: $Eu_{0.09}$ is found to be 100% with excellent color coordinate suggesting it as a suitable candidate for red phosphor. PL lifetime and TRES analysis confirm two site occupancies for Eu^{3+} in this host. The defect studies using PALS reveal the presence of oxygen vacancy and barium-oxygen vacancy complex in this host for the first time. TSL glow curves of γ-irradiated $BaCeO_3$: Eu exhibit multiple traps and a linear dose-response in the range of 0-1000 Gy suggesting it as a high-energy radiation dosimetry phosphor.

Chapter 6 presents the single-step synthesis of in $LiAl_5O_8$: Fe^{3+}/Cr^{3+}/Eu^{3+} nano phosphors through the SCS route at 600 °C. The powder XRD patterns confirm the single phase and inverse spinel structured cubic lattice of $LiAl_5O_8$. The morphology of synthesized phosphors shows the formation of spherical and compacted nano particles with an average size of 60 nm. The XAS investigations reveal the exact local coordination environment of dopants for the first time. The study confirms the presence of Eu^{3+} in Li^+-O_h site whereas Fe^{3+} in Li^+-O_h, Al^{3+}-O_h and Al^{3+}-T_d sites with a reduction in coordination number. The reduction in the coordination number indicates a lower symmetry and the presence of oxygen vacancy around the activators in this host resulting in intense deep red-NIR emission. The cause of the observed unusual broad emission of Fe^{3+} (620-830 nm) is due to its presence in multiple sites experiencing a different magnitude of CFS. TRES studies also corroborate the site occupancy of Fe^{3+} showing a blue-shift in different time domains. PL of $LiAl_5O_8$: Eu (0.5 mol%), $LiAl_5O_8$: Fe (500 ppm) and $LiAl_5O_8$: Cr (100 ppm) exhibits intense deep red-NIR emission with 100% color purity and improved color coordinates than that of the National Television Standard Committee recommendations suggesting them as potential nano phosphors for SSL, laser and biomedical applications.

Table of Contents

Chapter 1

Introduction

1.1. Definition and classification of luminescence

Eilhard Ernst Gustav Wiedemann was the pioneer to coin the term 'Luminescence' which is derived from the Latin word 'Lumen' which means light.[1] Basically, luminescence is a cold light phenomenon that is entirely different from thermal radiation in the sense that in thermal radiation, a material needs to be heated to a temperature of about 600 ºC for the material to emit radiation.[2] On the other hand, a luminescent material converts the incident input energy to electromagnetic radiation in the ultraviolet (UV), visible (VIS) or infrared (IR) regions. Luminescence is a broad concept and can be caused by photon excitation, chemical reaction, electrical energy, thermal energy or mechanical energy, etc. Table 1.1 shows the various classifications of luminescence depending on the excitation source along with a few typical applications against each type of luminescence. It may be noted that although different types of luminescence are listed in Table 1.1 for the sake of completion. Nevertheless, photoluminescence (PL) and thermally stimulated luminescence (TSL) are studied vastly owing to their potential applications in various fields such as compact fluorescent lamp (CFL), light-emitting diodes (LEDs), plasma display panel (PDP), detector, laser, biomedical imaging and radiation dosimetry.[3-6] Luminescent materials in solid-state are referred to as phosphors and they are generally preferred in many applications because they have a substantial density of atoms and as a consequence, absorption and emission intensity are very high. This leads to a sizeable optical effect even in very thin samples allowing one to make compact optical devices that fulfill the requirement of the modern optoelectronics industry. To keep pace with the recent demand for advanced lighting technology, active research is being carried out to develop highly efficient phosphors that meet the industrial standards.

Table 1.1 Classification of various types of luminescence based on the excitation source along with a few typical applications

Types	Acronym	Excitation source	Applications
Photoluminescence	PL	UV, VIS, NIR photons	CFL, LEDs
Radioluminescence	RL	Ionizing radiation, Charged particles	Signage, Scintillation, Cold light sticks
Cathodoluminescence	CL	Energetic electrons	TVs, Monitors
Electroluminescence	EL	Electric field	LEDs, LCD, OLEDs
Chemiluminescence	CRL	Chemical reaction	Luminous paints
Thermally Stimulated Luminescence	TSL	Thermal energy, Charged particles	Dosimetry, Dating
Optically Stimulated Luminescence	OSL	Photons, Charged particles	Dosimetry, Dating

1.2. Photoluminescence processes and principles

Photoluminescence is a process in which a phosphor emits light after absorbing a photon. Excitation and emission are two sequential phenomena, and there is always a difference in the wavelength of observed emission in comparison to the wavelength of excitation. Stokes shift occurs when the emission wavelength is longer than the excitation wavelength while the anti-Stokes shift occurs when the emission wavelength is shorter than the excitation wavelength. The absolute shift here can be expressed in terms of energy, frequency or wavenumber. Luminescence materials that exhibit Stokes and anti-Stokes shifts are observed in down-conversion (DC) and up-conversion (UC) materials, respectively. Moreover, in case of up-conversion process the absorbed two or more lower energy photons are converted into a higher energy photon whereas in case of down-conversion process, a higher energy photon is converted into more than one lower energy photons. In contrast to down-conversion, in case of down-shifting (DS) material, the number of photons emitted equals the number of photons absorbed though it involves the Stokes shift. These materials find numerous applications in solid-state lighting.[7-10] It may be noted that UC material involves excitation to an intermediate energy level and by subsequent absorption of one or more photons, electron finally reaches an energy level that is well above the emitting level. This is possible for those luminescent centers which show cooperative phenomena[11] and this particular topic is beyond the scope of the present study. In the present work, the luminescence properties of DS materials alone have been discussed in detail.

A phosphor can be a host or host activated with a luminescent center called activator or dopant. A phosphor can emit in UV to IR regions mainly depending on its host lattice and the activator. Therefore in principle, one can generate a specific wavelength of light through the proper choice of host and dopant. A suitable host should have high thermal and chemical stability, non-hygroscopicity, single-phase purity over a wide range of temperature, easy incorporation of activators, wide band gap (>3.2 eV) and low phonon vibrations.

1.2.1. A portmanteau of fluorescence and phosphorescence

Photoluminescence involves the excitation of an electron from the lowest vibrational level (v_o) of the ground electronic state (E_0) to a higher vibrational level ($>v_o'$) of the excited electronic state (E_i'). Before the excited electron returns to the v_o of E_0, it undergoes nonradiative and possible radiative processes. The former may be due to vibrational relaxation, internal conversion (within different vibrational states of the same electronic state) and intersystem crossing (between different spin multiplicities) without giving any photonic emission. The latter can be classified as fluorescence and phosphorescence based on their nature of transition and lifetime. An electron spends a specific time in a particular excited state before it returns to its ground state and the entire process shows a statistical dependence. The lifetime of a luminescent center may be defined as the time required for the excited population to depopulate to a level of 1/e (~37%) of its initial excited population. Fluorescence refers to the radiative return of the excited species from the singlet (^1S_i) excited state to the singlet ground state ($^1S_0$) which being spin allowed occurs in the time scale of 10^{-8} s. On the other hand, phosphorescence refers to the radiative return of the excited species from the triplet (^3T_i) excited state to the singlet ground state ($^1S_0$) which being spin forbidden occurs in the time scale of a few seconds to several hours.[12, 13] Apart from the time scale, another fundamental difference between fluorescence and phosphorescence is that the former occurs in shorter wavelengths (UV-VIS) whereas the latter occurs in the longer wavelengths (VIS-NIR). In some cases, fluorescence like phosphorescence exhibit longer time scales and this phenomenon is called delayed fluorescence, which can be easily distinguished from phosphorescence as it overlaps with the wavelength domain of fluorescence. The terminology of fluorescence and phosphorescence are applicable for hydrocarbon moieties or for molecules where energy levels can be assigned as singlet and triplet. However, emission in specific activators like lanthanides, the energy levels cannot be assigned as singlet or triplet and, therefore, is broadly classified as luminescence. For example, the characteristic $^5D_0 \rightarrow {}^7F_{0-4}$ transition of Eu^{3+} can neither be classified as a singlet or triplet.

1.2.2. Nature of luminescence observed in phosphors

The observed luminescence in a phosphor can be classified either as intrinsic or extrinsic. Intrinsic luminescence is mostly due to band to band and excitonic luminescence. Band to band luminescence is obtained when an excited electron from the conduction band (CB) recombines with a hole present in the valence band (VB) in materials like vanadate, niobate, molybdate, tungstate.[14, 15] This corresponds to the host excitation and emission bands. On the other hand, excitonic luminescence is obtained by the recombination of bound e^--h^+ pair called exciton while propagating through the lattice after being excited. Depending on the distance of separation between the e^- and h^+ in the excitons, they can be further classified as Frenkel or Wannier excitons. In the former, the separation is in the order of an atomic radius suggesting high binding energy (E_b) whereas in the latter, it is higher than the lattice constant and thus suggesting a lower E_b. For example, Kr (s) shows Frenkel exciton with an E_b of 2 eV for a radius of ~2 Å while InSb shows Wannier exciton with a very low

E_b of 0.6 meV for a radius of ~600 Å.[2] The excitation energy is transferred through the lattice by both types of excitons and ended up either radiatively or non-radiatively.

On the other hand, the extrinsic luminescence is obtained from the localized activator substituted in the host lattice. It is observed in different hosts doped with lanthanides (Ln) and transition metals (TM) ions. Figure 1.1 represents a simple schematic energy level diagram, known as a configurational coordinate (CC) diagram, plotted between potential energy and the internuclear distance between the central metal ion (activator) and the ligand. Such a diagram is used to illustrate the properties of electronic transitions between different energy levels. Irrespective of the type of luminescence, a source is required to excite a species electronically before it gives rise to emission. In case of PL, an electronic excitation always occurs from V_0 of E_0 to higher vibrational states ($v'>0$) of E_1, E_2, E_3, etc., since, at room temperature, it is expected that almost the entire electron is populated in V_o of E_o. As per the Franck-Condon principle, electronic transitions typically occurring in the time scale of 10^{-15} s are so fast that during the electronic transition, the nuclei do not see a change in their position and similarly the transiting electron does not see a change in its spin. So, the electronic excitations are always represented as vertical lines in the CC diagram. For the sake of simplicity and clarity, only one excitation transition is shown in Figure 1.1; however, many transitions are possible depending upon the spectral overlap of the vibronic states of the ground and excited electronic states. Therefore, maximum overlap indicates the most probable transition resulting in maximum luminescence. Once the electron reaches a higher vibrational state of E_1, it dissipates the excess energy as heat to the surrounding before it comes to $v'=0$. This is due to (i) the less energy difference between the vibrational states which is not enough to make radiative emission and (ii) the strong overlap between numerous vibrational wave functions. This process is referred to as internal vibrational relaxation and takes place in the time scales of

10^{-12}-10^{-14} s. Compared to vibrational relaxation, the time taken for the luminescence (10^{-8} s) is much longer[16] and as a result, regardless of which initial level the molecule is excited, luminescence will mostly originate from the lowest vibrational state of the lowest excited electronic state. Hence, the emission wavelength is independent of the excitation wavelengths. This rule is known as Kasha's rule. Thus, PL excitation and emission occur from the lowest vibrational states of the ground and excited states, respectively. However, Kasha's rule is not obeyed in many cases when there are large energy gaps between excited electronic states as emission from higher electronic levels other than E_1 is also seen. Examples of such molecules are azulene, azobenzene, biphenylene, 3, 6-diphenyl-s-tetrazine, diphenylacetylene, annulene.

Returning to the configurational coordinate diagram (Fig. 1.1), let's assume that an electron is promoted to E_1. Through vibrational relaxation, the excited system attains a new equilibrium position (R_e) compared to that of original equilibrium (R_g) with an offset of ΔR ($=R_e-R_g$) indicating that the system has undergone expansion. This is followed by the return of the electron to the ground state either radiatively or nonradiatively. As seen from Figure 1.1, the returning of the electron from $v'=0$ to higher vibrational levels of E_0 is represented by a vertical straight line indicating that emission too obeys the Franck-Condon principle conserving its spin and new equilibrium position. The probability of emission to a particular vibrational level of the ground state depends on the extent of the wave function of the involved vibrational levels. After the electron returns to the ground state, the internuclear distance comes back to its original position (R_g) from its excited position (R_e) and thus completing a cycle of expansion followed by contraction.

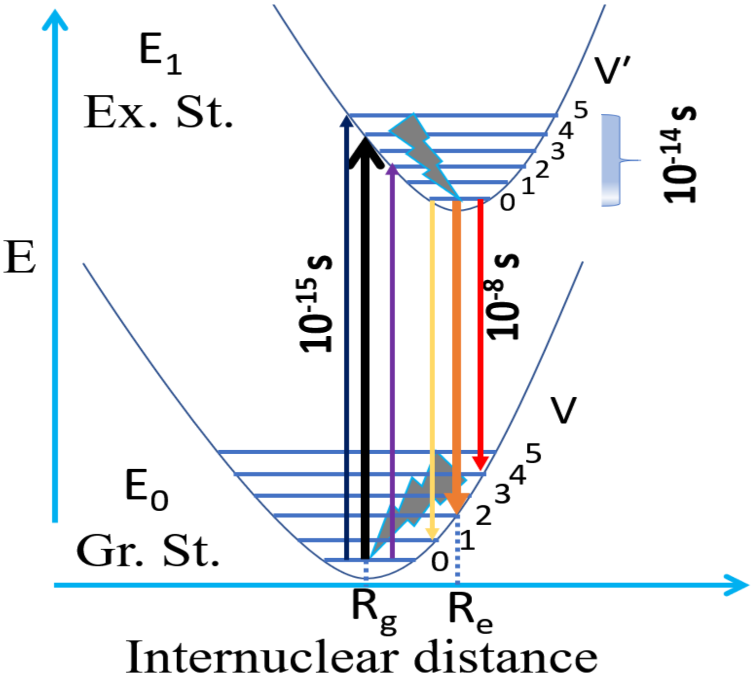

Figure 1.1 A simple configurational coordinate diagram showing vibronic transitions.

As seen from the above discussion, spectral broadening and narrowing are related to the offset ΔR. The higher the value of ΔR, the higher is the broadening. ΔR is, in turn, related to the vibrational relaxation energy loss (Shν) through the expression, $Sh\nu \propto \Delta R^2$; where hν corresponds to the energy spacing between two vibrational states and S is an integer called Huang-Rhys coupling constant or electron-lattice coupling constant.[17] The value of S denotes the strength of electron lattice coupling with S<1 indicating weak, 1<S<5 indicating intermediate and S>5 indicating strong coupling. Consider the case of lanthanides where 4*f*-4*f* and 4*f*-5*d* transitions are involved. In the case of the former, ΔR~0 and intermediate coupling (1<S<5) is observed due to which emission is narrow. On the other hand, for 4*f*-5*d* transitions ΔR≠0 and S>5 which causes the emission bands to be broad. For 4*f*-4*f* transitions, ΔR~0 since 4*f* orbitals are well shielded from the influence of the ligand field due to the presence of completely filled $5s^2$ and $5p^6$ orbitals. However, for 4*f*-5*d* transitions, ΔR≠0 since the 5*d* orbitals are prone to ligand field.

1.3. Luminescence of lanthanides and transition metals ions

1.3.1. Optical properties of lanthanides

Lanthanides (Ln) include fourteen elements following lanthanum (^{57}La) from cerium (^{58}Ce) to lutetium (^{71}Lu) wherein the last electron is filled in $4f^{1\text{-}14}$ orbitals chronologically with a general electronic configuration of [Xe]$4f^{1\text{-}14}5d^{0\text{-}1}6s^{2}$. According to the International Union of Pure and Applied Chemistry (IUPAC) recommendations, rare earths (RE) include 14 lanthanides, La, Y and Sc because they tend to occur in the same ore deposits as the lanthanides and exhibit similar chemical properties.[18] Sometimes, lanthanides are also referred to as rare earths as their abundance in nature is less. Among the lanthanide ions, Pm^{3+} which being radioactive and man-made is not studied for luminescence while La^{3+} and Lu^{3+} having an empty $4f^{0}$-configuration and a fully-filled $4f^{14}$-configuration, respectively, do not exhibit luminescence. On the other hand, lanthanide ions that give luminescence in UV-NIR regions are Ce^{3+}, Pr^{3+}, Nd^{3+}, Sm^{3+}, $Eu^{3+/2+}$, Gd^{3+}, Tb^{3+}, Dy^{3+}, Ho^{3+}, Er^{3+}, Tm^{3+} and Yb^{3+}. Lanthanides exhibit the most stable and common oxidation state of +3 as the electrons present in the outer $4f5d6s$ orbitals have lower ionization energy and thus are easily removed. Some lanthanides also exhibit +2 (Eu, Sm, Tm, Yb) and +4 (Ce, Pr, Tb) oxidation states. Among the lanthanide ions, UV-VIS emitters are listed in Table 1.2 along with their emission strength and energy states mainly involved in giving the luminescence.[19, 20]

Interconfigurational $4f$-$5d$ transitions, as is the case with Ce^{3+} and Eu^{2+}, display broad bands since $\Delta R>0$. The splitting of $5d$ orbitals shows a strong dependency on the host lattice, and hence its excitation/emission states can vary from UV to VIS region which in turn gives flexibility in choosing the emission in the desired wavelength. Further, being Laporte allowed the $4f$-$5d$ transitions show intense luminescence due to which the elements like Ce^{3+} and Eu^{2+} can be detected down to trace levels by PL spectroscopy. Regarding stability, Ce^{3+} is more stable than Ce^{4+} as the reduction potential of ceric to cerous ($Ce^{4+} \rightarrow Ce^{3+}$) is very high (1.74 eV), and hence Ce^{3+} is predominantly formed in phosphors synthesized in air atmosphere. On the other hand, Eu^{2+} is also quite stable due to its half-filled configuration and, as a consequence, it manifests itself in many hosts prepared even in the absence of a reducing atmosphere.[21-23] Except for Ce^{3+} and Eu^{2+}, other $Ln^{3+/2+}$ ions display narrow lines resulting from intraconfigurational 4*f*-4*f* transitions since $\Delta R \sim 0$.

Table 1.2 Ln energy states mainly associated with characteristics luminescence behavior.

E.C of Ln	E.C of $Ln^{+2/+3}$	Gr. state	Ex. state	Colour	Strength
$_{58}Ce\text{-}4f^1 5d^1 6s^2$	$Ce^{3+}\text{-}4f^1$	$^2F_{5/2,7/2}$	$^2D_{3/2}$	*UV-VIS	Excellent
$_{59}Pr\text{-}4f^3 5d^0 6s^2$	$Pr^{3+}\text{-}4f^2$	$^3H_4$	$^3P_0$, $^1D_2$	Red	Weak
$_{60}Nd\text{-}4f^4 5d^0 6s^2$	$Nd^{3+}\text{-}4f^3$	$^4I_{9/2}$	$^2P_{1/2,}$ $^4G_{7/2}$	Near IR	Weak
$_{62}Sm\text{-}4f^6 5d^0 6s^2$	$Sm^{2+}\text{-}4f^6$	$^7F_0$	$^5D_0$	Red	Weak
	$Sm^{3+}\text{-}4f^5$	$_6H^{5/2}$	$^4G^{5/2}$	Orange-Red	Medium
$_{63}Eu\text{-}4f^7 5d^0 6s^2$	$Eu^{2+}\text{-}4f^7$	$^8S_{7/2}$	$4f^6 5d$	*UV-VIS	Excellent
	$Eu^{3+}\text{-}4f^6$	$^7F_0$	$^5D_1$, $^5D_0$	Orange-Red	Strong
$_{64}Gd\text{-}4f^7 5d^1 6s^2$	$Gd^{3+}\text{-}4f^7$	$^8S_{7/2}$	$^6P_{7/2}$	UV-B	Strong
$_{65}Tb\text{-}4f^9 5d^0 6s^2$	$Tb^{3+}\text{-}4f^8$	$^7F_6$	$^5D_3$, $^5D_4$	Green	Strong
$_{66}Dy\text{-}4f^{10} 5d^0 6s^2$	$Dy^{3+}\text{-}4f^9$	$^6H_{15/2}$	$^4F_{9/2}$	Yellow	Medium
$_{67}Ho\text{-}4f^{11} 5d^0 6s^2$	$Ho^{3+}\text{-}4f^{10}$	$^5I_8$	$^5S_2$, $^5F_5$	Red	Weak
$_{68}Er\text{-}4f^{12} 5d^0 6s^2$	$Er^{3+}\text{-}4f^{11}$	$^4I_{15/2}$	$^4S_{3/2}$, $^4F_{9/2}$	Green	Weak
$_{69}Tm\text{-}4f^{13} 5d^0 6s^2$	$Tm^{3+}\text{-}4f^{12}$	$^3H_6$	$^1G_4$, $^3F_3$, $^3H_4$	Blue	Weak
$_{70}Yb\text{-}4f^{14} 5d^0 6s^2$	$Yb^{3+}\text{–}4f^{13}$	$^2F_{7/2}$	$^2F_{5/2}$	UV-Blue	Weak

The asterisk mark (*) indicates that the emission wavelength depends on the 5*d* states and is host-dependent. Also, the color of the emission is the sum of all the observed emitting photons. So, the final color of the emitter depends on the intensity of each transition.

The intensity of an electronic transition is governed by the following Selection rules:

- Spin selection rule: An allowed transition involves no change in the spin states ($\Delta S=0$).

- Parity selection rule: An allowed transition involves a change in parity ($\Delta L=\pm1$).

In accordance with the above selection rules, transitions that obey the Selection rules give intense luminescence. For instance, Ce^{3+} and Eu^{2+} give strong emissions while Sm^{3+}, Eu^{3+}, Gd^{3+}, etc. give weak emissions. However, in solids, the Selection rules are relaxed due to the mixing of various wave functions caused by certain physical phenomena such as spin-orbit (L-S) coupling, electronic-vibration coupling, crystal field splitting, etc. Due to these phenomena, the 4*f*-4*f* transitions of lanthanide in many solid-state phosphors display good luminescence. Unlike 4*f*-4*f* transitions, the charge transfer (CT) and 4*f*-5*d* transitions are allowed in nature and therefore, Ln ions display intense luminescence when excited at their CT (O^{2-}, $2p \rightarrow Ln^{3+/4+}$, $4f$) and 4*f*-5*d* ($4f^{n} \rightarrow 4f^{n-1}5d$) bands. It may be added that both the charge transfer and 4*f*-5*d* transitions have $\Delta R>0$ and, therefore, broad bands are seen in their spectral profiles. Strong CT bands are observed in certain lanthanides ions that exhibit multiple oxidation states (Ce^{4+}/Ce^{3+}, Pr^{4+}/Pr^{3+}, Tb^{4+}/Tb^{3+}, Sm^{3+}/Sm^{2+}, Eu^{3+}/Eu^{2+}, Yb^{3+}/Yb^{2+}). On the other hand, 4*f*-5*d* transitions are seen for certain trivalent (Ce^{3+}, Pr^{3+}, Tb^{3+}) and divalent lanthanide ions (Sm^{2+}, Eu^{2+}, Yb^{2+}).

1.3.2. Electronic transitions of 4*f*-5*d* configurations

The 4*f*-5*d* transitions in free Ce^{3+} ions occur above 6.2 eV ($5\text{x}10^{4}$ cm^{-1}). However, in solids, an increase in covalency between the Ce^{3+} and the ligand significantly downshifts the centroid of the 5*d* energy levels which is known as the Nephelauxetic effect. The 5*d*-levels split in the presence of crystal field to some $1.5\text{x}10^{4}$ cm^{-1}. This way the lowest crystal field component of 5*d* gets further lowered in energy as shown in Figure 1.2, with the extent of lowering depending on the crystal field of a host lattice. In addition to covalency and crystal field splitting, the Stokes shift also influences the position of the emission band. This is the reason for Ce^{3+} showing emission ranging from UV to visible region. It may be added that the shielded 4*f* levels of Ce^{3+} split to $^2F_{5/2,}$ and $^2F_{7/2}$ some 2000 cm^{-1}. As discussed already, the 4*f*-5*d* transitions being parity allowed give broad band with a very short lifetime (<100 ns). As the crystal field increases the emission wavelength as well as the lifetime increase. For such transitions, the lifetime (τ) is proportional to the square of emission wavelength: $\tau \alpha \lambda^2$.[24]

The host-dependent emission of Eu^{2+} ($4f^7$-$4f^6 5d$) is also determined by the same factors as in the case with Ce^{3+}. Though the transition in Eu^{2+} is parity allowed ($4f^6 5d^1 \rightarrow 4f^7$ transition) its lifetime (100 ns-1 μs) is higher as compared to that of Ce^{3+}. This is because an electronic transition to the ground state ($^8S_{7/2}$) is possible from both the sextet and the octet spin state with the former being spin forbidden. A transition from sextet state involving $^6P_{7/2}$ level of $4f^7$ configuration (361-363 nm) is possible in many Eu^{2+} doped matrices with the transition becoming more prominent at 4 K.[25] It is worth mentioning here that, if the crystal field is weak then the $^6P_{7/2}$ level of $4f^7$ will lie below the $4f^6 5d^1$ energy levels and a significant transition from $^6P_{7/2}$ to $^8S_{7/2}$ will also increase the lifetime remarkably.

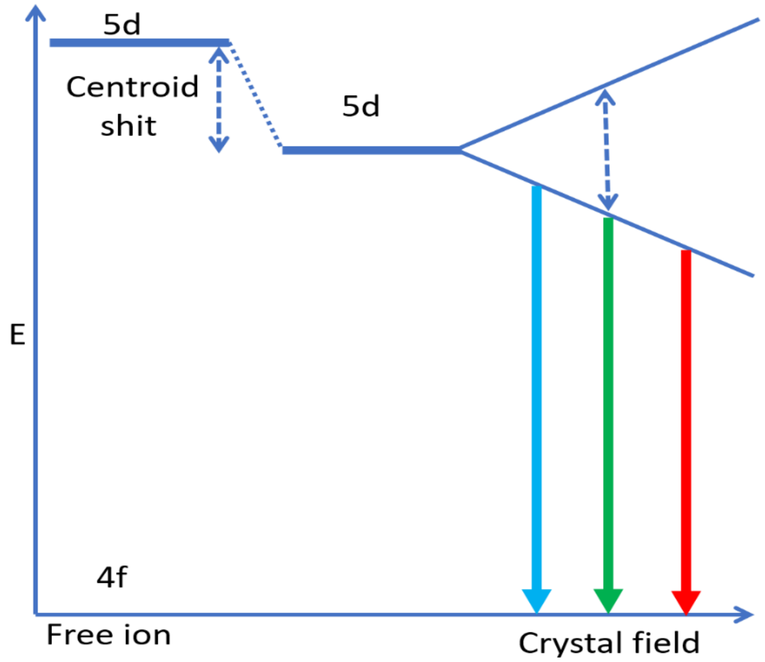

Figure 1.2 Simple schematic energy levels of 4f-5d transitions in Ce^{3+} and Eu^{2+}.

1.3.3. Intraconfigurational splitting pattern of lanthanides

The splitting of the electronic configuration of lanthanides due to various interactions is presented in Figure 1.3. Due to inter electronic repulsion, the 4*f* configuration splits into energy levels with possible values of total orbital angular momentum (L) and spin multiplicity (2S+1; S=total spin quantum number) called terms (^{2S+1}L). Due to spin-orbit (L-S) coupling, the terms further split into different energy levels with possible values ranging from |L+S| to |L-S| called states ($^{2S+1}L_J$). The states further split into (2J+1) energy levels called microstates in the presence of a crystal field. For example, Eu^{3+} with $4f^6$ configuration splits into several terms like ^7F, ^5D, ^5L, ^6H due to the coulombic repulsion. The terms split into several states like $^7F_0$, $^7F_1$, $^7F_2$, $^7F_3$, $^7F_4$, $^5D_0$, $^5D_1$, $^5D_2$, $^5D_3$ due to L-S coupling. Each state again splits into (2J+1) microstate like $^7F_0$: $^7F_0$, $^7F_1$: $^7F_{-1}$, $^7F_0$, $^7F_{+1}$, $^7F_2$: $^7F_{-2}$, $^7F_{-1}$, $^7F_0$, $^7F_{+1}$, $^7F_{+2}$ in presence of crystal field. The energy level separation between 4*f* and 5*d* configurations amounts to an order of 10^5 cm^{-1} that is quite larger compared to the energy level separation between (i) terms (10^4 cm^{-1}) (ii) states (10^3 cm^{-1}) and (iii) microstates (10^2 cm^{-1}). Though the 4*f*-microstates have the lowest energy separation, due to the complete shielding it gives rise to the narrow spectrum.

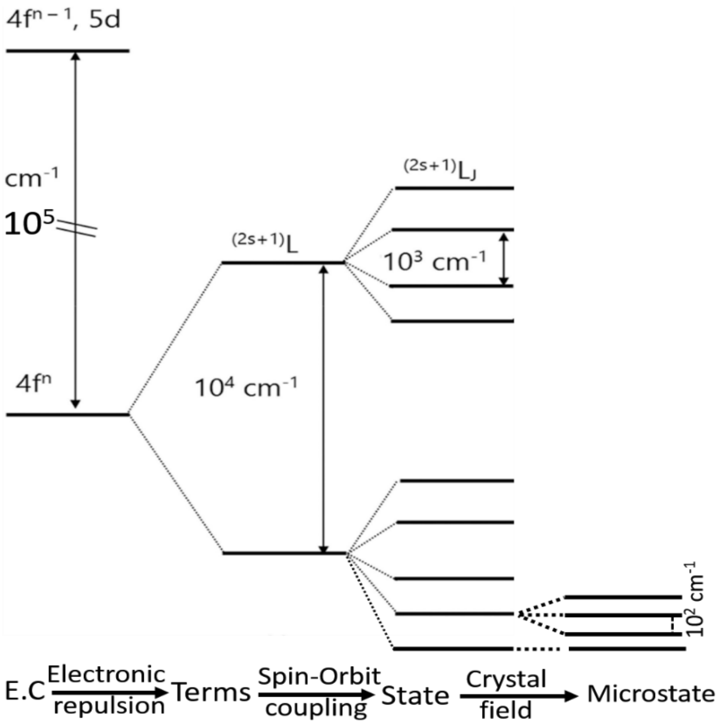

Figure 1.3 Simple schematic presentation of 4f-electronic configuration (EC) of lanthanides.

1.3.4. Electronic transitions of 4*f*-4*f* configurations

Among the trivalent lanthanides, Eu^{3+} ($4f^6$) is of particular interest owing to its optical sensitivity towards the symmetry of the host lattice. Before describing the optical sensitivity, the splitting pattern of Eu^{3+} can be visualized with the help of Figure 1.4. Eu^{3+} luminescence is interesting as it emits intense orange-red color that is useful in making LEDs, FED and PDP devices.[26, 27] Most importantly, it is used as a structural probe to study the microenvironment around it as well as around the host cation. The characteristic excitation and emission transitions of Eu^{3+} are shown in Figure 1.4. It can be seen that Eu^{3+} shows two types of excitations: CT (~ 255 nm) and 4*f*-4*f* transitions at 394 ($^7F_0 \rightarrow {}^5L_6$) and 464 nm ($^7F_0 \rightarrow {}^5D_2$) while the emissions are usually observed at 580, 593, 612, 650 and 698 nm corresponds to $^5D_0 \rightarrow {}^7F_{0\text{-}4}$ transitions, respectively.[28]

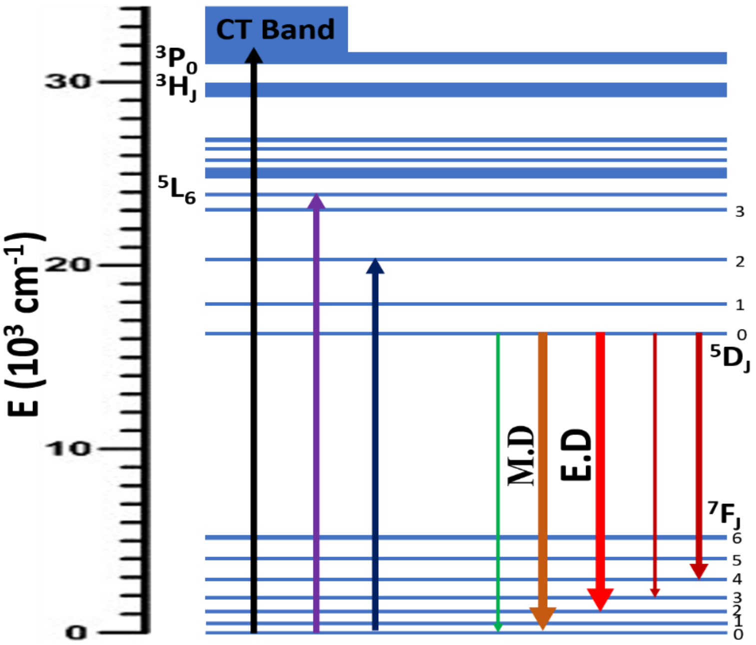

Figure 1.4 Simple schematic energy levels diagram of Eu^{3+}.

It may be added that in some host lattices with low phonon energy, Eu^{3+} shows emission from higher excited levels like $^5D_1$. The $^5D_0 \rightarrow {}^7F_1$ and $^5D_0 \rightarrow {}^7F_2$ are called allowed magnetic dipole (MD) and electric dipole (ED) transitions, respectively. The MD is least sensitive to ligand filed whereas the ED transition is hypersensitive. Eu^{3+} when present in a higher symmetric environment of the host lattice shows stronger MD transition than ED transition, and therefore, results in intense orange emission. However, when Eu^{3+} is present in a lower symmetric environment, ED transition dominates resulting in intense red emission. The hypersensitivity of Eu^{3+} is employed to probe the structural symmetry of a host lattice and is expressed in terms of asymmetry ratio (R_a). The value of R_a is obtained by taking the integral intensity ratio of ED and MD transition. $R_a<1$ indicates a higher symmetry (presence of center of inversion) and yields orange emission while a value >1 indicates lower symmetry (absence of inversion center) and yields intense red emission. It may be noted that the $^5D_0 \rightarrow {}^7F_J$ transitions split into a relevant number of microstates depending upon the crystal field and the symmetry. Thus, it acts as a structural probe in studying the symmetry at the doped site of the host lattice. The variation of R_a as a function of excitation wavelengths and activator concentration provides information about the preferential excitation from different sites and any change in the microenvironment of the activator, respectively.

Unlike other trivalent lanthanides, Gd^{3+} shows a sharp emission in UV-*B* (280-315 nm) region following strong absorption in UV-*C* region (100-280 nm), which is deployed in phototherapy for treating several dermatitis, water purifier for killing germs, photochemical reactions, low-pressure Hg-lamp.[29, 30] It acts as an excellent activator[31] giving intense UV-*B* emission at 313±2 nm as well as a very good sensitizer[32] when codoped in a suitable host for enhancing luminescence of certain lanthanides. Gd^{3+} derives its stability from its half-filled configuration ($4f^7$). It involves optical absorption from the ground state ($^8S_{7/2}$) to higher energy (>32000 cm^{-1}) levels that are mostly present above the emitting levels of the rest of the trivalent lanthanides. The excitation spectrum of Gd^{3+} exhibits an intense and narrow characteristic peak at 273 ($^8S_{7/2}\rightarrow{}^6I_{13/2,\,15/2}$) with shoulder peaks at 276 ($^8S_{7/2}\rightarrow{}^6I_{11/2}$) and 279 nm ($^8S_{7/2}\rightarrow{}^6I_{7/2}$). The ground state being non-degenerate exhibits a line emission spectrum at 313 nm ($^6P_{7/2}\rightarrow{}^8S_{7/2}$) even at low temperatures. The uniqueness of Gd^{3+} is that it can sensitize all Ln^{3+} ions (except Pr^{3+} and Tm^{3+}) through energy transfer from its $^6P_{7/2}$ level. However, in the case of Pr^{3+} and Tm^{3+}, their energy levels lie much below the emitting levels of Gd^{3+} ($^6P_{7/2}$), and as a result, there is no resonance spectral overlap. This forbids the energy transfer between Gd^{3+} to Pr^{3+}/Tm^{3+}.

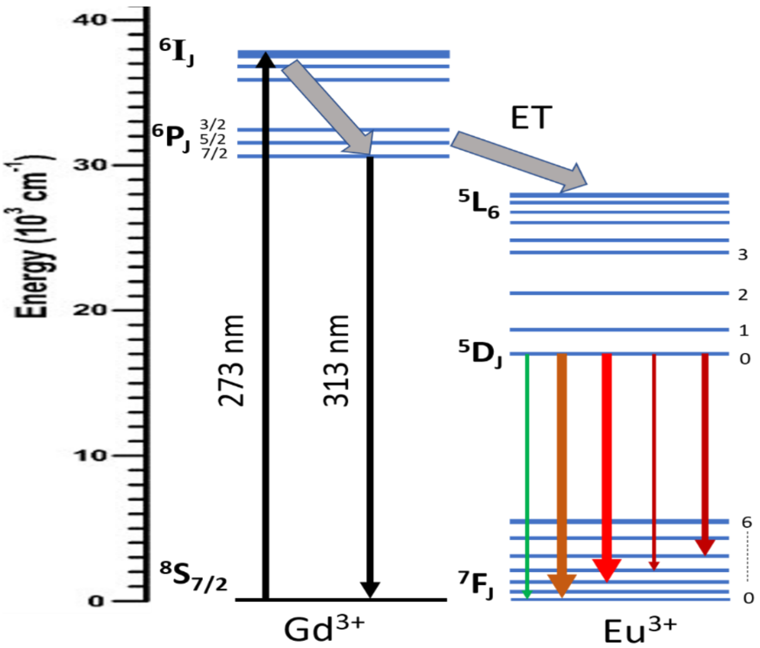

Figure 1.5 Schematic presentation of Gd^{3+} energy level and the energy transfer to Eu^{3+}.

The excited energy levels ($^7F_{0,1} \rightarrow {}^5H_{3,6}$) of Eu^{3+} that are known to be present in the range of 292-320 nm strongly resonate with the emitting levels of Gd^{3+} (^6P_J, 313 nm). Hence, with respect to energy transfer, Gd^{3+} and Eu^{3+} are the best couples in some suitable hosts for making efficient emission from Eu^{3+} phosphors as shown in Figure 1.5. Being Laporte forbidden, the radiative rate of 4*f*-4*f* transitions is small with a corresponding long lifetime value. On the other hand, the energy transfer rate is much faster than the radiative rate, and as a result, concentration quenching becomes effective with a few mol% of dopant concentrations (typically <10 mol%). For example, if we consider the Gd^{3+}-Eu^{3+} couple, the ET rate (10^7 s^{-1}) is 10^{4-5} times higher than the radiative rate (10^3 s^{-1}) indicating significant ET from Gd^{3+} to Eu^{3+}.

1.3.5. Electronic transitions of 3*d*-3*d* configurations

Transition metal (TM) ions as activators show interesting applications in LEDs, luminescence guided surgery, latent fingerprint (LPP) analysis, long-lasting phosphorescence (LLP) and lasers.[33, 34] TM ions have partially filled *d*-configuration and commonly involve in octahedral and tetrahedral coordination. While structures with tetrahedral coordination lack the center of symmetry those with octahedral coordination can have a center of symmetry. Generally, transition metals are expected to show poor luminescence on account of (i) Laporte forbidden *d*-*d* transition and (ii) presence of center of symmetry in certain complexes. However, in solids due to vibrionic coupling and large crystal field splitting energy (CFSE amounts to 1.5-2x10^4 cm^{-1}), specific transition metal ions exhibit intense luminescence from visible to NIR region. Moreover, as mentioned earlier, structures with either tetrahedral or octahedral coordination that lack the center of symmetry show profuse luminescence due to the breakdown of selection rules.

The energy levels of TM ions are illustrated using the Tanabe-Sugano (TS) diagram that takes inter electronic repulsion and crystal field splitting into account. Spin-orbit (L-S) coupling is not considered in TM ions because unlike 4*f* orbitals, 3*d* orbitals are more prone to the ligand field, and hence its L-S coupling ceases to exist. The transition metal ions which are characteristically used for different phosphor applications are $3d^3$: Cr^{3+}, Mn^{4+} and $3d^5$: Fe^{3+}, Mn^{2+}. Among the TM ions, Cr^{3+} ($3d^3$) and Fe^{3+} ($3d^5$) ions are in the limelight as they absorb strongly in the UV-VIS region and emit in deep red to NIR regions. The emission in the 650-1350 nm region, referred to as tissue optical window, is of special importance in the field of surgery as the light is intensively scattered when they interact with the tissues. The scattered light helps in better visualizing the affected tissue in luminescence guided surgery.[14] Figure 1.6 shows the schematic Tanabe-Sugano diagram of Cr^{3+} in an octahedral geometry. Cr^{3+} ($3d^3$) shows three optical absorptions, corresponding to ${}^4A_{2g}$ (${}^4F$) to ${}^4T_{1g}$ (${}^4P$), ${}^4T_{1g}$ (${}^4F$) and ${}^4T_{2g}$ (${}^4F$).

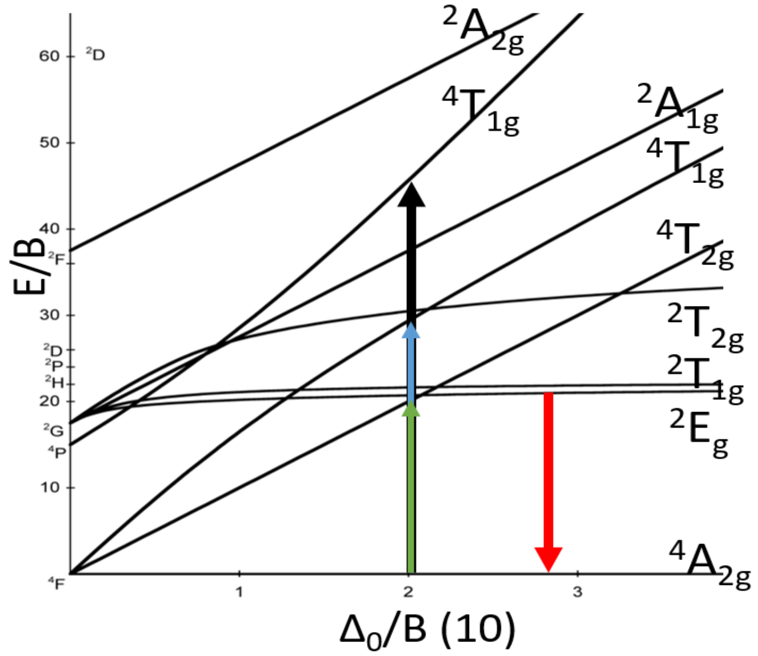

Figure 1.6 Schematic presentation of Tanabe-Sugano (TS) diagram of $3d^3$ *configuration in an octahedral geometry.*

Depending on the crystal field strength (CFS) of the host lattice, optical transitions are observed at certain energies only. In a strong crystal field ($\Delta_0/B>20$), $3d^3$ configuration gives red emission for $^2E_g(^2G)\rightarrow{}^4A_{2g}(^4F)$ transition while in a weak crystal field ($\Delta_0/B<20$), green-orange emission occurs for $^4T_{2g}(^4F)\rightarrow{}^4A_{2g}(^4F)$ transition. Moreover, the $^2E_g(^2G)\rightarrow{}^4A_{2g}(^4F)$ transition being spin forbidden its lifetime occurs in the order of milliseconds (ms) whereas the $^4T_{2g}(^4F)\rightarrow{}^4A_{2g}(^4F)$ transition being spin allowed its lifetime is shorter and occurs in the order of microseconds (μs).

Similarly, the splitting pattern of Fe^{3+} ($3d^5$) can be seen in the Tanabe-Sugano diagram reported elsewhere.[35] Fe^{3+} shows a broad emission in the deep red to NIR region depending on the crystal field of the host lattice. It is worth mentioning that the molar absorptivity of Cr^{3+} is two orders of magnitude higher than Fe^{3+} since the transitions involving Cr^{3+} are spin allowed and thereby allowing the detection of Cr^{3+} down to a few ppb (ng/g). Cr^{3+} shows narrow emissions since its emitting levels (^2E_g) are invariant to the change in crystal field and also the transition to ground level ($^4A_{2g}$) has a negligible offset ($\Delta R\sim0$). On the other hand, Fe^{3+} shows broad emission as its emitting state $^4T_{1g}$ shows a strong dependency on the crystal field and moreover, the transition to ground level ($^6A_{1g}$) has an offset ($\Delta R>0$). However, both Cr^{3+} and Fe^{3+} emit deep red to NIR emission having a millisecond lifetime that is useful for lighting, displays, solid-state laser and medical applications. On the other hand, Mn^{4+} ($3d^3$) is isoelectronic with Cr^{3+} but experiences a higher crystal field due to its higher oxidation state and hence, always gives red emission corresponding to $^2E_g(^2G)\rightarrow{}^4A_{2g}(^4F)$ transition.[36] Similarly, Mn^{2+} ($3d^5$) is isoelectronic with Fe^{3+} but due to a lower oxidation state, it forms a comparatively weaker covalent bond and, as a consequence, experiences weak CFS leading to green-red emission corresponding to $^2E_g(^2G)\rightarrow{}^4A_{2g}(^4F)$ transition. Mn^{2+} also shows a weaker CT band compared to higher charged Fe^{3+}. Hence, for getting intense deep red emission, Fe^{3+} may be preferred. Other $3d^n$ configuration transition metal ions include $3d^1$: Ti^{3+} and $3d^2$: Ti^{3+}, V^{3+}, Mn^{5+} give emission in IR region. The other heavy transition metal ions such as Pb^{2+} and Bi^{3+} with $6s^25d^0$ configuration give emission in the visible region, however, they are not often preferred as they are considered environmentally hazardous.

1.4. Energy transfer mechanism involved in photoluminescence

Lanthanide ions due to the forbidden nature of $4f$-$4f$ transitions yield poor color purity. However, the problem is circumvented by adding a suitable coactivator/sensitizer (S) that can effectively transfer its excitation energy to the activator/acceptor (A) and such an energy transfer becomes effective when

- The emission band of sensitizer overlaps with the excitation band of the activator
- Exchange interaction or multipolar interaction occurs between S and A.

Thus, the rate of ET depends on the spectral overlap and the Hamiltonian interaction (H_{SA}) of the initial state (S* and A) and the final state (S and A*) as given in Equation (1.1).

$$\boldsymbol{R_{SA}=\frac{2\pi}{\hbar}\,|\langle S,A^{*}|H_{SA}|S^{*},A\rangle|^{2}.\int g_{S}(E).\,g_{A}(E)dE} \tag{1.1}$$

In Equation (1.1), the integral presents the spectral overlap while g_X (E) represents the normalized optical line shape function of S/A. In the absence of spectral overlap, the integral vanishes such that R_{SA} becomes zero. However, if there is a good spectral overlap ET can take place through two different types of nonradiative processes, namely, Dexter type and Foster type mechanisms. For exchange type (Dexter) of interactions, the R_{SA} depends exponentially on the distance between S and A, whereas for multipolar interactions, the dependence is proportional to R^{-n}. Depending on the nature of the interaction, i.e., electric dipole-electric dipole (d-d), electric dipole-electric quadrupole (d-q) and electric quadrupole-electric quadrupole interaction (q-q), n takes a value of 6, 8 and 10, respectively.[37] In multipolar interactions, a high value of R_{SA} is expected when there is significant overlap and also when the d-d/d-q/q-q interactions are allowed. Further, using the Dexter-Reisfeld's approximation, one can derive information regarding the mechanism of multipolar interaction by plotting I_{so}/I_s versus $C^{1/n}$. Here, I_{so}/I_s is the ratio of the intensity of donor (S) in the absence and the presence of acceptor (A) while C is the combined concentration of S and A. Based on the best fit of χ^2 (= 1), the value of n is determined. The n value (6, 8, and 10) in turn, indicates the type of ET mechanism operating in the multipolar interaction. It is worth mentioning here that, one can ascertain the energy transfer between S to A by carrying out PL lifetime measurement studies since an ET is accompanied by a corresponding reduction in the lifetime of the donor.

Critical distance (C_d) is an essential parameter in ET studies as it reveals the ET mechanism operating in the system. C_d refers to the optimum distance between S and A beyond which observed luminescence decreases as nonradiative ET predominates. Further, as mentioned earlier the value of C_d indicates the type of ET mechanism. Dexter type mechanism is readily inferred when the calculated value of C_d is <10 Å, and a foster type mechanism is inferred when the C_d falls between 10 to 100 Å. C_d is calculated with the help of Equation (1.2) as given below.

$$\boldsymbol{C_d = 2\sqrt[3]{(3V / 4\pi N X_c)}} \qquad \textbf{(1.2)}$$

Where V= volume of unit cell, N= number of available cationic site for the substitution of dopant per unit cell, X_c= total concentration of donor and acceptor above which the concentration quenching is observed. It may be noted here that in general irrespective of the mechanism of energy transfer, the ET efficiency (η) can be determined by Equation (1.3).

$$\boldsymbol{\eta\ (\%) = [1 - (I_{so}/I_s)]x100} \qquad \textbf{(1.3)}$$

Where I_{so} and I_s refers to the ratio of the intensity of donor (S) in the absence and in the presence of acceptor (A).

1.5. Thermally stimulated luminescence processes and principles

TSL or thermoluminescence is defined as the emission of light from an insulator or semiconductor upon heating.[38] It is not to be confused with incandescence emission as TSL refers to the stimulated emission of light following the previous absorption of high energy radiation (UV-gamma). TSL involves several processes as depicted in Figure 1.7. Exposure of high energy radiation in excess to the band gap (E_g) of material causes the formation of electron-hole (e^--h^+) pairs. The electrons travel in the conduction band (CB) and get trapped in stable electron traps (e_T), and similarly, the holes travel across the valence band (VB) and get trapped in suitable hole traps (h_T) in the host lattice. The trapped electrons (e_T) remain undisturbed unless the material is thermally excited (>50 °C) in which case the electrons are promoted to CB. The thermal energy required for the detrapping is called trap depth or activation energy (E). Each trapped electron has its own escaping tendency/probability which is expressed in terms of frequency (S) and follows a certain order of kinetics (b). From CB, the electron can directly recombine with the hole following the first-order kinetics (b=1) or it can fall back into the electron trap. In the latter case, a further rise in temperature causes the electron to successfully recombine with the hole following the second-order kinetics (b=2). Depending on the stability of various traps, electrons have different trap depths. The emission of thermally stimulated photons, due to the recombination of e^{-}-h^{+} pairs, as a function of temperature is called as glow curve (GC) while the energy of the stimulated photon is called the recombination energy (E_r). In case of hosts containing a dopant, E_r may excite a luminescent center which in turn returns to the ground state by giving rise to a glow curve. In such cases, one cannot assign the origin of the glow curve to either recombination of electron-hole pair or to luminescent center. However, information regarding the mechanism can be readily extracted by recording the TSL emission spectrum wherein the wavelength is plotted as a function of intensity. For a particular value of E and S, an electron can spend a specific time in the trap at room temperature which is called the lifespan or storage time (Γ). Thus, the study of TSL provides information on the physical properties such as activation energy, frequency, the order of kinetics and storage time. The estimation of these physical trap parameters is carried out following different methods like Chen Peak Shape (CPS) and Variable Heating Rate (VHR).[39]

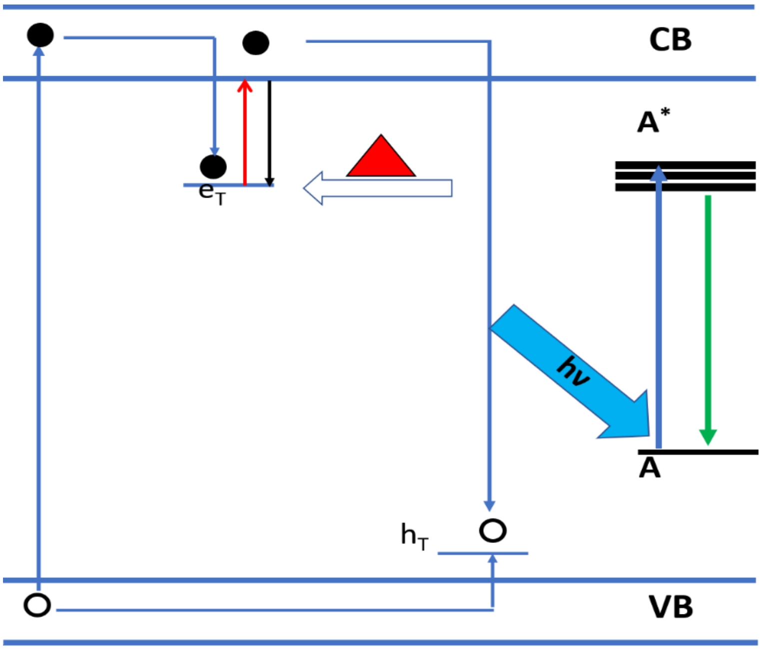

Figure 1.7 Schematic presentation of TSL mechanism in activated phosphors. Here, VB: valence band, CB, conduction band, e_T*: electron trap,* h_T*: hole trap, A: luminescent center, filled circle: electron and empty circle: hole.*

TSL materials are classified based on the activation energy and, as a consequence, the temperature needed to produce a glow curve. TSL materials show GC in the following temperature windows, namely, 50-180, 180-280, 280-480 °C. The glow peak corresponding to 50-180 °C usually has low activation energy (<0.5 eV) and gets quickly faded. The glow peak corresponding to 180-280 °C, called a dosimetric peak, has an ideal trap depth (0.5-1.1 eV) with very low fading and therefore is very useful for radiation dosimetry applications. The glow peak corresponding to 280-480 °C usually requires very high activation energy (<1.1 eV) and does not get easily faded and electrons can be stored for a long time which is useful for radiation dating applications. It may be added that above 500 °C material starts to show incandescence. There are many thermoluminescent dosimeters (TLD) available like $CaSO_4$: Dy, LiF: Mg, Ti – called TLD 100, CaF_2: Dy, $BaSO_4$: Eu, Mg_2SiO_4: Tb, and Al_2O_3: Ti, Si – called TLD 200.[40, 41] These TLD materials are well reproducible and show a linear dose-response over a wide range from µGy to Gy. However, the development of new phosphors that show good reproducibility and dose linearity in the intermediate (mGy to Gy) as well as in the high dose (Gy to kGy) radiation dosimetry needs to be explored.

1.6. Comparison of photoluminescence with optically and thermally stimulated luminescence

Optically stimulated luminescence (OSL) and TSL are closely related techniques and are employed in radiation dosimetry and dating. As with TSL, in OSL also high energy radiation creates electron-hole pairs. However, in OSL the excitation source is photons rather than thermal energy. A suitable photon source promotes the trapped electrons from the trap to CB. The electrons from CB can either fall back into the trap or can recombine with the hole releasing the recombination energy. Moreover, the recombination energy can stimulate a luminescent center if present in the host matrix which in turn can provide a decay curve. The decay curve is constructed by plotting the intensity as a function of time by varying the source strength. One can infer from the above discussion that the phenomenon of TSL and OSL are closely related except for the excitation source. A qualitative description among PL, OSL and TL is given in Table 1.3. Herein, OSL has been briefly described for the sake of clarity and will not be discussed henceforth.

Table 1.3 Distinction among PL, OSL and TSL.

Properties	PL	OSL	TSL
Profile	Wavelength vs. Intensity	Time vs. Intensity	Temperature vs. Intensity
Excitation	Photon	Photon	Heat
Emission	Spontaneous	Stimulated	Stimulated
Transition	Excitation and emission of electron involve the ground and excited states of activator. Participation of CB is not necessary except, host excitation/emission.	Excitation involves the electron trap and emission involves the hole trap or activator. The participation of CB is essential.	Excitation involves the electron trap and emission involves the hole trap or activator. The participation of CB is essential.

Intensity	May not be correlated directly to the dose of irradiation.	Increases with the dose of irradiation up to a certain dose.	Increases with the dose of irradiation up to a certain dose.
Photoconductivity	Does not usually show.	Shows.	Shows.
Reproducibility	Multiple recording phenomenon.	Single recording phenomenon.	Single recording phenomenon.

1.7. Significance of the host materials

For an efficient phosphor, it is necessary to have a befitting combination of host lattice and activator. Many phosphors have been already reported for various applications in LEDs, imaging and radiation dosimetry, etc. Many of such phosphors have borate, phosphate, borophosphate, oxides of silicate and aluminate, and oxysulfide as hosts. Most importantly, the phosphors made up of hosts such as oxysulfide[42], halide[43], phosphate[44] and borate[23] have not been paid much attention owing to their hygroscopic nature, poor chemical and thermal stability. In this context, the silicate hosts[45-47] pose excellent thermo-chemical stability and non-hygroscopicity, though they require a very high calcination temperature (≥1250 °C) for their synthesis. However, the alkaline earth borophosphates ($MBPO_5$; M=Ca/Sr/Ba) possess good thermo-chemical stability as well as non-hygroscopicity.[43] Unlike silicates, $MBPO_5$ can be prepared by the conventional solid-state reaction route at lower calcination temperature (900-1000 °C). The primacy of the lower synthesis temperature is to effectively reduce the volatilization of the structural component and thereby the defect formation leading to efficient luminescence from the phosphor. Moreover, there is still the essence of making advanced luminescent materials that can have multi photonic applications, improved color quality, high longevity, non-hygroscopicity, environmentally sustainable, low cost and so on. In addition to these properties, for a good luminescent material the host must have a wide band gap (>3.2 eV) as in cases of semiconductor or insulator.[48] The band gap is the forbidden region where essentially no electronic transitions (absorption and emission) of the host are expected. This means the band gap is explicitly available for other electronic activities of the activator such that absorption and emission without being reabsorbed by the host lattice, making the phosphor free for efficient luminescence applications. In relation to these properties, stillwellite-type structured alkaline earth borophosphates ($MBPO_5$), perovskite structured cerate ($MCeO_3$) and cubic lithium aluminium oxide ($LiAl_5O_8$) hosts have drawn utmost attentions due to their own unique structural and optical properties.

$MBPO_5$ hosts belong to the stillwellite-type structure where the M^{2+} ion is very well connected by the tetrahedral borate (BO_4^{5-}) and phosphate (PO_4^{3-}) units forming a tortuous 3-dimensional rigid and stable network. Hence, borophosphates possess very high physiochemical stability. Additionally, the ionic size[49] of the M^{2+} ions is comparable with that of the lanthanide ions, allowing them to easily get incorporated into the host lattice with the least distortion in the host lattice up to a few atomic mol% of the activator concentration. On the other hand, the 3-dimensional rigid networks of $MBPO_5$ act as a feedback loop that protects the lanthanide ions to exist also in their lower valency state to some extent in the absence of any reducing atmosphere. For example, in $MBPO_5$: Eu phosphors, europium exits as both +2 and +3 oxidation states though prepared in the air atmosphere.[50, 51] Also, there are several hosts such as borates[23, 52], phosphate[21], silicates[53, 54], where the coexistence of Eu^{2+} and Eu^{3+} is observed. The coexistence of Eu^{2+} reduces the color quality of Eu^{3+} luminescence and remains a challenge that is yet to be addressed. Many researchers have reported prospective applications of $MBPO_5$: Ln (Ln=Ce^{3+}, Eu^{3+} and Eu^{2+}) phosphors in X-ray imaging, neutron storage and lighting display devices.[55-57] However, the optical properties of gadolinium doped and gadolinium-europium codoped phosphors are not studied yet. Also, there is no detailed comparative study of Ce^{3+}, Gd^{3+}, Eu^{3+} and Eu^{2+} in $MBPO_5$ hosts. In detail, there is no report on the effect of γ-radiation on the luminescence properties of Gd/Eu-activated $MBPO_5$ phosphors. Nature of defects and their role on luminescence properties of the lanthanides and thermoluminescence studies are yet to be reported. Also, there are no studies in $MBPO_5$ hosts where enhancement of Eu^{3+} luminesce is discussed. This motivated us to carry out a thorough investigation of the optical properties of Ce^{3+}, Gd^{3+}, Eu^{3+} and Eu^{2+} in $MBPO_5$.

Similarly, the perovskite structured MNO_3 (M=divalent and N=tetravalent cations) hosts have been of research interest due to their intriguing properties in industrial applications. The host, MNO_3 is made up of cuboctahedral MO_{12} and octahedral NO_6 units forming a stable network. The perovskite hosts are known to have wide applications such as hydrogen gas sensors and catalyst electrodes in a solid oxide fuel cell.[58, 59] Intense luminescence has been reported in many cerate hosts such as Sr_2CeO_4, $SrCeO_3$ and $BaCeO_3$.[60-62] A broad band emission spectrum has been observed from these host in the blue-red region. The cerate hosts are highly thermally stable and have numerous potential applications.[59, 63] Among the cerates, $BaCeO_3$ has high thermal stability (m.p.=1743 °C).[64] Lanthanides activated $BaCeO_3$ are reported to be high protonic and oxygen conductors.[65-67] However, a detailed investigation of lanthanide luminescence in this host is yet to be made.[61, 68] The types of defects present in the microenvironment of the dopant which influences its luminescence properties, are not reported in $BaCeO_3$. The radiation dosimetry properties of lanthanide doped $BaCeO_3$ has not been studied so far. Among the lanthanides, Eu^{3+} acts as an excellent structural probe revealing any change in the site symmetry in the host lattice as the site symmetry strongly influences its emission properties. However, there is no such report that explains the optical properties of orange-red emitting Eu^{3+} in this host. A few researchers have synthesized $BaCeO_3$ through the conventional solid-state synthesis calcining at very high temperatures (1300-1600 °C) and for long calcination duration.[64, 69, 70] It may be noted that synthesis of luminescent materials at these elevated conditions often accompanied by poor crystallinity, high agglomerations, lattice imperfections due to the volatilization of structural components, nonuniformity and bigger microcrystalline particles which ultimately lead to inefficient luminosity. Therefore, synthesis of $BaCeO_3$: Ln phosphors through a facile wet chemical route like solution combustion synthesis route at a lower calcination temperature and duration than that of solid-state synthesis to obtain efficient luminescence may be coveted.

A lot of research has been carried out on aluminium oxide host (Li_2O-Al_2O_3 system) doped with lanthanide and transition metal ions owing to their applications in solid-state lighting.[3, 35] Among various Li_2O-Al_2O_3 systems, the $LiAl_5O_8$ host has triggered paramount interest due to its excellent thermochemical and irradiation stability. It has potential applications in molten carbonate fuel cells[4, 5] and nuclear reactors[6] as radiation shield. $LiAlO_2$ and $LiAl_5O_8$ hosts can be synthesized via the combustion synthesis with single phase purity[71]. The host $LiAlO_2$ exists in different allotropic forms (α, β and γ) depending upon the calcination temperature (600-1000 °C) in the post-combustion treatment. The most stable allotropic form of $LiAlO_2$ is its γ-phase that requires high calcination temperature and time whereas $LiAl_5O_8$ is formed in a single step of the combustion process when ignited at 500-600 °C in a couple of minutes and does not need any post-combustion treatment.[72] Therefore, LAO has gained much attention owing to its ease of synthesis, high thermochemical stability and fascinating optical properties.[73, 74] Many researchers have studied the luminescence properties of several Ln and TM ions in this host. The importance of red-emitting Eu^{3+}, blue-emitting Ce^{3+} and green-emitting Tb^{3+} doped LAO phosphors in functional photonic devices have been well documented.[75-79] Also, intense green-emitting LAO: Mn^{2+} phosphor has been reported.[80] The narrow and deep red activated LAO: Cr^{3+} phosphor has shown a promising property towards photoluminescence thermometry and laser material.[73, 81] Similarly, LAO: Fe^{3+} phosphor has been found to be biocompatible and has broad emission in the deep red-NIR region suggesting its applications in the in-vivo temperature sensing and luminescence guided surgery.[82, 83]

Interestingly, the pristine LAO samples are known to contain Cr^{3+} and Fe^{3+} as intrinsic impurities.[84] The origin of these impurities is from the aluminum precursor.[85] However, the quantification of these impurities and their effect on luminescence from this phosphor are yet to be reported. Also, no report is available which suggest a facile solution combustion synthesis of the LAO phosphors. It may be noted that the synthesis via the SCS route proceeds without high calcination temperature to minimize the defects generation due to possible volatilization of Li_2O.[79] An explicit study of the luminescence characteristics including the decay time of $LiAl_5O_8$ phosphor synthesized through the SCS route is yet to be reported. Moreover, there has been an ambiguity regarding the site occupancy of the dopants at the available Li^+ octahedral, and Al^{3+} octahedral and tetrahedral cationic sites in this host which needs to be studied to understand the luminescence behavior of the dopants.[3, 34, 86] Hence, there is a necessity to probe the site speciation of the dopants for corroborating the observed luminescence behavior of the dopants.

1.8. Scope of the study

Photoluminescence being a non-destructive and highly sensitive technique, the availability of PL instruments from the early 19th century resulted in its widespread application in various fields. The development of luminescence can be briefly classified into four different generations as follows (i) wood fire, oil lamp, (ii) tungsten filament lamp, (iii) fluorescent lamp and (iv) Light-emitting diodes. In contrast to incandescence, LEDs which belong to the 4th generation neither require high temperature nor produce noticeable heat. Moreover, LEDs have high luminosity, coldness, cheapness, high longevity and are ecofriendly (free of Hg). With the advancement in solid-state lighting science and technology, efficient phosphors are required to be synthesized not only for LEDs but also for illuminating displays, phototherapy, X-ray imaging, neutron storage and radiation dosimetry applications.

In the present work, many advanced luminescent materials have been synthesized and characterized that find potential applications in the field of (i) phototherapy (ii) blue LEDs (iii) UV-*A* LEDs (iv) red LEDs (v) deep red-NIR LEDs and (vi) radiation dosimetry. Luminescence properties of UV-*B* emitting Gd^{3+}, UV-Blue emitting Eu^{2+} and Ce^{3+}, and orange-red emitting Eu^{3+} in $MBPO_5$ are studied in detail. Also, the optical properties of an intense red-emitting Eu^{3+} activated $BaCeO_3$ phosphor prepared through a facile solution combustion synthesis (SCS) is reported for red LEDs and a component of w-LEDs. Single-step solution combustion synthesized $LiAl_5O_8$: $Eu^{3+}/Cr^{3+}/Fe^{3+}$ nano phosphors that have biomedical and LEDs applications are investigated systematically.

Chapter 1: A brief introduction about the classification, principle and nature of luminescence is discussed in this chapter. Optical transitions of 4*f*-4*f*, 4*f*-5*d* transitions of lanthanides and 3*d*-3*d* transitions of transition metal ions are surveyed. This chapter also explains the energy transfer mechanism in photoluminescence and thermally stimulated luminescence processes. Moreover, the significance of a suitable host for good luminescent material, the gap areas and the motivations of the thesis work are presented.

Chapter 2: This chapter reports a detailed procedure of the synthesis routes followed for the preparation of phosphors and the characterization tools used for investigation. $MBPO_5$: Ce and $MBPO_5$: Eu/Gd phosphors have been prepared through conventional solid-state synthesis routes while the phosphors $BaCeO_3$: Eu and $LiAl_5O_8$: Eu/Cr/Fe are prepared via a facile solution combustion synthesis route. The characterization techniques used in this thesis work include X-ray diffraction (XRD), X-ray absorption spectroscopy (XAS), scanning electron microscopy (SEM), diffuse reflectance spectroscopy (DRS), spectrophotometry photoluminescence (PL), PL lifetime, time-resolved emission spectroscopy (TRES), thermally stimulated luminescence spectroscopy (TSL) and positron annihilation lifetime spectroscopy (PALS) are discussed.

Chapter 3: It presents the characterization and optical properties of Ce^{3+} in $SrBPO_5$ host prepared through the solid-state synthesis in an air atmosphere. The structure, morphology, band gap and luminescence properties of the phosphors are also investigated. Ce^{3+} doped phosphors are of interest as they give UVA (320-400 nm) emission whose utility is exploited in (i) security industry (ii) sensing fluorescent levels (ii) lithography and (iv) scintillators. The chapter deals with the study on the nature defects by positron annihilation lifetime spectroscopy (PALS), site occupancy of Ce^{3+} by time-resolved emission spectroscopy (TRES) and dosimetric properties of the glow curve by thermally stimulated luminescence (TSL) in SBP: Ce phosphors. With regard to the TSL mechanism, the generation of glow curve from the luminescent center (Ce^{3+}) is established. In chapter 3, a comparative luminescence study of Ce^{3+} among $SrBPO_5$, $CaBPO_5$ and $BaBPO_5$ hosts is also presented.

Chapter 4: Gd^{3+} activated phosphors that give narrow emission at 313 nm (UVB region) are known for treating specific skin alignments such as psoriasis and eczema. In chapter 4, the luminescence of Gd^{3+} in $SrBPO_5$ is optimized. The effect of Gd codoping on the PL and TSL properties of $SrBPO_5$: Eu phosphors are studied. The efficient energy transfer between Gd^{3+} and Eu^{3+}, the formation of Eu^{2+} in the absence of reducing atmosphere and possible mechanism of valency conversion of Eu^{2+} to Eu^{3+} in the presence of Gd^{3+} are explained in detail. This study is relevant towards making efficient orange-red LEDs (SBP: Eu^{3+}, Gd^{3+}), blue LEDs for solid-state lighting and neonatal care (SBP: Eu^{2+}) and phototherapy (SBP: Gd^{3+}). In chapter 4, in addition to PL, TSL investigations on SBP: Eu, SBP: Gd and SBP: Eu, Gd are reported in detail for the first time. The mechanism of TSL in SBP: Eu, SBP: Gd and SBP: Eu, Gd and calculation of trap parameters are presented. The chapter highlights the favorable TSL characteristics of SBP: Eu, Gd phosphor that has shown a linear dose-response covering two orders of magnitude in the dose range of 100 mGy-10Gy and useful trap parameters and therefore making the system suitable for radiation dosimetry. In the present thesis, the local coordination environment of Eu^{3+} has been investigated in $SrBPO_5$ host lattice using the X-ray absorption spectroscopy. In the present study, the basis for choosing Gd^{3+} as a codopant along with Eu^{3+} in alkaline earth borophosphate hosts is to enhance Eu^{3+} luminescence by energy transfer (ET) from Gd^{3+} to Eu^{3+}. In addition to the energy transfer, surprisingly Gd^{3+} facilitates the valency conversion of $Eu^{2+} \rightarrow Eu^{3+}$ which has not been reported so far, to the best of our knowledge and is addressed in the present work. A comparative study of the luminescence properties of $Gd^{3+,}$ Eu^{3+} and Eu^{2+} in these hosts is addressed to find out the optimum luminescence towards LEDs applications.

Chapter 5: In chapter 5, the PL and TSL properties of europium doped perovskite structured $BaCeO_3$ prepared through a facile solution combustion synthesis in an air atmosphere at different calcination temperatures (1000-1300 °C) are presented. Change in morphology and particle size as a function of calcination temperature, the observed difference in PL spectra of $BaCeO_3$: Eu samples at 77 and 300 K, the variation of asymmetric ratio as a function of dopant concentration, excitation wavelength and temperature are explained in detail. The color purity of Eu^{3+} in $BaCeO_3$ has been optimized w.r.t Eu-concentration and calcination temperature which resulted in an intense red emission with a higher color coordinates compared to the readily available red phosphors, suggesting it as a suitable candidate for red phosphor. The use of TRES and lifetime studies to determine the site occupancy of Eu^{3+} and the use of positron annihilation spectroscopy to study the defects caused by barium and oxygen are discussed. Thermally stimulated luminescence indicated multiple trap sites, and the intensity was linear with γ-dose in the range of 0-1000 Gy suggesting the possibility of using this material as a high dose radiation dosimetry phosphor.

Chapter 6: It presents the investigation of the optical properties of trivalent europium, iron and chromium activated lithium aluminate ($LiAl_5O_8$) nano phosphors consisting of spherical particles with an average size of 60 nm. The $LiAl_5O_8$ samples prepared at 600 ^oC form a single-phase cubic lattice. The study reports about the exact local coordination environment of dopants as determined by X-ray absorption spectroscopy studies for the first time. Apart from Cr^{3+} and Fe^{3+}, Eu^{3+} doped lithium aluminate is also investigated as a structural probe and also compared its emission characteristics with those of Cr^{3+} and Fe^{3+} as all the three strongly emit in the red region. The influences of calcination temperature, activator concentrations, excitation wavelength for all the three ions doped in lithium aluminate has been investigated. The site symmetry information is obtained probing Eu^{3+} in the samples. The cause of the observed unusual broad emission of Fe^{3+} in the NIR region and the sharp emission of Cr^{3+} in the deep red region is also presented in detail. It may be added that lithium aluminate contains a trace level of Cr^{3+} and Fe^{3+} as impurities which have also been qualitatively and quantitatively estimated. The activators in this host exhibit intense red and NIR emission with 100% color purity suggesting potential candidates as red phosphors and in biomedical applications.

Chapter 7: This chapter concludes the major findings of the present work and scope for the future work in this direction.

References

1. Dramićanin, M., *Luminescence Thermometry: Methods, Materials, and Applications*. Woodhead Publishing: 2018.
2. Grabmaier, B., *Luminescent materials*. Springer Verlag: 1994.
3. Bhargava, S. *Journal of Physics C: Solid State Physics* **1986,** 19, (35), 7045.
4. Jimenez-Becerril, J.; Bosch, P.; Bulbulian, S. *Journal of nuclear materials* **1991,** 185, (3), 304-307.
5. Terada, S.; Nagashima, I.; Higaki, K.; Ito, Y. *Journal of power sources* **1998,** 75, (2), 223-229.

6. Kawamura, Y.; Nishikawa, M.; Tanaka, K.; Matsumoto, H. *Journal of Nuclear Science and Technology* **1992,** 29, (5), 436-444.
7. Mukhopadhyay, L.; Rai, V. K.; Bokolia, R.; Sreenivas, K. *Journal of Luminescence* **2017,** 187, 368-377.
8. Zhou, J.; Teng, Y.; Zhou, S.; Qiu, J. *International Journal of Applied Glass Science* **2012,** 3, (4), 299-308.
9. Van Eijk, C. W. *Nuclear Instruments and Methods in Physics Research Section A: Accelerators, Spectrometers, Detectors and Associated Equipment* **2001,** 460, (1), 1-14.
10. Stranks, S. D.; Snaith, H. J. *Nature nanotechnology* **2015,** 10, (5), 391.
11. Ning, Y.; Zhu, M.; Zhang, J.-L. *Coordination Chemistry Reviews* **2019,** 399, 213028.
12. Castaing, V.; Sontakke, A. D.; Fernández-Carrión, A. J.; Touati, N.; Binet, L.; Allix, M.; Gourier, D.; Viana, B. *European Journal of Inorganic Chemistry* **2017,** 2017, (44), 5114-5120.
13. Ueda, J.; Leaño, J. L.; Richard, C.; Asami, K.; Tanabe, S.; Liu, R.-S. *Journal of Materials Chemistry C* **2019,** 7, (6), 1705-1712.
14. Xu, D.; Wu, X.; Zhang, Q.; Li, W.; Wang, T.; Cao, L.; Meng, J. *Journal of Alloys and Compounds* **2018,** 731, 156-161.
15. Blasse, G.; Bril, A. *The Journal of Chemical Physics* **1969,** 50, (7), 2974-2980.
16. Lakowicz, J. R., Introduction to fluorescence. In *Principles of fluorescence spectroscopy*, Springer: 1999; pp 1-23.
17. Henderson, B.; Imbusch, G. F., *Optical spectroscopy of inorganic solids*. Oxford University Press: 2006; Vol. 44.
18. Damhus, T.; Hartshorn, R.; Hutton, A. *Chemistry International* **2005**.
19. Voncken, J., The rare earth elements—a special group of metals. In *The Rare Earth Elements*, Springer: 2016; pp 1-13.
20. Carnall, W.; Goodman, G.; Rajnak, K.; Rana, R. *The Journal of Chemical Physics* **1989,** 90, (7), 3443-3457.
21. Tāle, I.; Kūlis, P.; Kronghauz, V. *Journal of Luminescence* **1979,** 20, (4), 343-347.
22. Peng, M.; Pei, Z.; Hong, G.; Su, Q. *Chemical Physics Letters* **2003,** 371, (1-2), 1-6.
23. Pei, Z.; Su, Q.; Zhang, J. *Journal of Alloys and Compounds* **1993,** 198, (1-2), 51-53.
24. Blasse, G.; Bril, A.; De Vries, J. *Journal of Inorganic and Nuclear Chemistry* **1969,** 31, (2), 568-570.
25. Blasse, G.; Grabmaier, B., How Does a Luminescent Material Absorb Its Excitation Energy? In *Luminescent materials*, Springer: 1994; pp 10-32.
26. Yang, J.; Quan, Z.; Kong, D.; Liu, X.; Lin, J. *Crystal growth & design* **2007,** 7, (4), 730-735.
27. Li, J.-G.; Li, X.; Sun, X.; Ishigaki, T. *The Journal of Physical Chemistry C* **2008,** 112, (31), 11707-11716.
28. Binnemans, K. *Coordination Chemistry Reviews* **2015,** 295, 1-45.
29. Singh, V.; Borkotoky, S.; Murali, A.; Rao, J.; Rao, T. G.; Dhoble, S. *Spectrochimica Acta Part A: Molecular and Biomolecular Spectroscopy* **2015,** 139, 1-6.
30. Vecht, A.; Newport, A.; Bayley, P.; Crossland, W. *Journal of applied physics* **1998,** 84, (7), 3827-3829.
31. Abdullah, M.; Waris, A.; Sutrisno, W.; Nurhasanah, I.; Vioktalamo, A. S. *Powder technology* **2008,** 183, (2), 297-303.
32. Blasse, G.; Van den Heuvel, G.; Van Dijk, T. *Chemical Physics Letters* **1979,** 62, (3), 600-602.

33. Bessière, A.; Jacquart, S.; Priolkar, K.; Lecointre, A.; Viana, B.; Gourier, D. *Optics express* **2011,** 19, (11), 10131-10137.
34. Teixeira, V.; Silva, A.; Manali, I.; Gallo, T.; Galante, D.; Ferreira, N.; Andrade, A.; Rezende, M. d. S. *Optical Materials* **2019,** 94, 160-165.
35. Abritta, T.; de Souza Barros, F. *Journal of Luminescence* **1988,** 40, 187-188.
36. Blasse, G.; De Korte, P.; Mackor, A. *Journal of Inorganic and Nuclear Chemistry* **1981,** 43, (7), 1499-1503.
37. Xia, M.; Wu, X.; Zhong, Y.; Hintzen, H. B.; Zhou, Z.; Wang, J. *Journal of Materials Chemistry C* **2019,** 7, (10), 2927-2935.
38. McKeever, S. W., *Thermoluminescence of solids*. Cambridge University Press: 1988; Vol. 3.
39. Pagonis, V.; Kitis, G.; Furetta, C., *Numerical and practical exercises in thermoluminescence*. Springer Science & Business Media: 2006.
40. Omanwar, S.; Koparkar, K.; Virk, H. S. In *Recent advances and opportunities in tld materials: a review*, Defect and Diffusion Forum, 2014; Trans Tech Publ: pp 75-110.
41. Matthews, R.; Stoebe, T. *Journal of Physics C: Solid State Physics* **1982,** 15, (30), 6271.
42. Park, S.; Mho, S.; Kim, C.; Jeong, B.; Park, H. *Solid state communications* **1992,** 83, (1), 47-52.
43. Karthikeyani, A.; Jagannathan, R. *Journal of luminescence* **2000,** 86, (1), 79-85.
44. Reis, S.; Karabulut, M.; Day, D. *Journal of Non-Crystalline Solids* **2001,** 292, (1-3), 150-157.
45. Baginskiy, I.; Liu, R.; Wang, C.; Lin, R.; Yao, Y. *Journal of The Electrochemical Society* **2011,** 158, (10), P118.
46. Kim, J. S.; Park, Y. H.; Kim, S. M.; Choi, J. C.; Park, H. L. *Solid state communications* **2005,** 133, (7), 445-448.
47. Ming, Z.; Qiao, J.; Molokeev, M. S.; Zhao, J.; Swart, H. C.; Xia, Z. *Inorganic Chemistry* **2020,** 59, (2), 1405-1413.
48. Das, A.; Saha, S.; Panigrahi, K.; Ghorai, U. K.; Chattopadhyay, K. K. *Microscopy and Microanalysis* **2019**, 1-9.
49. Shannon, R. D. *Acta crystallographica section A: crystal physics, diffraction, theoretical and general crystallography* **1976,** 32, (5), 751-767.
50. Kharabe, V.; Oza, A. H.; Dhoble, S. *Optik-International Journal for Light and Electron Optics* **2015,** 126, (23), 4544-4547.
51. Su, Q.; Liang, H.; Hu, T.; Tao, Y.; Liu, T. *Journal of alloys and compounds* **2002,** 344, (1-2), 132-136.
52. Zhou, X.; Yang, X.; Wang, Y.; Zhao, X.; Li, L.; Li, Q. *Journal of Alloys and Compounds* **2014,** 608, 25-29.
53. Peng, M.; Pei, Z.; Hong, G.; Su, Q. *Journal of Materials Chemistry* **2003,** 13, (5), 1202-1205.
54. Dai, W.; Lei, Y.; Yu, T.; Peng, M.; Zhang, Q. *Materials Research Bulletin* **2015,** 67, 176-184.
55. Sakasai, K.; Katagiri, M.; Toh, K.; Takahashi, H.; Nakazawa, M.; Kondo, Y. *Applied Physics A* **2002,** 74, (1), s1589-s1591.
56. Liang, H.; Su, Q.; Lu, S.; Tao, Y.; Hu, T.; Liu, T. *Materials research bulletin* **2002,** 37, (12), 1981-1989.
57. Han, B.; Zhang, J.; Lü, Y.; Liu, Y.; Cui, Q. *Russian Journal of Physical Chemistry A* **2014,** 88, (1), 143-148.
58. Taniguchi, N.; Kuroha, T.; Nishimura, C.; Iijima, K. *Solid State Ionics* **2005,** 176, (39-40), 2979-2983.

59. Kulkarni, A.; Ciacchi, F.; Giddey, S.; Munnings, C.; Badwal, S.; Kimpton, J.; Fini, D. *International Journal of Hydrogen Energy* **2012,** 37, (24), 19092-19102.
60. Van Pieterson, L.; Soverna, S.; Meijerink, A. *Journal of The Electrochemical Society* **2000,** 147, (12), 4688-4691.
61. Melekh, B.-T.; Egorov, V.; Baikov, Y. M.; Kartenko, N.; Filin, Y. N.; Kompan, M.; Novak, I.; Venus, G.; Kulik, V. *Solid State Ionics* **1997,** 97, (1-4), 465-470.
62. Zhang, C.; Jiang, W.; Yang, X.; Han, Q.; Hao, Q.; Wang, X. *Journal of Alloys and Compounds* **2009,** 474, (1-2), 287-291.
63. Jadhav, S.; Patil, S.; Bhosale, C.; Puri, V.; Jadhav, L. *Journal of Materials Science: Materials in Electronics* **2015,** 26, (7), 4854-4861.
64. Yamanaka, S.; Fujikane, M.; Hamaguchi, T.; Muta, H.; Oyama, T.; Matsuda, T.; Kobayashi, S.-i.; Kurosaki, K. *Journal of Alloys and Compounds* **2003,** 359, (1-2), 109-113.
65. Katahira, K.; Kohchi, Y.; Shimura, T.; Iwahara, H. *Solid State Ionics* **2000,** 138, (1-2), 91-98.
66. Pasierb, P.; Wierzbicka, M.; Komornicki, S.; Rekas, M. *Journal of Power Sources* **2009,** 194, (1), 31-37.
67. Kompan, M.; Baikov, Y. M.; Melekh, B.-T.; Volchek, B. *Solid state ionics* **2003,** 162, 1-5.
68. Kompan, M.; Baikov, Y. M.; Melekh, B.-T.; Yakubovich, A. *Physics of the Solid State* **2002,** 44, (7), 1263-1267.
69. Giannici, F.; Longo, A.; Balerna, A.; Martorana, A. *Chemistry of Materials* **2009,** 21, (4), 597-603.
70. Gorbova, E.; Maragou, V.; Medvedev, D.; Demin, A.; Tsiakaras, P. *Journal of Power Sources* **2008,** 181, (2), 207-213.
71. Suriyamurthy, N.; Panigrahi, B.; Natarajan, A. *Materials Science and Engineering: A* **2005,** 403, (1-2), 182-185.
72. Kale, M.; Joshi, C.; Moharil, S. *International Journal of Self-Propagating High-Temperature Synthesis* **2012,** 21, (1), 19-24.
73. Singh, V.; Chakradhar, R.; Rao, J.; Kwak, H.-Y. *Solid state sciences* **2009,** 11, (4), 870-874.
74. de Sousa, O. M. *Computational and Theoretical Chemistry* **2018,** 1123, 96-101.
75. Silva, A. J.; Nascimento, P. A.; Andrade, A. B.; Sampaio, D. V.; Moulton, B. J.; Silva, R. S.; Rezende, M. V. d. S. *Journal of Luminescence* **2018,** 199, 298-301.
76. Pitale, S. S.; Kumar, V.; Nagpure, I.; Ntwaeaborwa, O.; Swart, H. *Current Applied Physics* **2011,** 11, (3), 341-345.
77. Pitale, S. S.; Kumar, V.; Nagpure, I.; Ntwaeaborwa, O.; Coetsee, E.; Swart, H. *Journal of Applied Physics* **2011,** 109, (1), 013105.
78. Mohapatra, M.; Seshadri, M.; Naik, Y.; Meena, G.; Kadam, R.; Singh, V. *Journal of Materials Science: Materials in Electronics* **2018,** 29, (9), 7778-7784.
79. Singh, V.; Rao, T. G. *Journal of Solid State Chemistry* **2008,** 181, (6), 1387-1392.
80. Singh, V.; Chakradhar, R.; Rao, J.; Kim, D.-K. *Materials Chemistry and Physics* **2008,** 110, (1), 43-51.
81. Li, X.; Jiang, G.; Zhou, S.; Wei, X.; Chen, Y.; Duan, C. K.; Yin, M. *Sensors and Actuators B: Chemical* **2014,** 202, 1065-1069.
82. Shu, W.; Qiang, R.; Xiao, S.; Yang, X.; Ding, J. *Journal of alloys and compounds* **2011,** 509, (9), 3886-3888.
83. Kniec, K.; Tikhomirov, M.; Pozniak, B.; Ledwa, K.; Marciniak, L. *Nanomaterials* **2020,** 10, (2), 189.

84. Li, Z.; Zhang, Y.; Wu, X.; Wu, X.; Maudgal, R.; Zhang, H.; Han, G. *Advanced Science* **2015,** 2, (3).
85. Hashimoto, S.; Hattori, K.; Inoue, K.; Nakahashi, A.; Honda, S.; Iwamoto, Y. *Materials Research Bulletin* **2009,** 44, (1), 70-73.
86. Kobayashi, R.; Tamura, H.; Kamada, Y.; Kakihana, M.; Matsushima, Y. *ECS Transactions* **2018,** 88, (1), 225.

Table of Contents

Friday, May 14, 2021

Chapter 2

Experimental techniques

2.0. Introduction

This chapter describes a detailed account of the synthesis methods and characterization techniques carried out to study the structural, morphological and optical properties of phosphors. There are mainly two routes to synthesis phosphors, i.e. solid-state reaction and wet chemical reaction. The wet chemical methods include combustion, sol-gel, hydrothermal and co-precipitation syntheses, etc. The synthesis routes adopted in the present work were the conventional solid-state reaction (SSR) and facile solution combustion synthesis routes (SCS). The spectroscopic characterization techniques carried out were XRD, XAS, SEM, DRS, PL, TRPL, TRES, TSL glow curve, TSL emission and PALS.

2.1. Methods of synthesis

The route of synthesis of phosphor depends on the nature of the phosphor compound and the reactants. Each route plays a different role in the synthesis of the desired phosphor since its optical properties are greatly affected by synthesis routes. A phosphor is expected to exhibit high luminescence and to have that it should have good particle characteristics like uniform particles of smaller size and spherical morphology, minimum agglomeration, high crystallinity, homogeneous dopant distribution and high density, etc. These powder characteristics of a phosphor influence the conversion of UV/VIS light, color coordinates, decay time and so on. Hence, the synthesis route plays a distinctive role in its luminescence properties.[1]

2.1.1. Solid-state reaction (SSR) route

Usually, the conventional SSR route is followed to synthesize phosphors due to its simplicity. Most of the phosphors with hosts viz. borates, phosphates, borophosphates, oxides, silicates, and aluminates, etc. can be synthesized through the SSR route. The present work involves the synthesis of lanthanide doped alkaline earth borophosphate ($MBPO_5$: Ln; M=Ca, Sr, Ba) by SSR in the air atmosphere. In this route, the stoichiometric amounts of precursors, MCO_3 (Sigma Aldrich, >99.9%), H_3BO_3 (Fluka, >99.5%), $(NH_4)_2HPO_4$ (Merck, >98%) and Ln_2O_3 (Alfa Aesar, 99.99%) were ground thoroughly in solid-state using a mortar and pestle for 30 minutes to ensure homogenous mixing of reactant mixtures, and pelletized using a hydraulic pellet press. Palletization makes diffusion better as the precursors are closely compacted. Pellets were first pre-calcined at 500 °C for 5 h in a muffle furnace and then cooled naturally to room temperature. The pre-calcination removes the moisture and secondary products as given in Equation (2.1).

$$\begin{gathered}\boldsymbol{M_{1-x}CO_3 + \frac{x}{2}Ln_2O_3 + H_3BO_3 + (NH_4)_2HPO_4 \rightarrow} \\ \boldsymbol{M_{1-x}Ln_xBPO_5 + 3H_2O \uparrow + 2NH_3 \uparrow + CO_2 + \frac{3x}{4}O_2 \uparrow}\end{gathered} \qquad \textbf{(2.1)}$$

The pre-calcined pellets of $SrBPO_5$ samples were ground, pelletized and calcined at 1000 °C for 5 h, respectively, and subsequently left to cool naturally. For the comparative study, Ce/Eu/Gd activated $CaBPO_5$, $SrBPO_5$ and $BaBPO_5$ samples were prepared through the same SSR route calcined at 950, 1000 and 900 °C, respectively, for 10 h in the air atmosphere. The samples were then ground and taken for different characterizations. The calcination at elevated temperature improves the packing, crystallinity, homogeneity and morphology of the phosphor particles. SSR route needs repeated grinding to reduce particle size and heat treatment for better homogeneity of dopants. Since the increase in calcination temperature increases crystallinity as well as the agglomeration, the calcination temperature was optimized for obtaining maximum luminescence. $MBPO_5$ phosphors were synthesized adopting the SSR route as they cannot be prepared through the SCS route.

The SSR route follows the decomposition of the precursors, synthesis of host lattice and incorporation of the dopant by diffusion.[2] Decomposition of the precursor during calcination yields finer and reactive intermediate of the precursors which react in an in-situ manner to form the host lattice. The synthesis step takes a longer time as well as elevated temperature to favor the thermodynamics to achieve an appreciable reaction rate for completion of the reaction without leaving behind any unreactive intermediate. The most crucial step is the diffusion of dopant into the host lattice in a uniform manner that needs a long time and repeated heat treatment. The samples were prepared in a recrystallized alumina boat having a melting point (1900 °C) higher than that of the samples to avoid contamination. Since the SSR route is a diffusion-controlled reaction, it needs elevated temperature and extended time for calcination. This leads to several drawbacks like microcrystalline particles, nonuniformity in size, coarse surface and large agglomeration.

On the other hand, the presence of flux like H_3BO_3, NH_4Cl, $(NH_4)_2HPO_4$, $NH_4H_2PO_4$, etc., greatly influences the crystallization process. Basically, the presence of flux enhances the crystallization process lowering the calcination temperature and time by reducing the activation energy of the reaction. Usually, flux is added in a very small quantity (<5%) so that the added flux should not participate in any unwanted phase formation. Notably, in case of alkaline earth borophosphate, the host cations (M=Ca, Sr, Ba) have comparable ionic radii to that of lanthanide dopants. Hence, its incorporation/diffusion into the host lattice occurs easily.[3] Many phosphors were reported to show phase transitions with the increase in calcination temperature[4] indicating low thermal and chemical stability. Therefore, the phosphors were calcined at different temperatures and their phase purities were checked.

2.1.2. Solution combustion synthesis (SCS) route

The solution combustion synthesis is a facile wet chemical method to synthesize phosphors that yield higher luminescence as compared to the SSR route. The SCS route is a rapid synthesis route that does not need prolonged heat treatment and elevated temperature. Most ceramic oxide[5] phosphors are prepared from their nitrates through this route in the presence of some oxidizer called fuel. The commonly used fuels are urea (NH_2CONH_2), citric acid ($C_6H_8O_7$), glycine (NH_2CH_2COOH), hexamethylene tetraamine ($C_6N_4H_{12}$) and hydrazine (NH_2NH_2). In the present synthesis, the nitrate precursors and urea (as fuel) were dissolved in deionized water (~20-30 mL) in a tall beaker and heated at 120-150 °C to vaporize H_2O with constant stirring for better mixing on a magnetic hot plate till it formed froth. Then it was transferred to the muffle furnace that was maintained at 500-700 °C. Within a couple of minutes, it was ignited producing voluminous ultrafine powders. Then it was left to cool naturally. The ignition of the fuel is instantaneous and highly exothermic that provides sufficient heat to achieve the reaction rate for forming the compound. It is associated with the evolution of a large number of secondary gases leading to particles of the smaller size. It is sometimes called self-propagating high-temperature synthesis. The voluminous powder is nicely ground, pelletized and calcined at low calcination temperature for a few hours to improve the crystallinity, density and uniformity of dopant, etc. For getting optimum ignition from the phosphors, the oxidizer to fuel ratio (φ) is maintained to unity.[6] The value of φ is calculated by using Equation (2.2).[7]

$$\boldsymbol{\varphi} = \frac{\sum \boldsymbol{valency \times coefficient\ of\ oxidising\ elements\ in}}{\sum \boldsymbol{valency \times coefficient\ of\ reducing\ elements\ in}} \qquad \textbf{(2.2)}$$

The salient feature of the phosphors that were prepared through the SCS route are:

- Avoids elevated temperature, prolong calcination and large agglomeration.
- Low synthesis temperature minimizes the sub-stoichiometry of composition.
- Have spherical shape and nano-sized particles with narrow size distribution.
- Uniform distribution of the dopant in the host lattice is easily achieved.

In the present work, $BaCeO_3$: Eu and $LiAl_5O_8$: Eu, Fe, Cr phosphors were synthesized through the facile SCS route. The $BaCeO_3$ samples were heated at 700 °C for 5 min. to complete the combustion. Thereafter, the as-prepared $BaCeO_3$ samples were ground, pelletized and calcined at 1000-1300 °C for 5 h in the air atmosphere. However, the $LiAl_5O_8$ samples were just heated at 600 °C for 5 min. to complete the combustion without any calcination.

2.2. Characterization techniques

2.2.1. Powder X-ray diffraction (XRD) technique

X-ray diffraction pattern is a fingerprint technique for the identification of crystalline materials. It is an effective and non-destructive technique for determining the crystal structure and phase of materials. It is the foremost characterization technique to confirm the formation of the crystalline compound. It is based on the constructive interference of monochromatic X-rays of a powder crystalline sample. When an incident beam of X-rays interacts with the target atom, X-ray photons are scattered in different directions. Scattering waves may be elastic or inelastic. When the scattering waves are in-phase and out-of-phase give rise to constructive and destructive interference, respectively. Generally, X-rays generated from a cathode ray tube are filtered and collimated to produce monochromatic radiation that falls directly on the sample. For parallel planes of atoms, with a spacing d_{hkl}, constructive interference occurs only when the Bragg's law i.e., $n\lambda = 2d_{hkl} \sin\theta$, is satisfied. In order to keep the diffracted beams in phase, their path difference must be a whole number (n) multiple of $\lambda_{X\text{-ray}}$. The sample is scanned over a range of 2θ angles to get the complete diffraction pattern. In case of the crystalline sample, atoms in crystal planes form a periodic array of coherent scatterers. Diffraction from different parallel planes of atoms produces a diffraction pattern.

In case of a polycrystalline powder sample, all possible diffraction directions of the lattice can be obtained as sufficient microcrystals are randomly orientated in possible directions of the powdered material. The powder XRD measurements were recorded in reflection mode using a PW-1071, Philips diffractometer with Cu-K_α radiation (λ =1.5406 Å) continuously scanning from 10° to 80° with a scan step of 0.02-0.05° s^{-1}. The diffractometer is a θ:2θ type system where the source tube is fixed while the sample and detector rotate to scan the complete range of 2θ. Usually, the K_α radiation is generated by bombarding accelerated electrons on the target surface (Cu, Fe, Cr, Co). Most commonly, a copper target is used for generating K_α radiation (1.5406 Å). It uses nickel as a K_β filter to allow only K_α radiation and a silicon wafer with a (911) plane as a sample holder as it has a low X-ray background with no diffraction peaks. It uses NaI: Tl as a scintillation detector for signaling the diffracted beams. The X-ray diffraction pattern shows the intensity of the diffraction peak as a function of the detecting angle (2θ). The obtained XRD pattern was matched with the available standard ICDD (International Centre for Diffraction Data). The structure of the compound was obtained using VESTA software.

2.2.2. X-ray absorption spectroscopy (XAS) technique

X-ray absorption spectroscopy is an advanced technique to probe the local structure and oxidation states in depth. It employs a synchrotron X-ray beam as an excitation source that is produced when an electron beam is accelerated radially in the presence of a strong magnetic field. The XAS is the combination of X-ray absorption near edge structure (XANES) and extended X-ray absorption fine structure (EXAFS) studies. XANES involves the electronic transition from core-shell to an unoccupied state revealing the possible oxidation states, whereas EXAFS involves the single scattering of the photoelectron by surrounding atoms indicating the local coordination. XANES relates to the bound discrete states as it occurs below the ionization potential whereas EXAFS relates to the free continuum states as it occurs above the ionization potential of the absorbing atom.[8] It may be noted that above the IP the absorption cross-section attenuates[9] gradually with the X-ray energy. EXAFS deals with the analysis of the X-ray absorption beyond the X-ray absorption edge (XANES) where electrons/scattered waves undergo sinusoidal oscillation.[10] XANES provides information on symmetry and electronic transitions whereas EXAFS tells about the local coordination and bond distance, etc., within an exact distance between the atom and neighboring atom (R) as the absorption cross-section proportional to R^{-2}. So, EXAFS analysis turns out to be a powerful technique for local structure determination of amorphous, polycrystalline, polymers and solutions under different ambient and extreme environmental conditions.[11] The present work involves XAS analysis of $LiAl_5O_8$: Eu, Fe samples. The XAS measurements[12] were carried out at Beamline-9, Indus-2, Raja Ramana Centre for Advanced Technology (RRCAT), Indore, India using a synchrotron source of 2.5 GeV and 200 mA.

2.2.3. Scanning electron microscopy (SEM) technique

Scanning electron microscopy technique images the morphology by utilizing the interaction of the incident electron beam with the sample when scanned in a raster pattern across it. The electron beam is generated by thermionic emission from the electron gun using resistive heating to produce the source beam.[13] The electron beam passing through the electromagnetic lenses interacts with the sample. The interaction leads to two types of scattering viz. inelastic and elastic. The inelastically scattered electrons are produced from the sample after bombarded by the incident electron beam are called secondary electrons (SE). On the other hand, the elastically scattered electrons are produced due to the deflection of the incident electron beam upon interaction with the sample's atomic nucleus or electrons of comparable energy are called a backscattered electron (BSE). Both the SE and BSE are captured by a detector to produce surface-driven information. Secondary electrons originate from the surface of the sample and are more pronounced with low atomic number elements. By contrast, the backscattered electrons originate from deeper regions of the sample and are more pronounced with higher atomic numbers elements.[14] Imaging can be done either by SE or BSE mode. BSE mode involves the detection of the incident electron beam at higher energy (>50 eV) and a higher angle (>90°) and provides better information about the morphology. In the present thesis, the SEM images of $MBPO_5$, $BaCeO_3$ and $LiAl_5O_8$ samples were recorded using Carl Zeiss, Crossbeam-340 instrument. It has a flood gun as an electron beam source and an Inlens duo detector that captures both SE and BSE sequentially. It gives maximum flexibility for performing in-situ experiments having a variable pressure and outgassing samples that enable high-resolution images. The average size and distribution of the particles were analyzed using ImageJ software.

2.2.4. Diffuse reflectance spectroscopy (DRS) technique

Diffuse reflectance spectroscopy is an unambiguous technique to determine the band gap (E_g) by recording the reflectance spectrum of a powder sample using a UV-VIS spectrophotometer. Different methods are used for determining E_g based on the sample's physical and chemical properties. For example, for transparent material by recording either transmittance[15] or absorption spectrum[16], for semiconducting material by recording resistivity at different temperatures[17] and for opaque powder by recording the reflectance[18] spectrum. As the solid powder does not allow the light to pass through it, the reflectance method is preferred. When UV-VIS light falls on the solid powder some of the photons get absorbed, some get reflected and some after getting diffused get reflected and detected by an integrating sphere to provide reflectance spectrum as a function of wavelength. The diffuse reflectance spectra of the samples were recorded using a UV-VIS 2600 spectrophotometer, Shimadzu. The spectrophotometer has mainly four parts viz., excitation sources, monochromators, sample chamber and integrating sphere.

Excitation sources: The UV-VIS 2600 spectrophotometer has a dual excitation source, i.e., Tungsten-Iodine (W-I) lamp that emits UV light in 230-400 nm and a Deuterium (D_2) lamp that emits VIS light in 400-800 nm range. The instrument scans from lower energy to higher energy and the D_2 lamp switches off automatically to the W-I lamp in its respective region combinedly giving the excitation energy in the range of 230-800 nm. The

W-I lamp is an incandescent source consisting of tungsten filament and iodine mixed with inert gas. An ordinary incandescent lamp has only tungsten filament with low light output and lesser lifetime. The evaporated tungsten gradually gets deposited onto the inner surface of the bulb and blackens it and the filament gets weak and breaks with less operational hours. To resolve this, the lamp is filled with a mixture of iodine and inert gases. The iodine reacts with the evaporated tungsten and is given away by the inert gases throughout the bulb and dissociated at the filament as the temperature is quite high there giving back the evaporated tungsten to the filament. Thus, the tungsten-halogen cycle keeps the bulb clean as well as maintains constant output throughout the bulb’s lifetime. The lamp has a longer lifetime of 2000 hours.

Monochromator: The monochromator consists of the entrance slit, mirrors, grating, and exit slit that gives a monochromatic light to fall on the sample and the detector.

Sample chamber: It has two slots for keeping the sample and reference in their designated slot marked as S-slot and R-slot. Before recording the sample, barium sulfate ($BaSO_4$) powder is uniformly compacted in two solid disc/ sample holders and are placed in both the slot to begin the initialization process. As both the slots contain $BaSO_4$, so it nullifies the signal giving the baseline correction. $BaSO_4$ does not absorb in the UV-VIS range giving nearly 100% reflectance. The sample of interest is made by spreading uniformly 50 mg of the sample at the center over the $BaSO_4$ and compacted by applying pressure by means of a glass rod. For recording the reflectance spectrum of the sample, the pure $BaSO_4$ present in the S-slot is replaced by the sample of interest and keeping the reference slot intact. The reflectance spectrum was recorded in the wavelength range of 230-800 nm with an interval of 0.5 nm in a single scan mode. The slit width was kept 5 nm for all the measurements. The threshold of the instrument was set at 0.001 so that any peak above this value could appear as a signal. The accumulation time was set at 0.2 with stair correction off and normal S/R exchange. These parameters were set before recording the required reflectance spectra. It has an in-built software that can transform the recorded reflectance spectrum into the corresponding absorption spectrum using the Kubelka-Munk function. The values of reflectance or absorbance were noted either by peak-pick (automatic) or point-pick (manual) methods.

Estimation of E_g: In the present work, the values of E_g for all the phosphors were obtained following Kubelka-Munk Equations.[18, 19] The λ (nm) was converted into energy, E (eV) using Equation (2.3). The reflection coefficient (R) was obtained using Equation (2.4). K-M constant was calculated using Equation (2.5), where k relates to the absorption coefficient = $(1\text{-R})^2$ and S relates to the scattering coefficient = 2R. In the plot of E versus $[(k/s) * E)]^2$, the value of E_g was obtained by extrapolating the straight line in the graph at k=0.

$$\boldsymbol{E\ (eV) = \frac{1240}{\lambda\ (nm)}} \qquad \textbf{(2.3)}$$

$$\mathbf{R} = \frac{\textbf{Sample reflectance}}{\boldsymbol{BaSO_4}\ \textbf{reflectance}} = \frac{\mathbf{I}}{\mathbf{100}} \qquad \textbf{(2.4)}$$

$$\boldsymbol{\frac{k}{s} = \frac{(1 - R)^2}{2R}} \qquad \textbf{(2.5)}$$

In the present thesis, the E_g of $MBPO_5$ and $BaCeO_3$ samples was estimated following the above-mentioned procedures.

2.2.5. Photoluminescence (PL) technique

Photoluminescence is a highly sensitive and non-destructive technique employed to study the luminescent properties of phosphor. The luminescence properties can be derived from the excitation and emission spectra and their decay time measurements. Some of the important luminescence properties include the sample excitation and emission transition energies, lifetime, site occupancy, energy transfer efficiency, mechanism of energy transfer between luminescent centers, color coordinates, qualitative and quantitative estimation of different luminescent species and so on. These luminescent properties are required a priori to tailor an advanced luminescent material for their applications in optical devices for solid-state lighting, biomedical field for phototherapy and imaging, and nuclear field for detecting ionizing radiation. PL measurements in the present work were carried using FLS-980 spectrofluorophotometer, Edinburgh, UK. Its signal-to-noise ratio of the water Raman signal is 12,000:1. PL studies require five components: (1) excitation source (2) excitation monochromator (3) sample chamber (4) emission monochromator and (5) detector. A schematic diagram of the PL set up of the FLS-980 is shown in Figure 2.1.

Excitation sources: The FLS-980 has a continuous wave Xe lamp (450 W) for excitation over 230-830 nm. Xe being monoatomic gas emits the line spectrum in the UV-VIS region upon electrical discharge. However, under high pressure, it gives a continuous white light in 230-830 nm for sample excitation. With the 450 W continuous-wave Xe lamp significant heat is generated and the pressure inside the bulb automatically rises resulting in its spectral broadening.

In addition to the CW Xe lamp, the FLS-980 has another two pulsed sources for recording the lifetime in a microsecond (pulsed Xe lamp) and nanosecond time scale (pulsed H_2 lamp). The pulsed Xe lamp was used to record the lifetime of the luminescent center in the microsecond to seconds. It has a power of 60 W and is triggered with a repetition rate of 0.1-100 Hz. It has a pulse width of 1 μs that enables the recording of a sample that has a lifetime of more than 1 μs. The microsecond lamp housing is also coupled with a fan to keep its specific temperature and pressure. A pulsed H_2 lamp was used to record the lifetime in nano time scale. It triggers at a very high repetition rate of 40 kHz. It has a pulse width of 1 ns that enables the recording of a lifetime of more than 1 ns and less than 1 μs. The H_2 lamp is controlled by a dedicated power supply unit that delivers a high voltage of 7±0.02 KeV at 0.42±0.05 atm pressure to the Thyratron for the gas discharge. A warm-up period of nearly 10 minutes is given to Thyratron after switching the power supply and then the lamp is switched on. A fan is coupled to the Thyratron to maintain its specific temperature and pressure. The software displays the operational parameters such as gas pressure, voltage, etc.

Monochromator: The monochromator disperses the polychromatic light to monochromatic light. It consists of entrance and exit slits, gratings and mirrors. There are typically two types of dispersing elements available such as refractive prism and diffractive grating. Poor resolution of refractive prism limits application compared to the high-resolution diffractive grating. The high efficiency and better resolution of the spectrum are obtained for a lesser path difference between two adjacent grooves with a large number of grooves of the grating. The light is diffracted by the grooves at a certain angle in a selected wavelength range. The model FLS-980 has double grating at excitation and emission sides. The excitation monochromator allows a particular wavelength onto the sample while recording the emission spectrum, and sweeps with a certain step size (say, 1 nm) over the set excitation range while recording the excitation spectrum. In the sample chamber, the sample is sandwiched between two quartz plates and kept in its holder at a right angle between the incident radiation and detector. Similarly, the emission monochromator allows a particular wavelength while recording the excitation spectrum, and sweeps with a certain step size (say, 1 nm) over the emission range while recording the emission spectrum. Both the excitation and emission monochromators are equipped with two gratings to provide better resolution. A suitable Cut-off filter of a certain wavelength (λ_F) is used between the sample and the emission monochromator that allows emission wavelengths higher than λ_F.

Detector: The instrument FLS-980 has a photomultiplier tube (PMT) as a detector that works on the Photoelectric effect. It consists of mixed alkali metals from where electrons are ejected following the absorption of photons. The electrons are then multiplied in the tube by an array of dynodes. The multiplication of the electron signal depends on the number of dynodes. In the detection process, heat is generated in the tube that can produce noise/dark current. To reduce the heat of the PMT, it is coupled with a fan externally. To reduce the heat significantly, the PMT is also housed with Peltier cooling that reduces the dark current and increases the sensitivity. The advantage of having the Peltier is that it acts as a heat sink keeping the detector at as low as -22 °C. An in-built thermocouple is attached to the detector to measure its temperature.

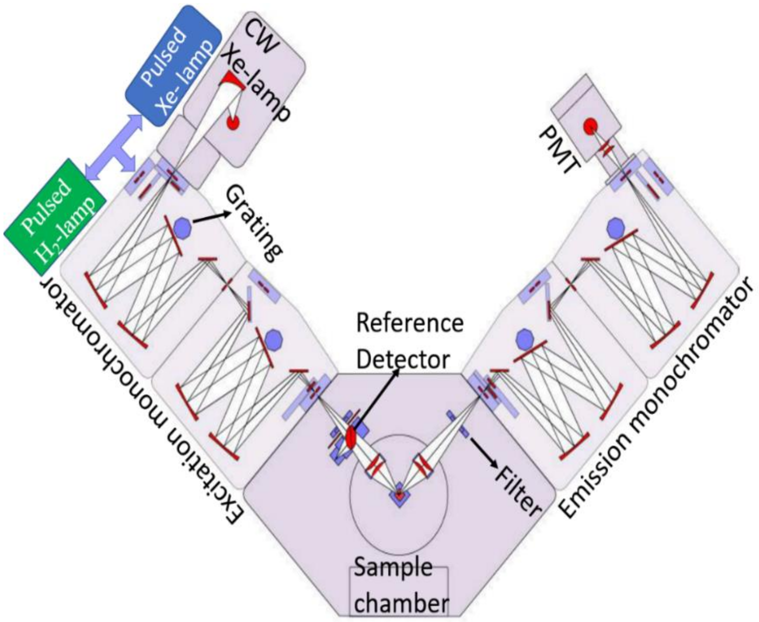

Figure 2.1 Schematic presentation of the FLS-980 PL instrument.

The FLS-980 has a Dewar set up for measuring PL at liquid nitrogen (LN) temperature (77 K). In this case, the sample is taken in a 5 mm quartz tube and put into the Dewar filled with LN.

Some PL measurements of this work were also recorded initially using RF-5301 PC, Shimadzu, Spectrofluorophotometer. It has a CW Xe lamp (150 W) as the excitation source and PMT as a detector. It operates at room temperature. The working principle is the same as discussed above. It does not have any lifetime measurement facility.

2.2.6. Thermally stimulated luminescence (TSL) technique

Thermally stimulated luminescence is a unique technique to get information on the interaction of ionizing radiation with the phosphor. TSL glow curve (Temperature versus Intensity) and emission spectrum (Wavelength versus Intensity) measurements were carried out using TL/OSL Research Reader, TL-1008, Nucleonix, India. The samples were irradiated with different gamma sources. For high dose, ^{60}Co, G.C-5000, BRIT, India, with a dose rate of 2.92 kGy/h and for low dose, ^{137}Cs, IGA-14194, BRIT, India, with a dose rate of 313 mGy/h sources were used. The glow curves provide information on the trap parameters like trap depth, frequency, the order of kinetics, etc. The TSL emission spectrum helps to know the mechanism of the TSL glow curve. When an irradiated-phosphor is gradually heated, the trapped electrons are de-trapped to the conduction band and eventually recombine with the holes. The recombination process results in the emission of electromagnetic radiation that is detected by the detector. The recombination energy may excite the doped luminescent center that subsequently gives emission or simply the recombination energy is seen as light. TSL glow curve measurement requires mainly a heating device and detector.

Heating device: The sample was spread uniformly over a Kanthal strip and heated from room temperature to a higher temperature (480 °C). All the TSL measurements were recorded for a constant weight of 20 mg of aliquot. The Kanthal strip is made of metallic mixtures like Fe (72%), Cr (23%), Al (3%) and Ni (2%). The strip needs low voltage and high current for its operation. The temperature of the strip is registered by means of a thermocouple (Cr-Al alloy) spot-welded at its bottom. The strip is coupled with brass to cool it after the completion of the recording. The linear heating of samples was carried out at a heating rate of 0.5-10 K/s. The linearity calibration was done at a regular interval. A blank recording was carried out before recording the TSL of the sample and used to subtract it from the sample signal to get only the pure signal.

Detector: TSL glow curves were recorded using a PMT detector which was mounted just above the sample. TSL emission spectra (Wavelength versus Intensity) were recorded using a charge-coupled device (CCD) detector (Ocean View software). The emitted light of the phosphor was detected by the CCD which is basically a semiconducting metal oxide. CCD is a state-of-art technology for digital imaging and, used for high-quality image data. The glow curve does not give any information about the emission wavelength of the luminescence center. The origin of the TSL glow curve could be obtained by recording the TSL emission spectrum that is more reliable in revealing the wavelength of the emitting center. Before recording the TSL emission spectra of the sample, a background spectrum was also recorded to subtract the noise from the signal.

2.2.7. Positron annihilation lifetime spectroscopy (PALS) technique

Positron annihilation lifetime spectroscopy is a non-destructive and sensitive technique. Positron (β^+) is an antiparticle of the electron (e^-) and is used as a probe in solids where they rapidly thermalize and diffuse until they get annihilated with e^-. The annihilation releases γ-radiation that is detected by a scintillation detector. The lifetime of a β^+ (or positronium) may be defined as the time between the emission of β^+ from a radioactive source and the detection of γ-rays due to annihilation. The lifetime of the β^+ in solids depends on the electron density that encapsulates it. In PALS, the β^+ lifetime (τ ps) gives the size of the open-volume defects and the intensity (I%) gives their relative concentration in solids. It may be noted that positronium is a bound state of an electron and β^+ that can exist either a singlet state with a short lifetime of about 125 ps or a triplet state with a comparatively longer lifetime of 140 ns in a vacuum.[20] Compared to the metallic conductor and semiconductor, the lifetime of the β^+ in the insulator is longer due to low free electron density.

In the present work, the defects in $BaCeO_3$ and $SrBPO_5$ phosphors were reported. PALS measurements were carried out using BaF_2 scintillator detectors based on a fast-fast coincidence set up having a time resolution of 260 ps. The source-sample geometry consists of a ^{22}Na radioactive source sealed in a 1.25 μm nickel foil sandwiched between two identical samples. A total of 10^6 annihilation events were recorded for each spectrum. The lifetime spectra were analyzed using the LT program.[21] The source lifetime was deduced using well annealed Ni samples having a β^+ lifetime of 110 ps. In this experiment, the γ-decay of 1.27 MeV from a ^{22}Na, β^+ source was used as a start signal for the decay time measurement. The time elapsed between the generation and annihilation of β^+ is known as the β^+ lifetime while the detection of two low energy γ-radiations (511 eV) indicates the annihilation in the sample. The time elapsed between the generation (1.27 MeV) and annihilation (511 eV) of β^+ refers to the positron lifetime of a particular defect environment. The larger the open volume defect or lesser the electron density around the trapped β^+, the longer is the positron lifetime.[22] Simply, it can be stated that PALS analysis involves two processes: firstly, generation of β^+ with a mean energy of 200 keV and 1.27 MeV (γ-ray); and secondly, the annihilation of β^+ and e^- giving two quanta of γ-radiation.[23, 24] Conversely, lifetime and intensity of β^+ depend on the size and number of free volume defects, respectively. Defects in solids with nonuniform microenvironments give rise to characteristics β^+ lifetimes of the respective environment. Thus, the PALS studies reveal information about defects that may influence the luminescence properties of phosphors.

2.3. Conclusion

This chapter discusses a detailed account of the synthesis of $MBPO_5$: Ce/Eu/Gd (via SSR route), and $BaCeO_3$: Eu and $LiAl_5O_8$: Eu/Cr/Fe (via SCS route) phosphors. It also provides necessary information about the experimental setup and principle of different characterization techniques involved such as XRD, XAS and SEM for structural and morphological analyses, and DRS, PL, TSL and PALS for probing the optical properties of the synthesized phosphors.

References

1. Huang, X.; Wang, G. *Journal of Physics D: Applied Physics* **2008,** 41, (22), 225401.
2. Rahaman, M. N., *Ceramic processing*. CRC press: 2017.
3. Shannon, R. D. *Acta crystallographica section A: crystal physics, diffraction, theoretical and general crystallography* **1976,** 32, (5), 751-767.
4. Minquan, W.; Wang, D.; Guanglie, L. *Materials Science and Engineering: B* **1998,** 57, (1), 18-23.
5. Kingsley, J.; Patil, K. *Materials Letters* **1988,** 6, (11-12), 427-432.
6. Jain, S.; Adiga, K.; Verneker, V. P. *Combustion and flame* **1981,** 40, 71-79.
7. Mimani, T.; Patil, K. *Materials Physics and Mechanics(Russia)* **2001,** 4, (2), 134-137.
8. Kniep, R.; Schäfer, G.; Engelhardt, H.; Boy, I. *Angewandte Chemie International Edition* **1999,** 38, (24), 3641-3644.
9. Ravel, B.; Newville, M. *Journal of synchrotron radiation* **2005,** 12, (4), 537-541.
10. Kelly, S.; Hesterberg, D.; Ravel, B. *Methods of Soil Analysis Part 5—Mineralogical Methods* **2008,** 5, 387-463.
11. Basu, S.; Nayak, C.; Yadav, A.; Agrawal, A.; Poswal, A.; Bhattacharyya, D.; Jha, S.; Sahoo, N. In *A comprehensive facility for EXAFS measurements at the INDUS-2 synchrotron source at RRCAT, Indore, India*, Journal of Physics: Conference Series, 2014; IOP Publishing: p 012032.
12. Poswal, A.; Agrawal, A.; Yadav, A.; Nayak, C.; Basu, S.; Kane, S.; Garg, C.; Bhattachryya, D.; Jha, S.; Sahoo, N. In *Commissioning and first results of scanning type EXAFS beamline (BL-09) at INDUS-2 synchrotron source,* AIP Conference Proceedings, 2014; American Institute of Physics: pp 649-651.
13. Abd Mutalib, M.; Rahman, M.; Othman, M.; Ismail, A.; Jaafar, J., Scanning electron microscopy (SEM) and energy-dispersive X-ray (EDX) spectroscopy. In *Membrane characterization*, Elsevier: 2017; pp 161-179.
14. Zhou, W.; Apkarian, R.; Wang, Z. L.; Joy, D., Fundamentals of scanning electron microscopy (SEM). In *Scanning microscopy for nanotechnology*, Springer: 2006; pp 1-40.
15. Mártil, I.; Díaz, G. G. *American Journal of Physics* **1992,** 60, (1), 83-86.
16. Deshpande, M.; Patel, S.; Bhatt, N. *Indian Journal of Physics* **1999,** 73, 275-282.
17. Collings, P. J.; Goodby, J. W., *Introduction to liquid crystals: chemistry and physics*. Crc Press: 2019.
18. Mackenzie, M., *Advances in Applied Fourier Transform Infrafred Spectroscopy*. John Wiley & Sons: 1988.
19. He, T.; Ehrhart, P.; Meuffels, P. *Journal of applied physics* **1996,** 79, (6), 3219-3223.
20. YC, J. J.; Schrader, D., *Principles and applications of positron and positronium chemistry*. World Scientific: 2003.
21. Kansy, J. *Nuclear Instruments and Methods in Physics Research Section A: Accelerators, Spectrometers, Detectors and Associated Equipment* **1996,** 374, (2), 235-244.
22. Krause-Rehberg, R.; Leipner, H. S., *Positron annihilation in semiconductors: defect studies*. Springer Science & Business Media: 1999; Vol. 127.

23. Wang, C.; Solodovnikov, D.; Lynn, K. *Physical Review B* **2006,** 73, (23), 233204.
24. Fong, C.; Dong, A. W.; Hill, A. J.; Boyd, B. J.; Drummond, C. J. *Physical Chemistry Chemical Physics* **2015,** 17, (27), 17527-17540.

Table of Contents

Friday, May 14, 2021

Chapter 3

Optical properties of cerium activated alkaline earth borophosphate ($MBPO_5$; M=Ca/Sr/Ba) phosphors

3.1. Introduction

Lanthanide (Ln) ions doped solid-state phosphors have been the center of attention due to their prospective applications in lighting industry for LEDs and displays, biomedical field for imaging and phototherapy, nuclear industry for scintillations and dosimetry, etc.[1-3] Among the Ln ions, Ce^{3+} is the one and only trivalent ion that exhibits distinctive optical properties in the UV-VIS region due to the $4f\leftrightarrow 5d$ transitions. Ce^{3+} with a simple electronic configuration of $[Xe]4f^1 5d^0 6s^0$ displays interesting luminescence properties as an activator.[4, 5] It can emit in the UV-VIS region as the position of the 5*d* band strongly depends on the crystal field strength (CFS). The CFS is, on the other hand, influenced by a number of factors such as host lattice and synthesis conditions.[6-10] Unlike Ln^{3+} ions, the 4*f*-5*d* transitions of Ce^{3+} being parity allowed show intense and broad luminescence that often sensitizes other Ln^{3+} ions. Since the last decade, researchers have paid immense attention for making efficient green phosphors that can have multiple applications such as green laser, silicon-based detector, solar cell, compact fluorescence lamp (CFL), cathode ray tube (CRT) and plasma display panel (PDP).[5, 11-14] In particular, the efficiency of green-emitting Tb^{3+} doped phosphor can be remarkably enhanced by codoping with Ce^{3+} in a suitable host due to energy transfer from Ce^{3+} to Tb^{3+} making it useful for tricolor lamps applications.[15, 16] Furthermore, the white light-emitting diodes (w-LED) can be fabricated by the combination of blue-green emitting (Ce^{3+}) phosphor with a red-emitting phosphor or yellow-red emitting phosphors on a 430 nm blue LED chip.[17] In addition to this, Ce doped inorganic phosphors are of importance for γ-ray and thermal neutron scintillation.[18] The $5d\rightarrow 4f$ transitions of Ce^{3+}

being parity allowed electric dipole transitions show fast decay time, high luminescence output and high effective nuclear charge that make it a better candidate for scintillation applications.[19]

Stillwellite-structured alkaline earth borophosphates ($MBPO_5$) are considered suitable hosts due to their high thermal stability and good stability against moisture. Lanthanide ions activated $MBPO_5$ have been known for several potential applications spanning from X-ray imaging to display devices.[20-25] Sakasai et al. have probed the neutron storage ability of $SrBPO_5$ host wherein doping of Ce^{3+} has enabled faster readout as its photoluminescence lifetime is very short (<50 ns) compared to that of Eu^{2+} (700-900 ns).[26] Kumar et al. have reported the thermally stimulated luminescence (TSL) behavior for γ-irradiated $SrBPO_5$: Ce and proved that Ce^{3+} acts as a thermoluminescence center.[27] The photoluminescence of some lanthanide ions (Ce^{3+}, Eu^{3+} and Eu^{2+}) has been sparsely studied in $SrBPO_5$ and $CaBPO_5$ hosts.[3] Though authors have reported PL and TSL properties of Ce^{3+} in $SrBPO_5$, a detailed discussion about the luminescence properties and the role of defects are yet to be made. Therefore, the PL and TSL properties of $SrBPO_5$: Ce^{3+} phosphors synthesized through the solid-state reaction (SSR) route is explored and discussed under section 3.2. Furthermore, this chapter also reports a comparative study of Ce^{3+} luminescence in $CaBPO_5$, $SrBPO_5$ and $BaBPO_5$ hosts that is discussed explicitly under section 3.3.

3.2. UV-Blue emitting cerium activated $SrBPO_5$ phosphor

In the present chapter, section 3.1 deals with the synthesis and investigation of optical properties of pristine and Ce doped $SrBPO_5$ (SBP) phosphors. The phase purity and structural properties of the phosphors are analyzed from the powder XRD patterns. The band gap of both the undoped and Ce doped phosphors is estimated using diffuse reflectance spectroscopy (DRS). The photoluminescence and lifetime decay of Ce^{3+} are studied over a wide range of Ce-concentration (1x10^{-5}-3 mol%) at 300 K. This section also accounts the PL and lifetime decay properties of SBP: Ce (0.1 mol%) sample at 77 K. The presence of the defects as well as the site occupancy of Ce^{3+} in SBP: Ce are also discussed. Time-resolved emission spectra are recorded to observe the contributions of Ce^{3+} emission from different sites at different time domains. The efficiency and reusability of the Ce doped phosphor on its PL are investigated subsequent to γ-irradiation and bleaching. The presence of stable defects significantly influences the optical properties of a material. Therefore, the thermoluminescence behavior of these phosphors following γ-irradiation from their TSL glow curves and emission spectrum have also been studied. For the first time, the positron annihilation lifetime spectroscopy measurements are carried out to probe the nature of defects present in undoped and Ce doped SBP.

3.2.1. Results and discussion

3.2.1.1. Phase purity and structural analysis

Figure 3.1 shows the powder XRD patterns of SBP: Ce (0 and 1 mol%) phosphors along with the standard ICDD pattern (file no: 18-1270). The obtained XRD patterns of the undoped and nominally doped SBP match well with its standard pattern confirming the formation of a single-phase hexagonal crystal system with space group $P3_221$ and C_2 symmetry. The crystal structure of the SBP is obtained using VESTA software and presented in Figure 3.2. In the stillwellite-structured SBP, the tetrahedral BO_4^{5-} and PO_4^{3-} units are interconnected with each other and Sr^{2+} through extensive O^{2-}-bridging forming a stable 3D network.[20]

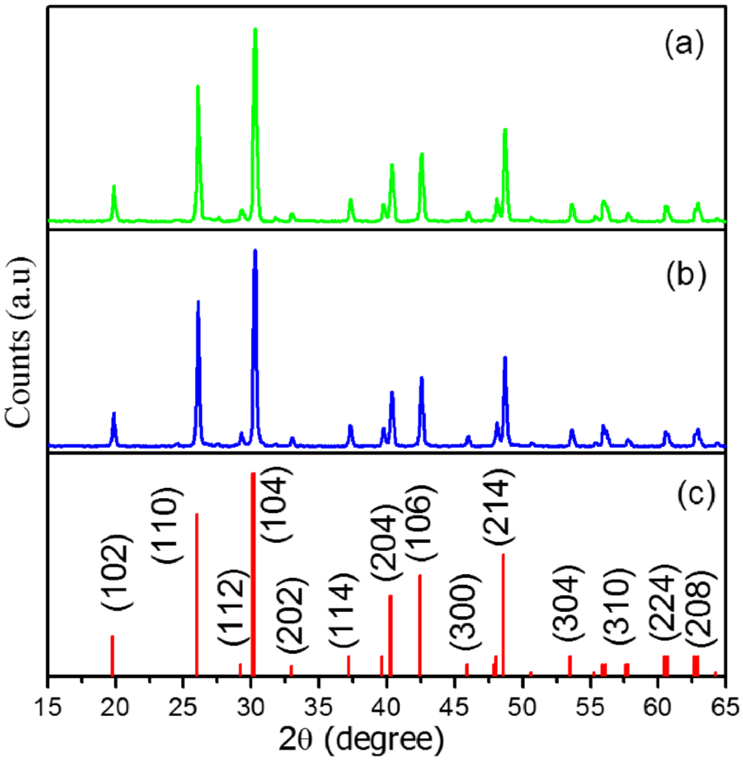

Figure 3.1 Powder XRD patterns of SBP (a) $Ce_{0.01}$ (b) undoped and (c) ICDD: 18-1270.

The structure also shows ten-fold coordination for Sr^{2+} having three formula units per unit cell. The ionic radius of 10-coordinated Sr^{2+} is 136 pm whereas that of Ce^{3+} is 125 pm.[28, 29] Therefore, consequent to doping, Ce^{3+} is expected to occupy the Sr^{2+} site in the host lattice.

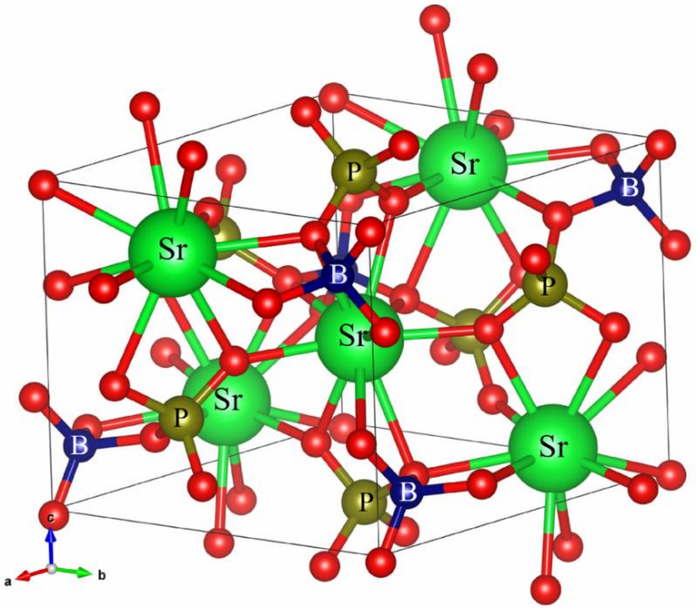

Figure 3.2 The crystal structure of $SrBPO_5$.

3.2.1.2. Estimation of band gap of the undoped and Ce doped $SrBPO_5$

Diffuse reflectance spectrum is recorded to find out the optical band gap (E_g) corresponding to the band edges of the top of the valence band (VB) and bottom of the conduction band (CB). Figure 3.3A shows the reflectance spectra of both undoped and 0.1 mol% Ce doped samples. For the undoped sample, a broad band is observed around 247 nm which could be the host excitation. For the doped sample, bands are observed around 247, 284 and 320 nm. The strong bands observed around 284 and 320 nm are due to the absorptions from the ground state $^2F_{5/2}$ (4*f*) to the excited $^2T_2$ and ^2E states (5*d*) of Ce^{3+}.[30, 31] in case of the Ce doped sample, bands corresponding to 5*d*-configurations of Ce^{3+} are overlapping with the CB and observed at longer wavelength indicating a reduction in the band gap. It may be noted that the doping of Ce^{3+} having defined excited energy levels is responsible for several distinct band transitions to its higher states unlike the undoped one.

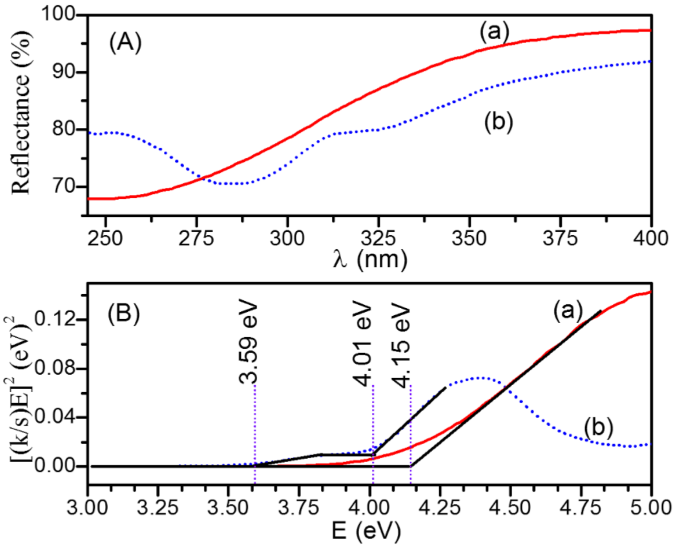

Figure 3.3 (A) Diffuse reflectance spectra and (B) K-M plot of (a) undoped and (b) 0.1 mol% Ce doped SBP.

Figure 3.3B shows the band gap of undoped and 0.1 mol% Ce doped SBP estimated using the Kubelka-Munk (K-M) method.[32] The K-M method considers the absorption coefficient (k) and scattering coefficient (s) for the powder samples which are calculated from the reflectance coefficient, R (= observed reflectance (%)/100) using the Equations (1-3).

$$k = (1 - R)^2 \tag{1}$$

$$s = 2R \tag{2}$$

$$\mathrm{E\ (eV)} = 1240/\lambda\ (nm) \tag{3}$$

The band gap is obtained by plotting photon energy E versus $[(k/s)*E)]^2$ and extrapolating the straight line to k=0. The band gap obtained for the undoped SBP is 4.15 eV as shown in Figure 3.3B (a). In case of Ce doped SBP, the band gap is found to reduce to 4.01 eV (Fig. 3.3B (b)) with the appearance of a hump at 3.59 eV which could be due to the formation of some localized defects. The formation of localized defect state might be due to the aliovalent doping of trivalent ion (Ce^{3+}) at divalent cationic (Sr^{2+}) site in the host.

3.2.1.3. Effect of temperature and concentration on PL

Figure 3.4 shows the PL excitation and emission spectra of SBP: $Ce_{0.001}$ at 300 and 77 K monitored at λ_{em} = 365 and λ_{ex} = 315 nm, respectively. At both temperatures, the excitation peaks are seen at 262 and 315 nm whereas the emission peak is seen around 365 nm. Ce^{3+} involves $4f \rightarrow 5d$ transitions with ground state term ^2F_J that splits into $^2F_{5/2}$ and $^2F_{7/2}$ states, and the excited 5*d* term splits into $^2T_2$ and ^2E states.[30, 31] So, the excitation peaks 262 and 315 nm peaks are assigned as $^2F_{5/2} \rightarrow {}^2T_2$ and $^2F_{5/2} \rightarrow {}^2E$ transitions. Unlike 4*f*-orbitals, 5*d*-orbitals are exposed directly to the ligand field resulting in the broadening of the peaks and being Laporte allowed gives a very intense spectrum. The broad emission peak (365 nm) at 300 K (Fig. 3.4a') is deconvoluted to two peaks using Gaussian functions which are centered at 359 nm (peak 1) and 392 nm (peak 2) as shown in the inset of Figure 3.4. The emission maxima observed at 359 and 392 nm are assigned to the transition from the lowest excited states of 5*d* to ground states, i.e., $^2E\rightarrow{}^2F_{5/2}$ and $^2E\rightarrow{}^2F_{7/2}$ transitions, respectively. At 77 K, both the excitation and emission spectra (Fig. 3.4b and b') are narrower than at 300 K (Fig. 3.4a and a'). The broad emission spectrum shows a shoulder peak when recorded at 77 K indicating partial overlapping of $^2E\rightarrow{}^2F_{5/2}$ and $^2E\rightarrow{}^2F_{7/2}$ transitions which is not seen at 300 K.

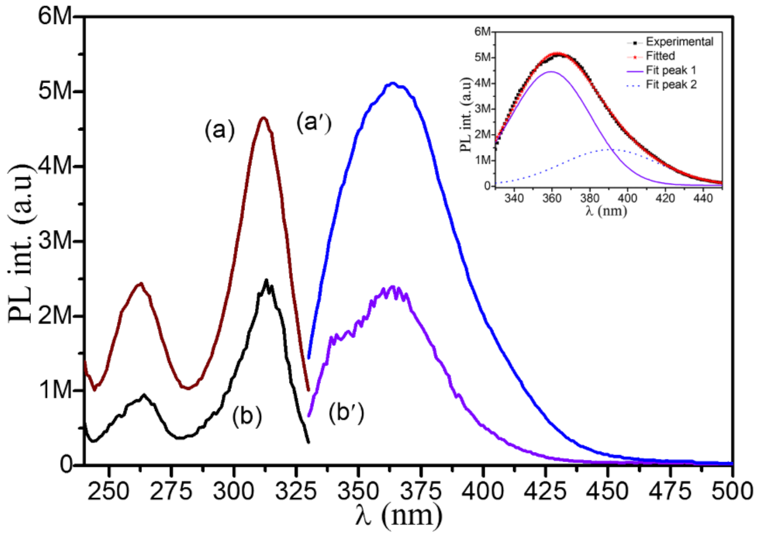

Figure 3.4 PL excitation and emission spectra of SBP: $Ce_{0.001}$ at (a, a') 300 K and (b, b') 77 K monitored at λ_{em} = 365 and λ_{ex} = 315 nm, respectively. Inset shows deconvoluted emission profile at 300 K.

3.2.1.4. Effect of γ-irradiation and bleaching on PL of $SrBPO_5$: $Ce_{0.01}$

Figure 3.5 shows the PL emission spectra of unirradiated, irradiated (42 Gy) and bleached SBP: $Ce_{0.01}$ phosphors at λ_{ex} = 315 nm. The irradiated phosphor shows nearly the same intensity for Ce^{3+} emission as that of the unirradiated phosphor suggesting no valency conversion of $Ce^{4+}\leftrightarrow Ce^{3+}$ following γ-irradiation. The irradiated phosphor is bleached by keeping it under IR-lamp for 2 hours. PL of the γ-irradiated sample following the thermal bleaching also shows almost the same intensity as that of the unirradiated sample. The irradiation and bleaching cycles are repeated a few times and no significant change in PL intensity is observed. The reproducibility of PL of the SBP: $Ce_{0.01}$ phosphor suggests its possible reusability.

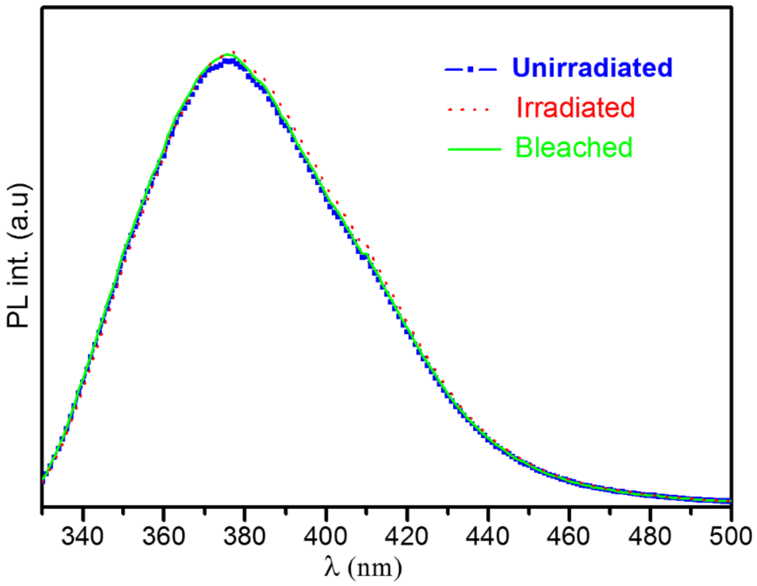

Figure 3.5 PL emission spectra of unirradiated, irradiated and bleached SBP: $Ce_{0.01}$ at λ_{ex} = 315 nm.

3.2.1.5. PL lifetime studies of Ce^{3+} in $SrBPO_5$ at different temperatures and concentrations

Figure 3.6 shows the PL lifetime decays of Ce^{3+} in SBP: $Ce_{0.001}$ at λ_{ex} = 315 and λ_{em} = 365 nm. The decays are fitted to the expression, i.e., $I\ (t) = \sum_i^4 A_i \exp(-t/\tau_i)$; where I (t) is PL intensity at measurement time t, A_i is the residual weighting factor of lifetime τ_i. For SBP: $Ce_{0.001}$ at 300 K (Fig. 3.6a), the fitting is found to be of the second order giving two lifetimes of τ_1=17 ns (15 %) and τ_2=36 ns (85%) with χ^2=0.98. Similarly, SBP: $Ce_{0.001}$ at 77 K (Fig. 3.6b) also exhibits two lifetimes of τ_1=12 ns (3 %) and τ_2=30 ns (97%) with χ^2=0.96. The lifetimes of Ce^{3+} for 1, 2 and 3 mol% (Fig. 3.6c-e) Ce-concentration are observed to be τ_1=14 ns (12 %), τ_2=36 ns (88%); τ_1=9 ns (8 %), τ_2=23 ns (92%) and τ_1=17 ns (20 %), τ_2=21 ns (80%), respectively. The lifetime value of τ_1 and τ_2 decreases above 1 mol% Ce-concentration which could be due to the concentration quenching (Fig. 3.14). Observation of two lifetimes reveals the presence of Ce^{3+} in two different environments. For the incorporation of Ce^{3+} ions at the Sr^{2+} site, three Sr^{2+} ions need to be replaced with two Ce^{3+} ions to conserve the charge neutrality.

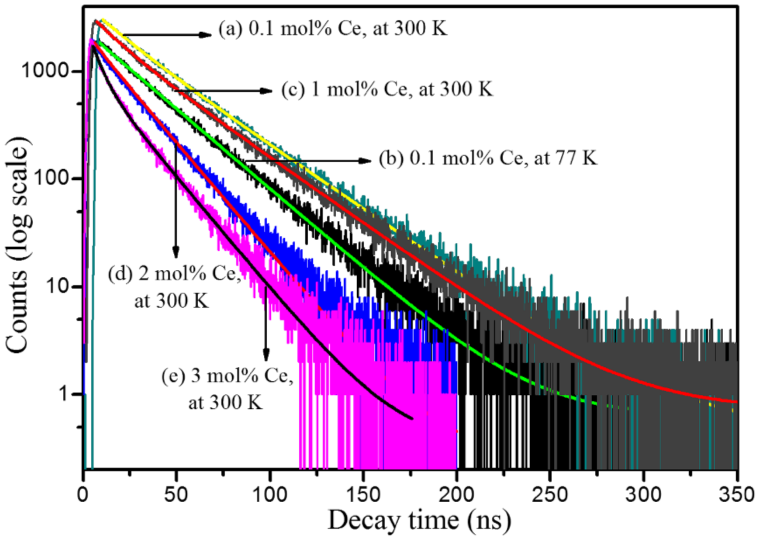

Figure 3.6 PL lifetime decays of Ce^{3+} *in SBP doped with 0.1 mol% Ce at (a) 300 and (b) 77 K, and (c-e) 1-3 mol% Ce at 300 K.*

In this process, charge compensating defects are expected to be generated.[33] The observed two different lifetimes (τ_1 and τ_2) of Ce^{3+} in the SBP host may be attributed to the presence of charge compensating defects. The short lifetime value (τ_1) is due to the presence of charge compensating defects at close proximity whereas the long lifetime (τ_2) is due to the presence of such defects far from Ce^{3+}.[34] On the other hand, the high intensity of the τ_2 component suggests that most Ce^{3+} are far from the charge compensating defects. At 77 K, the contribution from the short lifetime component (τ_1) decreases to 3% and simultaneously the same from the long lifetime component (τ_2) increases to 97% probably due to redistribution/elimination of some defects. Due to the dipole allowed $5d\rightarrow4f$ transitions, a very short lifetime (<50 ns) is usually observed for Ce^{3+} suggesting a possible application of SBP: Ce phosphor in the scintillation field.[35] To explore the presence of Ce^{3+} in two different environments, a time-resolved emission spectrum is recorded.

3.2.1.6. Time-resolved emission spectroscopy (TRES) of $SrBPO_5$: $Ce_{0.001}$

TRES of SBP: $Ce_{0.001}$ is recorded at λ_{ex} = 315 in the time range of 0-30, 30-70, 80-120 and 150-220 ns as shown in Figure 3.7. In the time zone of 0-30 ns, τ_1 (17 ns) would have completed nearly two lifetimes while τ_2 (36 ns) is yet to complete one lifetime suggesting Ce^{3+} contribution predominantly from the site associated with τ_1 component. In this time range, the Ce^{3+} emission maximum (λ_{em}) is observed at 361 nm (Fig. 3.7a). In the time zone of 30-70 ns, τ_1 would have completed nearly four-five lifetimes while τ_2 would have completed two lifetimes with λ_{em} at 366 nm (Fig. 3.7b) suggesting the contribution from both the components. In the time zone of 80-120 ns, τ_1 would have completed nearly seven lifetimes and therefore, its contribution to the emission spectrum could be considered as the bare minimum while τ_2 would have completed three lifetimes. In this time zone, the predominant contribution would be from τ_2 with λ_{em} at 371 nm (Fig. 3.7c). Similarly, in the time zone of 150-220 ns, τ_1 would have completed nearly thirteen lifetimes suggesting its negligible contribution while τ_2 would have completed six lifetimes with λ_{em} at 376 nm suggesting a pure contribution from the latter (Fig. 3.7d).

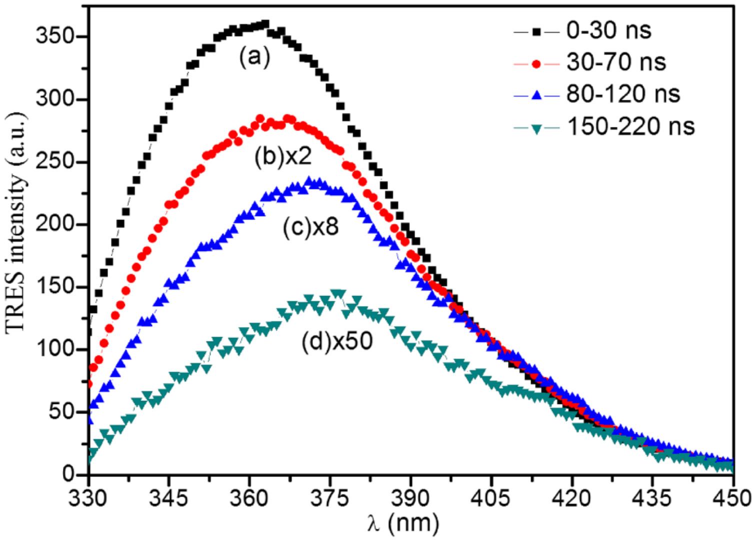

Figure 3.7 TRES of SBP: $Ce_{0.01}$ recorded at λ_{ex} = 315 in the time range of (a) 0-30 (b) 30-70 (c) 80-120 and (d) 150-220 ns.

A progressive red-shift in the position of λ_{em} of Ce^{3+} is observed (361, 366, 371 and 376) with the increase in decay time. The red-shift in λ_{em} confirms that Ce^{3+} occupies two different environments in SBP. The Ce^{3+} emission observed around 361-366 nm is predominantly related to τ_1 and the emission around 371-376 nm is more related to τ_2. Hence, the defects generated due to the substitution of Ce^{3+} at Sr^{2+} provide two different environments around Ce^{3+} depending on the concentration and proximity of such defects around it in the SBP host.

3.2.1.7. Thermally stimulated luminescence (TSL) of γ-irradiated $SrBPO_5$: $Ce_{0.01}$

Figure 3.8 shows the TSL glow curve (GC) of γ-irradiated SBP: $Ce_{0.01}$ phosphor (7 Gy) recorded at a heating rate (β) of 2 K/s. The broad GC is deconvoluted into three peaks with maxima at T_{m1}, T_{m2} and T_{m3}. Trap parameters such as symmetry factor (μ), trap depth (E), frequency (S), concentration (Ƞ) and lifespan (Ls) of electrons in traps at 300 K are estimated using Equations (4-8), respectively.[29, 36-38] For the deconvoluted GC, the value of μ is estimated using Equation (4) where T_1 and T_2 are the low and high-temperature ends of the glow peak at full-width half maxima (w). The value of μ is found to be close to the theoretical value of 0.52 indicating the kinetics of detrapping process to be of the second-order (b=2). It can be seen from Table 3.1 that the trap depths of different traps lie at 0.75 -1.28 eV with a frequency of about 10^9 s^{-1}.

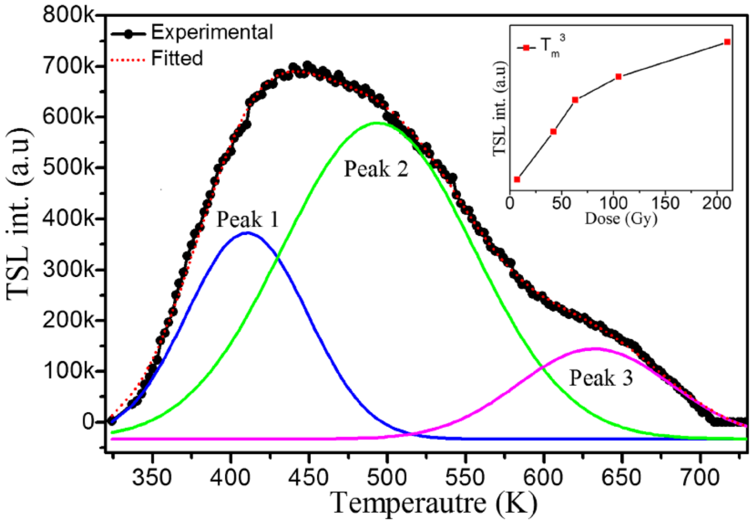

Figure 3.8 TSL glow curve of γ-irradiated SBP: $Ce_{0.01}$ phosphor (7 Gy) recorded at a heating rate (β) of 2 K/s. The glow peak is deconvoluted to peak 1, 2 and 3. The inset shows TSL intensity of peak 3 as a function of dose (7-210 Gy).

$$\mu = (T_2 - T_m)/(T_2 - T_1) = (T_2 - T_m)/w \qquad \textbf{(4)}$$

$$E = 23\,k\,T_m = T_m/500 \qquad \textbf{(5)}$$

$$S = (\beta E/kT_m^2)\exp(E/kT_m)\,[1 + (b-1)\,(2kT_m/E)]^{-1} \qquad \textbf{(6)}$$

$$\eta = (I \times w)/\beta \qquad \textbf{(7)}$$

$$\mathrm{Ls} = (1/S)\exp(E/kT_m) \qquad \textbf{(8)}$$

The full-width half maxima (w) and integrated intensity (I) of each peak are calculated to determine the concentration of trapped electrons, which is found to be nearly 10^7-10^8 cc at different doses. The long lifespan (Ls) of the trapped electrons indicates the presence of stable defects in the SBP host. The inset in Figure 3.8 shows the dose-response of SBP: $Ce_{0.01}$. With the increase in γ-irradiation dose from 7 to 63 Gy, the intensity of peak 3 (T_m^3) increases linearly up to 63 Gy, and thereafter, saturation is initiated.

Table 3.1 Trap parameters of SBP: $Ce_{0.01}$ at different doses (7-210 Gy)

Dose (Gy)	Peak	T_m (K)	I (a.u)	w	μ	E (eV)	S (s^{-1})	η (cc)	Ls (hour)
7	1	408	442703	100	0.51	0.82	1.26×10^9	2.2×10^7	9.41
	2	495	664283	149	0.52	0.99	1.04×10^9	4.9×10^7	9207
	3	640	229773	132	0.52	1.28	8.03×10^8	1.5×10^7	8.3×10^8
42	1	379	521789	55	0.51	0.76	1.36×10^9	1.4×10^7	0.94
	2	430	840019	115	0.51	0.86	1.19×10^9	4.8×10^7	53.89
	3	535	1242250	220	0.49	1.07	9.60×10^8	1.4×10^8	2.1×10^5
63	1	412	1007790	77	0.52	0.82	1.25×10^9	3.9×10^7	12.93
	2	470	1484560	115	0.49	0.94	1.09×10^9	8.5×10^7	1278
	3	569	1911810	166	0.51	1.14	9.03×10^8	1.6×10^8	3.1×10^6
105	1	407	1167440	74	0.51	0.81	1.26×10^9	4.3×10^7	8.69
	2	466	1943820	116	0.51	0.93	1.10×10^9	1.1×10^8	931.36
	3	578	2407260	156	0.50	1.15	8.89×10^8	1.9×10^8	6.3×10^6
210	1	390	866966	48	0.51	0.78	1.32×10^9	2.1×10^7	2.25
	2	442	2313630	121	0.52	0.88	1.16×10^9	1.4×10^8	139.44
	3	568	3141910	189	0.52	1.13	9.04×10^8	3.0×10^8	2.9×10^6

In the present study, the TSL emission spectrum of the γ-irradiated SBP: $Ce_{0.01}$ following thermal excitation shows a broad peak centered at 365 nm (Fig. 3.9) that is similar to the PL emission spectrum confirming Ce^{3+} emission. Kumar et al., have studied the EPR of the γ-irradiated SBP and reported the presence of two hole-trapped species (O^- and BO_3^{2-}) and three electron-trapped species (F-center, O^{2-} and Ce^{4+}).[27] As there are more than one electron trap species in the host, it may be expected to give multiple traps. In our study, three deconvoluted peaks are observed from the irradiated sample confirming the presence of the multiple electron traps. Upon thermal excitation, recombination of the de-trapped electrons with the holes takes place following the transfer of recombination energy to excite Ce^{3+} and results in its emission.[39] This suggests that Ce^{3+} acts as a thermoluminescent center in SBP.

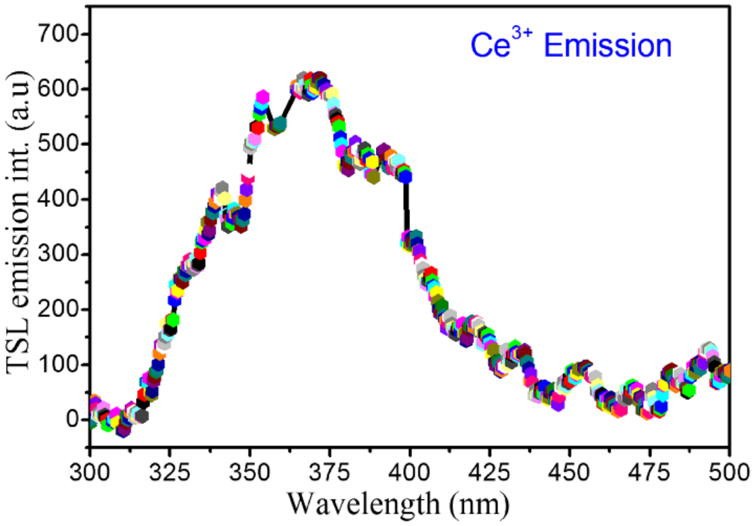

Figure 3.9 TSL emission spectrum of Ce^{3+} in γ-irradiated SBP: $Ce_{0.01}$ (42 Gy) by heating up to 673 K.

3.2.1.8. Positron annihilation lifetime spectroscopy (PALS) of undoped and Ce doped $SrBPO_5$

PALS is a highly sensitive and nondestructive technique for studying defects in solids. In this technique, positron (β^+) which is an antiparticle of electron (e^-) is used as a probe of solids where they rapidly thermalize and diffuse until they annihilate with e^-. PALS analysis can be depicted in two ways: firstly, the generation of β^+ with a mean energy of 200 and 1274 keV (γ-ray) and secondly, the annihilation of β^+ and e^- giving two quanta of γ-ray (511 keV) that are exactly opposite due to the momentum conservation.[40, 41] The time elapsed between the generation and annihilation of β^+ is a direct measure of the time of positrons in the defect in which they annihilate called positron lifetime. Conversely, positron lifetime and intensity depend on the size and number of free volume defects present in the material, respectively. In solids with non-uniform microenvironments, for instance, defects or domains of variable electron densities give rise to characteristics positron lifetimes of the respective environment. In the present case, positron annihilation lifetime decays are recorded for undoped and $Ce_{0.01}$ doped SBP samples as shown in Figure 3.10.

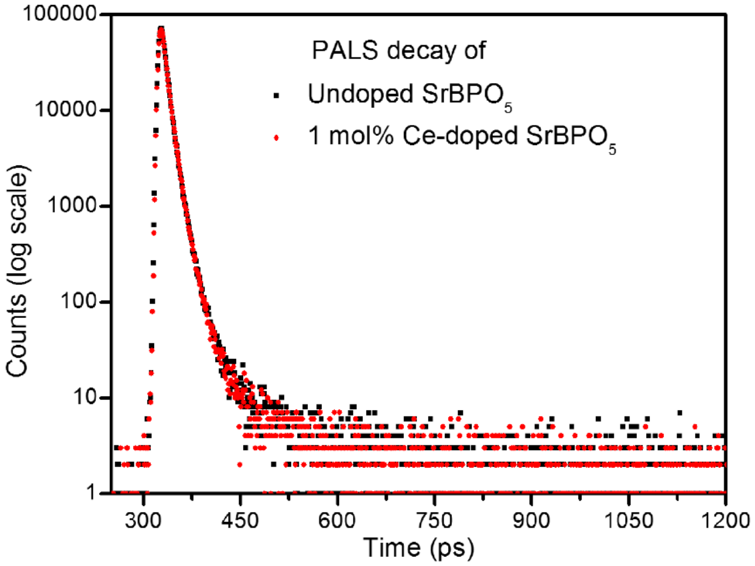

Figure 3.10 Positron annihilation lifetime decay of undoped and $Ce_{0.01}$ *doped SBP.*

The PALS decays show a bi-exponential behavior revealing two types of defect centers in SBP. It can be seen from Table 3.2 that PALS intensity corresponding to the shorter lifetime (τ_1=193-196 ps) is predominant compared to that of the longer lifetime (τ_2=533-547 ps). The τ_1 component may be referred to the presence of β^+ in defects associated with more electron density (ρ) whereas the τ_2 component with the defects associated with less ρ or larger domain of free volume. This is because the β^+ lifetime decreases with the increase in the electron density at the annihilation site.[42] Also, the values of positron lifetime and intensity in the 1 mol% Ce doped phosphor do not show any significant change compared to that of the undoped sample. Therefore, the PALS studies corroborate the presence of two types of defects that are the same in both the undoped and Ce doped SBP.

Table 3.2 Positron lifetime and PALS intensity in undoped and Ce doped SBP

$SrBPO_5$	τ_1 ± error (ps)	I_1 ± error (%)	τ_2 ± error (ps)	I_2 ± error (%)
Undoped	193 ± 0.45	94 ± 0.21	547 ± 9	6 ± 0.21
1 mol% Ce	196 ± 0.67	94 ± 0.31	533 ± 10	6 ± 0.31

3.3. A comparative study of UV-Blue emitting cerium activated $MBPO_5$ phosphors

3.3.1. Results and discussion

3.3.1.1. Phase purity and structural analysis

Figure 3.11 shows the powder XRD patterns of $MBPO_5$: $Ce_{0.01}$ phosphors along with the standard ICDD patterns. The obtained XRD patterns of the undoped and nominally doped CBP, SBP and BBP samples match well with their respective standard patterns with file number 89-7584, 18-1270 and 89-4624, respectively. This confirms the single-phase formation of $MBPO_5$ samples. The three hosts belong to the primitive lattice of hexagonal crystal system with space group $P3_221$ and have three formula units per unit cell.

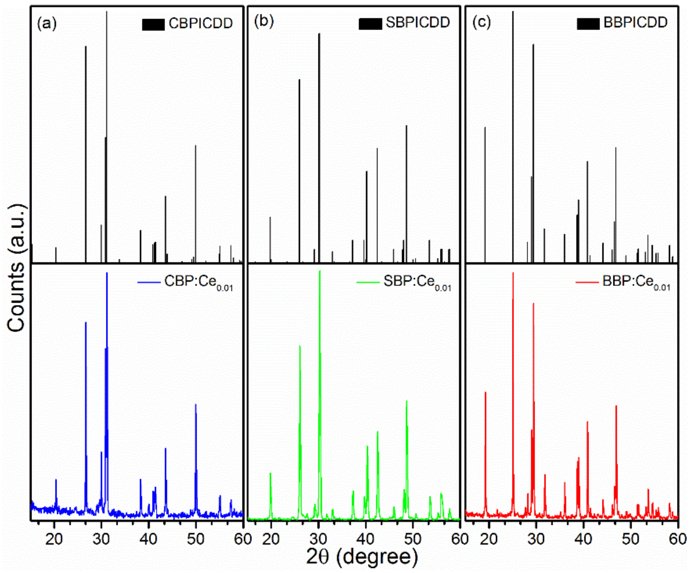

Figure 3.11 Powder XRD patterns of (a) $CaBPO_5$, ICDD: 89-7584 (b) $SrBPO_5$, ICDD: 18-1270 and (c) $BaBPO_5$, ICDD: 89-4624.

3.3.1.2. Morphological analysis of MBPO$_5$ samples

The morphology of the synthesized MBPO$_5$ samples is ascertained from the SEM images (Fig. 3.12). It can be seen from the images that nonuniform sized phosphor particles ranging from 200-500 nm are formed. The morphology of BBP sample (Fig. 3.12c) synthesized at 900 °C is observed to have minimum agglomeration and compacted particles with better uniformity compared to that of the CBP (950 °C) and SBP (1000 °C) samples (Fig. 3.12a and b) which could be due to the lower synthesis temperature of the former.

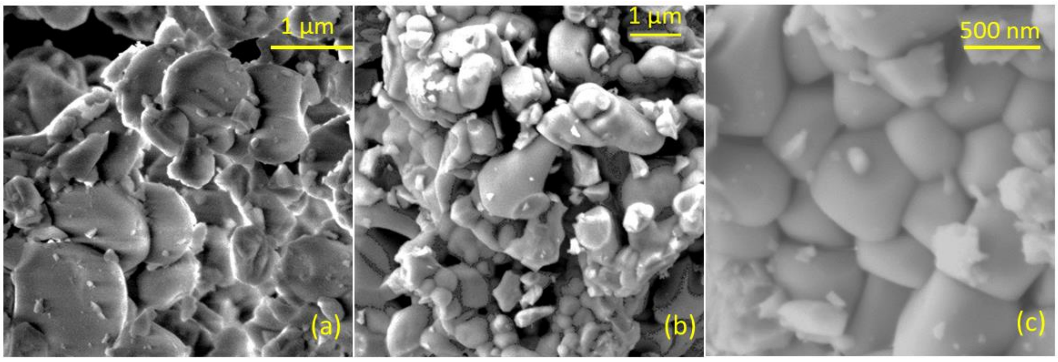

Figure 3.12 SEM images of (a) CBP: Ce$_{0.01}$ (b) SBP: Ce$_{0.01}$ and (c) BBP: Ce$_{0.01}$ calcined at 950, 1000 and 900 °C, respectively.

3.3.1.3. PL properties of Ce^{3+} in MBPO$_5$

Figure 3.13 shows the excitation and emission spectra of Ce^{3+} in MBPO$_5$: Ce$_{0.01}$. Ce^{3+} in MBP hosts exhibits its characteristics broad band spectral profiles owing to the parity allowed 4*f*↔5*d* transitions. However, the spectral profiles are different in the three hosts as the energy levels of 5d-orbital strongly varies with the crystal field strength. In case of CBP: Ce$_{0.01}$, Ce^{3+} exhibits well-resolved absorptions at 256 and 282 nm while emits at 318 nm with a shoulder peak at 335 nm. In case of SBP: Ce$_{0.01}$, it absorbs at 262 and 315 nm while emits at 365 nm. However, in case of BBP: Ce$_{0.01}$, it shows an unresolved broad absorption at 301 nm and emission at 338 nm. It is known that the covalency as well as the crystal field strength decrease down the group from Ca^{2+} to Ba^{2+}. Hence, the energy separation between the excited ^{2}T and ^{2}E states of 5*d*-

configuration decreases. Similarly, the separation between the ground $^2F_{5/2}$ and $^2F_{7/2}$ states 4*f*-configuration decreases. This decrease in the energy separation leads to the well-resolved spectral profiles in CBP to SBP and finally to an unresolved spectral profile in BBP.

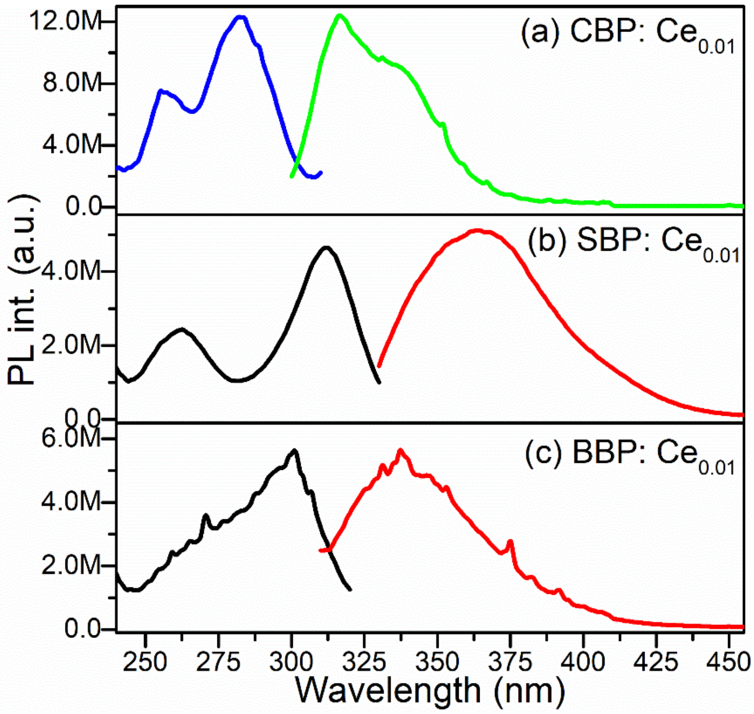

Figure 3.13 PL excitation and emission spectra of (a) CBP: $Ce_{0.01}$ (b) SBP: $Ce_{0.01}$ and (c) BBP: $Ce_{0.01}$.

3.3.1.4. Optimization of Ce-concentration in MBP: Ce^{3+}

Figure 3.14 shows the PL intensity of Ce^{3+} emission as a function of Ce-concentration in MBP. In cases of CBP: Ce (Fig. 3.14a) and BBP: Ce (Fig. 3.14c), the PL intensity of Ce^{3+} emission increases with the increase in its concentration from 10^{-4} to 0.1 mol% and thereafter, the intensity decreases significantly due to the concentration quenching. In case of SBP: Ce (Fig. 3.14b), the PL intensity is maximum at 1 mol% Ce-concentration and above that, the concentration quenching is observed. Moreover, cerium at a concentration of as low as $1x10^{-5}$ mol% could be observed in SBP: Ce. Hence, the study suggests the low-level analytical detection of Ce as impurity by doping it in a suitable host like SBP.

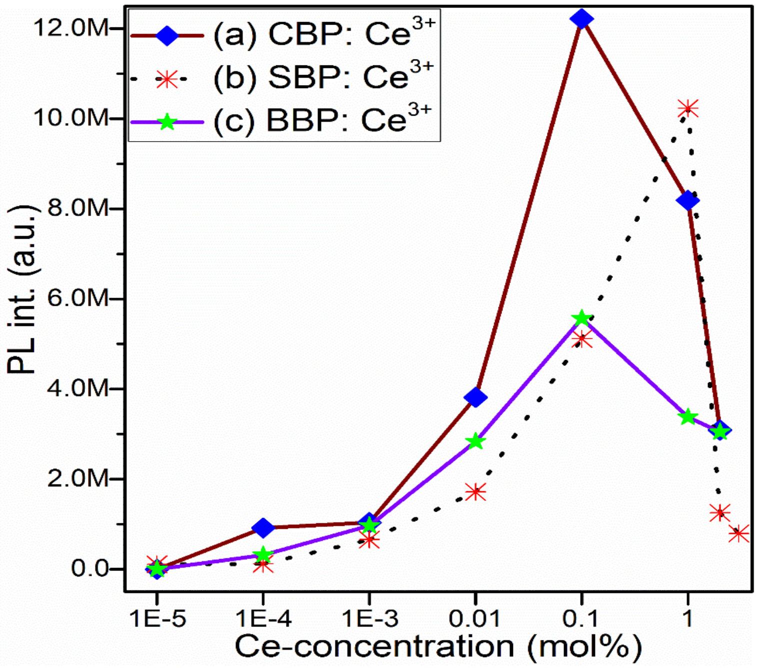

Figure 3.14 PL intensity of Ce^{3+} emission as a function of Ce-concentration in (a) CBP (b) SBP and (c) BBP excited at 282, 315 and 301 nm, respectively.

3.3.1.5. PL lifetime studies of Ce^{3+} in $MBPO_5$

The PL lifetime decays of Ce^{3+} are recorded and analyzed for CBP: $Ce_{0.001}$, SBP: $Ce_{0.01}$ and BBP: $Ce_{0.001}$ phosphors for which maximum luminescence is observed. The lifetime values obtained for Ce^{3+} in MBP: Ce are listed in Table 3.3. Ce^{3+} exhibits two lifetimes indicating its site occupancy in two different sites in MBP hosts. It is also observed that the average lifetime of Ce^{3+} decreases down the group. The shorter lifetime observed in SBP: $Ce_{0.01}$ and BBP: $Ce_{0.001}$ phosphors may be suitable for scintillation application.

Table 3.3 PL lifetime of Ce^{3+} in CBP (λ_{ex} = 282, λ_{em} = 318 nm), SBP (λ_{ex} = 315, λ_{em} = 365 nm) and BBP (λ_{ex} = 301, λ_{em} = 338 nm)

Sample	τ_1 (ns)	B_1	τ_2 (ns)	B_2	τ_{av} (ns)	χ^2
CBP: $Ce_{0.001}$	31±0.4	668	98±1.3	177	61.5	0.99
SBP: $Ce_{0.01}$	14±1.6	556	36±0.84	1351	33	1.04
BBP: $Ce_{0.001}$	8±0.16	579	24±0.16	566	20	1.11

3.4. Conclusions

This chapter reports the successful synthesis of MBP: Ce phosphors through the SSR route in the air atmosphere. PL studies reveal maximum luminescence for CBP: $Ce_{0.001}$, SBP: $Ce_{0.01}$ and BBP: $Ce_{0.001}$ phosphors suggesting their applications in UV-Blue LEDs. PL lifetime decay and time-resolved emission spectroscopy analysis confirms the presence of Ce^{3+} in two different sites in MBP hosts. The shorter lifetime of SBP: $Ce_{0.01}$ (τ_{av}=33 ns) and BBP: $Ce_{0.001}$ (τ_{av}=20 ns) makes them useful for fast readout in scintillation applications. The bleached and γ-irradiated SBP: $Ce_{0.01}$ samples show the same Ce^{3+} emission intensity as that of the unirradiated sample establishing the reusability and the absence of valency conversion ($Ce^{3+}\leftrightarrow Ce^{4+}$) which are essential properties for a scintillating phosphor. Furthermore, the TSL studies of γ-irradiated SBP: $Ce_{0.01}$ confirm that Ce^{3+} acts as the thermoluminescence center in this host.

References

1. Weber, M. J. *Journal of Luminescence* **2002,** 100, (1-4), 35-45.
2. Dhoble, S.; Moharil, S. *Nuclear Instruments and Methods in Physics Research Section B: Beam Interactions with Materials and Atoms* **2000,** 160, (2), 274-279.
3. Kharabe, V.; Oza, A. H.; Dhoble, S. *Optik-International Journal for Light and Electron Optics* **2015,** 126, (23), 4544-4547.
4. Yen, W.; Basun, S.; Happek, U.; Raukas, M. *Acta Physica Polonica-Series A General Physics* **1996,** 90, (2), 257-266.
5. Xia, Z.; Liu, R.-S. *The Journal of Physical Chemistry C* **2012,** 116, (29), 15604-15609.
6. Setlur, A. A.; Heward, W. J.; Gao, Y.; Srivastava, A. M.; Chandran, R. G.; Shankar, M. V. *Chemistry of materials* **2006,** 18, (14), 3314-3322.
7. Kasuya, R.; Isobe, T.; Kuma, H.; Katano, J. *The Journal of Physical Chemistry B* **2005,** 109, (47), 22126-22130.
8. Xia, G.; Zhou, S.; Zhang, J.; Xu, J. *Journal of Crystal Growth* **2005,** 279, (3-4), 357-362.
9. Li, Q.; Gao, L.; Yan, D. *Materials chemistry and physics* **2000,** 64, (1), 41-44.
10. Li, J.; Li, J.-G.; Liu, S.; Li, X.; Sun, X.; Sakka, Y. *Science and technology of advanced materials* **2013,** 14, (5), 054201.
11. Velázquez, J.; Fernández-González, R.; Marrero-Jerez, J.; Rodríguez, V.; Lukowiak, A.; Chiappini, A.; Chiasera, A.; Ferrari, M.; Núñez, P. *Optical Materials* **2015,** 46, 109-114.
12. Dotsenko, V.; Berezovskaya, I.; Zubar, E.; Efryushina, N.; Poletaev, N.; Doroshenko, Y. A.; Stryganyuk, G.; Voloshinovskii, A. *Journal of Alloys and Compounds* **2013,** 550, 159-163.

13. Tshabalala, K.; Cho, S.-H.; Park, J.-K.; Pitale, S. S.; Nagpure, I.; Kroon, R.; Swart, H.; Ntwaeaborwa, O. *Journal of Alloys and Compounds* **2011,** 509, (41), 10115-10120.
14. Ghosh, P.; Kar, A.; Patra, A. *Nanoscale* **2010,** 2, (7), 1196-1202.
15. Lu, C.-H.; Godbole, S.; Natarajan, V. *Materials chemistry and physics* **2005,** 94, (1), 73-77.
16. Wang, F.; Song, H.; Pan, G.; Fan, L.; Dong, B.; Liu, L.; Bai, X.; Qin, R.; Ren, X.; Zheng, Z. *Journal of luminescence* **2008,** 128, (12), 2013-2018.
17. Komuro, N.; Mikami, M.; Shimomura, Y.; Bithell, E. G.; Cheetham, A. K. *Journal of Materials Chemistry C* **2015,** 3, (1), 204-210.
18. Van Eijk, C. W. *Nuclear Instruments and Methods in Physics Research Section A: Accelerators, Spectrometers, Detectors and Associated Equipment* **2001,** 460, (1), 1-14.
19. Huang, C.-H.; Chen, T.-M. *The Journal of Physical Chemistry C* **2011,** 115, (5), 2349-2355.
20. Blasse, G.; Bril, A.; De Vries, J. *Journal of Inorganic and Nuclear Chemistry* **1969,** 31, (2), 568-570.
21. Nakamura, T.; Takeyama, T.; Takahashi, N.; Jagannathan, R.; Karthikeyani, A.; Smith, G.; Riedi, P. *Journal of luminescence* **2003,** 102, 369-372.
22. Karthikeyani, A.; Jagannathan, R. *Journal of luminescence* **2000,** 86, (1), 79-85.
23. Sakasai, K.; Katagiri, M.; Toh, K.; Takahashi, H.; Nakazawa, M.; Kondo, Y. *Applied Physics A* **2002,** 74, (1), s1589-s1591.
24. Liang, H.; Su, Q.; Lu, S.; Tao, Y.; Hu, T.; Liu, T. *Materials research bulletin* **2002,** 37, (12), 1981-1989.
25. Han, B.; Zhang, J.; Lü, Y.; Liu, Y.; Cui, Q. *Russian Journal of Physical Chemistry A* **2014,** 88, (1), 143-148.
26. Sakasai, K.; Katagiri, M.; Matsubayashi, M.; Nakamura, T.; Kondo, Y. *Nuclear Instruments and Methods in Physics Research Section A: Accelerators, Spectrometers, Detectors and Associated Equipment* **2004,** 529, (1-3), 378-383.
27. Kumar, M.; Kadam, R.; Seshagiri, T.; Natarajan, V.; Page, A. *Journal of radioanalytical and nuclear chemistry* **2004,** 262, (3), 633-637.
28. Shannon, R. D. *Acta crystallographica section A: crystal physics, diffraction, theoretical and general crystallography* **1976,** 32, (5), 751-767.
29. Kumar, M.; Seshagiri, T.; Godbole, S. *Bulletin of Materials Science* **2013,** 36, (5), 913-918.
30. Berezovskaya, I.; Dotsenko, V.; Efryushina, N.; Voloshinovskii, A.; Van Eijk, C.; Dorenbos, P.; Sidorenko, A. *Journal of alloys and compounds* **2005,** 391, (1-2), 170-176.
31. Tosaka, Y.; Adachi, S. *ECS Journal of Solid State Science and Technology* **2014,** 3, (2), R14-R18.
32. Manjunatha, S.; Krishna, R. H.; Thomas, T.; Panigrahi, B.; Dharmaprakash, M. *Materials Research Bulletin* **2018,** 98, 139-147.
33. Gupta, S. K.; Pathak, N.; Kadam, R. *Journal of Luminescence* **2016,** 169, 106-114.
34. Sahu, M.; Gupta, S. K.; Jain, D.; Saxena, M.; Kadam, R. *Spectrochimica Acta Part A: Molecular and Biomolecular Spectroscopy* **2018,** 195, 113-119.
35. Derenzo, S.; Weber, M.; Bourret-Courchesne, E.; Klintenberg, M. *Nuclear Instruments and Methods in Physics Research Section A: Accelerators, Spectrometers, Detectors and Associated Equipment* **2003,** 505, (1-2), 111-117.

36. Barve, R.; Suriyamurthy, N.; Panigrahi, B.; Venkatraman, B. *Radiation protection dosimetry* **2014,** 163, (4), 430-438.
37. Pagonis, V.; Kitis, G.; Furetta, C., *Numerical and practical exercises in thermoluminescence*. Springer Science & Business Media: 2006.
38. Mashangva, M.; Singh, M. N.; Singh, T. B. **2011**.
39. Matthews, R.; Stoebe, T. *Journal of Physics C: Solid State Physics* **1982,** 15, (30), 6271.
40. Fong, C.; Dong, A. W.; Hill, A. J.; Boyd, B. J.; Drummond, C. J. *Physical Chemistry Chemical Physics* **2015,** 17, (27), 17527-17540.
41. Wang, C.; Solodovnikov, D.; Lynn, K. *Physical Review B* **2006,** 73, (23), 233204.
42. Krause-Rehberg, R.; Leipner, H. S., *Positron annihilation in semiconductors: defect studies*. Springer Science & Business Media: 1999; Vol. 127.

Table of Contents

Chapter 4 Effect of gadolinium codoping on europium luminescence and its in-situ valency conversion in $MBPO_5$

Friday, May 14, 2021

Chapter 4

Effect of gadolinium codoping on europium luminescence and its in-situ valency conversion in $MBPO_5$

4.1. Introduction

Lanthanide luminescence is widely studied due to the interesting spectral characteristics arising from the 4*f*-4*f* and 4*f*-5*d* transitions. Ln ions show a low photo-bleaching effect. The excitation and the emission peak positions of Ln ions (except Ce^{3+} and Eu^{2+}) do not change significantly irrespective of different hosts due to the shielding effect. Among the Ln ions, Eu^{2+} is of significant importance as it emits in the UV-VIS region depending on the position of 5*d* levels in a host. Anthony et al. have reported the color tuning of Eu^{2+} emission by changing the coordination number (CN) at the activator site.[1] The red emission from Eu^{2+} with CN=8 and 9 has been reported in $LiBa_2B_5O_{10}$ and $Ba_2MgB_2O_6$ hosts, respectively.[2, 3] However, Blasse and Nakamura et al. have observed intense blue emission from Eu^{2+} with CN=10 in $MBPO_5$ (M= Ca, Sr, Ba) suggesting these phosphors as better candidates for X-ray imaging.[4-6] Karthikeyani et al. have reported more intense blue emission from Eu^{2+} in non-hygroscopic $SrBPO_5$ host than in hygroscopic BaFBr.[7] Based on this, they have suggested $SrBPO_5$: Eu^{2+} to be a better phosphor than BaFBr: Eu^{2+} for X-ray imaging. Sakasai et al. have also reported $SrBPO_5$: Eu^{2+} as an excellent neutron imaging phosphor.[8]

The choice of a suitable host plays an important role, considering the wide applications of solid-state lanthanide luminescence. The phosphate-based phosphors are good luminescent materials, but the hygroscopic nature is the reason for their poor chemical stability.[9] Ln doped borate host, though exhibit strong luminescence has low thermal stability.[10] Borophosphate hosts have been of significant interest for their non-hygroscopic nature, better thermal and chemical stability as compared to that of borates and phosphates.[11, 12] The Ln^{3+} ions get easily incorporated into the M^{2+} sites of the $MBPO_5$ (MBP) hosts due to their large polarizing power. It is worth mentioning that some lanthanide ions in MBP[13] hosts as well as in several other hosts like borate[14], phosphate[15], oxide[16] and oxy-sulfide[17] exhibit luminescence in dual valences. For example, europium, both as Eu^{2+} as well as Eu^{3+}, exhibits luminescence in these hosts even though the samples are prepared in the absence of any reducing atmosphere (i.e., in air atmosphere). The existence of the reduced state (Eu^{2+}) in these hosts limits the color purity of the higher valency state (Eu^{3+}). The existence of europium in both oxidation states (Eu^{3+} and Eu^{2+}) in MBP hosts offers a wide range of color tuning. Moreover, these hosts with europium as an activator can be either a blue (Eu^{2+}) or red (Eu^{3+}) phosphor if one of the oxidation states can be controlled. Red phosphors are used in PDP, CRT, w-LEDs and laser.[18, 19] Though many of red phosphors are readily available, a phosphor with high efficiency is desired. Among the Ln^{3+} ions, Gd^{3+} is the only ion that emits narrow emission in the UV-*B* region which is very useful in phototherapy for treating several skin diseases.[20] Gd^{3+} is also known as an excellent sensitizer as its emitting energy level overlaps with some of the Ln ions like Eu^{3+}. The luminescence properties of Gd^{3+} in MBP hosts are yet to be reported. Furthermore, the effect of gadolinium codoping and γ-irradiation on PL and TSL properties of europium doped MBP is also not explored so far to the best of my knowledge.

In this chapter, the photoluminescence properties of Gd doped and Eu-Gd codoped $SrBPO_5$ are explored and discussed under section 4.1. PL lifetime and TRES measurements are carried out to get insight into the luminescence behavior and site occupancy of the activators in this host. The effects of gadolinium and γ-irradiation on luminescence properties of activators are also investigated. Following γ-irradiation, TSL glow curves and dose-response are reported here for the first time.

This chapter also reports a detailed comparative study of the structure and optical properties of Gd doped and Eu-Gd codoped MBP phosphors which are depicted under section 4.2. The optical band gap of these phosphors is obtained from the diffuse reflectance measurements following the Kubelka-Munk method. The effect of gadolinium codoping on Eu^{3+} and Eu^{2+} luminescence in $CaBPO_5$ (CBP), $SrBPO_5$ (SBP) and $BaBPO_5$ (BBP) phosphors, is also investigated. The site occupancy of the activators (Gd^{3+}, Eu^{3+} and Eu^{2+}) is studied by carrying out lifetime decay measurements.

4.2. Effect of gadolinium codoping on PL and TSL properties of $SrBPO_5$: Eu

4.2.1. Results and discussion

4.2.1.1. Structural analysis of $SrBPO_5$

Figure 4.1 shows the powder XRD patterns of the synthesized phosphors along with the standard pattern of SBP. The diffraction patterns of the samples match well with the standard pattern of SBP (ICDD file no. 18-1270) confirming the single phase purity of the samples with less than 10 mol% activator concentration. In case of SBP: $Gd_{0.10}$, some impurity peaks of very low intensities are observed in the 2θ range of 19-32° that match with the secondary phase of SBP (ICDD file No. 85-0065). The stillwellite-structured SBP belongs to the hexagonal crystal system ($P3_221$). The SBP host consists of interconnected tetrahedral borate (BO_4^{5-}) and phosphate (PO_4^{3-}) units wherein Sr^{2+} is bonded with O^{2-} with ten coordination number. This gives high rigidity and thermal stability to its structure.[21, 22]

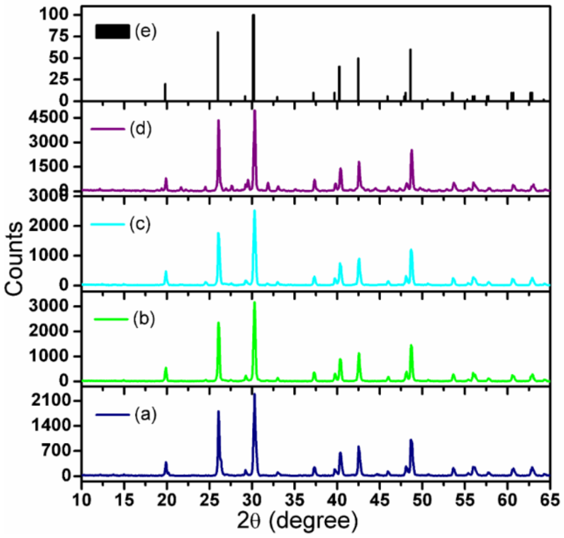

Figure 4.1 The PXRD pattern of SBP (a) undoped (b) Eu$_{0.01}$, Gd$_{0.01}$ (c) Eu$_{0.01}$, Gd$_{0.075}$ (d) Gd$_{0.10}$ and (e) standard ICDD pattern with file No. 18-1270.

4.2.1.2. Photoluminescence properties of SrBPO$_5$: Eu/Gd

Figure 4.2 shows the excitation and emission spectra of Gd^{3+} in SBP: Gd$_{0.075}$ at λ_{em} = 313 and λ_{ex} = 273 nm, respectively. The excitation spectrum exhibits an intense and narrow characteristic peak of Gd^{3+} at 273 nm ($^8S_{7/2} \rightarrow {}^6I_{13/2, 15/2}$) with shoulder peaks at 276 ($^8S_{7/2} \rightarrow {}^6I_{11/2}$) and 279 nm ($^8S_{7/2} \rightarrow {}^6I_{7/2}$).[23] The emission spectrum also exhibits its characteristic narrow peak at 313 nm ($^6P_{7/2} \rightarrow {}^8S_{7/2}$). Gd^{3+} luminescence is optimized varying Gd-concentration as shown in the inset of Figure 4.2. With the increase in Gd-concentration, the emission intensity of Gd^{3+} increases up to 7.5 mol% and thereafter it decreases due to the concentration quenching. The observed intense and narrow UV-*B* emission (313 nm) of the non-hygroscopic and thermally stable SBP: Gd$_{0.075}$ phosphor indicates its possible use for phototherapy and low-pressure discharge Hg-lamp applications.[20, 24-26]

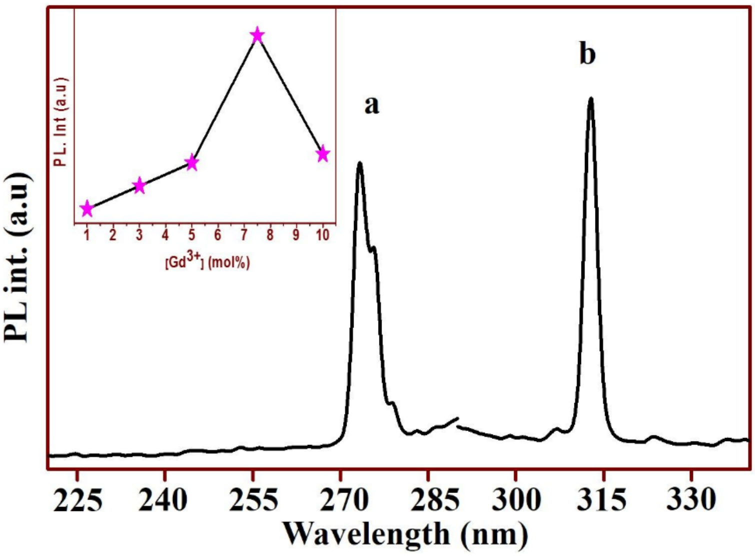

Figure 4.2 PL excitation (a) and emission (b) spectra of SBP: $Gd_{0.075}$. Inset shows the emission intensity of Gd^{3+} as a function of Gd-concentration.

Usually, lanthanides are incorporated in their reduced state in a host by synthesizing in a reducing atmosphere. However, Eu^{2+} luminescence has been reported in many hosts even though the synthesis is carried out in air atmosphere.[13, 15, 16, 27-30] The charge compensation due to the aliovalent substitution of Eu^{3+} at Sr^{2+} site, the absence of oxidizing ions, and similar ionic radii (r) of Eu^{2+} (CN =10, r =135 pm) and Sr^{2+} (CN =10, r =136 pm) facilitate the significant formation of Eu^{2+} in air fired SBP: Eu.[31] Another reason for the formation of Eu^{2+} in the SBP host is the feedback loop of the rigid 3D-network composing of tetrahedral BO_4^{5-} and PO_4^{3-} groups that can isolate and shield Eu^{2+} from oxidation.[32] In the present study, luminescence from Eu^{2+} as well as Eu^{3+} is also observed in SBP: $Eu_{0.01}$ prepared in the air (Fig. 4.3). The luminescence from Eu^{2+} is seemingly stronger than that from Eu^{3+} due to the parity allowed nature of the 4*f*-5*d* transitions of the former as compared to the parity forbidden nature of the 4*f*-4*f* transition of the latter. Eu^{2+} exhibits an intense excitation band at 302 nm ($^8S_{7/2} \rightarrow {}^4f^6 5d$) and emission band at 390 nm ($4f^6 5d \rightarrow {}^8S_{7/2}$) as shown in Figure 4.3(b, b′).

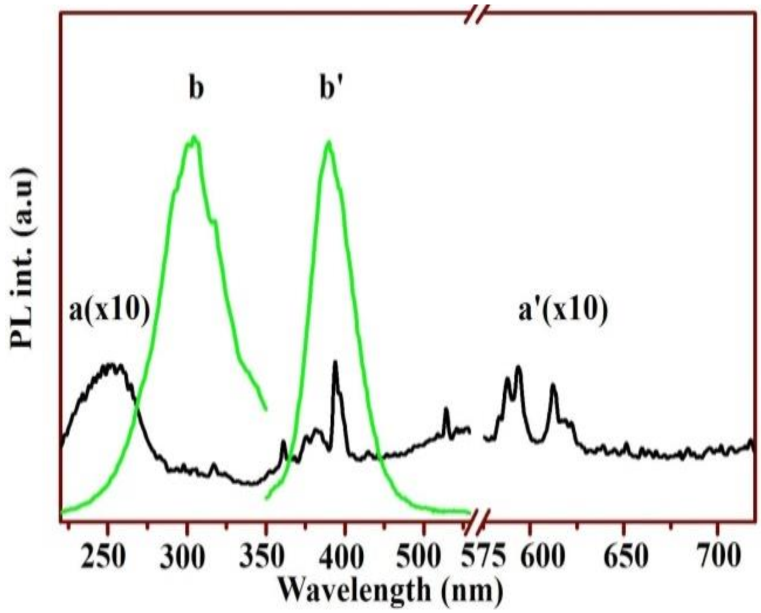

Figure 4.3 Excitation and emission spectra of SBP: Eu$_{0.01}$ *for (a, a') Eu*$^{3+}$ *at* λ_{em} *= 593,* λ_{ex} *= 393 nm and (b, b') Eu*$^{2+}$ *at* λ_{em} *= 390,* λ_{ex} *= 302 nm.*

In SBP: Eu$_{0.01}$, Eu^{3+} exhibits strong excitation peaks at 255 (charge transfer band), 393 ($^7F_0 \rightarrow {}^5L_6$) and 464 nm ($^7F_0 \rightarrow {}^5D_2$) along with weak peaks at 298, 304, 310, 318, 361, 382 and 416 nm (Fig. 4.3a). The characteristic emission peaks Eu^{3+} are observed at 578, 593, 612, 652 and 698 nm corresponding to $^5D_0 \rightarrow {}^7F_{0-4}$ transitions (Fig. 4.3a′).[33] The $^5D_0 \rightarrow {}^7F_1$ transition is an allowed magnetic dipole (MD) transition and least sensitive to the ligand field. In contrast, the $^5D_0 \rightarrow {}^7F_2$ transition is an allowed electric dipole (ED) transition and hypersensitive to the crystal field. The integral intensity ratio of ED to MD transitions (I_{ED}/I_{MD}) called asymmetry ratio is an important feature to study the local environment around Eu^{3+} in the host lattice.

Figure 4.4 shows the excitation and emission spectra of Eu^{3+} in SBP: Eu$_{0.01}$ and SBP: Eu$_{0.01}$, Gd$_{0.01-0.10}$ at λ_{em} = 593 and λ_{ex} = 273 nm, respectively. The energy transfer between a donor and an acceptor is efficient when the overlap of the donor’s emission and acceptor’s excitation spectrum is strong. The excitation spectrum of Eu^{3+} (Fig. 4.3a) and the emission spectrum of Gd^{3+} (Fig. 4.2b) display a significant overlap suggesting the possibility of ET from Gd^{3+} to Eu^{3+}.

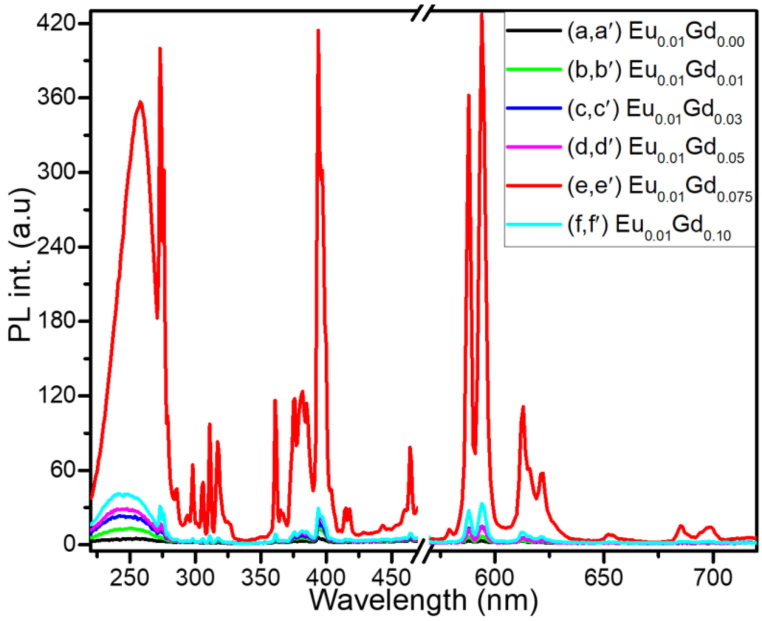

Figure 4.4 Excitation and emission spectra of Eu^{3+} *at* λ_{em} *= 593 and* λ_{ex} *= 273 nm in SBP: (a, a') $Eu_{0.01}$ (b, b') $Eu_{0.01}$, $Gd_{0.01}$ (c, c') $Eu_{0.01}$ $Gd_{0.03}$ (d, d') $Eu_{0.01}$, $Gd_{0.05}$ (e, e') $Eu_{0.01}$, $Gd_{0.075}$ and (f, f') $Eu_{0.01}$, $Gd_{0.10}$.*

There is no significant excitation peak for Eu^{3+} in SBP: $Eu_{0.01}$ at 273 nm (Fig. 4.4a) whereas an intense 273 nm peak is observed (Figure 4.4(b-f)) in the excitation spectrum of Eu^{3+} in the presence of Gd^{3+}. The 273 nm peak is the excitation peak for Gd^{3+} as discussed earlier. With the increase in Gd-concentration (1-10 mol%), the intensity of the 273 nm peak also increases. Correspondingly in the presence of Gd^{3+}, excitation at 273 nm results in enhancement of Eu^{3+} emission intensity as seen in Figure 4.4(b′-f′). In the codoped samples, Eu^{3+} luminescence increases gradually with the increase in Gd-concentration up to 7.5 mol% (Fig. 4.4e′) and thereafter it decreases due to the concentration quenching. This suggests that the presence of Gd^{3+} sensitizes Eu^{3+} luminescence in this host through ET from Gd^{3+} to Eu^{3+}.[34]

Further, the critical distance (C_d) of energy transfer is determined for SBP: $Eu_{0.01}$, $Gd_{0.075}$ phosphor using the expression, $C_d = 2[3V/4\pi NC]^{1/3}$. Where V is the volume of the unit cell (282.03 Å^3), N is the number of cationic sites (5) available for the activator per unit cell and C is the critical concentration (8.5 mol%) of activators. The value of C_d is calculated to be 2.33 Å (<10 Å) indicating an effective Dexter type of non-radiative ET.[35]

Interestingly, Figure 4.3 also shows that there is an overlap between the emission spectrum of Eu^{2+} (Fig. 4.3b′) and the excitation spectrum of Eu^{3+} (Fig. 4.3a). Therefore, ET from Eu^{2+} to Eu^{3+} could not have been ruled out considering the overlap criteria. However, no excitation peak around 302 nm (Eu^{2+} excitation peak) is observed in the excitation spectrum of Eu^{3+}. Furthermore, excitation at 302 nm does not also result in the enhancement of Eu^{3+} luminescence ruling out any ET from Eu^{2+} to Eu^{3+}.[36]

Apart from the appearance and the increase in the 273 nm excitation peak intensity with respect to Eu^{3+} emission in the presence of gadolinium, all other excitation peaks of Eu^{3+} on either side of 273 nm are also enhanced as observed in Figure 4.4(b-f). In case of a simple ET from Gd^{3+} to Eu^{3+}, only the excitation peak at 273 nm should have been enhanced while recording the excitation spectrum for Eu^{3+} monitoring its emission at 593 nm. However, the enhancement of all the excitation peaks of Eu^{3+} along with the significant emergence of 273 nm peak suggests that ET is not the only phenomenon leading to the enhancement of Eu^{3+} luminescence.

Figure 4.5 shows the emission spectra of Gd^{3+} and Eu^{2+} in the absence and the presence of gadolinium. The emission of Gd^{3+} is reduced significantly in SBP: $Eu_{0.01}$, $Gd_{0.075}$ (Fig. 4.5a) as compared to that of SBP: $Gd_{0.075}$ (Fig. 4.5b). Apart from the increase in Eu^{3+} intensity and decrease in Gd^{3+} intensity, notably Eu^{2+} luminescence in SBP: $Eu_{0.01}$, $Gd_{0.075}$ (Fig. 4.5c) is also decreased in the presence of gadolinium as compared to that of SBP: $Eu_{0.01}$ (Fig. 4.5d). In case of ET from Gd^{3+} to Eu^{3+}, there is no reason for the decrease in Eu^{2+} luminescence. The extent of the decrease in Eu^{2+} intensity progressively increases with the increase in Gd-concentration. Simultaneously, the intensity of all the excitation peaks of Eu^{3+} also gets increased. Weak excitation peaks of Eu^{3+} are known to be present in the range of 292-320 nm due to $^7F_{0,1}\rightarrow{}^5H_{3,6}$ transitions[33], but some of them are seen and some not seen in case of SBP: $Eu_{0.01}$.

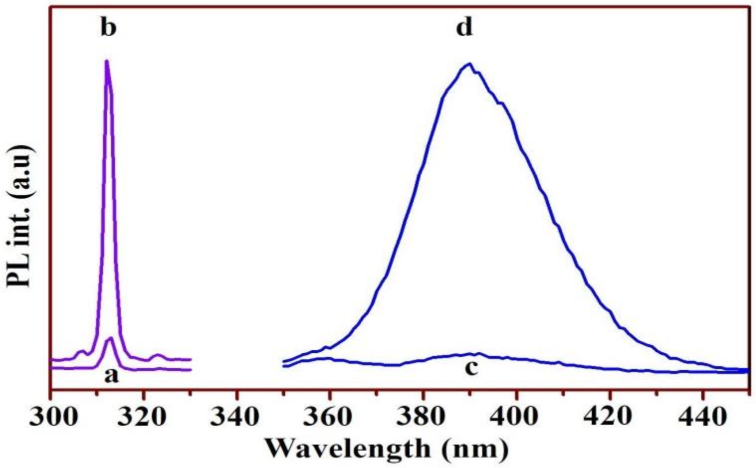

Figure 4.5 Emission spectra of Gd^{3+} *at* $\lambda_{ex} = 273$ *nm in SBP (a)* $Eu_{0.01}$, $Gd_{0.075}$ *and (b)* $Gd_{0.075}$, *and* Eu^{2+} *at* $\lambda_{ex} = 302$ *nm (c)* $Eu_{0.01}$, $Gd_{0.075}$ *and (d)* $Eu_{0.01}$.

However, in the presence of Gd^{3+}, those weak excitations of Eu^{3+} are observed prominently as shown in Figure 4.4(b-f). The ET could have only increased 273 nm (Gd^{3+} excitation) peak intensity without any increase in the intensities of other excitation peaks of Eu^{3+} with the increase in the Gd-concentration in the coactivated sample. Moreover, the higher energy CT band centered at 255 nm has also increased with the increase in Gd-concentration and this excitation band is not associated with any excitation peak of Gd^{3+}. This indicates that the presence of gadolinium in the coactivated SBP leads to the valency conversion (VC) of europium from Eu^{2+} to Eu^{3+}. Therefore, the enhancement of Eu^{3+} luminescence in the presence of gadolinium observed here is due to both the ET ($Gd^{3+}\rightarrow Eu^{3+}$) and VC ($Eu^{2+}\rightarrow Eu^{3+}$). But, the VC of Eu^{3+} to Eu^{2+} in the presence of terbium in SrB_4O_7[14] and Y_2O_2S[17] hosts has been earlier reported by G. Yong et al. The observed VC explained by them is based on the one-electron transfer phenomenon, whereby both Tb^{3+} and Eu^{2+} attain the half-filled configuration ($4f^7$). However, in the present study, Eu^{2+} ($4f^7$) is observed to be converted into Eu^{3+} ($4f^6$) and consequently Gd^{3+} ($4f^7$) is expected to be converted into Gd^{2+} ($4f^7 5d$). Therefore, the stability gained through the half-filled configuration, as proposed by G. Yong et al., may not be the sole factor for the VC of europium in the presence of other lanthanides. More investigations are required to understand the VC phenomenon of europium.

The asymmetry ratio reveals information about the occupancy, symmetry and the change in the immediate environment of Eu^{3+}. Figure 4.6 shows the variation of the asymmetry ratio of Eu^{3+} at different excitations (λ_{ex} = 255, 273 and 393 nm) in SBP: $Eu_{0.01}$, $Gd_{0-0.10}$. The asymmetry ratio for λ_{ex} = 393 nm (4*f*-4*f*) is higher than that observed for λ_{ex} = 255 nm (CT) and 273 nm (ET). This indicates that Eu^{3+} gets preferentially excited from the lower symmetry site by the 4*f*-4*f* excitation resulting in a higher asymmetry ratio whereas from the higher symmetry site by the CT band resulting in a lower asymmetry ratio. For all excitations, with the increase in Gd-concentration, the asymmetry ratio decreases up to 7.5 mol% Gd and thereafter the ratio increases. This indicates that the environment around Eu^{3+} becomes more symmetric as Gd-concentration increases to 7.5 mol% and thereafter the symmetry probably gets lowered.

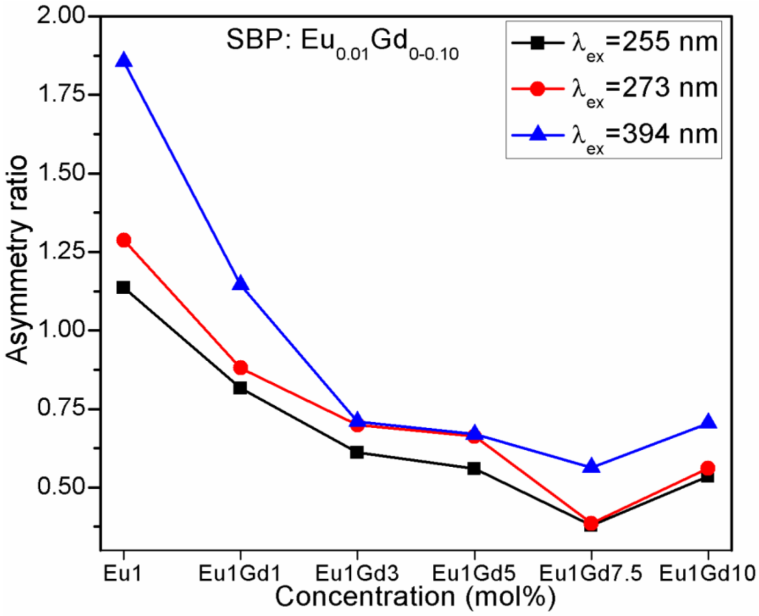

Figure 4.6 Asymmetry ratio of Eu^{3+} at different excitations and Gd-concentration in SBP: $Eu_{0.01}$, $Gd_{0-0.10}$.

4.2.1.3. PL lifetime studies of Gd^{3+}, Eu^{3+} and Eu^{2+}

Figure 4.7 shows the lifetime decays of SBP: $Gd_{0.01}$, SBP: $Eu_{0.01}$ and SBP: $Eu_{0.01}$, $Gd_{0.01}$ phosphors. Eu^{3+} exhibits two lifetimes of τ_1=331 (38%) and τ_2=2305 μs (62%) in SBP: $Eu_{0.01}$ (Fig. 4.7a) whereas τ_1=581 μs (58%) and τ_2=2081 μs (42%) in SBP: $Eu_{0.01}$, $Gd_{0.01}$ (Fig. 4.7a′). Eu^{2+} exhibits a single lifetime of 560 ns in SBP: $Eu_{0.01}$ (Fig. 4.7b) and 554 ns in SBP: $Eu_{0.01}$, $Gd_{0.01}$ (Fig. 4.7b′). The two lifetimes for Eu^{3+} suggest its occupancy in two different sites in this host. Eu^{3+} being present in two different sites is expected to show different emission spectra in different time domains.

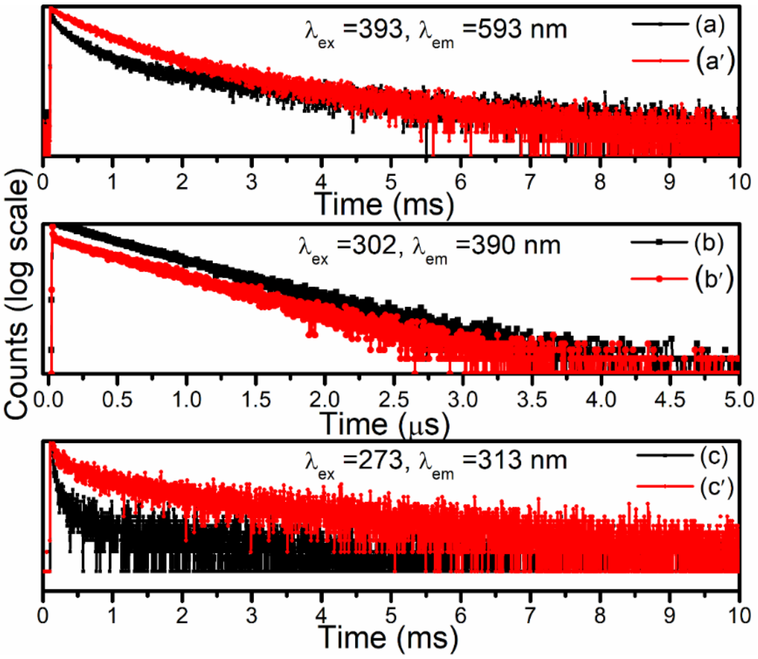

Figure 4.7 Lifetime decays of Eu^{3+} (a) $Eu_{0.01}$ (a′) $Eu_{0.01}$, $Gd_{0.01}$; Eu^{2+} (b) $Eu_{0.01}$ (b′) $Eu_{0.01}$, $Gd_{0.01}$; and Gd^{3+} (c) $Gd_{0.01}$ (c′) $Eu_{0.01}$, $Gd_{0.01}$.

Figure 4.8 shows the time-resolved emission spectra (TRES) of Eu^{3+} in SBP: $Eu_{0.01}$ in two different time domains of 0-2000 (Fig. 4.8a) and 2000-7500 μs (Fig. 4.8b). In the time domain of 0-2000 μs, Eu^{3+} present in a site with a lifetime of 331 μs completes more than six lifetimes and in the other site with 2305 μs lifetime is yet to complete its one lifetime. Therefore, Eu^{3+} present in the site with 331 μs lifetime contributes predominantly to the emission obtained during this period. In the time domain of 2000-7500 μs, the contribution to the emission spectrum is mostly from Eu^{3+} present in the site with 2305 μs lifetime as by 2000 μs, Eu^{3+} in the first site completes six lifetimes and its contribution to the emission spectrum would be insignificant. The observed difference in the Eu^{3+} emission intensities of MD and ED transitions in the two different time domains (Fig. 4.8) confirms the presence of Eu^{3+} occupancy in two different sites.

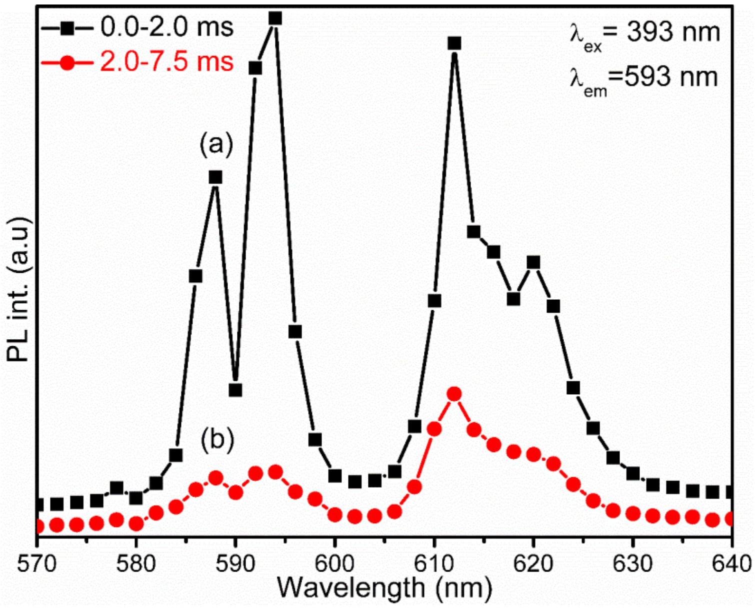

Figure 4.8 TRES profiles of Eu^{3+} in SBP: $Eu_{0.01}$ in the time domain of 0-2.0 and 2.0-7.5 ms.

Similarly, Gd^{3+} in SBP: $Gd_{0.01}$ also exhibits two lifetimes of τ_1=265 (16%) and τ_2=3891 μs (84%) (Fig. 4.7c) suggesting its occupancy in two different sites. Two lifetimes are observed at all Gd-concentrations (1-10 mol%) in this host. Both the lifetime values of Gd^{3+} in SBP: $Eu_{0.01}$, $Gd_{0.01}$ decrease to τ_1=235 μs (12%) and τ_2=2699 μs (88%) in the presence of europium (Fig. 4.7c′) corroborating the ET ($Gd^{3+}\rightarrow Eu^{3+}$) and in-situ VC ($Eu^{2+}\rightarrow Eu^{3+}$) phenomena. However, in the coactivated SBP: Eu, Gd samples, only a single lifetime is found for higher Gd-concentration (≥3 mol%). The lifetime value of Gd^{3+} consistently decreases with further increase in its concentration and simultaneously Eu^{3+} luminescence gets enhanced till 7.5 mol% of gadolinium.

4.2.1.4. Evaluation of color coordinates of Eu^{3+} in $SrBPO_5$

The performance of a light-emitting material is determined using the CIE (International Commission on Illumination) chromaticity coordinates. Color coordinates (CRI) coordinates for the samples studied here are evaluated adopting standard procedure. The CRI coordinates obtained for $\lambda_{ex} = 273$ nm for Eu^{3+} (1 mol%) in the codoped phosphors with varying Gd-concentration 0, 1, 3, 5, 7.5 and 10 mol% are (0.45, 0.52), (0.49, 0.49), (0.52, 0.46), (0.53, 0.45), (0.57, 0.42), (0.54, 0.45), respectively. It can be seen from Figure 4.9 that SBP: $Eu_{0.01}$, $Gd_{0.075}$ phosphor exhibits good CRI coordinates of (0.57, 0.42) showing intense orange-red color. The CRI observed here for the codoped phosphor is better than Eu doped yttrium phosphate, gadolinium phosphate[37] and gadolinium oxide[38] suggesting its possible use as a lamp phosphor.

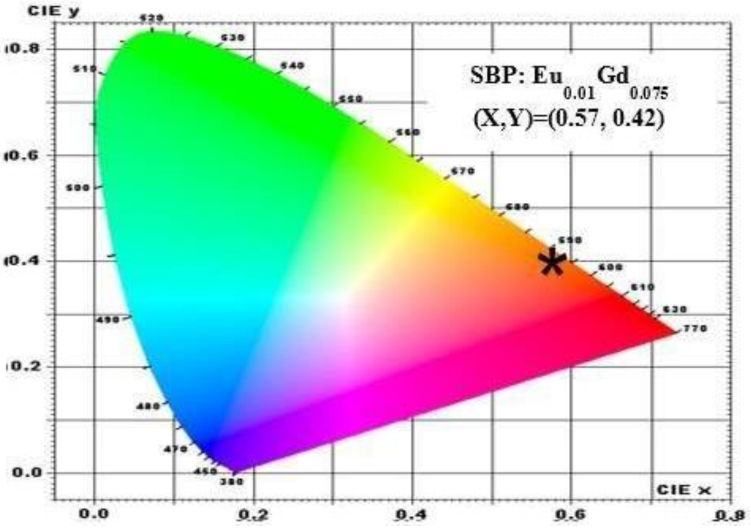

Figure 4.9 Chromaticity diagram shows the CRI coordinates of SBP: $Eu_{0.01}$, $Gd_{0.075}$ phosphor obtained for $\lambda_{ex} = 273$ nm.

4.2.1.5. Effect of γ-irradiation on PL of Gd^{3+}, Eu^{3+} and Eu^{2+}

The effect of γ-irradiation on PL of gadolinium and europium activated SBP is reported here for the first time. The PL emission spectra of SBP: Eu, SBP: Gd and SBP: Eu, Gd before and after γ-irradiation are shown in Figure 4.10. Usually, exposure to γ-radiation results in the reduction of Ln^{3+} and thereby, the intensity of Ln^{2+} emission increases in the irradiated samples.[39] However, it can be seen from Figure 4.10(a, b) that luminescence of

Eu^{2+} in the irradiated SBP: Eu reduced nearly 1.7 times compared to that of the unirradiated sample but a corresponding increase in the Eu^{3+} intensity is not observed; rather a marginal decrease is seen following the irradiation (Fig. 4.10e-f). In case of codoped samples, no significant change in the Eu^{2+} intensity is observed (Fig. 4.10c-d) following the irradiation, whereas Eu^{3+} intensity gets quenched (Fig. 4.10g-h). Gd^{3+} luminescence decreases following the irradiation irrespective of the presence of coactivator europium (Fig. 4.10i-l). In case of SBP, the substitution of Sr^{2+} by Eu^{3+} creates two positive defects of Eu^{+}_{Sr} and one vacancy defect V''_{Sr} with two negative charges. It has been reported that the hole trapped species (BO_3^{2-} and O^-), and the electron trapped species (O_2^- and F-centers) are generated in SBP following gamma irradiation.[40] These different types of defects may influence europium luminescence. Probably, it may be the reason for the observed quenching of Eu^{2+} and Eu^{3+} luminescence in the present study. After the TSL measurement and thermal bleaching, Eu^{2+} luminescence could recover nearly 50% whereas Eu^{3+} luminescence could recover nearly 30% indicating some of the defects are not reversible.

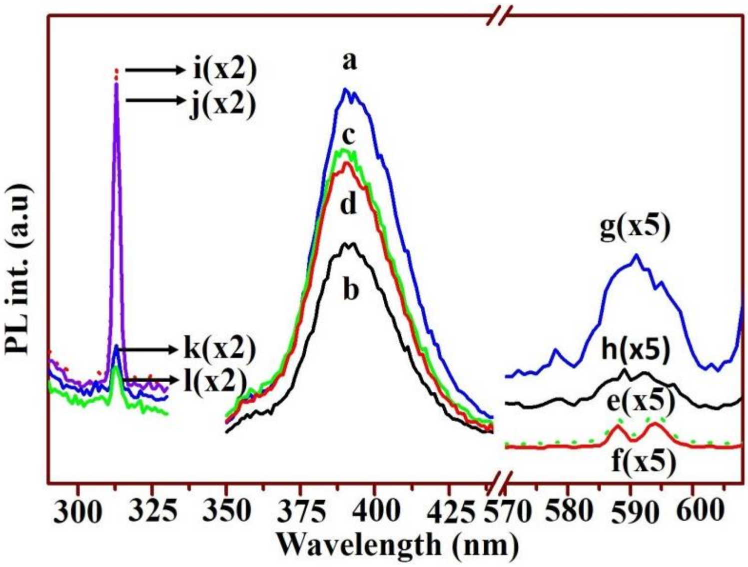

Figure 4.10 Emission of Eu^{2+} at λ_{ex} = 302 nm (a) Eu, UR (b) Eu, R (c) Eu, Gd, UR (d) Eu, Gd, R; Eu^{3+} at λ_{ex} = 393 nm (e) Eu, UR (f) Eu, R (g) Eu, Gd, UR (h) Eu, Gd, R; Gd^{3+} at λ_{ex} = 273 nm (i) Gd, UR (j) Gd, R (k) Eu, Gd, UR (l) Eu, Gd, R. The concentration of Eu and Gd is 1 mol% each. [UR: unirradiated and R: irradiated phosphor]

4.2.1.6. **Thermally stimulated luminescence (TSL) studies**

TSL glow curves (GCs) provide information on trap parameters such as trap depth (E), attempt-to-escape frequency (S), order of kinetics of de-trapping (b), symmetry factor (μ) and lifespan (Γ) of trapped charge at 300 K. In chapter 3, the TSL properties of Ce-activated SBP is discussed. In this chapter, TSL studies of γ-irradiated SBP: Eu/Gd are reported for the first time. Figure 4.11 shows the GCs of unirradiated SBP and irradiated (24 Gy) SBP: $Eu_{0.01}$, SBP: $Gd_{0.01}$ and SBP: $Eu_{0.01}$, $Gd_{0.01}$ phosphors recorded at a heating rate (β) of 2.5 K/s. In case of unirradiated SBP (Fig. 11a), a very weak glow peak is observed at 666 K indicating the presence of intrinsic defects in the host. In case of irradiated SBP: Eu (Fig. 4.11b), an intense peak at 411 K and for irradiated SBP: Gd (Fig. 4.11c) relatively weak peaks at 406, 554 and 655 K are observed. In case of irradiated SBP: Eu, Gd, intense peaks at 413 and 532 K are observed (Fig. 4.11d).

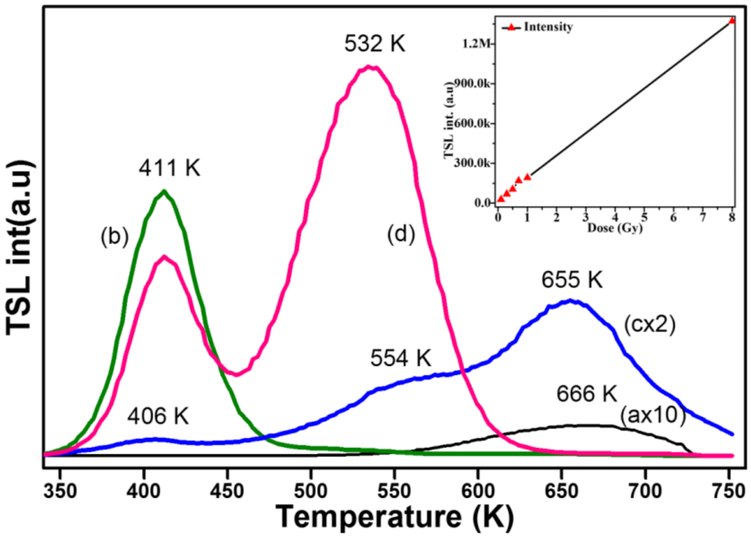

Figure 4.11 Glow curves of SBP: (a) undoped, 0 Gy (b) $Eu_{0.01}$, 24 Gy (c) $Gd_{0.01}$, 24 Gy and (d) $Eu_{0.01}$, $Gd_{0.01}$, 24 Gy recorded at β=2.5 K/s. Inset shows dose-response of SBP: $Eu_{0.01}$, $Gd_{0.01}$ for the 532 K peak in the dose range of 100 mGy - 8 Gy.

Usually, the temperature of glow peak lying in the range of 450-550 K, sometimes called the dosimetry peak, is suitable for dosimetry studies since glow peak below 450 K gets faded with low thermal excitation whereas that above 550 K requires a very high thermal excitation. Among the phosphors studied here, SBP: Eu, Gd may be a suitable thermoluminescent phosphor as it shows an intense glow peak in the required temperature range (450-550 K). The codoped phosphor shows a linear dose-response up to second order in the dose range of 100 mGy to 8 Gy (inset of Fig. 4.11) and thereafter saturation is initiated. M. Kumar et al. have reported TSL for both SBP: Eu^{2+} and SBP: Eu^{3+}.[22] In their study, SBP: Eu prepared in the air and reducing atmosphere exhibits only Eu^{3+} and Eu^{2+} luminescence, respectively. However, in the present study, SBP: Eu samples prepared in the air show both Eu^{2+} and Eu^{3+} luminescence as discussed above. Therefore, the TSL characteristics observed here are ascribed to europium in SBP rather than to Eu^{2+} or Eu^{3+}. For all these samples, TSL emission spectra are recorded and only Eu^{2+} emission in SBP: Eu and SBP: Eu, Gd could be observed.

The trap parameters such as E, S, μ, b and Γ of all the phosphors studied here are determined (Table 4.1) following Chen's peak shape (CPS) method.[41, 42] The frequency can be determined using the general expression, $S = (\beta E/kT_m^2) \exp(E/kT_m) [1/ \{1+ (2kT_m/E) (b-1)\}]$. The lifespan of the trapped charge depends on the respective E and S values and can be calculated using the expression, $\Gamma = (1/S) \exp(E/0.026)$. The theoretical values of μ of the glow curves corresponding to the first and second-order kinetics are 0.42 and 0.52, respectively. For all our irradiated samples, the values of μ are close to 0.52 indicating the second-order kinetics except for the unirradiated and undoped sample which follows the first-order kinetics having μ close to 0.42. In case of SBP: Eu, Gd phosphor, E values obtained following the CPS method for the peaks 413 and 532 K are 0.88 eV and 0.84 eV, respectively. It may be noted the glow peak observed at high temperature (532 K) is expected to have a higher value of trap depth than that of the low-temperature peak (413 K) whereas the trap depth of 413 K peak is observed to be higher than that of 532 K peak. According to the CPS method, E is inversely related to the full-width at half maxima (w). Thus, the 532 K peak having a higher value of FWHM (w=84 K) than that of 413 K peak (w=52 K) shows a lower E value. For the glow peak 532 K, the lifespan is reasonably high (~3x10^6 years) and the linear dose-response is over two orders of magnitude suggesting its possible use in radiation dosimetry.

Table 4.1 Trap parameters of undoped-unirradiated and Eu/Gd-doped irradiated SBP based on CPS method.

Phosphor	T_m (K)	w (K)	μ	b	E (eV)	S (s^{-1})	Γ years
SBP, 0 Gy	666	116	0.41	1	0.69	7.5x10^3	1.0x10^4
SBP: Eu, 24 Gy	411	53	0.53	2.03	0.92	5.3x10^9	8.7x10^7
SBP: Gd, 24 Gy	406	-	-	-	-	-	-
	554	101	0.50	1.94	0.75	7.7x10^4	1.0x10^5
	655	97	0.50	1.94	1.14	7.5x10^6	3.6x10^{11}
SBP: Eu, Gd, 24 Gy	413	53	0.51	1.95	0.86	8.6x10^8	9.3x10^6
	532	84	0.50	1.92	0.84	1.3x10^6	3.4x10^6

The trap parameters of the irradiated (24 Gy) SBP: $Eu_{0.01}$, $Gd_{0.01}$ phosphor are also determined following the VHR (Various Heating Rates) method which employs variable heating rates during measurements of glow curves. The phosphor exhibits two glow peaks at T_{m1} (400-420 K) and T_{m2} (522-547 K) that are found to shift to higher T_m values with a corresponding reduction in intensity as β increased from 1 to 6 K/s (Table 4.2). The values of E obtained by this method for the low-temperature peak 1 and high-temperature peak 2 are 1.02 eV (S=4.3x10^{11} s^{-1}) and 1.55 eV (S=6.9x10^{13} s^{-1}), respectively, indicating higher trap depth for higher glow peak temperature.

Table 4.2 Trap parameters of irradiated (24 Gy) SBP: $Eu_{0.01}$, $Gd_{0.01}$ based on the VHR method.

Heating rate, β (K/s)	Peak 1, T_{m1} (K)	Intensity, I_1 (a.u)	Peak 2, T_{m2} (K)	Intensity, I_2 (a.u)
6	420	7.14x10^5	547	1.09x10^6
5	419	7.18x10^5	545	1.16x10^6
4	417	7.89x10^5	542	1.32x10^6
3	414	8.12x10^5	539	1.48x10^6
2.5	411	8.14x10^5	532	1.60x10^6
2	409	8.80x10^6	530	1.81x10^6
1	400	9.66 x10^6	520	2.62x10^6

4.3. Effect of gadolinium codoping on PL properties of $MBPO_5$: Eu

4.3.1. Results and discussion

4.3.1.1. Structural analysis of $MBPO_5$

Figure 4.12 shows the powder XRD patterns of undoped and $Gd_{0.10}$ doped (A) CBP (B) SBP and (C) BBP samples. The recorded XRD patterns are found to match well with the respective standard ICDD patterns with file numbers: 89-7584 (CBP), 18-1270 (SBP) and 89-4624 (BBP). In cases of CBP: $Gd_{0.10}$, a few impurity peaks (*) of low intensity are seen at higher dopant concentration suggesting the presence of a secondary phase. Compared to the diffraction intensity of CBP, SBP and BBP samples exhibit higher intensity without any significant impurity peaks indicating better phase purity, though the calcination duration is the same. However, no improvement could be observed in the diffraction intensity of the CBP samples synthesized at different calcination duration (5 to 30 h).

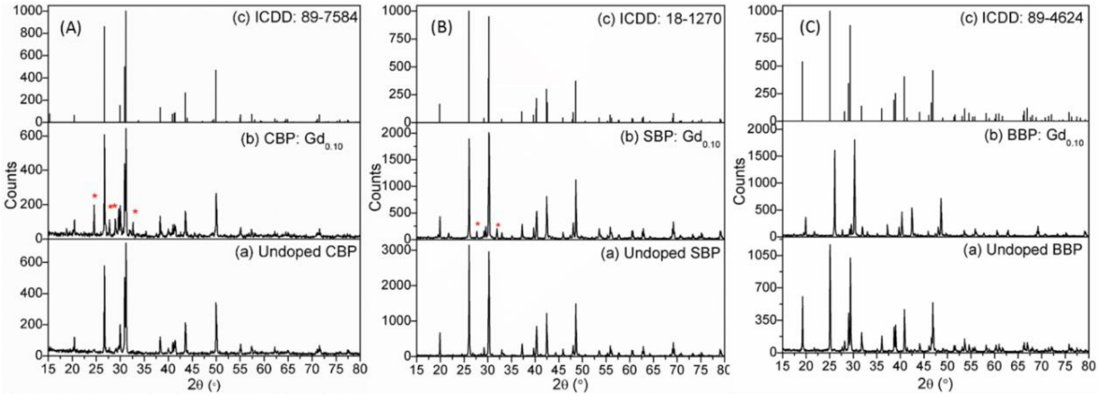

Figure 4.12 Powder XRD patterns of undoped, $Gd_{0.01}$ doped and ICDD of (A) CBP (B) SBP and (C) BBP samples.

The crystal structures of CBP, SBP and BBP hosts are shown in Figure 4.13. The stillwellite-structured MBP hosts have crystallized in the primitive lattice of the hexagonal crystal system belonging to $P3_221$ space group and having three formula units per unit cell. In the MBP, the tetrahedral BO_4^{5-} and PO_4^{3-} units share common vertexes and are interconnected to the M^{2+} ion through extensive oxygen bridging forming a loop-like rigid network[43].

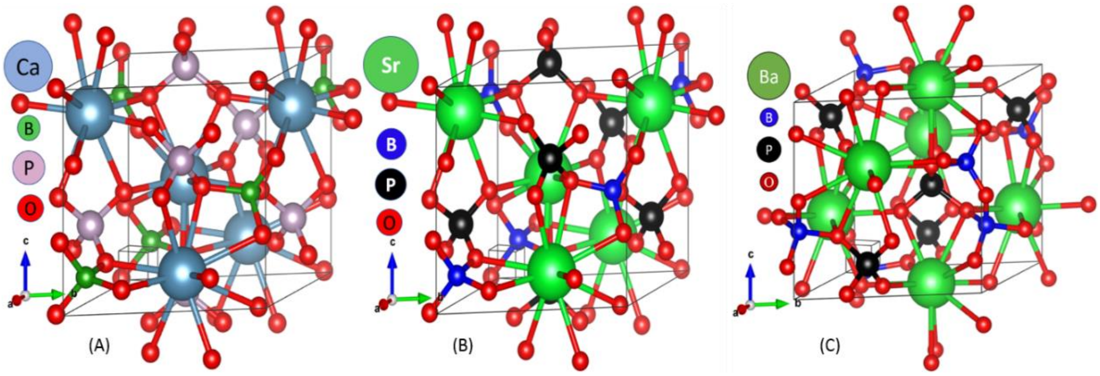

Figure 4.13 The crystal structure of (A) CBP (B) SBP and (C) BBP hosts.

The structure also shows that the M^{2+} ions have 10-fold coordination[22] with the O^{2-} ions. The same coordination number has been experimentally corroborated through extended X-ray absorption fine structure spectroscopy.[32] The higher ionic radius of the 10-coordinated Ca^{2+} (123 pm), Sr^{2+} (136 pm) and Ba^{2+} (152 pm) than that of Gd^{3+} and Eu^{3+} (112-120 pm) allowing Ln^{3+} for easy incorporation into the host lattice[31]. In case of BBP, Ba^{2+} has six atomic positions that occupy the six surfaces of its unit cell whereas, in cases of CBP and SBP, Ca^{2+} and Sr^{2+} have five atomic positions wherein four atoms reside on the surfaces and one at the center of the respective unit cell. Unlike CBP and SBP (Fig. 4.13 2A and 2B), the tetrahedral BO_4^{5-} and PO_4^{3-} units are differently positioned in BBP to accommodate the higher sized Ba^{2+} ions (Fig. 4.13 2C). However, BBP retains the same number of formula units and coordination number as in the other two hosts.

4.3.1.2. Estimation of band gap of undoped, Eu doped and Eu-Gd codoped $MBPO_5$

Measuring the band gap (E_g) of the phosphor is important as it sheds light on the possible reabsorption of the photon emitted from the activator by the host lattice itself. A phosphor can emit efficiently in the visible region when E_g is greater than 3.2 eV[44] and in the UV-B region and below when the E_g is above 4 eV. The E_g of undoped, $Eu_{0.01}$ doped and $Eu_{0.01}$, $Gd_{0.01}$ codoped MBP samples are obtained following Kubelka-Munk function using DRS as shown in Figure 4.14. The detailed calculation procedure is discussed in chapter 3. In case of undoped CBP, the E_g is calculated to be 4.20 eV whereas that of both the Eu doped and Eu-Gd codoped CBP samples are calculated to be 4.60 eV (Fig. 4.14a-c). Like CBP, the E_g of Eu doped and Eu-Gd codoped SBP (4.69 eV) is larger as compared to that of the undoped SBP (4.30 eV) as shown in Figure 4.14 (d-f). A similar observation is also seen (Fig. 4.14g-i) in undoped (4.39 eV) and activated BBP (4.61 eV). The higher band gap value observed in Eu/Gd doped MBP phosphors could be due to the high lying empty 5d-orbitals of the lanthanide ions effectively changing its band structure. In cases of all the activated MBP, the E_g is higher than 4 eV indicating them suitable as UV phosphors. From Figure 4.14, it may be noted that some localized defect states at 3.90, 3.91 and 3.95 eV are seen for undoped CBP, SBP and BBP samples, respectively. However, these defects states are well above the threshold limit of 3.2 eV which is necessary for a phosphor to emit efficiently in the UV-VIS region.

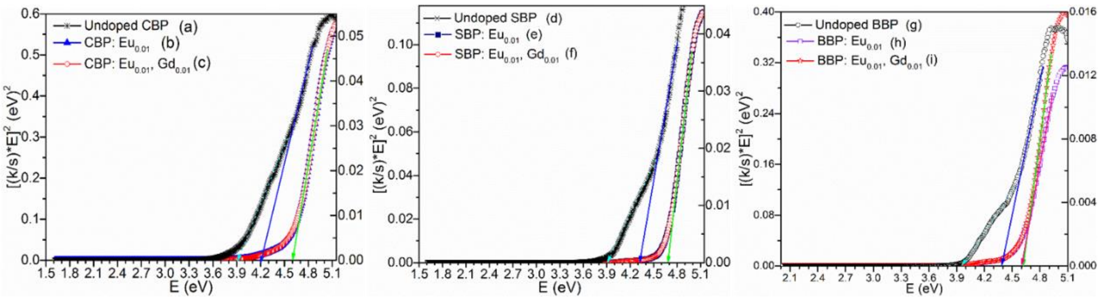

Figure 4.14 Band gap of undoped, Eu doped and Eu-Gd codoped (a-c) CBP (d-f) SBP and (g-i) BBP estimated following Kubelka-Munk function.

4.3.1.3. Photoluminescence (PL) properties of $MBPO_5$: Eu/Gd

The excitation and emission spectra of Gd^{3+} in MBP: $Gd_{0.01}$ are presented in Figure 4.15. The excitation (Fig. 4.15a-c) and the emission spectra (Fig. 4.15a′-c′) of Gd^{3+} exhibit its characteristics narrow peak at 273 nm and 313 nm, respectively, as discussed earlier. Unlike other optically active trivalent lanthanide ions, the ground state of Gd^{3+} ($^8S_{7/2}$) is degenerate and its emitting state is much above the emitting levels of Ln^{3+}. Hence, Gd^{3+} gives a single and narrow emission in the UV-*B* region (280-320 nm). The inset of Figure 4.15 shows the PL intensity of Gd^{3+} (313 nm) in MBP as a function of Gd-concentration. In case of CBP: Gd, up to 7.5 mol%, Gd^{3+} luminescence increases with the increasing Gd-concentration and thereafter its intensity remains almost unchanged. As observed earlier in SBP: Gd (Section 4.1), in case of BBP: Gd, the PL intensity of Gd^{3+} is maximum at 7.5 mol% Gd doping beyond which it decreases due to the concentration quenching. This study shows that the observed intense UV-*B* emission from SBP: $Gd_{0.075}$ and BBP: $Gd_{0.075}$ phosphors may be suitable in phototherapy for treating several skin diseases and for Hg-discharge lamp applications.

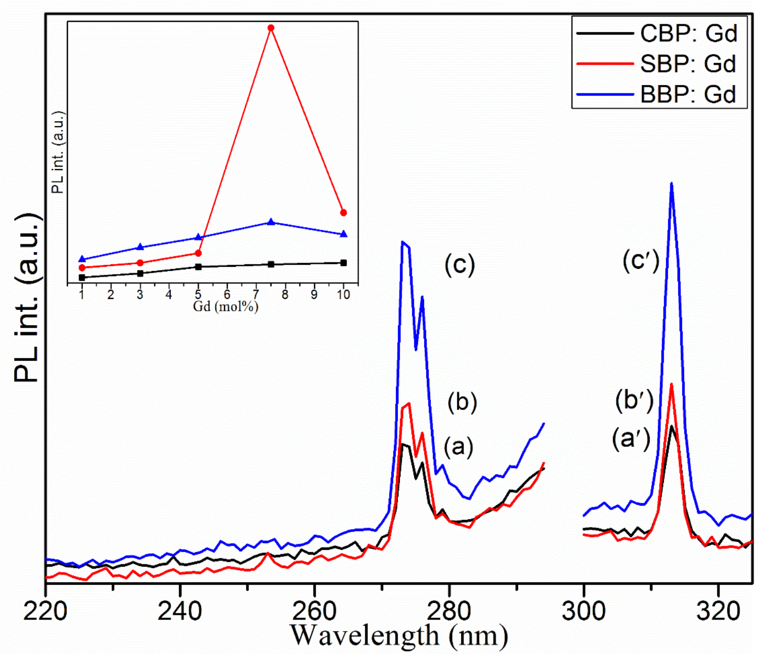

Figure 4.15 Excitation and emission spectra of $Gd_{0.01}$ doped (a, a′) CBP (b, b′) SBP and (c, c′) BBP at λ_{em} = 313 and λ_{ex} = 273 nm, respectively. Inset shows the PL intensity of Gd^{3+} as a function of Gd-concentration.

The excitation and emission spectra of Eu^{3+} in MBP: $Eu_{0.01}$ are shown in Figure 4.16. As seen earlier in SBP: Eu (Section 4.1), in cases of CBP: Gd and BBP: Eu, Eu^{3+} exhibits the characteristic strong absorptions at 262, 394 and 464 nm (Fig. 4.16 a-c) and the characteristic emissions at 578, 594, 612, 652 and 698 nm (Fig. 4.16 a´-c´). Typically, one can extract information on the symmetry around Eu^{3+} by probing its magnetic dipole transition ($^5D_0 \rightarrow {}^7F_1$) and its electric dipole transition ($^5D_0 \rightarrow {}^7F_2$). While both the transitions are allowed, the former is insensitive to its immediate environment while the latter is hypersensitive. It can be seen from Figure 4.16 that the emission intensity ratios of the MD and ED transitions of Eu^{3+} in the three hosts are different. Hence, the asymmetry ratio of Eu^{3+} is calculated to correlate with its site symmetry and the emission color of the phosphor. In the present study, the asymmetry ratios for $Eu_{0.01}$ doped CBP, SBP and BBP are calculated to be 0.91, 1.09 and 1.22, respectively. The asymmetry ratios for the codoped CBP: $Eu_{0.01}$, $Gd_{0.10}$, SBP: $Eu_{0.01}$, $Gd_{0.10}$ and BBP: $Eu_{0.01}$, $Gd_{0.05}$ phosphors are calculated to be 0.48, 0.52 and 0.51, respectively. Notably, the codoped MBP: Eu, Gd phosphors from which the maximum luminescence is obtained (discussed later) have a lower asymmetric ratio (< 1) indicating Eu^{3+} presence in a higher symmetric environment giving predominantly orange or orange-red emission.

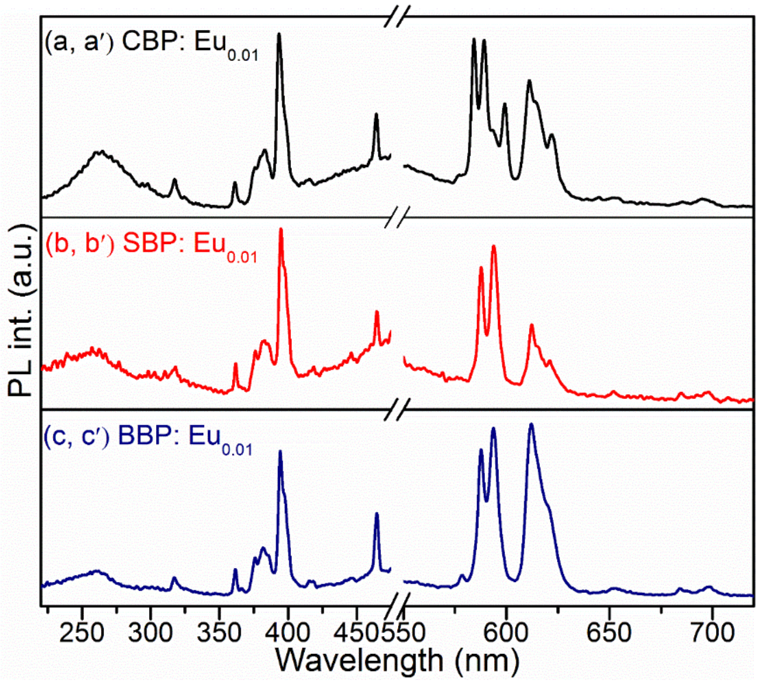

Figure 4.16 Excitation and emission spectra of Eu^{3+} in $Eu_{0.01}$ doped (a, a′) CBP (b, b′) SBP and (c, c′) BBP at λ_{em} = 594 and λ_{ex} = 394 nm, respectively.

Figure 4.17 shows the excitation and emission spectra of Eu^{2+} in MBP: $Eu_{0.01}$ phosphors prepared in the air atmosphere. The coexistence of Eu^{2+} in addition to Eu^{3+} in MBP has been well documented by many researchers[6, 13, 21]. The existence of Eu^{2+} in the stillwellite-structured MBP is mainly due to (i) the charge compensation resulting from the doping of trivalent europium at divalent host cation (M^{2+}) and (ii) the feedback-loop of the

3D-network of MBP that shields Eu^{2+} well from being oxidized to Eu^{3+}. The observed intense and broad luminescence of Eu^{2+} is due to the parity allowed nature of the $4f^7 \leftrightarrow 4f^6 5d$ transitions.

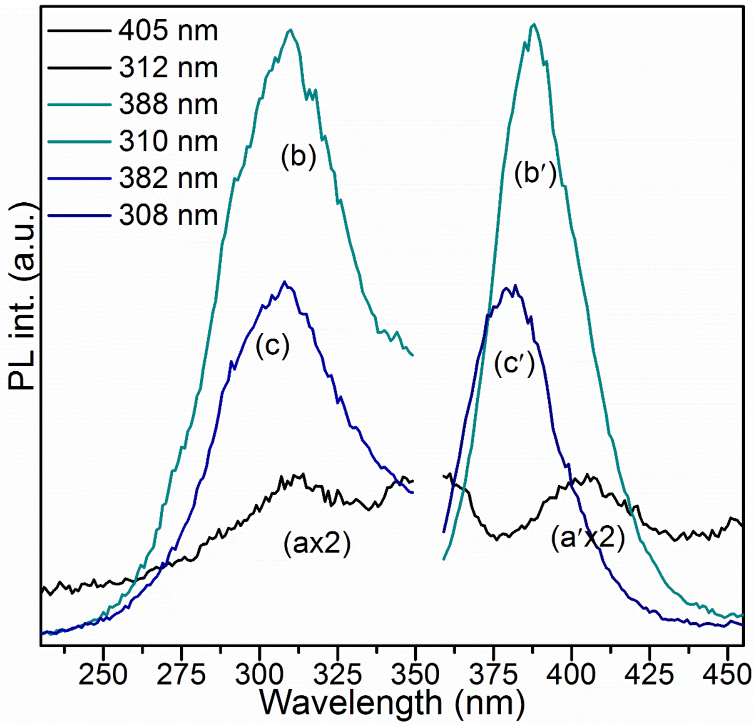

Figure 4.17 Excitation and emission spectra of Eu^{2+} in (a, a′) CBP: $Eu_{0.01}$ at λ_{em} = 405 and λ_{ex} = 312 nm (b, b′) SBP: $Eu_{0.01}$ at λ_{em} = 388 and λ_{ex} = 310 nm, and (c, c′) BBP: $Eu_{0.01}$ at λ_{em} = 382 and λ_{ex} = 308 nm.

It can be seen from Figure 4.17 that there is a blue shift in the excitation and the emission maxima when moving from CBP (312, 405 nm) to SBP (310, 388 nm) and finally to BBP (308, 382 nm) for $Eu_{0.01}$ doped samples. This is attributed to the decrease in the centroid shift of the 5*d* orbital due to the corresponding decrease in covalency while moving down the group ($Ca^{2+} \rightarrow Ba^{2+}$). Furthermore, the lowering of the non-degenerate 5*d* levels caused by the crystal field strength (CFS) in the respective hosts also decreases down the group. Compared to the 4*f*-orbitals, the 5*d*-orbitals are more prone to the crystal field and hence, depending upon the CFS its energy states vary in different hosts. The CFS experienced by the dopant increases with (i) the increase in coordination number (ii) the decrease in bond length (iii) the increase in covalency or (iv) if the dopant occupies a smaller cationic site.[35] Since the ionic radius of ten coordinated M^{2+} ions, i.e., Ca^{2+} (123 pm)→Sr^{2+} (136 pm)→Ba^{2+} (152 pm), increases down the group, hence, the CFS strength experienced by Eu^{2+} (135 pm) decreases down the group. Conversely, the covalency of M^{2+}-O^{2-} increases with the decrease in cationic size while moving up the group. Consequently, the electrons spread over a wide region and require less energy to make a particular transition. Therefore, the excitation and emission maxima show the blue-shift with the lowest energy (312 and 405 nm) in CBP while the same is observed at the highest energy (308 and 382 nm) in BBP.

The coexistence of Eu^{2+} in MBP in addition to Eu^{3+} curtails the color purity of the latter. Hence, the efficiency of orange-red emitting Eu^{3+} doped phosphors gets affected in the host where both coexist as luminescent centers. Moreover, the enhancement in Eu^{3+} can be achieved through the radiationless energy transfer from Gd^{3+} to Eu^{3+}. A significant energy transfer from Gd^{3+} to Eu^{3+} in SBP has been observed by codoping gadolinium as reported earlier in section 4.1. Surprisingly, an unusual in-situ valency conversion of Eu^{2+} to Eu^{3+} has also been observed in Gd codoped SBP: Eu. Hence, the present research work is carried out for understanding the energy transfer and in-situ valency conversion phenomena for enhancing the Eu^{3+} luminescence in Eu-Gd codoped MBP systems.

Figure 4.18 shows the PL intensity of the $^5D_0\rightarrow{}^7F_1$ transition of Eu^{3+} excited at 262 nm (CT band) and 394 nm ($^7F_0\rightarrow{}^5L_6$), and 273 nm ($^8S_{7/2}\rightarrow{}^6I_J$) in MBP: $Eu_{0.01}$, $Gd_{0-0.10}$. In case of codoped CBP, Eu^{3+} luminescence at all the above excitations increases with the increase in Gd-concentration and the increase is observed up to 10 mol% without any concentration quenching (Fig. 4.18A). However, in cases of codoped SBP and BBP, Eu^{3+} luminescence, at all three excitation wavelengths, increases up to 7.5 and 5 mol%, respectively, and thereafter it shows a decrease in the intensity due to the concentration quenching (Fig. 4.18B and C). The enhancement in Eu^{3+} luminescence at 273 nm (Gd^{3+}) excitation in the Gd codoped samples is due to the ET from Gd^{3+} to Eu^{3+}. However, the enhancement in Eu^{3+} is observed to be more significant at its CT band (262 nm) and 4*f*-4*f* (394 nm) excitations than at the Gd^{3+} excitation (273 nm). This comparative study suggests that there is also an unusual in-situ valence conversion from Eu^{2+} ($4f^7$) to Eu^{3+} ($4f^6$) in addition to the energy transfer ($Gd^{3+}\rightarrow Eu^{3+}$) in CBP and BBP hosts as discussed in SBP host earlier. The mechanism of radiationless energy transfer in BBP: $Eu_{0.01}$, $Gd_{0.05}$ is derived by calculating the critical distance of energy transfer, $C_d = 2[3V/4\pi NX_c]^{1/3}$ as mentioned earlier.

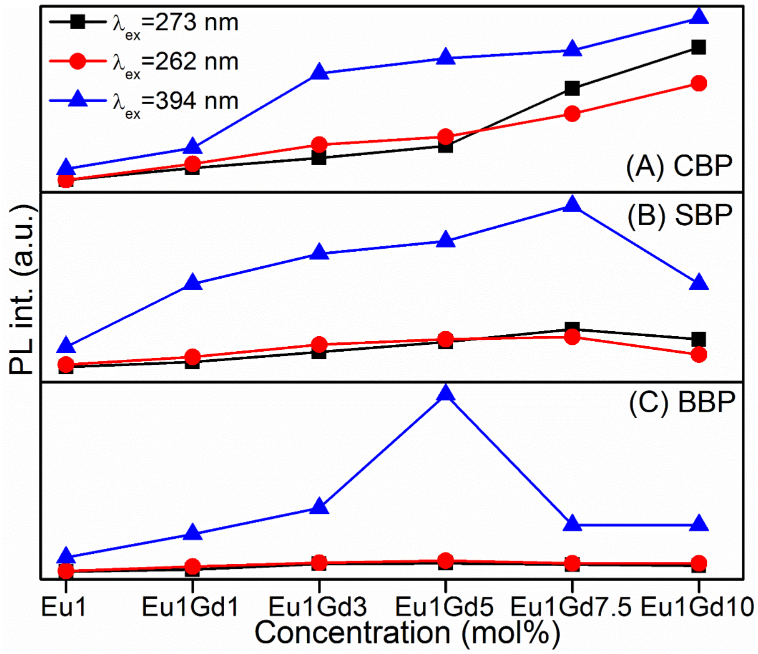

Figure 4.18 PL intensity of $^5D_0\rightarrow{}^7F_1$ *transition of* Eu^{3+} *in (A) CBP (B) SBP and (c) BBP:* $Eu_{0.01}$, $Gd_{0\text{-}10}$ *at different excitations.*

In case of BBP: $Eu_{0.01}$, $Gd_{0.05}$, the values of V, N *and* X_c *are* 353.209 Å^3, 6 and 6 mol%, respectively. The value of C_d in Eu-Gd coped BBP is calculated to 2.66 Å while that of SBP: $Eu_{0.01}$, $Gd_{0.075}$ is 2.33 Å as calculated earlier. The lower value of C_d in Eu-Gd coped BBP as well as in SBP indicates an effective Dexter type (<10 Å) of radiationless energy transfer from Gd^{3+} to Eu^{3+}. The presence of more number (N=6) of the cationic site for dopants substitution in BBP could be one of the reasons for the observed concentration quenching at lower activator concentration compared to that of SBP.

Figure 4.19 displays the PL intensity of the $4f^65d \rightarrow 4f^7$ transition of Eu^{2+} in MBP: $Eu_{0.01}$, $Gd_{0-0.10}$. It can be seen from Figure 4.19A that the PL intensity of Eu^{2+} in MBP decreases with the increase in Gd-concentration while a negligible signal is observed at 10 mol% Gd. This indicates almost complete oxidation (VC) of Eu^{2+} to Eu^{3+}. As observed earlier, Eu^{2+} exhibits a very poor luminescence in CBP: $Eu_{0.01}$ (Fig. 4.19a´) as compared to that of SBP: $Eu_{0.01}$ and BBP: $Eu_{0.01}$ (Fig. 4.19b´ and c´). Similarly, Eu^{2+} luminescence in SBP and BBP decreases significantly with the increase in Gd-concentration though some signal still exists at 10 mol% Gd (Fig. 4.19B and C). The reduction in Eu^{2+} luminescence with simultaneous enhancement in Eu^{3+} luminescence corroborates the unusual in-situ valency conversion of europium from Eu^{2+} to Eu^{3+} in all three hosts.

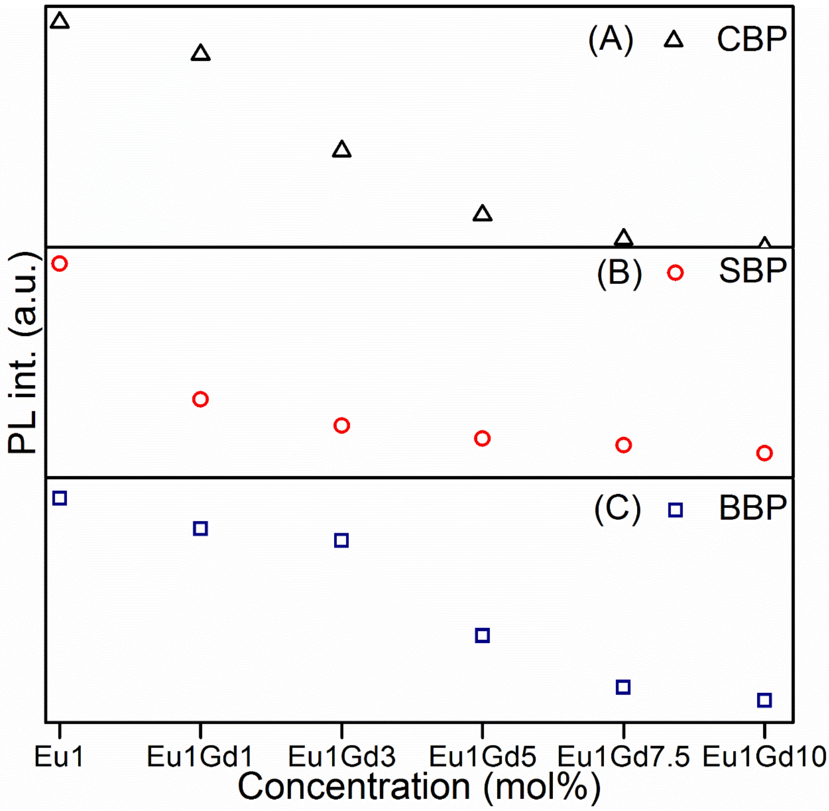

Figure 4.19 PL intensity of Eu^{2+} in $Eu_{0.01}$, $Gd_{0-0.10}$ doped (A) CBP (B) SBP (C) BBP at λ_{ex} = 312, 310 and 308 nm, respectively.

4.3.1.4. PL lifetime studies of Gd^{3+}, Eu^{3+} and Eu^{2+} in $MBPO_5$

PL lifetime decay curves of Gd^{3+}, Eu^{3+} and Eu^{2+} in MBP: Gd, MBP: Eu and MBP: Eu, Gd are analyzed to find out the site occupancy and site symmetry of dopants, and corroborate the possible energy transfer and in-situ valency conversion mechanism.

In case of in CBP: $Gd_{0.01}$, the lifetimes of Gd^{3+} at λ_{ex} = 273 and λ_{em} = 313 nm are found to be τ_1=2.22 (11%) and τ_2=5.60 ms (89%) whereas the values reduce to τ_1=2.03 (11%) and τ_2=5.45 ms (89%) in CBP: $Eu_{0.01}$, $Gd_{0.075}$. In case of in SBP: $Gd_{0.01}$, the lifetimes of Gd^{3+} are found to be τ_1=0.27 (10%) and τ_2=3.72 ms (90%) which are higher than in CBP: $Eu_{0.01}$, $Gd_{0.075}$, τ_1=0.19 (7%) and τ_2=3.45 ms (93%). Similarly, in case of BBP: $Gd_{0.01}$, the lifetimes of Gd^{3+} are found to be τ_1=1.40 (20%) and τ_2=3.98 ms (80%) which are also higher in BBP: $Eu_{0.01}$, $Gd_{0.075}$, τ_1=1.35 (28%) and τ_2=3.62 ms (93%). Furthermore, the two types of the well-resolved lifetime of Gd^{3+} in both Gd doped and Eu-Gd codoped MBP confirm its occupancy in two different electronic environments.

In cases of CBP: $Eu_{0.01}$, Eu^{3+} at λ_{ex} = 394 and λ_{em} = 594 nm exhibits two lifetimes of τ_1=0.29 (25%) and τ_2=2.54 ms (75%) whereas the lifetime value significantly increases to τ_1=2.01 (46%) and τ_2=4.50 ms (44%) in CBP: $Eu_{0.01}$, $Gd_{0.075}$. In case of SBP: $Eu_{0.01}$, Eu^{3+} exhibits two shorter lifetimes of τ_1=0.35 (32%) and τ_2=1.97 ms (68%) whereas longer lifetimes of τ_1=2.01 (46%) and τ_2=4.50 ms (44%) are observed in SBP: $Eu_{0.01}$, $Gd_{0.075}$. Similarly, in case of BBP: $Eu_{0.01}$, the lifetimes of Eu^{3+} are found to be τ_1=0.74 (46%) and τ_2=2.31 ms (54%) that get increased to τ_1=2.83 (61%) and τ_2=4.74 ms (39%) in BBP: $Eu_{0.01}$, $Gd_{0.05}$. The increase in the lifetime of Eu^{3+} with a simultaneous decrease in the lifetime of Gd^{3+} in the Eu-Gd codoped MBP phosphors complements the observed PL enhancement in Eu^{3+} due to the energy transfer (Gd^{3+}→Eu^{3+}), the valency conversion (Gd^{3+}→Eu^{3+}) and the occupancy of Eu^{3+} in higher symmetry site.

In case of CBP: $Eu_{0.01}$, Eu^{2+} (λ_{ex} = 312 and λ_{em} = 405 nm) exhibits two lifetimes of τ_1=88 (90%) and τ_2=303 ns (10%) whereas the lifetime value reduces to a single lifetime of

88 ns (100%) in CBP: $Eu_{0.01}$, $Gd_{0.075}$. In case of SBP: $Eu_{0.01}$, Eu^{2+} exhibits a single lifetime of 636 ns (100%) that reduces to 591 ns in SBP: $Eu_{0.01}$, $Gd_{0.075}$. Similarly, in case of BBP: $Eu_{0.01}$, Eu^{2+} exhibits a single lifetime of 1099 ns (100%) that reduces to 974 ns in MBP: $Eu_{0.01}$, $Gd_{0.075}$. The decrease in the lifetime of Eu^{2+} in Gd codoped MBP signifies the observed quenching of Eu^{2+} luminescence resulting from the in-situ valency conversion of europium from the $Eu^{2+} \rightarrow Eu^{3+}$. Moreover, an increase in the lifetime of Eu^{2+} observed while moving down the group in MBP is due to the decrease in the crystal field strength and covalency as discussed in PL studies. Additionally, the overlapping of $^6P_{7/2}$ state (360-363 nm) of the 4*f*-configuration with the lowest emitting states of 5*d*-configurations forbids[35] the transition to the ground $^8S_{7/2}$ state of Eu^{2+}. As seen in PL of Eu^{2+}, the emission maxima of Eu^{2+} in MBP show the blue-shift down the group, and consequently, the overlapping integral of $^6P_{7/2}$ state of the 4*f*-configuration with the lowest emitting states of 5*d*-configurations of Eu^{2+} becomes maximum for BBP and minimum for CBP. Therefore, Eu^{2+} has a longer lifetime in BBP and SBP compared to that in CBP.

4.3.1.5. CRI coordinates and color purity of Eu^{3+} in $MBPO_5$

A chromaticity diagram is a 2D interpretation used to perceive visually the color quality of a phosphor. The color coordinates (CRI) coordinates are determined for Eu^{3+} in MBP: Eu, Gd phosphors as shown in Figure 4.20. The CRI coordinates of Eu^{3+} at $\lambda_{ex} = 394$ nm in CBP: $Eu_{0.01}$, $Gd_{0.10}$, SBP: $Eu_{0.01}$, $Gd_{0.075}$ and BBP: $Eu_{0.01}$, $Gd_{0.05}$ are calculated to be (0.531, 0.460), (0.537, 0.453) and (0.562, 0.430), respectively. The CRI coordinates observed for Eu-Gd codoped SBP and BBP are better than the existing europium activated phosphate[37] and oxide-based[38] phosphors suggesting them as efficient orange-red phosphors for possible use in solid-state lighting applications.

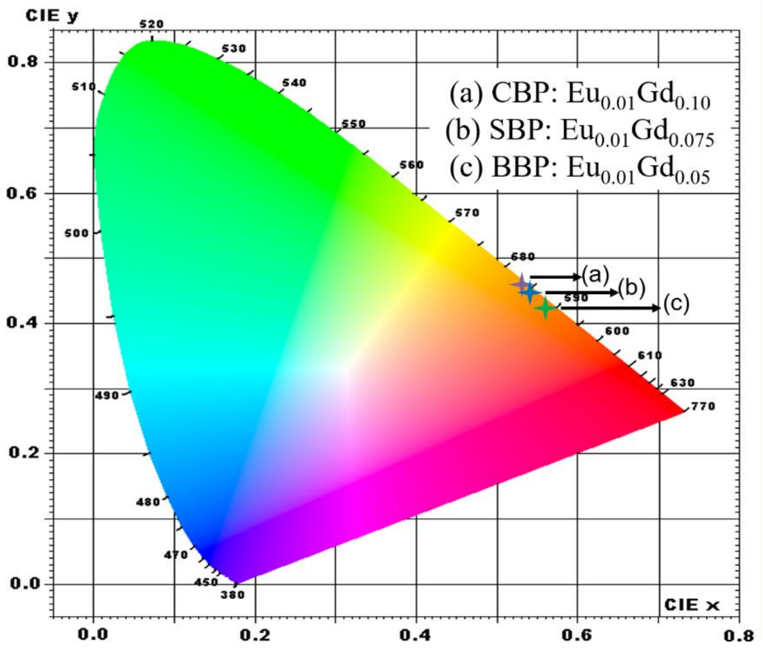

Figure 4.20 CRI coordinates of Eu^{3+} in (a) CBP: $Eu_{0.01}Gd_{0.10}$ (b) SBP: $Eu_{0.01}Gd_{0.075}$ and (c) BBP: $Eu_{0.01}Gd_{0.05}$ at λ_{ex} = 394 nm.

Further, the color purity of the phosphors is determined using Equation (4.2).

$$\boldsymbol{Color\ purity}\ (\%) = \frac{\sqrt{(\boldsymbol{x_s} - \boldsymbol{x_i})^2 + (\boldsymbol{y_s} - \boldsymbol{y_i})^2}}{\sqrt{(\boldsymbol{x_d} - \boldsymbol{x_i})^2 + (\boldsymbol{y_d} - \boldsymbol{y_i})^2}}\ \boldsymbol{X\ 100} \tag{4.2}$$

The CRI coordinates (x_s, y_s), (x_d, y_d) and (x_i, y_i) correspond to the coordinates of sample, dominant wavelength and illuminate point, respectively. According to the CIE-1931, the coordinates of (x_i, y_i) which refer to the white point in the chromaticity diagram are (0.333, 0.333). The coordinates of (x_d, y_d) refer to the intersection point on the locus of the chromaticity diagram obtained by extrapolating a straight line connecting (x_i, y_i) through (x_s, y_s). Here, the (x_d, y_d) coordinates of CBP: $Eu_{0.01}$, $Gd_{0.10}$, SBP: $Eu_{0.01}$ and BBP: $Eu_{0.01}Gd_{0.05}$ are found at (0.530, 0.475), (0.548, 0.465) and (0.570, 0.432), respectively. In the present study, the color purity from CBP: $Eu_{0.01}$, $Gd_{0.10}$, SBP: $Eu_{0.01}$ and BBP: $Eu_{0.01}Gd_{0.05}$ is evaluated to be 97, 94 and 97%, respectively, indicating them as ultra-high color purity orange, pale orange and orange-red phosphors toward solid-state lighting applications.

4.4. Conclusion

MBP: Gd and MBP: Eu, Gd phosphors are synthesized through the SSR route in the air atmosphere. The optical band gap values obtained for the undoped CBP (4.20 eV), SBP (4.30 eV) and BBP (4.39 eV) indicate that MBP phosphors are highly suitable for efficient UV-VIS emission. PL studies reveal that SBP: $Gd_{0.075}$ and BBP: $Gd_{0.075}$ phosphors display the most intense and narrow UV-*B* emission (313 nm) suggesting their possible use in phototherapeutic treatment. Gd codoping in MBP hosts efficiently enhances the orange-red emission of Eu^{3+} by both the energy transfer (Gd^{3+}→Eu^{3+}) and the in-situ valency conversion (Eu^{2+}→Eu^{3+}), simultaneously quenching Gd^{3+} and Eu^{2+} luminescence. The radiationless energy transfer from Gd^{3+}→Eu^{3+} is Dexter type with an effective critical distance of 2.33 and 2.66 Å for SBP: $Eu_{0.01}$, $Gd_{0.075}$ and BBP: $Eu_{0.01}$, $Gd_{0.05}$, respectively. Ultra-high color purity orange-red emission is obtained from Eu^{3+} in CBP: $Eu_{0.01}$, $Gd_{0.10}$ (97%), SBP: $Eu_{0.01}$, $Gd_{0.10}$ (94%) and BBP: $Eu_{0.01}$, $Gd_{0.10}$ (97%). The analysis of PL lifetime decays shows that Gd^{3+} and Eu^{3+} occupy two sites whereas Eu^{2+} (except for CBP: $Eu_{0.01}$) occupies a single site in MBP. Notably, the increase in Eu^{3+} lifetime with simultaneously quenching in the lifetime of Gd^{3+} and Eu^{2+} corroborates the observed (i) increase in symmetry around Eu^{3+} (ii) energy transfer (Gd^{3+}→Eu^{3+}) and (iii) in-situ valency conversion (Eu^{2+}→Eu^{3+}) in Eu-Gd codoped MBP.

References

1. Diaz, A.; Keszler, D. A. *Materials Research Bulletin* **1996,** 31, (2), 147-151.
2. Dirksen, G.; Blasse, G. *Journal of Solid State Chemistry* **1991,** 92, (2), 591-593.
3. Akella, A.; Keszler, D. A. *Materials research bulletin* **1995,** 30, (1), 105-111.
4. Blasse, G.; Bril, A.; De Vries, J. *Journal of Inorganic and Nuclear Chemistry* **1969,** 31, (2), 568-570.
5. Blasse, G. *Philips Res. Reps.* **1968,** 23, 201.
6. Nakamura, T.; Takeyama, T.; Takahashi, N.; Jagannathan, R.; Karthikeyani, A.; Smith, G.; Riedi, P. *Journal of luminescence* **2003,** 102, 369-372.
7. Karthikeyani, A.; Jagannathan, R. *Journal of luminescence* **2000,** 86, (1), 79-85.
8. Sakasai, K.; Katagiri, M.; Toh, K.; Takahashi, H.; Nakazawa, M.; Kondo, Y. *Applied Physics A* **2002,** 74, (1), s1589-s1591.

9. Reis, S.; Karabulut, M.; Day, D. *Journal of Non-Crystalline Solids* **2001,** 292, (1-3), 150-157.
10. Agarwal, A.; Pal, I.; Sanghi, S.; Aggarwal, M. *Optical Materials* **2009,** 32, (2), 339-344.
11. Sumalatha, B.; Omkaram, I.; Rao, T. R.; Raju, C. L. *Journal of Molecular Structure* **2011,** 1006, (1-3), 96-103.
12. Karabulut, M.; Melnik, E.; Stefan, R.; Marasinghe, G.; Ray, C.; Kurkjian, C.; Day, D. *Journal of Non-Crystalline Solids* **2001,** 288, (1-3), 8-17.
13. Su, Q.; Liang, H.; Hu, T.; Tao, Y.; Liu, T. *Journal of alloys and compounds* **2002,** 344, (1-2), 132-136.
14. Gao, Y.; Shi, C.; Wu, Y. *Materials research bulletin* **1996,** 31, (5), 439-444.
15. Tāle, I.; Kūlis, P.; Kronghauz, V. *Journal of Luminescence* **1979,** 20, (4), 343-347.
16. Peng, M.; Pei, Z.; Hong, G.; Su, Q. *Chemical Physics Letters* **2003,** 371, (1-2), 1-6.
17. Park, S.; Mho, S.; Kim, C.; Jeong, B.; Park, H. *Solid state communications* **1992,** 83, (1), 47-52.
18. Prasad, V. R.; Damodaraiah, S.; Babu, S.; Ratnakaram, Y. *Journal of Luminescence* **2017,** 187, 360-367.
19. Dubey, V.; Kaur, J.; Agrawal, S.; Suryanarayana, N.; Murthy, K. *Optik* **2013,** 124, (22), 5585-5587.
20. Ramteke, D.; Gedam, R. *Journal of Rare Earths* **2014,** 32, (5), 389-393.
21. Liang, H.-B.; Su, Q.; Tao, Y.; Hu, T.-D.; Liu, T.; Shulin, S. *Journal of Physics and Chemistry of Solids* **2002,** 63, (5), 719-724.
22. Kumar, M.; Seshagiri, T.; Godbole, S. *Bulletin of Materials Science* **2013,** 36, (5), 913-918.
23. Singh, V.; Borkotoky, S.; Murali, A.; Rao, J.; Rao, T. G.; Dhoble, S. *Spectrochimica Acta Part A: Molecular and Biomolecular Spectroscopy* **2015,** 139, 1-6.
24. Gawande, A.; Sonekar, R.; Omanwar, S. *Optik-International Journal for Light and Electron Optics* **2016,** 127, (8), 3925-3927.
25. Taoli, D.; Shirun, Y.; Jianguo, H. *Journal of Rare Earths* **2016,** 34, (2), 137-142.
26. Chauhan, A.; Gawande, A.; Omanwar, S. *Optik* **2016,** 127, (16), 6647-6652.
27. Madhusoodanan, U.; Jose, M.; Lakshmanan, A. *Radiation measurements* **1999,** 30, (1), 65-72.
28. Zhou, X.; Yang, X.; Wang, Y.; Zhao, X.; Li, L.; Li, Q. *Journal of Alloys and Compounds* **2014,** 608, 25-29.
29. Pei, Z.; Su, Q.; Zhang, J. *Journal of Alloys and Compounds* **1993,** 198, (1-2), 51-53.
30. Dai, W.; Lei, Y.; Yu, T.; Peng, M.; Zhang, Q. *Materials Research Bulletin* **2015,** 67, 176-184.
31. Shannon, R. D. *Acta crystallographica section A: crystal physics, diffraction, theoretical and general crystallography* **1976,** 32, (5), 751-767.
32. Kumar, M.; Mohapatra, M.; Natarajan, V. *Materials Research Bulletin* **2014,** 60, 858-863.
33. Binnemans, K. *Coordination Chemistry Reviews* **2015,** 295, 1-45.
34. Li, J.-G.; Li, X.; Sun, X.; Ishigaki, T. *The Journal of Physical Chemistry C* **2008,** 112, (31), 11707-11716.
35. Grabmaier, B., *Luminescent materials*. Springer Verlag: 1994.
36. Biswas, K.; Balaji, S.; Karmakar, P.; Annapurna, K. *Optical Materials* **2015,** 39, 153-159.
37. Koparkar, K.; Omanwar, S. *Journal of Luminescence* **2016,** 175, 176-181.

38. Tamrakar, R. K.; Upadhyay, K.; Sahu, I. P.; Bisen, D. P. *Optik* **2017,** 135, 281-289.
39. Huang, Y.; Jang, K.; Zhao, W.; Cho, E.; Lee, H. S.; Wang, X.; Qin, D.; Zhang, Y.; Jiang, C.; Seo, H. J. *Journal of Solid State Chemistry* **2007,** 180, (12), 3325-3332.
40. Kumar, M.; Kadam, R.; Seshagiri, T.; Natarajan, V.; Page, A. *Journal of radioanalytical and nuclear chemistry* **2004,** 262, (3), 633-637.
41. Barve, R.; Suriyamurthy, N.; Panigrahi, B.; Venkatraman, B. *Radiation protection dosimetry* **2014,** 163, (4), 430-438.
42. Pagonis, V.; Kitis, G.; Furetta, C., *Numerical and practical exercises in thermoluminescence*. Springer Science & Business Media: 2006.
43. Han, B.; Zhang, J.; Lü, Y.; Liu, Y.; Cui, Q. *Russian Journal of Physical Chemistry A* **2014,** 88, (1), 143-148.
44. Das, A.; Saha, S.; Panigrahi, K.; Ghorai, U. K.; Chattopadhyay, K. K. *Microscopy and Microanalysis* **2019**, 1-9.

Table of Contents

Friday, May 14, 2021

Chapter 5

Optical properties of Eu^{3+} activated $BaCeO_3$ -An efficient red phosphor for w-LED applications

5.1. Introduction

The orange-red emitting Eu^{3+} luminescence has been discussed in alkaline earth borophosphate ($MBPO_5$: Eu, Gd) phosphors in chapter 4. The effect of gadolinium codoping on the luminescence properties of europium in $MBPO_5$ has been explored there. The orange-red emission of Eu^{3+} in the codoped $MBPO_5$: Eu, Gd phosphors could be enhanced due to the in-situ valence conversion ($Eu^{2+}\rightarrow Eu^{3+}$) and the energy transfer ($Gd^{3+}\rightarrow Eu^{3+}$). The present chapter deals with the intense red emission of Eu^{3+} in one of the promising perovskite oxide hosts, viz., barium cerate ($BaCeO_3$), synthesized via a facile solution combustion synthesis (SCS) route. Perovskite materials have been gaining attention due to their intriguing properties from both science and technological point of view. These materials have potential applications in the following areas such as (i) hydrogen gas sensors (ii) hydrogen-permeable membrane (iii) desulfurization of natural fuel (iv) steam electrolysis (v) decomposition of alkane to alkene (vi) ammonia synthesis and (vii) catalyst electrodes in solid oxide fuel cells.[1-7] The perovskite phosphors can be used for field emission display (FED) and plasma display panel (PDP) devices.[8, 9] Among several perovskites, $BaCeO_3$ has manifold applications due to its high thermal stability (m.p. =1743 °C).[10] This host doped with lanthanides acts as a high protonic and oxygen conductor.[11-16] Doping of lanthanides introduce extrinsic oxygen vacancy in $BaCeO_3$ host due to aliovalent substitution leading to improved conductivity.[17] The energy states of Ln ions are significantly influenced by the crystal field, local symmetry, covalency and site occupancy in the host. Eu^{3+} is used as a structural probe to obtain the local symmetry since the site symmetry strongly influences its emission spectrum. The ionic conductivities of $BaCeO_3$

doped with different lanthanide ions have been widely studied whereas the lanthanide luminescence in this host is sparsely investigated. Ce^{3+} and Eu^{3+} luminescence though reported from this host[18, 19], a detailed discussion about the luminescence characteristics is yet to be reported. Luminescence efficiency of phosphors is greatly influenced by many factors such as size and shape of the particle and distribution of dopant in the phosphor. Therefore, the method of synthesis plays a vital role in tuning luminescence efficiency. Synthesis of perovskites through conventional SST route typically requires elevated calcination temperatures (1300-1600 °C) and long calcination duration (12-24 h).[10, 20, 21] Moreover, the resulting phosphor may lack homogeneity and form microcrystalline sized particles due to high agglomeration. Therefore, the wet chemical routes like the SCS route are preferred due to their lower synthesis temperature, lesser calcination duration and better homogeneity leading to efficient luminescence.

This chapter reports the synthesis of intense red-emitting $BaCeO_3$: Eu phosphors through a facile SCS route followed by calcination at different temperatures (1000-1300 °C) in the air atmosphere. The effect of calcination temperature on the morphology is ascertained by analyzing the SEM images. The band gap of both the undoped and Eu doped $BaCeO_3$ samples is estimated from the reflectance measurements. PL properties of Eu^{3+} is studied at room temperature (300 K) and liquid nitrogen temperature (77 K). This chapter details the optimization of activator concentration and calcination temperatures to obtain maximum color purity from the synthesized phosphors. PL lifetime and TRES studies are carried out to probe the site occupancy of Eu^{3+} in $BaCeO_3$. An effort is made to probe the defects using positron annihilation lifetime spectroscopy (PALS). Finally, this chapter covers the results obtained from TSL studies of γ-irradiated $BaCeO_3$: Eu phosphors for radiation dosimetry applications.

5.2. Results and discussion

5.2.1. Structural and morphological analysis of $BaCeO_3$

The powder XRD patterns of $BaCe_{0.99}O_3$: $Eu_{0.01}$ samples calcined at different calcination temperatures (1000-1300 °C) match well with the standard ICDD pattern (file no. 82-2425) of $BaCeO_3$ (Fig. 5.1). All the samples show a single-phase purity. These phosphors belong to the primitive lattice of the orthorhombic crystal system (Pmcn). The $BaCeO_3$ host has four formula units per unit cell. The Rietveld refined pattern of $BaCe_{0.99}O_3$: $Eu_{0.01}$ calcined at 1200 °C is also shown in Figure 5.1. Results of the refinement crystallographic parameters are provided in Table 5.1. The estimated lattice parameters compare well with that of earlier reported values, i.e., a=8.773, b=6.234 and c=6.213 Å with V=339.86 $Å^3$.[24] The orthorhombic crystal structure of the perovskite $BaCeO_3$ is presented in Figure 5.2. In $BaCeO_3$, Ce^{4+} and Ba^{2+} are in an octahedron (CeO_6) and a cuboctahedron (BaO_{12}) environments, respectively. The ionic radii of Ce^{4+} (CN=6), Eu^{3+} (CN=6) and Ba^{2+} (CN=12) are 97, 95 and 142 pm, respectively.[25]

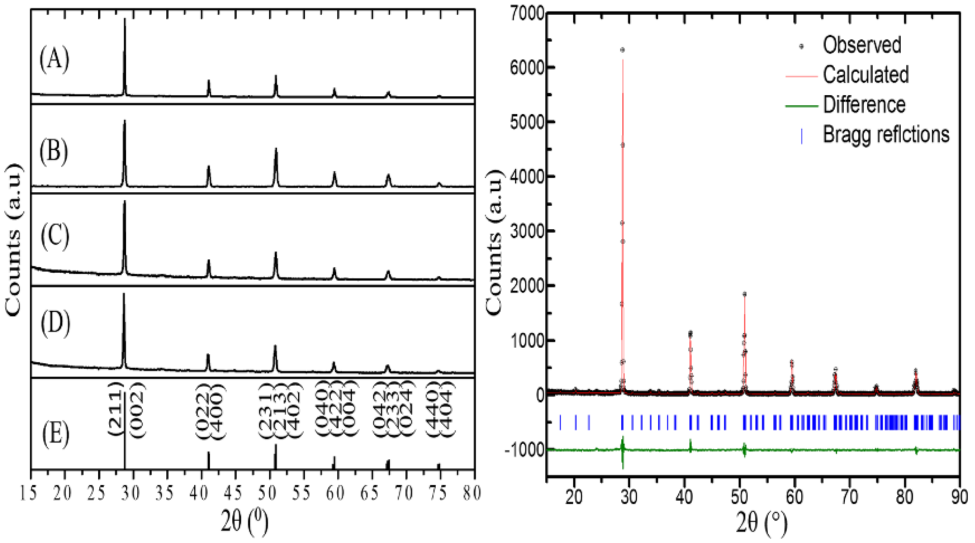

Figure 5.1 PXRD patterns of $BaCe_{0.99}O_3$: $Eu_{0.01}$ calcined at (A) 1300 (B) 1200 (C) 1100 (D) 1000 °C and (E) ICDD pattern with file No. 82-2425 along with the Rietveld refined pattern of $BaCe_{0.99}O_3$: $Eu_{0.01}$ calcined at 1200 °C.

Table 5.1 Rietveld refinement fitting parameters of $BaCe_{0.99}O_3$: $Eu_{0.01}$.

Space group and crystal system			Pmcn (62), Primitive, Orthorhombic				
Refined lattice parameters			a=8.7762(3) Å, b=6.2362(1) Å, c=6.2157(2) Å, α=β=γ=90°, V=340.19(1) $Å^3$				
Refined fractional coordinates	Atom	Site	x	y	z	Occ.	U_{iso}
	Ba	4c	¼	-0.0104(3)	0.0209	1	0.028(6)
	Ce	4b	0	½	0	0.99	0.021(5)
	Eu	4b	0	½	0	0.01	0.022(3)
	O1	4c	¼	0.43(5)	-0.005(1)	1	0.004(1)
	O2	8d	0.04 (1)	0.71(5)	0.28(5)	1	0.109(8)
Rietveld fitting parameters			Reduced χ^2=1.931, R_p=0.1350, wR_p=0.1456				

The extended X-ray absorption fine structure (EXAFS) study of Gd doped $BaCeO_3$ has revealed that Gd^{3+} occupies the Ce^{4+} site.[20] Therefore, Eu^{3+} is also expected to substitute Ce^{4+} rather than Ba^{2+} due to the large difference in their ionic radii, and there is also no report on 12-coordinated Eu^{3+}. The structure shows that 6-coordinated Ce^{4+} has two axials ($Ce-O_{ax}$: 223.84 pm) and four equatorials ($Ce-O_{eq}$: 224.44 pm) coordination that differs in the bond distance. The bond angle of axial coordination ($O_{ax}-Ce-O_{ax}$) is exactly 180°; however, the angle between equatorial coordination ($O_{eq}-Ce-O_{eq}$) is 89.6° to 91.5°. This suggests that Ce^{4+} is present in a lower symmetric (distorted) octahedral environment in this host.

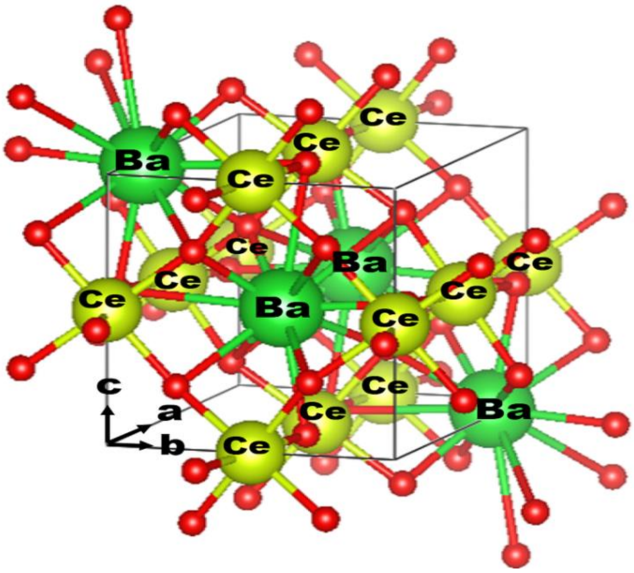

Figure 5.2 The crystal structure of orthorhombic $BaCeO_3$.

To ascertain the effect of calcination temperature (1000-1300 °C) on the morphology of the synthesized phosphors, the SEM micrographs of $BaCeO_3$: $Eu_{0.01}$ (Fig. 5.3a-d) are analyzed. It is observed that above 1200 °C the agglomeration of the particle is significantly higher. As a result, the PL intensity of Eu^{3+} from the sample calcined at 1300 °C gets decreased which is discussed later.

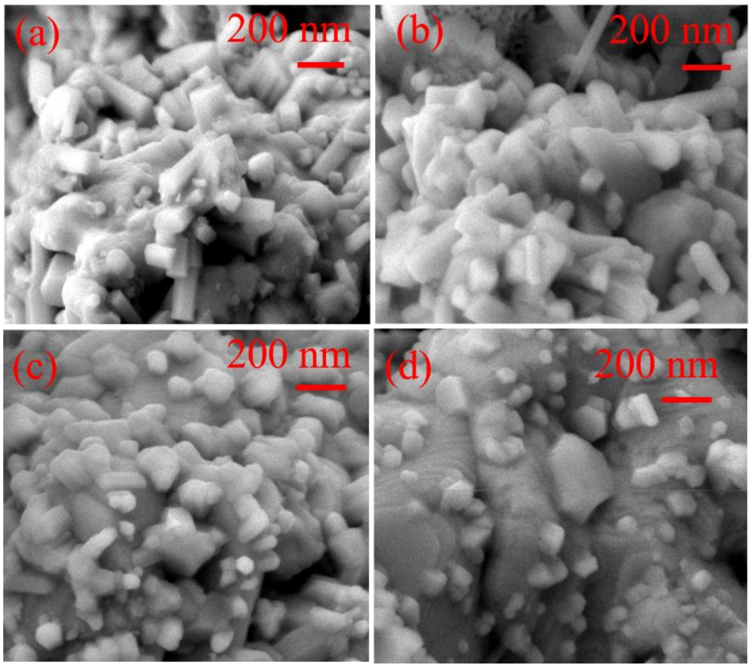

Figure 5.3 SEM images of $BaCeO_3$: Eu calcined at (a) 1000 (b) 1100 (c) 1200 and (d) 1300 °C with a scale (−) = 200 nm.

5.2.2. Estimation of band gap of undoped and Eu doped $BaCeO_3$

DRS is an effective spectroscopic tool to estimate the band gap (E_g) unambiguously in powder samples. Figure 5.4A shows the absorption spectra of both undoped and $Eu_{0.01}$ doped $BaCeO_3$ samples calcined at 1200 °C. For both the samples, two broad absorption bands are observed around $\lambda_1 = 260$ and $\lambda_2 = 320$ nm corresponding to the charge transfer (CT) of O^{2-} to Ce^{4+} as two types of Ce-O (axial and equatorial) bonds are present.[26] As discussed earlier, the Ce-O_{ax} bond is shorter than that of Ce-O_{eq} bond, and therefore, the average bond energy is expected to be higher in the former. On the other hand, the CT energy linearly depends on the average energy of the chemical bond.[27]

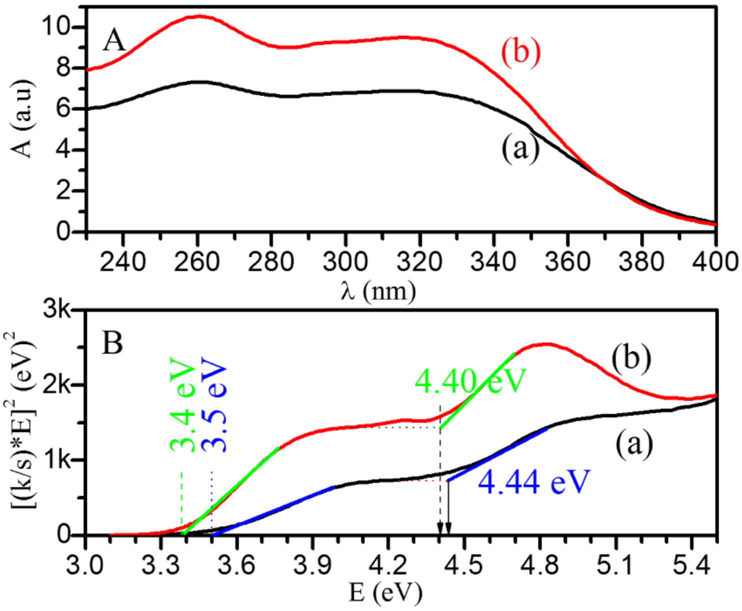

Figure 5.4 Absorbance spectra (A) and band gap (B) estimated using the K-M function of (a) undoped and (b) $Eu_{0.01}$ doped $BaCeO_3$ calcined at 1200 °C.

Hence, the band corresponding to higher energy (λ_1) and lower energy (λ_2) are referred to as the CT band edges of $O_{ax}^{2-}\rightarrow Ce^{4+}$ and $O_{eq}^{2-}\rightarrow Ce^{4+}$, respectively. No characteristic 4*f*-4*f* transition of $Eu^{3+}$is observed in the absorption spectra as these transitions are weak due to its parity forbidden nature. The absorbance in case of the Eu doped sample (Fig. 5.4A (b)) is higher than that of the undoped sample (Fig. 5.4A (a)) due to the higher absorption coefficient of Eu^{3+} in the range of 2.6-5.2 eV.[28]

Figure 5.4B shows the band gap obtained for both the samples following the Kubelka-Munk function as discussed in chapter 2 and chapter 3. In cerates, the valence band is composed of 2*p* states of O_{ax}^{2-} and O_{eq}^{2-} while the conduction band is composed of 4*f* and 5*d* states of Ce^{4+}.[29] The band gap (E_g) of the undoped sample is found to be 3.5 eV corresponding to the band edges of Ce^{4+} and O_{eq}^{2-}. For the Eu doped sample, the E_g (3.4 eV) is not significantly different from that of the undoped sample. Interestingly, another E_g is obtained at 4.44 eV for undoped and 4.40 eV for doped phosphors which could be due to the band edges of Ce^{4+} and O_{ax}^{2-}.

5.2.3. Effect of temperature and Eu-concentration on PL of Eu^{3+} in $BaCeO_3$

Figure 5.5 shows the PL intensity of Eu^{3+} as a function of calcination temperature (T_c=1000-1300 ˚C) and Eu-concentration (1-10 mol%). The Eu^{3+} PL is monitored at its known emissions, viz., at 594 and 610 nm. With the increase in T_c from 1000 to 1200 ˚C, the Eu^{3+} intensity increases and reaches a maximum at 1200 ˚C and thereafter it decreases (Fig. 5.5A). However, the PL trends monitored at 594 and 610 nm emission are not the same due to the difference in their nature of transitions. The emission intensity of electric dipole transition (610 nm) is observed to be more than that of the magnetic dipole transition (594 nm) for the sample calcined at 1200 ˚C suggesting a lower symmetric environment around Eu^{3+} at that calcination temperature (1200 ˚C).

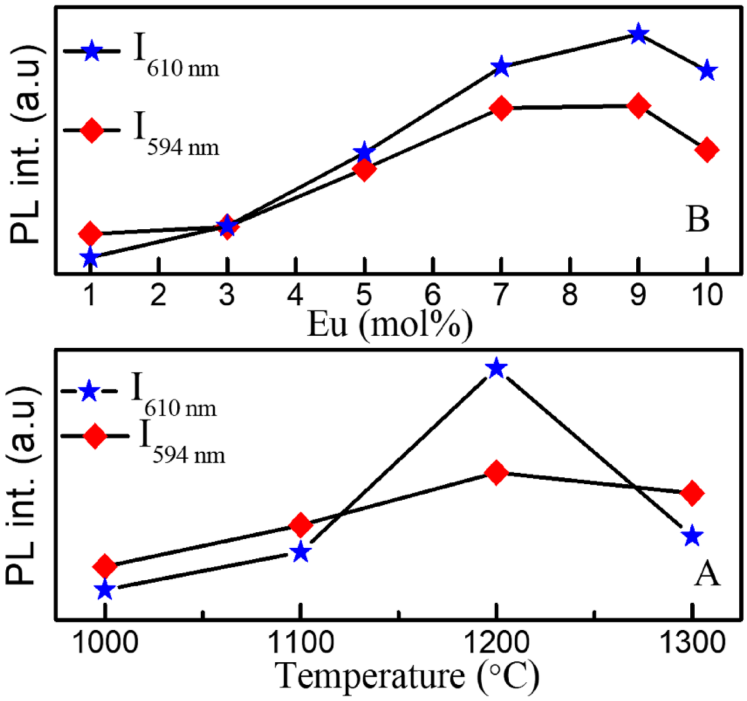

Figure 5.5 PL intensity of Eu^{3+} *in* $BaCeO_3$ *at* λ_{ex} *= 320 nm recorded at 300 K varying (A) calcination temperature (1000-1300 ˚C) with 1 mol% Eu doping and (B) Eu-concentration (1-10 mol%) with calcination at 1200 ˚C.*

It is worth mentioning that a lower symmetric environment is preferred for getting maximum emission from parity forbidden 4*f*-4*f* transition due to the relaxation in the selection rule. Therefore, the samples are prepared at 1200 ˚C and considered for further studies as the maximum intensity of Eu^{3+} is observed at this temperature. The effect of Eu-concentration on its luminescence intensity (Fig. 5.5B) is also studied. The intensity of Eu^{3+} emission increases with the increase in the Eu-concentration up to 9 mol% and thereafter it decreases probably due to the concentration quenching.

Figure 5.6 shows the excitation and emission spectra of Eu^{3+} recorded at 300 K by monitoring λ_{em} = 594 and λ_{ex} = 320 nm, respectively. The excitation spectrum exhibits two strong broad CT bands at 255 and 320 nm ($O^{2-} \rightarrow Ce^{4+}$) as seen in the absorption spectra (Fig. 5.4A). The characteristic narrow peaks at 394 ($^7F_0 \rightarrow {}^5L_6$) and 464 ($^7F_0 \rightarrow {}^5D_2$) nm are weak due to the forbidden 4*f*-4*f* transitions of Eu^{3+} (Fig. 5.6a). The emission spectrum exhibits the characteristic narrow peaks of Eu^{3+} at 528 ($^5D_1 \rightarrow {}^7F_0$), 540 ($^5D_1 \rightarrow {}^7F_1$), 560 ($^5D_1 \rightarrow {}^7F_2$), 580 ($^5D_0 \rightarrow {}^7F_0$), 594 ($^5D_0 \rightarrow {}^7F_1$), 610 ($^5D_0 \rightarrow {}^7F_2$), 650 ($^5D_0 \rightarrow {}^7F_3$) and 706 ($^5D_0 \rightarrow {}^7F_4$) nm.[30]

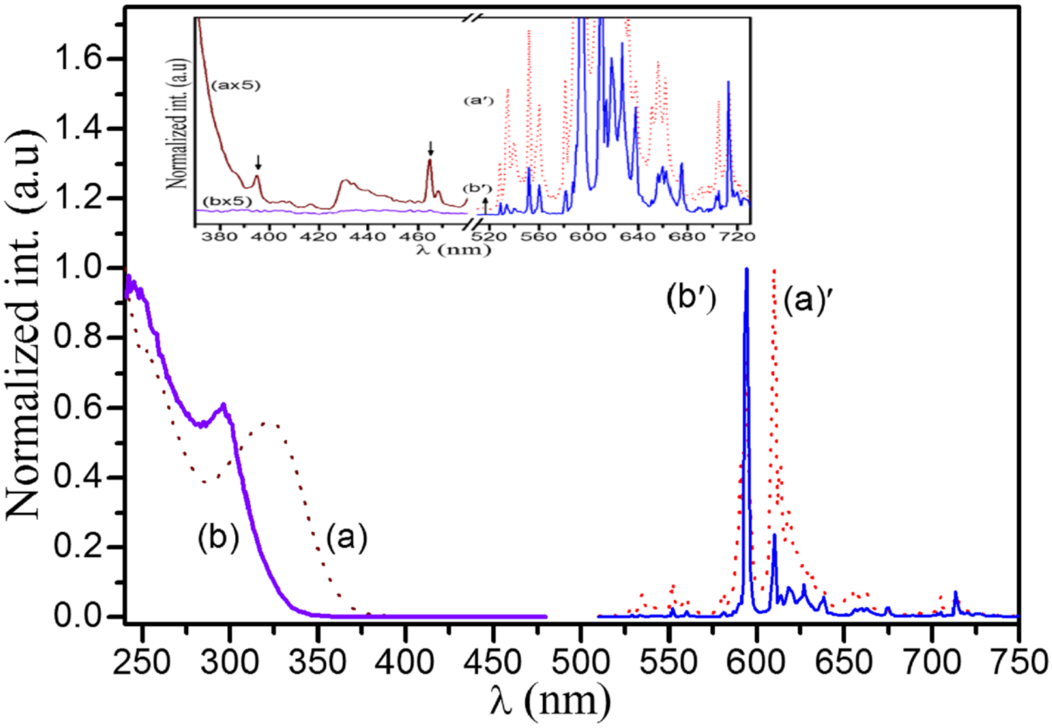

Figure 5.6 Excitation and emission spectra of $BaCeO_3$: $Eu_{0.01}$ at (a, a') 300 K, λ_{em} = 594 and λ_{ex} = 320 nm, and (b, b') 77 K, λ_{em} = 594 and λ_{ex} = 300 nm.

Figure 5.6 also shows the excitation and emission spectra of $BaCeO_3$: Eu^{3+} at 77 K. In the excitation spectrum (Fig. 5.6b), both the CT bands show a blue-shift to 245 and 300 nm, and in the emission spectrum (Fig. 5.6b') peaks are relatively narrow and well resolved as expected due to the reduced non-radiative probability. The FWHM of 594 nm peak is 2.47 nm at 77 K and 4.02 nm at 300 K. The 4*f*-4*f* transitions at 394 and 464 nm in the excitation spectrum are not observed at 77 K (inset of Fig. 5.6b).

The selection rule is strictly obeyed for lanthanide ions in the gas phase where they are in the centrosymmetric environment. However, in solids, it is partially relaxed due to vibronic coupling or mixing of higher configurations.[31] The lifting of the degeneracy of Eu^{3+} is primarily due to the inter-electronic repulsion, spin-orbit coupling, and crystal field splitting. Orthorhombic $BaCeO_3$ has low symmetry (C_{2V}), so the degeneracy gets lifted, giving rise to stark splitting as observed in the emission profile. The $^5D_0 \rightarrow {}^7F_0$ transition is a forbidden EDT observed only for systems having low symmetry (C_n, $C_{nv,}$ or C_s) or due to J-mixing caused by a strong crystal field.[32] In the case of $BaCeO_3$ with C_{2V} symmetry, this transition is seen at 581 nm (Fig. 5.6). Qiang Ju et al. have reported that in C_{2V} symmetry due to crystal field the $^5D_0$ to $^7F_{0,}$ $^7F_1$, $^7F_2$, $^7F_3$ and $^7F_4$ transitions of Eu^{3+} split into one, three, four, five and seven peaks, respectively.[33] In the present study, the $^5D_0 \rightarrow {}^7F_0$ transition exhibits a single peak at 581 nm and the $^5D_0 \rightarrow {}^7F_1$ transition exhibits three peaks at 589, 591 and 594 nm. The $^5D_0 \rightarrow {}^7F_2$ transition exhibits in four peaks at 610, 613, 618 and 623 nm. The $^5D_0 \rightarrow {}^7F_3$ transitions being a forbidden EDT is of very low intensity while its appearance is indicative of a strong crystal field exhibiting five peaks at 645, 650, 656, 662 and 674 nm. The $^5D_0 \rightarrow {}^7F_4$ being an allowed EDT, exhibits seven peaks at 690, 697, 699, 705, 710, 713 and 719 nm. In addition to the peaks discussed above, peaks at 627, 632 and 638 nm are also observed which may be attributed to the $^5D_1 \rightarrow {}^7F_J$ transitions.

5.2.4. Asymmetry ratio of Eu^{3+} at different excitations and Eu-concentration

It is reported that the asymmetry ratio (R_a) does not change with different λ_{ex} when present at one site in the host lattice, but it changes when present in more than one site or sites associated with defects.[34] In the present study, the R_a value is found to change with the change in the excitation wavelength as shown in Figure 5.7. For the same Eu-concentration, the change in the R_a value is significantly greater when excited at 394 nm (4*f*-4*f* transition) as compared to the excitations at 255 or 320 nm (CT bands). This clearly shows that Eu^{3+} is present at multiple sites in $BaCeO_3$.

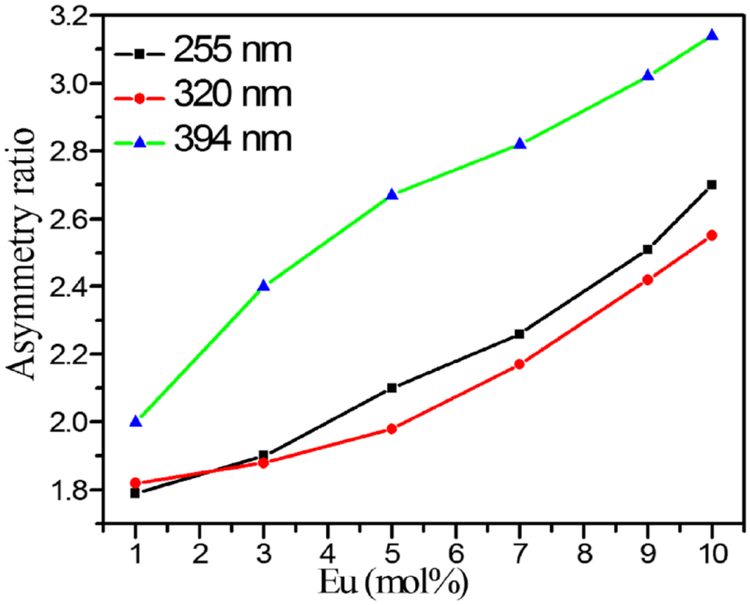

Figure 5.7 Asymmetry ratio of Eu^{3+} *in* $BaCeO_3$: $Eu_{0.01\text{-}0.10}$ *at* λ_{ex} = *255, 320 and 394 nm.*

Figure 5.7 also shows the variation of R_a as a function of Eu-concentration (1-10 mol%) excited at different wavelengths. For λ_{ex} = 255, 320 and 394 nm, the R_a value increases consistently with the increase in the Eu-concentration. For λ_{ex} = 394 nm, the value of R_a (2-3.14) is more than that of for λ_{ex} = 255 (1.79-2.70) and 320 nm (1.82-2.55). The observed increase in R_a with increased Eu-concentration indicates a lowering of symmetry around Eu^{3+}. The 4*f*-4*f* excitation (394 nm) excites the Eu^{3+} preferentially from the asymmetric sites. In contrast, CTB excitations (255 and 320 nm) preferentially excite the Eu^{3+} present at the symmetric sites and this observation is consistent with the earlier report.[35] Interestingly, in the emission profile recorded at 77 K, the intensity of 594 nm peak is more than that of 610 nm leading to an entirely different asymmetry ratio of 0.6. It suggests a more symmetric environment around Eu^{3+} at 77 K than at 300 K. It is known that the defect concentration decreases with the decrease in temperature.[36] This could be the reason for the observed change in the asymmetry ratio at 77 K.

5.2.5. PL lifetime decay and TRES studies of Eu^{3+} in $BaCeO_3$

The PL lifetime values obtained at different excitations (λ_{ex} = 255, 320 and 394 nm) and Eu-concentration (1-10 mol%) at 300 K are shown in Figure 5.8. The increase in Eu-concentration leads to the generation of more defects as trivalent europium substitutes for tetravalent cerium. Eu^{3+} being present in sites with different extent of asymmetry, its decay is expected to give more than one lifetime. The defects near Eu^{3+} increase the asymmetry around its environment leading to relaxation of selection rule, and therefore, a fast decay is expected. Conversely, with fewer defects and a more symmetric environment, Eu^{3+} is expected to decay slowly as the relaxation of the selection rule is restricted due to higher symmetry.

In the present study, the lifetime values decrease for λ_{ex} = 255 and 320 nm with an increase in the Eu-concentration due to the increased asymmetry around $Eu^{3+.}$ It is observed that lifetime values corresponding to CT band excitations (λ_{ex} = 255 and 320 nm) are higher than that involving 4*f*-4*f* excitation (λ_{ex} = 394 nm) since the former preferentially excites the Eu^{3+} present in higher symmetric site whereas in latter preferentially excites form lower symmetric. This corroborates the fact that the symmetry present around the Eu^{3+} plays an important role in its emission.

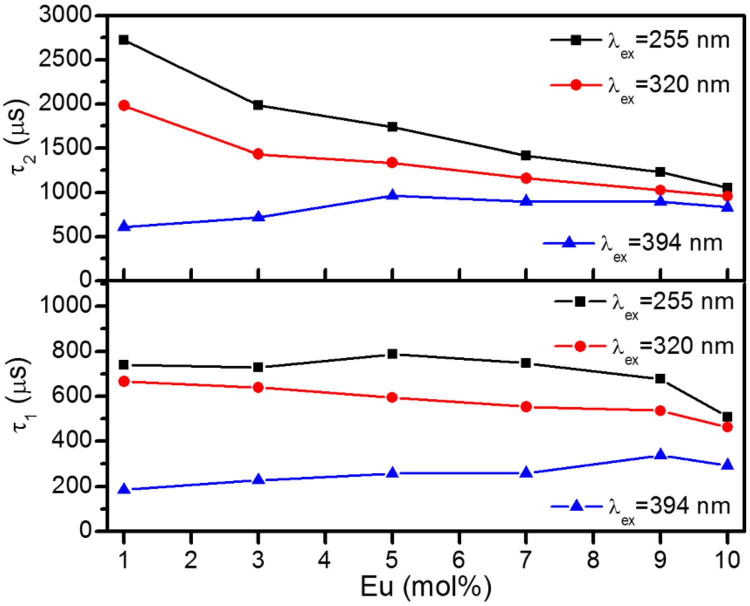

Figure 5.8 PL lifetimes of Eu^{3+} *at different* λ_{ex} *= 255, 320 and 394 nm in* $BaCeO_3$*:* $Eu_{0.01-0.10}$*.*

To probe the asymmetry further, we have also recorded the TRES of $BaCeO_3$: Eu over 0-0.7 and 2-5 ms at λ_{ex} = 320 nm, as shown in Figure 5.9. In the time zone of 0-0.7 ms, the fast component (τ_1) has completed one lifetime, and the slow component (τ_2) is yet to complete one lifetime. During 0.0-0.7 ms, the intensity of 610 nm peak is higher than that of 594 nm (Fig. 5.9a) which confirms that the τ_1 is more related to the Eu^{3+} in the asymmetric site. Similarly, in the time range of 2-5 ms (Fig. 5.9b), the τ_2 (slow component) has mostly contributed to the decay because the τ_1 has a negligible contribution as more than three fast lifetimes are completed. Here, the intensity of the 594 nm peak is more than that of the 610 nm suggesting τ_2 is related to the more symmetric environment of Eu^{3+}. This clearly shows that Eu^{3+} is present in two different sites with different emission characteristics. Due to similar ionic radii of Eu^{3+} (r=95 pm) and Ce^{4+} (r=97 pm), as discussed earlier, Eu^{3+} substitutes Ce^{4+} in the host lattice. However, due to the difference in their oxidation states defects are generated. Therefore, the two different sites for Eu^{3+} are expected to be associated with defects to a different extent resulting in different emissions from Eu^{3+}.

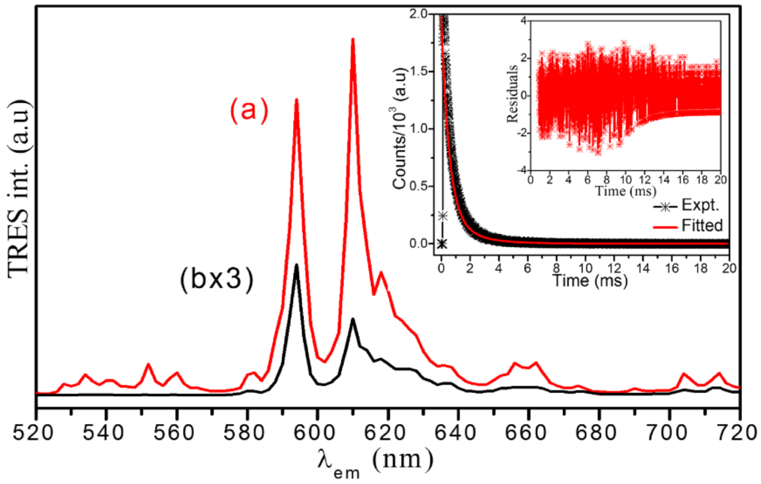

Figure 5.9 TRES of $BaCeO_3$*:* $Eu_{0.01}$ *recorded at 300 K and* λ_{ex} *= 320 nm in the time range of (a) 0-0.7 and (b) 2.0-5 ms. Inset shows the lifetime decay of* Eu^{3+} *recorded at 300 K at* λ_{ex} *= 320 and* λ_{em} *= 594 nm along with the residuals.*

The inset of Figure 5.9 shows PL lifetime decay profile along with the residuals of Eu^{3+} in $BaCeO_3$: $Eu_{0.01}$ at 300 K. The observed lifetime decays at 300 and 77 K are of second order. The lifetimes of Eu^{3+} at 300 K are τ_1=665 (53%) and τ_2=1982 μs (47%) whereas at 77 K the lifetimes are τ_1=1896 (18%) and τ_2=4379 μs (82%) with χ^2=1.01-1.22. The long lifetimes observed at low temperature (77 K) are due to the expectedly reduced non-radiative decay. The point to be noted here is that the amount of europium contributing to the fast component has significantly come down whereas the amount of europium contributing to the slow component has significantly increased corroborating the fact that the defects concentration get reduced significantly at low temperature as discussed earlier.

5.2.6. Color coordinates and color purity of $BaCeO_3$: Eu phosphors

To explore the possibility of $BaCeO_3$: Eu as a red-emitting phosphor, the chromaticity diagram with color coordinates is generated as a function of dopant concentration. For Eu-concentration of 1, 3, 5, 7, 9 and 10 mol%, the obtained color coordinates are (0.609, 0.389), (0.625, 0.373), (0.634, 0.365), (0.636, 0.363), (0.640, 0.360) and (0.638, 0.357), respectively. The color coordinates increase with the increase in Eu-concentration and are maximum for $BaCeO_3$: $Eu_{0.09}$ prepared at 1200 °C with color coordinates of (0.640, 0.360) as shown in Figure 5.10. The color coordinates improve when there is a relatively less contribution of emission from the higher excited states. In case of BaCeO$_3$: Eu, higher Eu-concentration has favored emission from the $^5D_0$ level with decreased emission at 525, 535, 540, 555 and 560 nm (from $^5D_1$). With the increase in Eu-concentration, the emission intensity from the $^5D_0$ state has increased nearly 6-7 times whereas the emission from $^5D_1$ has increased by only two times. The asymmetry ratio also increases with the increase in Eu-concentration due to greater intensity of 610 nm emission leading to better color coordinates. It may be noted that the color coordinates for the red phosphor according to the National Television Standard Committee (NTSC) are (0.670, 0.330).[37] In the present study, the color coordinates exhibited by BaCeO$_3$: Eu$_{0.09}$ (0.640, 0.360) phosphor are much better than that of the commercially used red phosphors such as Y$_2$O$_3$: Eu (0.620, 380) and Y$_2$O$_2$S: Eu^{3+} (0.622, 0.351).[38-41] Furthermore, the color purity of BaCeO$_3$: Eu$_{0.09}$ phosphor is determined as mentioned in chapter 4. Interestingly, the color purity of BaCeO$_3$: Eu$_{0.09}$ phosphor is found to be 100% suggesting it as a potential candidate for red LEDs and a component of white-LEDs applications.

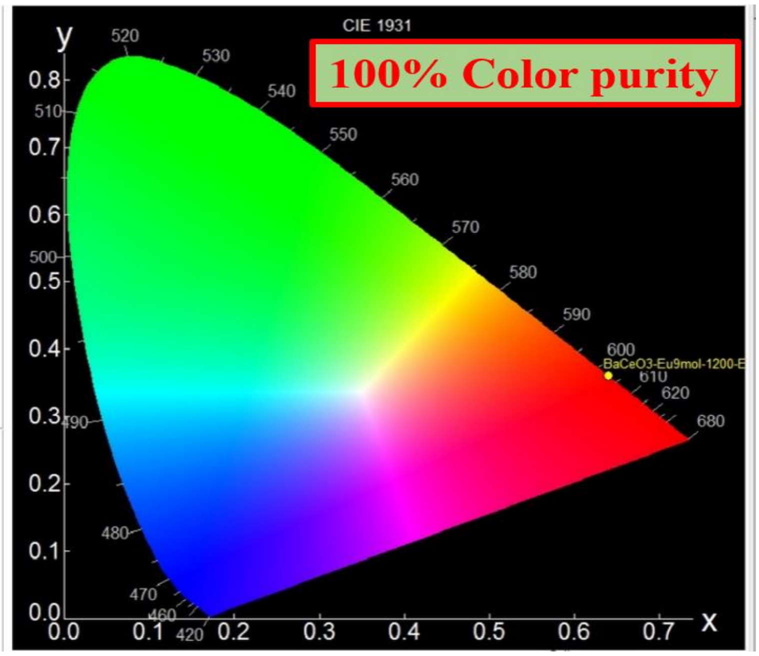

Figure 5.10 Chromaticity diagram of BaCeO$_3$: Eu$_{0.09}$ at λ_{ex} = 320 nm.

5.2.7. TSL studies of γ-irradiated $BaCeO_3$: $Eu_{0.01}$

After finding $BaCeO_3$: Eu as a good luminescent phosphor, the possibility of using this material as a dosimetry phosphor is explored by studying its thermoluminescence characteristics. On doping, to maintain the charge neutrality, four Eu^{3+} are required to substitute three Ce^{4+} leading to an oxygen vacancy creation in the $BaCeO_3$ host. The γ-irradiation also introduces defects and electron-hole (e^--h^+) pairs. The thermoluminescence may result in two steps such as de-trapping and recombination of e^--h^+ pairs. The de-trapping process involves the release of the trapped electrons from the traps to the conduction band (CB) upon suitable thermal excitation. The released electrons recombine with the holes leading to luminescence or again get trapped at some other defects. The energy released as a result of e^--h^+ recombination is known as recombination energy (E_r). The E_r may excite the nearby activators which upon deexcitation results in luminescence where the activator acts as a luminescent center.

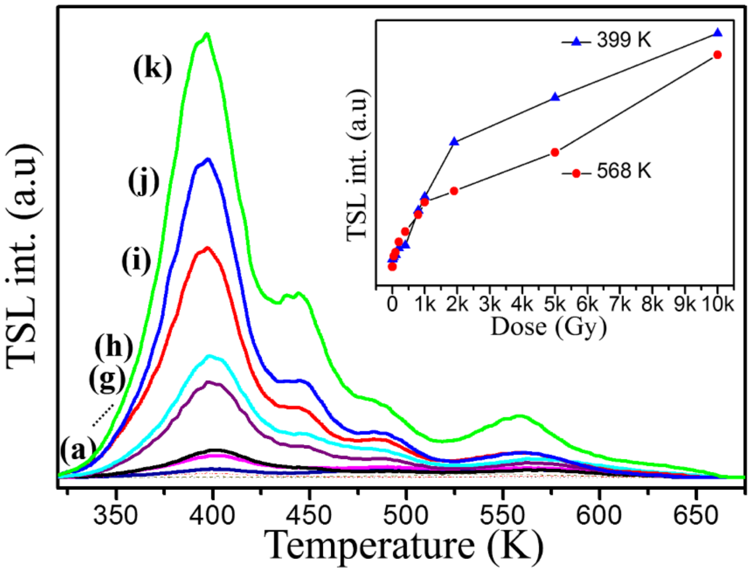

Figure 5.11 GC of $BaCeO_3$: $Eu_{0.01}$ at (a) 0 (b) 10 (c) 42 (d) 100 (e) 200 (f) 400 (g) 800 (h) 1000 (i) 1900 (j) 5000 and (k) 10000 Gy. Inset show the TSL intensity of the 399 and 568 K peaks as a function γ-dose.

Figure 5.11 shows TSL glow curves of $BaCeO_3$: $Eu_{0.01}$ in the dose range of 0-10 kGy at a constant heating rate (β) of 2 K/s. The glow curves are broad with multiple shoulders that are deconvoluted for calculating the trap parameters. For the samples irradiated up to 200 Gy, three glow peaks are observed around 399, 470 and 568 K. Beyond the dose of 200 Gy, four glow peaks are observed around 399, 450, 480 and 568 K. The unirradiated Eu-doped phosphor exhibits very low-intense glow peak around 533 K that indicates the presence of intrinsic defects in the Eu doped $BaCeO_3$. The glow peak observed below 500 K in the irradiated samples indicates the presence of extrinsic defects formed following γ-irradiation. However, in all the cases, the glow peak around 400 K is the predominant one. The symmetry factor (μ) calculated for each glow curve (0.47-0.53) is nearly equal to the theoretical value of 0.52 suggesting the de-trapping process to be of the second-order kinetics. The TSL emission spectra are recorded to investigate the TSL process further. No characteristic emission from Ce^{3+} or Eu^{3+} is observed indicating neither Ce^{3+} nor Eu^{3+} acted as a luminescent center in this host. After γ-irradiation, no Ce^{3+} luminescence is observed in PL measurement, indicating no valence reduction of Ce^{4+}. The TSL emission spectra of the irradiated $BaCeO_3$: $Eu_{0.01}$ phosphors are recorded to observe the Eu^{3+} emission profile, however, no such signal is observed. Though Eu^{3+} displays the characteristics of PL emission spectra, it acts as a non-luminescent center in the TSL process. Therefore, the mechanism of thermoluminescence observed here is only due to host emission resulting from e^--h^+ recombination. The dose-response of $BaCeO_3$: $Eu_{0.01}$ is shown in the inset of Figure 5.11 for the glow peaks observed around 399 and 568 K. Both the glow peaks exhibit linearity in the range of 0-1000 Gy and 2000-10000 Gy with the former range having a greater slope than the latter. From the inset, a sharp change in the slope is readily observed in the region of 1000-2000 Gy for both the glow curves. The trap parameters such as μ, E, S and L_s are determined following Chen's peak shape method as mentioned in chapter 4. The trap parameters, at 1 kGy for T_m=568 K glow peak, are found to be μ=0.51, E=1.18 eV, *S*=2.2x10^{9} s^{-1} and L_s=947 years. The dose-response and trap parameters of this phosphor suggest its potential use in high energy radiation dosimetry.

5.2.8. Nature of defects in $BaCeO_3$ using PALS

To probe further about the nature of defects present in the $BaCeO_3$, positron annihilation lifetime spectroscopy studies are carried out. PALS is a non-destructive technique having sensitivity up to ppm levels of monovacancy. In PALS, the positron lifetime (τ in ps) depends on the size of the open-volume defects and the intensity (I in %) gives their relative concentration. For the first time, the nature of the defects present in undoped and Eu doped $BaCeO_3$ is studied here. Figure 5.12 shows the positron lifetime and PALS intensity for $BaCeO_3$: $Eu_{0.01}$ samples at different calcination temperatures (1000-1300 ˚C). For both the undoped and Eu doped $BaCeO_3$, two different positron lifetimes (τ_1 and τ_2) are observed indicating the trapping of positrons at two different defect centers as mentioned in Table 5.2. The lifetimes are 159 and 264 ps for the undoped sample whereas 169 and 305 ps for the $BaCeO_3$: $Eu_{0.01}$. The Ab initio calculations for positron lifetime in $BaTiO_3$ for $V_O^{\cdot\cdot}$, V_{Ba}'' and V_{Ti}'''' vacancies are reported to be 162, 293 and 204 ps, respectively.[42] Both $BaTiO_3$ and $BaCeO_3$ being perovskites, the short lifetime (τ_1) observed here is ascribed to the presence of positron at oxygen vacancies ($V_O^{\cdot\cdot}$) and the long lifetime (τ_2) to the presence of barium vacancies (V_{Ba}'') or barium-oxygen vacancy complexes (V_{Ba}''-$V_O^{\cdot\cdot}$)[43] as high-temperature synthesis involves V_{Ba}'' due to the localization of BaO on the grain boundaries.[44] In the case of $BaTiO_3$, the lifetime for $V_O^{\cdot\cdot}$ is reported in the range of 162-187 ps,[45] which is close to the observed value in the present study. With the increase in temperature from 1100 to 1300 ˚C, the PALS intensity corresponding to τ_1 decreases from 91 to 71 % whereas that of τ_2 increases in the same trend from 9 to 29 % possibly due to the change in the morphology. The undoped sample has more metal ion vacancies and fewer oxygen vacancies compared to that of Eu doped sample calcined at 1200 ˚C as doping of Eu^{3+} at

Ce^{4+} resulted in more $V_O^{\cdot\cdot}$. Both types of vacancies are stable enough as an appreciable amount of vacancies exists in this host at a higher temperature. The defects arising due to oxygen and barium related vacancies seem to have a considerable effect on the photoluminescence and thermoluminescence properties of $BaCeO_3$: Eu phosphor.

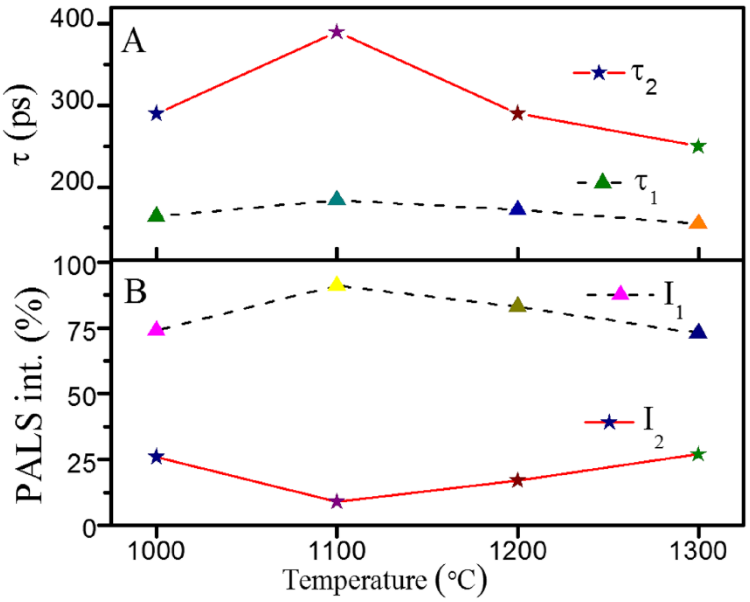

Figure 5.12 Calcination temperature (1000-1300 °C) versus (A) positron lifetime and (B) PALS intensity of $BaCeO_3: Eu_{0.01}$.

Table 5.2 Positron lifetime and PALS intensity observed at different Tc for undoped and Eu-doped $BaCeO_3$.

[Eu] at T_c °C	τ_1 ± error, ps	I_1 ± error, %	τ_2 ± error, ps	I_2 ± error, %
0 mol%, 1200	159 ± 2.8	72 ± 2.5	264 ± 5.7	28 ± 2.5
1 mol%, 1000	158 ± 4.6	73 ± 3.5	286 ± 12	27 ± 3.4
1 mol%, 1100	183 ± 0.65	91 ± 0.63	397 ± 12	9 ± 0.63
1 mol%, 1200	169 ± 2.8	84 ± 2.6	305 ± 14	16 ± 2.6
1 mol%, 1300	151 ± 1.9	71 ± 1.3	244 ± 1.7	29 ± 1.3

5.3. Conclusion

$BaCeO_3: Eu_{0.01-0.10}$ phosphors are prepared through a facile solution combustion synthesis route. Photoluminescence intensity is found to be maximum for $BaCeO_3: Eu_{0.09}$ calcined at 1200 °C. At 300 K, the asymmetry ratio is significantly higher than that observed at 77 K suggesting a more asymmetric environment for europium at room temperature. The asymmetry ratio and emission intensity increase with Eu-concentration for both the charge transfer bands and the 4*f*-4*f* excitations. PL lifetime decay studies suggest two different sites for Eu^{3+} in this host. The TRES analysis confirms the presence of Eu^{3+} at two different sites with different asymmetry ratio. The better color coordinates (0.640, 0.360) with 100% color purity for the $BaCeO_3$: $Eu_{0.09}$ calcined at 1200 °C makes it an efficient red phosphor. The PALS studies reveal the presence of more oxygen and less barium vacancy defects that influence the Eu^{3+} luminescence in this phosphor. The TSL studies of γ-irradiated samples show the presence of multiple defects and the observed thermoluminescence is due to the host emission. The suitable TSL trap parameters and linear dose-response indicate $BaCeO_3$: Eu as a potential candidate for high radiation dosimetry applications.

References

1. Kulkarni, A.; Ciacchi, F.; Giddey, S.; Munnings, C.; Badwal, S.; Kimpton, J.; Fini, D. *International Journal of Hydrogen Energy* **2012,** 37, (24), 19092-19102.
2. Coey, J.; Viret, M.; Von Molnar, S. *Advances in physics* **1999,** 48, (2), 167-293.
3. Taniguchi, N.; Kuroha, T.; Nishimura, C.; Iijima, K. *Solid State Ionics* **2005,** 176, (39-40), 2979-2983.
4. Fu, X.-Z.; Luo, J.-L.; Sanger, A. R.; Luo, N.; Chuang, K. T. *Journal of Power Sources* **2010,** 195, (9), 2659-2663.
5. Yin, J.; Wang, X.; Xu, J.; Wang, H.; Zhang, F.; Ma, G. *Solid State Ionics* **2011,** 185, (1), 6-10.
6. Li, J.; Luo, J.-L.; Chuang, K. T.; Sanger, A. R. *Electrochimica Acta* **2008,** 53, (10), 3701-3707.
7. Tao, Z.; Yan, L.; Qiao, J.; Wang, B.; Zhang, L.; Zhang, J. *Progress in Materials Science* **2015,** 74, 1-50.
8. Gupta, S. K.; Pathak, N.; Kadam, R. *Journal of Luminescence* **2016,** 169, 106-114.
9. Stranks, S. D.; Snaith, H. J. *Nature nanotechnology* **2015,** 10, (5), 391.
10. Yamanaka, S.; Fujikane, M.; Hamaguchi, T.; Muta, H.; Oyama, T.; Matsuda, T.; Kobayashi, S.-i.; Kurosaki, K. *Journal of Alloys and Compounds* **2003,** 359, (1-2), 109-113.
11. Katahira, K.; Kohchi, Y.; Shimura, T.; Iwahara, H. *Solid State Ionics* **2000,** 138, (1-2), 91-98.
12. Pasierb, P.; Wierzbicka, M.; Komornicki, S.; Rekas, M. *Journal of Power Sources* **2009,** 194, (1), 31-37.
13. Kompan, M.; Baikov, Y. M.; Melekh, B.-T.; Yakubovich, A. *Physics of the Solid State* **2002,** 44, (7), 1263-1267.
14. Ranran, P.; Yan, W.; Lizhai, Y.; Zongqiang, M. *Solid State Ionics* **2006,** 177, (3-4), 389-393.
15. Medvedev, D.; Gorbova, E.; Demin, A.; Tsiakaras, P. *international journal of hydrogen energy* **2014,** 39, (36), 21547-21552.
16. Wang, W.; Liu, J.; Li, Y.; Wang, H.; Zhang, F.; Ma, G. *Solid State Ionics* **2010,** 181, (15-16), 667-671.

17. Knight, K. *Solid state communications* **1999,** 112, (2), 73-78.
18. Melekh, B.-T.; Egorov, V.; Baikov, Y. M.; Kartenko, N.; Filin, Y. N.; Kompan, M.; Novak, I.; Venus, G.; Kulik, V. *Solid State Ionics* **1997,** 97, (1-4), 465-470.
19. Kompan, M.; Baikov, Y. M.; Melekh, B.-T.; Volchek, B. *Solid state ionics* **2003,** 162, 1-5.
20. Giannici, F.; Longo, A.; Balerna, A.; Martorana, A. *Chemistry of Materials* **2009,** 21, (4), 597-603.
21. Gorbova, E.; Maragou, V.; Medvedev, D.; Demin, A.; Tsiakaras, P. *Journal of Power Sources* **2008,** 181, (2), 207-213.
22. Rietveld, H. M. *Journal of applied Crystallography* **1969,** 2, (2), 65-71.
23. Toby, B. H. *Journal of applied crystallography* **2001,** 34, (2), 210-213.
24. Knight, K. S.; Bonanos, N. *Materials Research Bulletin* **1995,** 30, (3), 347-356.
25. Shannon, R. D. *Acta crystallographica section A: crystal physics, diffraction, theoretical and general crystallography* **1976,** 32, (5), 751-767.
26. Li, L.; Zhou, S.; Zhang, S. *Chemical Physics Letters* **2008,** 453, (4-6), 283-289.
27. Li, L.; Zhou, S.; Zhang, S. *The Journal of Physical Chemistry C* **2007,** 111, (7), 3205-3210.
28. Chen, X.; Liu, G. *Journal of Solid State Chemistry* **2005,** 178, (2), 419-428.
29. Swift, M.; Janotti, A.; Van de Walle, C. G. *Physical Review B* **2015,** 92, (21), 214114.
30. Dejneka, M.; Snitzer, E.; Riman, R. *Journal of Luminescence* **1995,** 65, (5), 227-245.
31. Binnemans, K. *Coordination Chemistry Reviews* **2015,** 295, 1-45.
32. Porcher, P.; Caro, P. *Journal of Luminescence* **1980,** 21, (2), 207-216.
33. Ju, Q.; Liu, Y.; Li, R.; Liu, L.; Luo, W.; Chen, X. *The Journal of Physical Chemistry C* **2009,** 113, (6), 2309-2315.
34. Kolesnikov, I. E.; Povolotskiy, A. V.; Mamonova, D. V.; Kolesnikov, E. Y.; Kurochkin, A. V.; Lähderanta, E.; Mikhailov, M. D. *Journal of Rare Earths* **2018,** 36, (5), 474-481.
35. Kolesnikov, I.; Povolotskiy, A.; Mamonova, D.; Lähderanta, E.; Manshina, A.; Mikhailov, M. *RSC advances* **2016,** 6, (80), 76533-76541.
36. Kittel, C. *New York* **1996**, 402.
37. Huang, X.; Guo, H.; Li, B. *Journal of Alloys and Compounds* **2017,** 720, 29-38.
38. Li, J.-G.; Li, X.; Sun, X.; Ishigaki, T. *The Journal of Physical Chemistry C* **2008,** 112, (31), 11707-11716.
39. Dhanaraj, J.; Jagannathan, R.; Kutty, T.; Lu, C.-H. *The Journal of Physical Chemistry B* **2001,** 105, (45), 11098-11105.
40. Park, S.; Mho, S.; Kim, C.; Jeong, B.; Park, H. *Solid state communications* **1992,** 83, (1), 47-52.
41. Som, S.; Das, S.; Dutta, S.; Visser, H. G.; Pandey, M. K.; Kumar, P.; Dubey, R. K.; Sharma, S. *RSC Advances* **2015,** 5, (87), 70887-70898.
42. Ghosh, V. J.; Nielsen, B.; Friessnegg, T. *Physical Review B* **2000,** 61, (1), 207.
43. Mangalam, R.; Chakrabrati, M.; Sanyal, D.; Chakrabati, A.; Sundaresan, A. *Journal of Physics: Condensed Matter* **2009,** 21, (44), 445902.
44. Haile, S.; Staneff, G.; Ryu, K. *Journal of Materials Science* **2001,** 36, (5), 1149-1160.
45. Castro, M. S.; Salgueiro, W.; Somoza, A. *Journal of Physics and Chemistry of Solids* **2007,** 68, (7), 1315-1323.

Table of Contents

Friday, May 14, 2021

Chapter 6

Probing the site occupancy of dopants in deep red-NIR emitting $LiAl_5O_8$: Eu^{3+}, Cr^{3+} and Fe^{3+} nano phosphors using photoluminescence and X-ray absorption spectroscopy

6.1. Introduction

The orange-red emitting stillwellite-structured $MBPO_5$: Eu, Gd and the red emitting perovskite-structured $BaCeO_3$: Eu phosphors have been discussed in chapter 4 and 5, respectively. The present chapter deals with the deep red-NIR emission of Eu^{3+}, Cr^{3+} and Fe^{3+} activated $LiAl_5O_8$ nano phosphors prepared through the facile SCS route in a single step. Red phosphors are enormously used in FED, PDP, CRT, red LEDs and w-LEDs.[1-5] The deep red-NIR light has also potential applications for non-destructive and non-invasive examinations such as analysis of foodstuffs, health monitoring, iris recognition, endoscopy, optical thermometry and infrared cameras.[6, 7] Of late, the deep red-NIR phosphors have been emerged as indispensable solid-state light sources and preferred to the commercially available sources such as tungsten-halogen lamp and laser diodes, owing to the spectral stability, broad emission range, low electrical consumption, longer lifetimes, compactness and no heat generation. Many of the lanthanides (Ln) and transition metal (TM) ions are known for their intense orange-NIR emission and hence, these ions in suitable hosts are used for phosphor applications. These red phosphors can broadly be classified into three types based on their emission characteristics, viz., (I) narrow and orange-red (II) narrow and deep red, and (III) broad and deep red-NIR emissions. Lanthanides belonging to type-I are Pr^{3+}, Sm^{3+} and Eu^{3+}. Eu^{3+} shows unique optical characteristics as its emission color depends upon the symmetry of the host lattice, and hence, many a time it is used as a structural probe.[8] Eu^{3+} in a site with the center of inversion (higher symmetry) exhibits predominantly orange emission whereas without the center of inversion (lower symmetry) exhibits strong red emission. Therefore, Eu^{3+} emission can be tuned from orange to red by choosing a suitable host. Trivalent chromium, a transition metal ion with narrow emission around 713 nm in deep red region, belongs to type-II phosphor. This narrow characteristic emission of Cr^{3+} is utilized in laser, in-vivo imaging,[9] and plant growth[10], etc. Another transition metal ion, Fe^{3+} with a broad emission profile in the deep red-NIR region, belongs to type-III red phosphors. The Fe^{3+} emission in the tissue optical window (650-1350 nm) has potential applications for luminescence guided surgery. Although numerous reports on deep red-NIR phosphors are available, an efficient phosphor may be looked for effective performance over a broad spectral region.

Fe^{3+} luminescence has been reported in many phosphate hosts (MPO_4; M=Sc, Y, La, Lu) with the emission maximum at 700±20 nm.[11] Similarly, persisted Cr^{3+} luminescence has been reported in $MgGa_2O_4$ host.[9] Intense red emission from Eu^{3+} in oxy-sulfide (Y_2O_2S)[1] and borate (SrB_4O_7)[12] hosts has been observed though these hosts suffer from low thermal stability and incomplete valence conversion of europium (as Eu^{2+} also exists). Lithium aluminium oxide hosts have been of particular interest due to their excellent thermochemical and irradiation stability. Apart from being good luminescent materials,[13, 14] they have been reported to have potential applications in molten carbonate fuel cells[15, 16] and also in nuclear reactors as radiation shield.[17] There are many oxide hosts of Li_2O-Al_2O_3 systems like $Li_2Al_4O_7$, Li_5AlO_4, $LiAlO_2$ and $LiAl_5O_8$. The $Li_2Al_4O_7$ and Li_5AlO_4 hosts have low thermal stability[18] and also it is difficult to prepare them with single phase purity. $LiAlO_2$ and $LiAl_5O_8$ can be synthesized via combustion synthesis with single phase purity.[10] Lanthanide and transition metal ion dopants in these aluminate hosts are known to exhibit good luminescence characteristics. The γ-$LiAlO_2$ needs post-combustion treatment, high calcination temperature and long calcination duration whereas $LiAl_5O_8$ does not need any post-combustion treatment though it has a higher melting point than that of γ-$LiAlO_2$.[18] The

$LiAl_5O_8$ (LAO) host has gained much attention owing to its easy synthesis, high thermochemical stability and interesting optical properties.[19, 20] Luminescence properties of several Ln and TM ions have been studied in this LAO host. The importance of Eu/Ce/Tb doped LAO phosphors in functional photonic devices has been well documented.[21-25] Intense green emission from LAO: Mn^{2+} ($3d^5$) phosphor has also been reported.[26] Cr^{3+} activated LAO phosphor has displayed promising application towards photoluminescence thermometry.[19, 27] Similarly, LAO: Fe^{3+} has been reported to have biocompatibility and emission in the deep red region suggesting its utility for in-vivo temperature sensing.[28, 29]

Interestingly, the pristine LAO sample was observed to contain chromium and iron as intrinsic impurities exhibiting luminescence from Cr^{3+} and Fe^{3+}.[30] Though the origin of these impurities has reportedly from the aluminum precursor,[31] the quantification of these impurities and their effect on luminescence from this phosphor are yet to be reported. Moreover, the site occupancy of Cr^{3+} and Fe^{3+} in this host is not studied in detail as there is ambiguity regarding the local symmetry of Fe^{3+} in this host.[14, 32, 33]

The present chapter reports the synthesis of pristine and Eu^{3+}, Cr^{3+} and Fe^{3+} doped $LiAl_5O_8$ nano phosphor through the SCS route at 600 °C without high calcination temperature to minimize the generation of defects due to possible volatilization of Li_2O. For identification of phase purity and morphological analysis, powder XRD and SEM recordings are performed. Detailed optical properties of $LiAl_5O_8$: $Eu^{3+}/Cr^{3+}/Fe^{3+}$ are investigated using steady-state luminescence and time-resolved luminescence studies. For the first time, the local coordinate environments of Eu^{3+} and Fe^{3+} are probed in this host through XAS. Further, the dopant concentration is optimized to obtain 100% color purity from Eu^{3+}, Cr^{3+} and Fe^{3+} luminescence for making them as potential deep red-NIR phosphors for various spectroscopy applications.

6.2. Results and discussion

6.2.1. Structural and morphological studies

Figure 6.1 shows the powder XRD patterns of as-prepared pristine and $Eu_{0.01}$ doped samples. The XRD patterns of the AP pristine and Eu doped samples (Fig. 6.1a and b) are found to match well with the standard ICDD pattern (Fig. 6.1c) with file no. 87-1278 confirming the single phase purity of cubic $LiAl_5O_8$. All samples show a high degree of crystallinity as confirmed by their high intensity and well-defined peaks. The $LiAl_5O_8$ belongs to the cubic crystal system with space group $P4_332$ (212) and has four formula units per unit cell. The crystal structure of LAO is shown in Figure 6.2a. It can be seen from the structure that Li^+ has octahedral (O_h) geometry while Al^{3+} has both octahedral and tetrahedral (T_d) geometries.

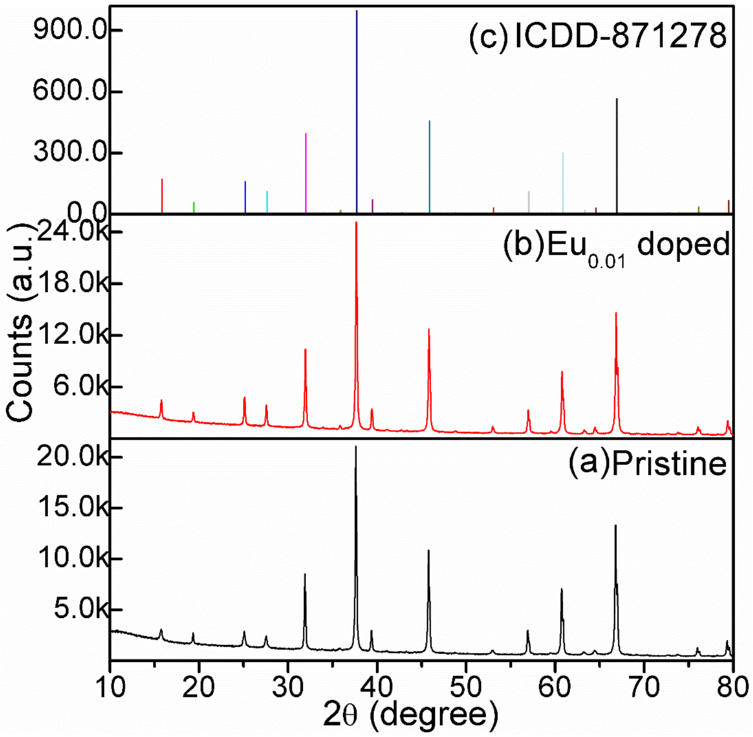

Figure 6.1 XRD patterns of (a) pristine (b) $Eu_{0.01}$ doped as-prepared samples and (c) ICDD pattern (file no. 87-1278) of $LiAl_5O_8$.

Figure 6.2b shows the SEM image of $LiAl_5O_8$. The image shows the formation of highly compacted spherical nano particles with minimum agglomeration. The average particle size of the nano phosphor is calculated to be 60 nm.

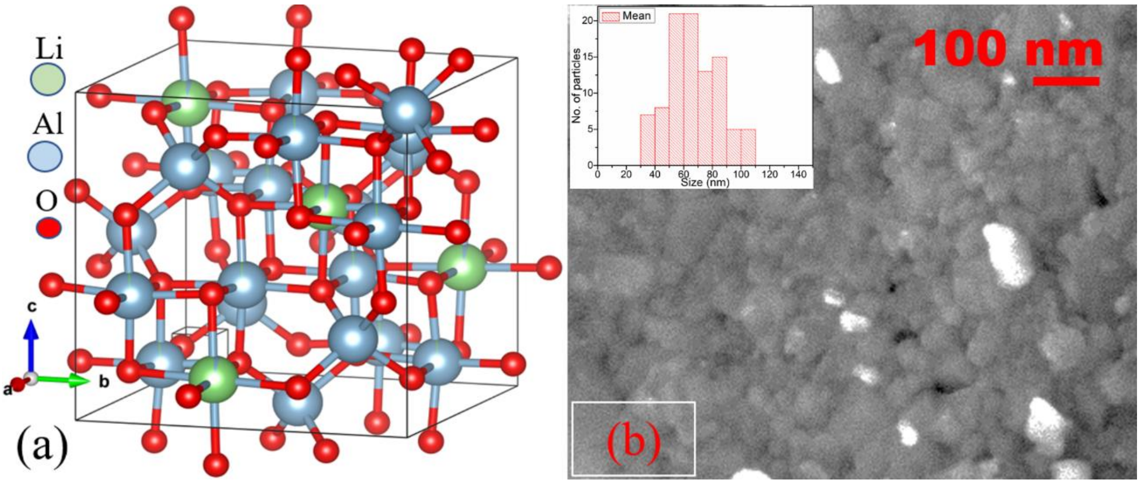

Figure 6.2 (a) The crystal structure and (b) SEM image of as-prepared $LiAl_5O_8$ *sample. The inset represents the distribution of particle size.*

6.2.2. Photoluminescence studies of Fe^{3+}, Cr^{3+} and Eu^{3+} in LAO

6.2.2.1. Fe^{3+} photoluminescence

Figure 6.3 shows the PL excitation and emission spectra of Fe^{3+} in LAO: Fe (500 ppm) recorded at $\lambda_{em} = 690$ and $\lambda_{ex} = 263$ nm, respectively. The excitation spectrum (Fig. 6.3a) exhibits a very strong charge transfer (CT) band of $Fe^{3+} \leftarrow O^{2-}$ at 263 nm followed by three weak 3*d*-3*d* transitions at 390 nm: $^6A_1(^6S) \rightarrow {}^4E(^4D)$, 445 nm: $^6A_1(^6S) \rightarrow {}^4T_2(^4D)$ and 534 nm: $^6A_1(^6S) \rightarrow {}^4T_2(^4G)$.[28, 34, 35] The weak 3*d*-3*d* transitions of Fe^{3+} are due to both spin and parity forbidden nature (inset of Fig. 6.3).[36] The absorbance spectrum of LAO: Fe (500 ppm) recorded using DRS shows only a broad peak around 250 nm (Fig. 6.4). The emission spectrum (Fig. 6.3b) of LAO: Fe (500 ppm) sample shows a very broad and intense peak at 690 nm corresponding to $^4T_1(^4G) \rightarrow {}^6A_1(^6S)$ transition.[37] The pristine LAO sample also exhibits similar Fe^{3+} luminescence. The broad emission from iron is very intense and it could mask the emission from other dopants as chromium and europium studied here. Therefore, excitation spectra of $LiAl_5O_8$: $Fe^{3+}/Cr^{3+}/Eu^{3+}$ are recorded taking one of the dopant concentrations much higher than that of the other two to get information about the excitation spectrum of the dopants as discussed later. The LAO is known to have Fe^{3+} and Cr^{3+} impurities as discussed earlier. The iron content in the aluminium nitrate precursor is estimated by spectrophotometry and found to be 1.7 ppm.

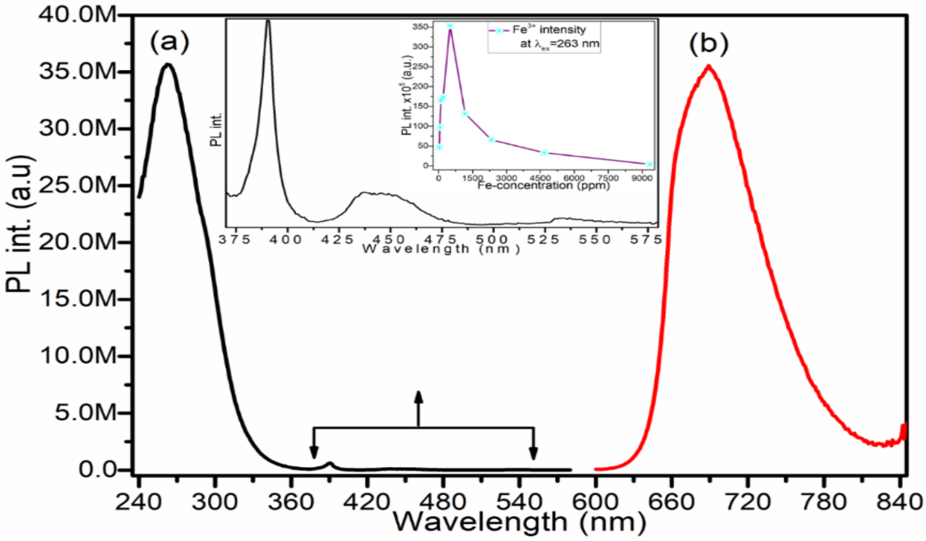

Figure 6.3 PL excitation and emission spectra of Fe^{3+} in LAO: Fe (500 ppm) at λ_{em} = 690 and λ_{ex} = 263 nm, respectively. Inset shows the enlarged portion of the excitation spectrum and PL intensity of Fe^{3+} as a function of Fe-concentration.

To optimize the iron luminescence, emission spectra of LAO samples with different Fe-concentrations (25-9340 ppm: 25, 50, 100, 200, 500, 1170, 2335, 4670, 9340 ppm) are recorded. It is observed that the PL intensity of Fe^{3+} gets increased with the increase in Fe-concentration with maximum intensity is observed for 500 ppm; thereafter, the intensity gets decreased probably due to the concentration quenching as shown in the inset of Figure 6.3. The emission peak maximum shows a red-shift beyond 2335 ppm of Fe-concentration and the extent of shift varies with further increase in its concentration. However, no shift is observed in the excitation peak position over the concentration range studied here. The Fe^{3+} luminescence has been reported around 700±20 nm in case of rare earth hosts.[11] Similarly, it has been observed around 730 and 670 nm in $LiAlO_2$ [10] and $LiAl_5O_8$ [28] hosts, respectively. Such a variation in emission is due to the dependence of the emitting level of Fe^{3+} on the crystal field strength (CFS).[36] The lowest emitting energy level $^4T_1(^4G)$ of Fe^{3+} changes significantly with the CFS and therefore, its emission can be seen in a wide range of wavelengths from visible to NIR region. The observed shift in the luminescence maxima could be due to iron occupying multiple sites in the host and experiencing a different magnitude of the CFS. Such an observation has also been made by Ming et al. [38] for Eu^{2+}

luminescence whose emitting energy level varies with the CFS. Occupancy in multiple sites with different CFS might have contributed to the observed larger broadening of Fe^{3+} luminescence as observed in the present study. The intense and broad deep red-NIR emission over 200 nm (620-830 nm) of LAO: Fe (500 ppm) nano phosphor in the tissue optical window (650-1350 nm) may be suitable for luminescence guided surgical applications.

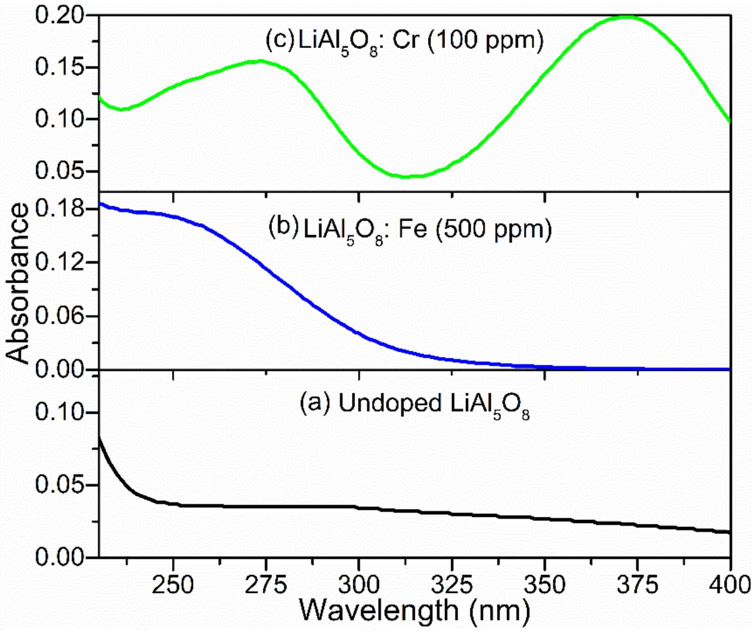

Figure 6.4 Absorbance spectra of (a) undoped LAO (b) LAO: Fe (500 ppm) and (c) LAO: Cr (100 ppm).

Figure 6.5a shows the lifetime decay of Fe^{3+} in LAO: Fe^{3+} (500 ppm). In case of LAO: Fe (500 ppm), two lifetimes of τ_1=3.5 ms (14%) with B_1=514 and τ_2=8.2 ms (86%) with B_2=1383 are obtained for Fe^{3+} suggesting its occupancy in two different sites. The average lifetime of Fe^{3+} is calculated to be 7.5 ms.

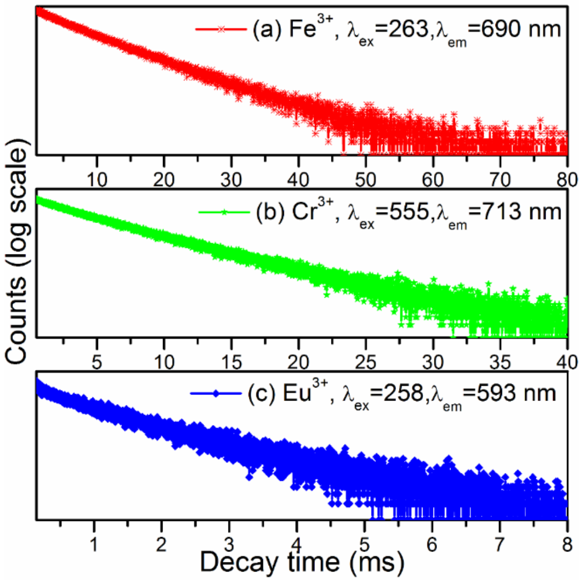

Figure 6.5 Lifetime decays of LAO: (a) Fe (500 ppm) (b) Cr (100 ppm) and (c) Eu (0.5 mol%).

Figure 6.6 shows the PL of Fe^{3+} at 77 K monitored at different excitation and emission wavelengths. At 77 K, the emission spectra (Fig. 6.6e-h) of Fe^{3+} showed a narrow peak at 658 nm corresponding to its zero-phonon line (ZPL) [11] and a broad emission (660-820 nm) associated with the $^4T_1(^4G)\rightarrow{}^6A_1(^6S)$ transition. The excitation spectra (Fig. 6.6a-d) of Fe^{3+} at 77 K monitored at λ_{em} = 658, 685, 695 and 740 nm resulted in better resolved CT bands (263 and 303 nm) of different FWHM along with the 3*d*-3*d* transitions indicating the presence of iron at different sites. To confirm the multiple site occupancy, the emission spectra (Fig. 6.6e-h) were recorded at λ_{ex}=253, 263, 293 and 303 nm of the CT band. Consequently, the $^4T_1(^4G)\rightarrow{}^6A_1(^6S)$ emission exhibited a red-shift with a change in the spectral profile. This could be due to iron experiencing a different magnitude of CFSE at different sites. Exciting Fe^{3+} at 263 nm, the average lifetimes of 8.3, 8.0 and 6.7 ms were obtained for emission at 658, 685 and 740 nm, respectively. Similarly, average lifetimes of 8.3, 6.4 and 4.8 ms were obtained by exciting at 303 nm for emission at 658, 685, 740 nm, respectively. This further corroborates the presence of iron in multiple sites.

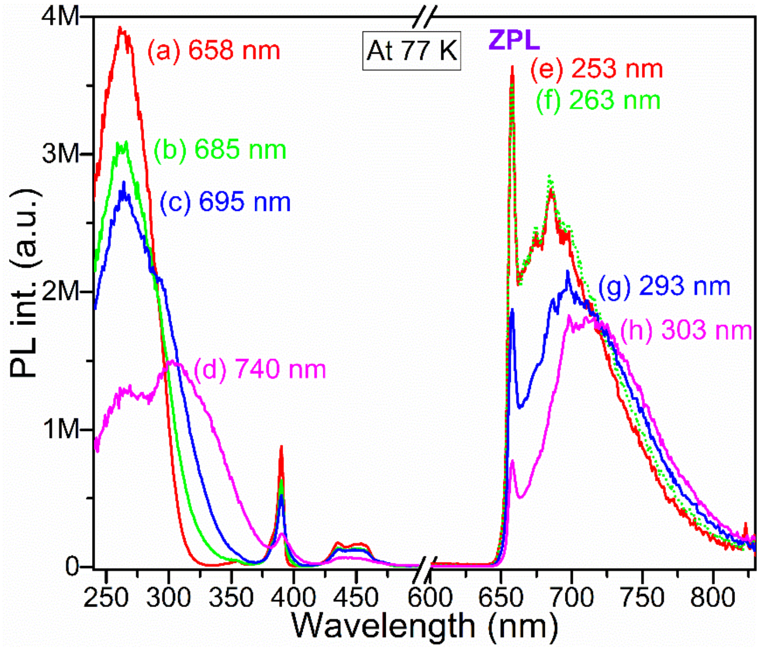

Figure 6.6 PL of Fe^{3+} in LAO: Fe (500 ppm) recorded at 77 K. ZPL represents the zero-phonon line (ZPL) of Fe^{3+} emission.

To further probe the Fe^{3+} occupancy at more than one site, TRES of LAO: Fe^{3+} are recorded as shown in Figure 6.7. In the time domain of 0-3.5 ms, the emission maximum observed at 693 nm is predominantly from Fe^{3+} associated with the site corresponding to the τ1 (3.5 ms). During this time period, Fe^{3+} at the site associated with τ_1 could have contributed more to the Fe^{3+} luminescence profile as iron at the site associated with τ_2 (8.2 ms) is yet to complete the first lifetime decay. With the increase in time, the PL intensity of Fe^{3+} emission decreases and the emission maximum shows a blue-shift as seen from Figure 6.7. In the time domain of 21-28 ms, the luminescence from the site associated with τ_1 could have decayed by six-seven lifetimes whereas luminescence from the site associated with τ_2 could have decayed by only three lifetimes. Therefore, the Fe^{3+} luminescence profile (680 nm) recorded for this time period is predominantly from the site associated with τ_2. The lifetime and TRES studies suggest that Fe^{3+} occupies at least two different sites in the LAO host. Moreover, the two sites of Fe^{3+} are not identical as the Fe^{3+} emission profiles observed are different (inset of Fig. 6.7). Apart from different emission maxima, the FWHM of the

Fe^{3+} emission profiles is also different. Therefore, it can be concluded that Fe^{3+} experiences different CFS at different sites of occupancy leading to its broad emission.

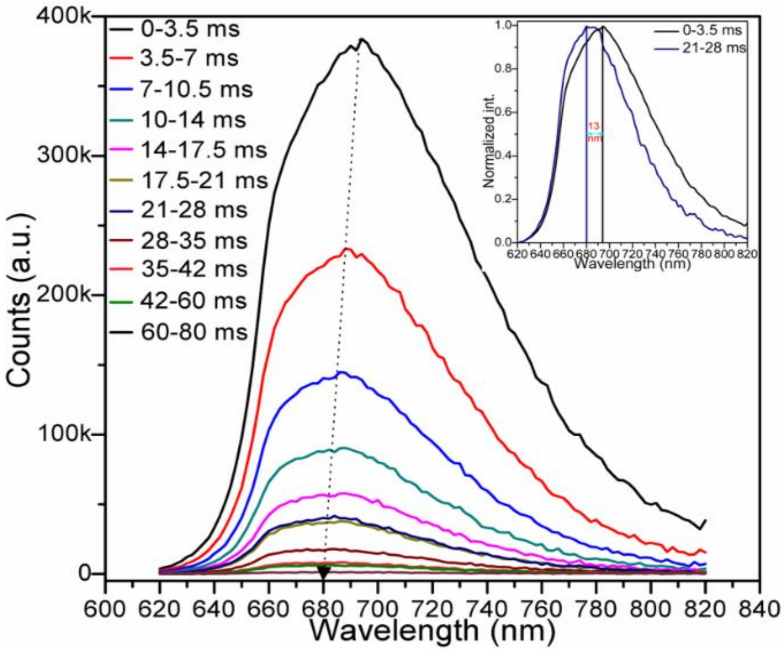

Figure 6.7 TRES spectra of Fe^{3+} in LAO: Fe (500 ppm) at λ_{ex} = 263 nm at different time domains. Inset represents the normalized spectra at time domains of 0-3.5 and 21-28 ms.

6.2.2.2. Cr^{3+} photoluminescence

Figure 6.8 shows the PL excitation and emission spectra of Cr^{3+} in LAO: Cr at λ_{em} = 713 and λ_{ex} = 555 nm, respectively, for different Cr-concentrations (219 ppb-300 ppm). The excitation spectrum of 219 ppb Cr (Fig. 6.8a) exhibits an intense broad band corresponding to CT band at 256 nm ($Cr^{3+} \leftarrow O^{2-}$) and the spin allowed 3*d*-3*d* transitions of octahedral Cr^{3+} at 288 nm: $^4A_2(^4F) \rightarrow {}^4T_1(^4P)$, 395 nm: $^4A_2(^4F) \rightarrow {}^4T_1(^4F)$ and 563 nm: $^4A_2(^4F) \rightarrow {}^4T_2(^4F)$.[9] With the increase in Cr-concentration up to 15 ppm, the excitation peaks do not show any shift in the peak maxima as shown in Figure 6.8(a-d). However, at Cr-concentration of 100 ppm (Fig. 6.8e), the CT band (256 nm) and $^4A_2(^4F) \rightarrow {}^4T_2(^4F)$ transitions (563 nm) are blue-shifted to 250 and 555 nm, respectively, while the 395 nm peak is red-shifted to 404 nm. Further, above 100 ppm of Cr-concentration (Fig. 6.8f and g), the CT band is observed around 256 nm while $^4A_2(^4F) \rightarrow {}^4T_1(^4F)$ transition shifts to 408 nm and $^4A_2(^4F)\rightarrow^4T_2(^4F)$ transition shifts to 560 nm. The PL intensity of all the excitation peaks of Cr^{3+} gets increased gradually with the increase in Cr-concentration from 219 ppb to 100 ppm and beyond that, it gets reduced indicating the concentration quenching. Moreover, below 15 ppm Cr-concentration, the CT band (256 nm) is more intense than the 3*d*-3*d* transitions (395 and 563 nm) whereas at 100 and 125 ppm, the 3*d*-3*d* transitions become more intense than the CT transition. At 300 ppm Cr-concentration, the PL intensity of both the CT band and 3*d*-3*d* transitions becomes comparable. The shift in the excitation peak positions could be due to the change in its local environment. In the emission spectra (Fig. 6.8e′), a narrow and intense zero-phonon line centered at 713 nm ($^2E\rightarrow^4A_2$) is observed. In addition, two shoulder peaks on either side of the 713 nm peak are observed around 700 and 727 nm. The narrow peak seen at 700 nm is known as the R-line and attributed to the crystal field component of $^2E\rightarrow^4A_2$ transition at Cr^{3+}-O_h site[33, 39] whereas the broad peak seen at 727 nm is attributed to the exchange interactions within the nearest Cr^{3+}-Cr^{3+} pairs.[40] The broad background emission is ascribed to the phonon-assisted side bands.[41] The Cr^{3+} emission does not shift with the change in CFS irrespective of its occupancy at the octahedral or tetrahedral sites as its lowest emitting level $^2E_g(^2G)$ varies insignificantly with the CFS.[42] With the increase in Cr-concentration from 219 ppb to 100 ppm, the intensity of Cr^{3+} emission (713 nm) gets increased up to 100 ppm (Fig. 6.8a′-e′) and the emission profiles are not changed. Beyond this concentration, the emission intensity (Fig. 6.8f′-g′) gets decreased due to the concentration quenching. In case of pristine LAO, it is challenging to observe Cr^{3+} emission for the CT band excitation as the Fe^{3+} emission obscures the Cr^{3+} emission. However, Cr^{3+} emission is observed by exciting at the 3*d*-3*d* transition (λ_{ex} = 555 nm) as at this excitation Fe^{3+} does not show any luminescence. Figure 6.4c shows the absorbance spectra of undoped and LAO: Cr (100 ppm) samples. In case of Cr doped sample, peaks around 274 and 372 nm are observed whereas no significant spectral features could be observed for the undoped sample probably due to the presence of impurities at trace level. Figure 6.5b shows the lifetime decay of Cr^{3+} in LAO: Cr (100 ppm) sample recorded at λ_{em} = 713 and λ_{ex} = 555 nm. The lifetime values of Cr^{3+} are τ_1=2.9 ms (20%) with B_1=519 and τ_2=5.7 ms (80%) with B_2=1053 indicating two sites of occupancy for it. The average lifetime of Cr^{3+} in LAO: Cr^{3+} (100 ppm) is 5.1 ms which is more than that of Al_2O_3: Cr^{3+} (3.2 ms)[43] and LAO: Cr (3.6 ms)[27] suggesting it as a better candidate for laser material. The PL of Cr^{3+} is also recorded at 77 K and the observed spectral profiles are similar to that at room temperature but for narrowing the peak widths. The average lifetime of Cr^{3+} (5.44 ms) is slightly higher than observed at room temperature probably due to the reduction in non-radiative rate.

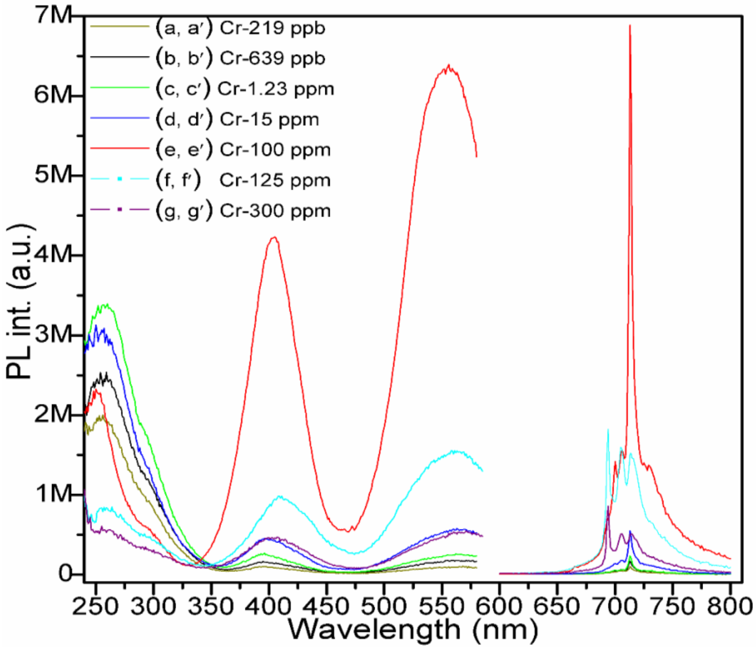

Figure 6.8 PL excitation and emission spectra of Cr^{3+} in LAO: Cr (219 ppb-300 ppm) at λ_{em} = 713 and λ_{ex} = 555 nm, respectively.

6.2.2.3. Eu^{3+} photoluminescence

Figure 6.9 shows the PL excitation and emission spectra of Eu^{3+} in LAO: $Eu_{0.005}$ phosphor monitored at λ_{em} = 593 nm and λ_{ex} = 258, 393 nm, respectively. The excitation spectrum (Fig. 6.9a) shows the characteristic intense peaks of Eu^{3+} at 258 and 393 nm corresponding to the strong CT band ($Eu^{3+}\leftarrow O^{2-}$) and intraconfigurational 4*f*-4*f* ($^7F_0\rightarrow{}^5L_6$)

transitions, respectively. The other weak excitation peaks of 4*f*-4*f* transitions are observed at 362 ($^7F_0 \rightarrow ^5D_2$), 380 ($^7F_0 \rightarrow ^5D_2$), 401 ($^7F_0 \rightarrow ^5D_2$), 412 ($^7F_0 \rightarrow ^5D_2$), 429 ($^7F_0 \rightarrow ^5D_2$) and 464 ($^7F_0 \rightarrow ^5D_2$) nm.[8] The emission spectrum obtained for 258 nm excitation (Fig. 6.9b) exhibits the characteristics peaks of Eu^{3+} centered at 578 ($^5D_0 \rightarrow ^7F_0$), 593 ($^5D_0 \rightarrow ^7F_1$) and 616 ($^5D_0 \rightarrow ^7F_2$) nm while its other emission peaks usually observed around 650 ($^5D_0 \rightarrow ^7F_3$) and 698 nm ($^5D_0 \rightarrow ^7F_4$) are masked by the broad emission peak of Fe^{3+} ranging from 635 to 800 nm. For excitation at 393 nm (Fig. 6.9c), Eu^{3+} emission peaks at 578, 593, 616 and 654 nm corresponding to the $^5D_0 \rightarrow ^7F_{0, 1, 2, 3}$ transitions are observed while its other emission peak at 698 nm ($^5D_0 \rightarrow ^7F_4$) is masked by the Cr^{3+} emission in the wavelength region of 670-800 nm. In the present case, the asymmetry ratio for 258 nm excitation is found to be 4 suggesting a lower symmetric environment around Eu^{3+}. The luminescence of Eu^{3+} is optimized by taking different Eu-concentration (0.25-1 mol%). The LAO doped with 0.5 mol% europium displayed maximum luminescence suggesting it to be a potential red phosphor.[44] In case of LAO: Eu^{3+} (Fig. 6.5c), a single and short lifetime of 1.25 ms (100%) is obtained for Eu^{3+} indicating its occupancy at a single site with lower symmetry. The PL and lifetime decay of Eu^{3+} are also recorded at 77 K that shows narrower spectral profiles with a slightly higher lifetime of 1.40 ms than observed at room temperature.

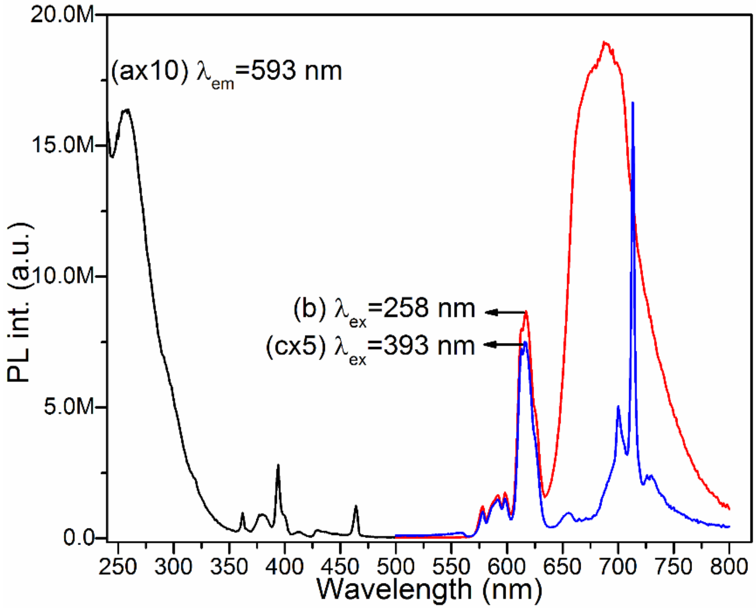

Figure 6.9 PL excitation and emission spectra of LAO: $Eu_{0.005}$ monitored at (ax10) λ_{em} = 593 nm, and (b) λ_{ex} = 258 and (cx5) λ_{ex} = 393 nm, respectively.

6.2.3. Color coordinates and color purity of the LAO nano phosphors

The color of the synthesized phosphors is expressed in terms of color coordinates and color purity (%) to evaluate its brightness for device applications. The color coordinates of LAO: Eu (0.5 mol%), LAO: Cr (100 ppm) and LAO: Fe (500 ppm) nano phosphors are estimated to be (0.674, 0.325), (0.717, 0.283) and (0.726, 0.274), respectively, as shown in the chromaticity diagram (Fig. 6.10). The color coordinates of the National Television Standard Committee (NTSC) for the red phosphor are (0.670, 0.330)[45] whereas that of the commercially available red phosphor, Y_2O_2S: Eu^{3+} are (0.622, 0.351).[46, 47] The LAO: Eu nano phosphor synthesized here has shown better color coordinates as compared to that of the reported LAO: Eu synthesized via conventional SSR route.[24] Similarly, LAO: Cr (100 ppm) and LAO: Fe (500 ppm) phosphors synthesized through the SCS route exhibit better color purity than that of $LiAl_5O_8$: Cr^{3+}/Fe^{3+} and $LiAl_4O_6F$: Cr^{3+}/Fe^{3+} synthesized thorough the SSR route.[32]

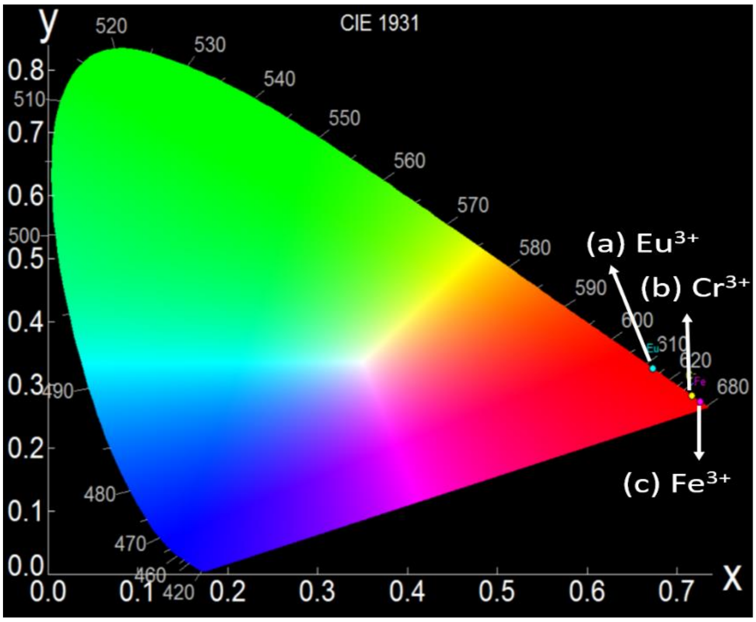

Figure 6.10 Chromaticity diagram of LAO: (a) Eu (0.5 mol%) (b) Cr (100 ppm) and (c) Fe (500 ppm) phosphors.

Further, the color purity of the synthesized nano phosphors is determined as mentioned in chapter 4. Strikingly, it can be seen from the chromaticity diagram (Fig. 6.10) that the color coordinates corresponding to the dominant wavelength (x_d, y_d) of all the three phosphors, LAO: Fe (500 ppm), LAO: Cr (100 ppm) and LAO: Eu (0.5 mol%) are the same as their respective color coordinates (x_s, y_s). Hence, the color purity for the three phosphors is found to be 100% suggesting them as potential candidates for deep red-NIR applications.

6.2.4. Site speciation studies of Eu and Fe in $LiAl_5O_8$

Li^+ has octahedral coordination whereas Al^{3+} has both octahedral and tetrahedral coordination in $LiAl_5O_8$ host as discussed earlier (Fig. 6.2a). The site speciation of the activator is essential as the luminescence behavior depends on its geometry and symmetry. However, the local coordination number and geometry of different dopants in this host are yet to be known. Therefore, this has been investigated here in detail using X-ray absorption spectroscopy. XAS is the combination of X-ray absorption near edge structure (XANES) and extended X-ray absorption fine structure (EXFAS) spectroscopy techniques.

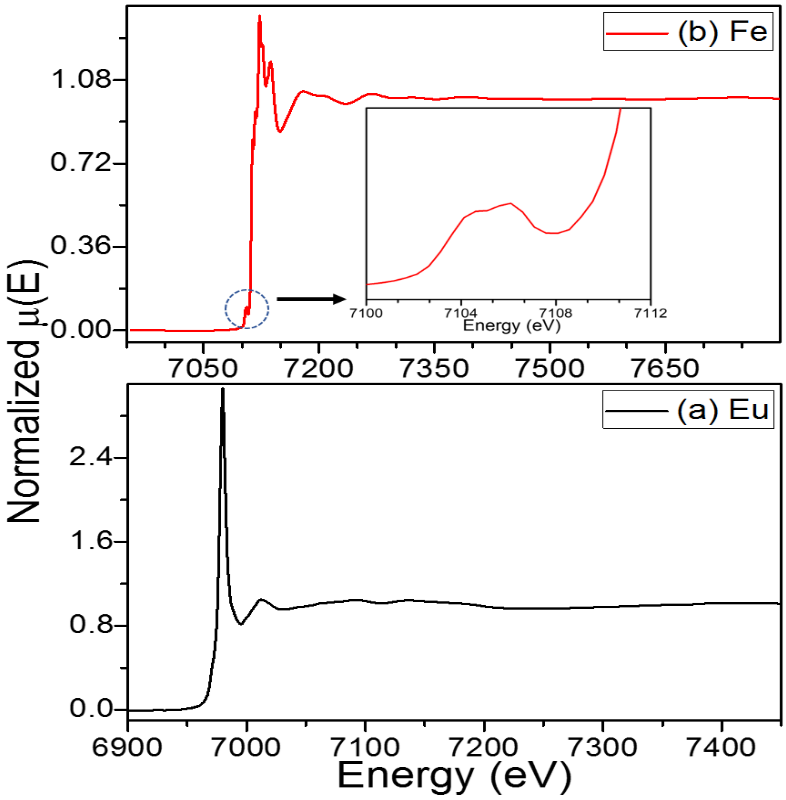

Figure 6.11 XAS spectra at (a) Eu L_3-edge in LAO: Eu0.01 and (b) Fe K-edge in LAO: Fe (500 ppm). The inset of Figure 11b represents the pre-edge of Fe.

XANES corresponds to the typical energy of -50 eV to +200 eV with respect to the absorption edge energy and gives information about the electronic transitions, oxidation state and symmetry of the atom under investigation.[48] Beyond +200 eV, EXAFS spectroscopy provides the local coordination environment pertaining to the coordination number and bond length of the atom of choice with the nearest neighborhood. Figure 6.11(a and b) shows the XAS spectra of LAO: $Eu_{0.01}$ and LAO: Fe (500 ppm) samples at Eu L_3-edge and Fe K-edge, respectively. A single sharp pre-edge peak in the XANES region indicated a tetrahedral (T_d) coordination whereas octahedral (O_h) coordination is indicated if the peak splits into multiple peaks.[49]

A sharp X-ray absorption edge without any pre-edge feature (Fig. 6.11a) is observed in the XANES region of Eu L_3-edge profile indicating occupation of Eu in an O_h site in the LAO host. Interestingly in this study, the pre-edge peak for Fe K-edge is appeared to be a doublet as shown in the inset of Figure 6.11b. This indicates that Fe occupies the O_h site in the LAO host and is attributed to $1s \rightarrow 3d$ transitions [49].

The local coordination number (CN) and geometry (O_h/T_d) around Eu and Fe are obtained from the EXAFS oscillations of the absorption spectra following the standard procedure.[48, 50] The $\chi(k)$ function is weighted by k^2 to amplify the oscillations at high k and the functions $\chi(k)*k^2$ are Fourier transformed in r space to generate the $\chi(d)$ as a function of d plots in terms of the real distances from the center of the absorbing atom. The real space fittings are performed between 1-4 Å. The $\chi(k)*k^2$ as a function of k plots is shown in Figure 6.12. The $\chi(d)$ as a function of d plots of LAO: $Eu_{0.01}$ at Eu L_3-edge and LAO: Fe (500 ppm) at Fe K-edge are shown in Figure 6.13. The ionic size of Eu^{3+} (r=94.7 pm, CN=6) is close to Li^+ (r=76 pm, CN=6).[51] Hence, Li^+ is replaced with Eu^{3+} in the Li^+-Oh position and a FEFF model is generated following the crystal structure of $LiAl_5O_8$.[52] Only single scattered paths below 4 Å are considered for fitting. Each path is associated with four variable parameters such as coordination number (CN), bond length (d), Debye-Waller factor (σ^2) and the goodness of fit (R-factor). The parameters are optimized and the fitted parameters are given in Table 6.1.

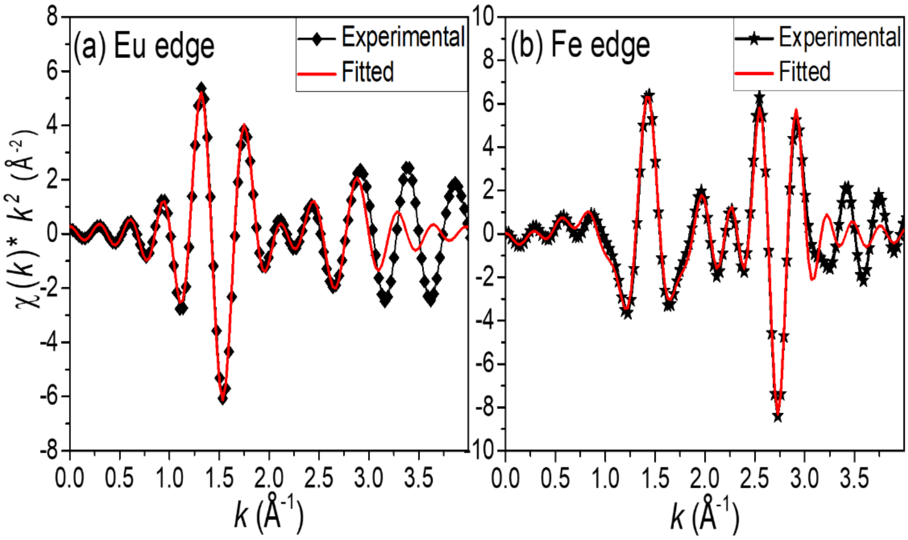

Figure 6.12 The EXFAS fittings of the $\chi(k)*k^2$ as a function of k plots of (a) LAO: Eu (1 mol%) and (b) LAO: Fe (500 ppm) samples.

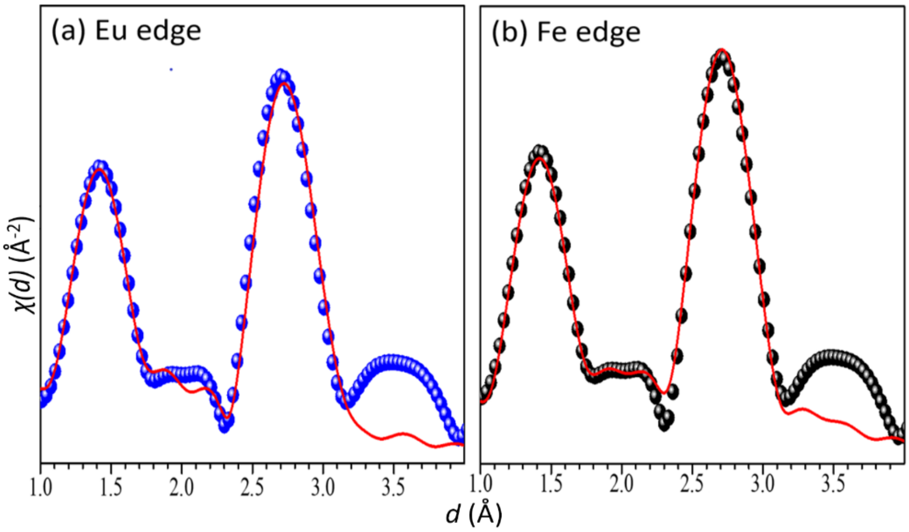

Figure 6.13 The EXFAS fittings of the $\chi^2(d)$ *(Å*$^{-2}$*) as a function of d (Å) plots of (a) LAO: Eu (1 mol%) and (b) LAO: Fe (500 ppm) samples.*

From the results following the fitting and optimization, it is observed that the coordination number of Eu^{3+} with O^{2-} is reduced from 6 to 5.28 with d=2.05 Å due to the creation of some oxygen vacancy suggesting lowering of symmetry around Eu^{3+} in the host lattice. Therefore, the XAS studies confirm the substitution of Eu^{3+} at the Li^+-O_h site with CN=5.28. The lowering of the symmetry of Eu^{3+} seen here is in agreement with the observation of the high asymmetry ratio for Eu^{3+} photoluminescence as discussed earlier.

Table 6.1 EXAFS analysis of Eu L_3*-edge and Fe K-edge in LAO: Eu (1 mol%) and LAO: Fe (500 ppm).*

Edge	Path	CN	d (Å)	σ^2	R-factor
Eu L_3	$(Eu\text{-}O)_{Li\text{-}Oh}$	5.28(3)	2.05(2)	0.001(2)	0.02
Fe K	$(Fe\text{-}O)_{Al\text{-}Td1}$	3.06(2)	1.91(1)	0.007(0)	0.01
	$(Fe\text{-}O)_{Al\text{-}Td2}$	0.88(2)	1.88(3)	0.005(0)	
	$(Fe\text{-}O)_{Al\text{-}Oh1}$	1.68(1)	1.88(2)	0.005(1)	
	$(Fe\text{-}O)_{Al\text{-}Oh2}$	2.20(1)	2.10(1)	0.015(2)	
	$(Fe\text{-}O)_{Al\text{-}Oh3}$	1.56(0)	1.80(0)	0.009(2)	
	$(Fe\text{-}O)_{Li\text{-}Oh}$	4.20(2)	2.02(1)	0.002(1)	

Note:

I. Notations: $(Fe\text{-}O)_{Al\text{-}Td1}$, $(Fe\text{-}O)_{Al\text{-}Td2}$ is pertaining to Fe in aluminium tetrahedral position. $(Fe\text{-}O)_{Al\text{-}Td1}$ Fe-O bonds at the basal plane and $(Fe\text{-}O)_{Al\text{-}Td2}$ Fe-O bonds at the apical position.

II. $(Fe\text{-}O)_{Al\text{-}Oh1,}$ $(Fe\text{-}O)_{Al\text{-}Oh2,}$ $(Fe\text{-}O)_{Al\text{-}Oh3}$ are paths pertaining to Fe in aluminium octahedral position.

In LAO host, Al^{3+} occupies both O_h and T_d sites with ionic radii of 53.5 and 39 pm, respectively.[51] Therefore, Fe^{3+} having ionic radii of 64.5 (O_h) and 49 pm (T_d) is substituted in both Al^{3+}-O_h and Al^{3+}-T_d positions for generating scattering paths from FEFF simulations. In addition, as the ionic radius of Li^+ in O_h position is 76 pm, Fe^{3+} occupying Li^+-O_h position is not ruled out. Hence, another FEFF simulation is also carried out to obtain scattering paths for Fe^{3+} occupying the Li^+-O_h site. For fitting the data, only single scattered paths having path length below 4 Å are considered (Fig. 6.12b and Fig.13tableb). In this case, two paths from Al^{3+}-T_d, three paths from Al^{3+}-O_h and one path from Li^+-O_h FEFF simulations are considered for fitting. The EXAFS analysis reveals that Fe^{3+} occupies the Al^{3+}-T_d position forming a distorted tetrahedron (CN=3.94) with three oxygen atoms at the base with *d*=1.91 Å and one apical oxygen atom with *d*=1.88 Å. The analysis also confirms that Fe^{3+} occupies the Al^{3+}-O_h position with a coordination number of 5.44 forming a distorted octahedron with two oxygen atoms each at a distance of 1.88, 2.10 and 1.80 Å. The analysis further confirms the occupancy of Fe^{3+} in the Li^+-O_h position but with a lower coordination number (4.2) forming a tetrahedron wherein the oxygen atoms are at a distance of 2.02 Å. The lower coordination number at the Li^+-O_h site for Fe^{3+} may be attributed to the oxygen vacancy at this site. The XAS studies of LAO: Fe^{3+} shows that Fe^{3+} occupies both the Al^{3+}-O_h and Al^{3+}-T_d sites apart from occupying the Li^+-O_h site also. The luminescence from Fe^{3+} in tetrahedral symmetry is expected to be more intense due to the absence of the center of symmetry. Moreover, the broad luminescence of Fe^{3+} could be due to its occupancy in multiple sites with different CFS. The site occupancy of Cr^{3+} could not be carried out as the XAS signal was too low to record measurements.

6.3. Conclusion

$LiAl_5O_8$: Eu^{3+}, Cr^{3+} and Fe^{3+} nano phosphors with an average particle size of 60 nm are prepared through the SCS route. The Cr^{3+} and Fe^{3+} luminescence are observed from the intrinsically present iron and chromium impurities in the pristine $LiAl_5O_8$. Optimization of Cr^{3+} and Fe^{3+} concentration significantly enhances their luminescence. LAO: $Eu^{3+}_{0.005}$, LAO: Cr^{3+} (100 ppm) and LAO: Fe^{3+} (500 ppm) phosphors display intense deep red emission with 100% color purity suggesting them as better candidates for deep red-NIR applications. Lifetime decay measurements reveal two lifetimes for Cr^{3+} and Fe^{3+} indicating more than one site occupancy whereas a single lifetime is observed for Eu^{3+}. The XAS studies confirm the presence of Fe^{3+} at Al^{3+}-O_h, Al^{3+}-T_d and Li^+-O_h sites with the coordination numbers of 5.44, 3.94 and 4.20, respectively. However, Eu^{3+} is found to occupy only at the Li^+-O_h site. The broad iron emission observed is due to its occupancy in multiple sites with different CFS. The occupancy of Fe^{3+} in tetrahedral symmetry could result in intense deep red emission due to the absence of the center of symmetry. The intense red emission observed from Eu^{3+} is due to the reduction in its coordination number from 6 to 5.28 at the Li^+-O_h site with a lowered symmetry.

References

1. Park, S.; Mho, S.; Kim, C.; Jeong, B.; Park, H. *Solid state communications* **1992,** 83, (1), 47-52.
2. Liu, X.; Lin, C.; Lin, J. *Applied physics letters* **2007,** 90, (8), 081904.
3. Yang, J.; Quan, Z.; Kong, D.; Liu, X.; Lin, J. *Crystal growth & design* **2007,** 7, (4), 730-735.
4. Bessière, A.; Jacquart, S.; Priolkar, K.; Lecointre, A.; Viana, B.; Gourier, D. *Optics express* **2011,** 19, (11), 10131-10137.
5. Xu, D.; Wu, X.; Zhang, Q.; Li, W.; Wang, T.; Cao, L.; Meng, J. *Journal of Alloys and Compounds* **2018,** 731, 156-161.

6. Rajendran, V.; Fang, M.-H.; Guzman, G. N. D.; Lesniewski, T.; Mahlik, S.; Grinberg, M.; Leniec, G.; Kaczmarek, S. M.; Lin, Y.-S.; Lu, K.-M. *ACS Energy Letters* **2018,** 3, (11), 2679-2684.
7. van Swieten, T. P.; Yu, D.; Yu, T.; Vonk, S. J.; Suta, M.; Zhang, Q.; Meijerink, A.; Rabouw, F. T. *Advanced Optical Materials* **2020**, 2001518.
8. Binnemans, K. *Coordination Chemistry Reviews* **2015,** 295, 1-45.
9. Basavaraju, N.; Sharma, S.; Bessière, A.; Viana, B.; Gourier, D.; Priolkar, K. *Journal of Physics D: Applied Physics* **2013,** 46, (37), 375401.
10. Suriyamurthy, N.; Panigrahi, B.; Natarajan, A. *Materials Science and Engineering: A* **2005,** 403, (1-2), 182-185.
11. Van Schaik, W.; Blasse, G. *Journal of alloys and compounds* **1993,** 198, (1-2), 69-72.
12. Pei, Z.; Su, Q.; Zhang, J. *Journal of Alloys and Compounds* **1993,** 198, (1-2), 51-53.
13. Abritta, T.; de Souza Barros, F. *Journal of Luminescence* **1988,** 40, 187-188.
14. Bhargava, S. *Journal of Physics C: Solid State Physics* **1986,** 19, (35), 7045.
15. Jimenez-Becerril, J.; Bosch, P.; Bulbulian, S. *Journal of nuclear materials* **1991,** 185, (3), 304-307.
16. Terada, S.; Nagashima, I.; Higaki, K.; Ito, Y. *Journal of power sources* **1998,** 75, (2), 223-229.
17. Kawamura, Y.; Nishikawa, M.; Tanaka, K.; Matsumoto, H. *Journal of Nuclear Science and Technology* **1992,** 29, (5), 436-444.
18. Kale, M.; Joshi, C.; Moharil, S. *International Journal of Self-Propagating High-Temperature Synthesis* **2012,** 21, (1), 19-24.
19. Singh, V.; Chakradhar, R.; Rao, J.; Kwak, H.-Y. *Solid state sciences* **2009,** 11, (4), 870-874.
20. de Sousa, O. M. *Computational and Theoretical Chemistry* **2018,** 1123, 96-101.
21. Silva, A. J.; Nascimento, P. A.; Andrade, A. B.; Sampaio, D. V.; Moulton, B. J.; Silva, R. S.; Rezende, M. V. d. S. *Journal of Luminescence* **2018,** 199, 298-301.
22. Pitale, S. S.; Kumar, V.; Nagpure, I.; Ntwaeaborwa, O.; Swart, H. *Current Applied Physics* **2011,** 11, (3), 341-345.
23. Pitale, S. S.; Kumar, V.; Nagpure, I.; Ntwaeaborwa, O.; Coetsee, E.; Swart, H. *Journal of Applied Physics* **2011,** 109, (1), 013105.
24. Mohapatra, M.; Seshadri, M.; Naik, Y.; Meena, G.; Kadam, R.; Singh, V. *Journal of Materials Science: Materials in Electronics* **2018,** 29, (9), 7778-7784.
25. Singh, V.; Rao, T. G. *Journal of Solid State Chemistry* **2008,** 181, (6), 1387-1392.
26. Singh, V.; Chakradhar, R.; Rao, J.; Kim, D.-K. *Materials Chemistry and Physics* **2008,** 110, (1), 43-51.
27. Li, X.; Jiang, G.; Zhou, S.; Wei, X.; Chen, Y.; Duan, C. K.; Yin, M. *Sensors and Actuators B: Chemical* **2014,** 202, 1065-1069.
28. Shu, W.; Qiang, R.; Xiao, S.; Yang, X.; Ding, J. *Journal of alloys and compounds* **2011,** 509, (9), 3886-3888.
29. Kniec, K.; Tikhomirov, M.; Pozniak, B.; Ledwa, K.; Marciniak, L. *Nanomaterials* **2020,** 10, (2), 189.
30. Li, Z.; Zhang, Y.; Wu, X.; Wu, X.; Maudgal, R.; Zhang, H.; Han, G. *Advanced Science* **2015,** 2, (3).
31. Hashimoto, S.; Hattori, K.; Inoue, K.; Nakahashi, A.; Honda, S.; Iwamoto, Y. *Materials Research Bulletin* **2009,** 44, (1), 70-73.
32. Kobayashi, R.; Tamura, H.; Kamada, Y.; Kakihana, M.; Matsushima, Y. *ECS Transactions* **2018,** 88, (1), 225.

33. Teixeira, V.; Silva, A.; Manali, I.; Gallo, T.; Galante, D.; Ferreira, N.; Andrade, A.; Rezende, M. d. S. *Optical Materials* **2019,** 94, 160-165.
34. Kutty, T.; Nayak, M. *Journal of alloys and compounds* **1998,** 269, (1-2), 75-87.
35. Neto, J. M.; Abritta, T.; Barros, F. d. S.; Melamed, N. *Journal of Luminescence* **1981,** 22, (2), 109-120.
36. Grabmaier, B., *Luminescent materials*. Springer Verlag: 1994.
37. Pathak, N.; Gupta, S. K.; Sanyal, K.; Kumar, M.; Kadam, R.; Natarajan, V. *Dalton Transactions* **2014,** 43, (24), 9313-9323.
38. Ming, Z.; Qiao, J.; Molokeev, M. S.; Zhao, J.; Swart, H. C.; Xia, Z. *Inorganic Chemistry* **2020**.
39. Liao, B.-T.; Mei, Y.; Zheng, W.-C. *Optik* **2018,** 155, 213-215.
40. MacCraith, B.; Glynn, T.; Imbusch, G.; Remeika, J.; Wood, D. *Physical Review B* **1982,** 25, (6), 3572.
41. Liu, F.; Yan, W.; Chuang, Y.-J.; Zhen, Z.; Xie, J.; Pan, Z. *Scientific reports* **2013,** 3, 1554.
42. Blasse, G.; Grabmaier, B., How Does a Luminescent Material Absorb Its Excitation Energy? In *Luminescent materials*, Springer: 1994; pp 10-32.
43. Hu, Y.; Zhang, Z.; Grattan, K.; Palmer, A.; Meggitt, B. *Sensors and Actuators A: Physical* **1997,** 63, (2), 85-90.
44. Li, J.-G.; Li, X.; Sun, X.; Ishigaki, T. *The Journal of Physical Chemistry C* **2008,** 112, (31), 11707-11716.
45. Huang, X.; Guo, H.; Li, B. *Journal of Alloys and Compounds* **2017,** 720, 29-38.
46. Dhanaraj, J.; Jagannathan, R.; Kutty, T.; Lu, C.-H. *The Journal of Physical Chemistry B* **2001,** 105, (45), 11098-11105.
47. Huang, Y.; Seo, H. J. *Materials Letters* **2012,** 84, 107-109.
48. Kelly, S.; Hesterberg, D.; Ravel, B. *Methods of Soil Analysis Part 5—Mineralogical Methods* **2008,** 5, 387-463.
49. Wilke, M.; Farges, F.; Petit, P.-E.; Brown Jr, G. E.; Martin, F. *American Mineralogist* **2001,** 86, (5-6), 714-730.
50. Koningsberger, D.; Prins, R. **1988**.
51. Shannon, R. D. *Acta crystallographica section A: crystal physics, diffraction, theoretical and general crystallography* **1976,** 32, (5), 751-767.
52. Kniep, R.; Schäfer, G.; Engelhardt, H.; Boy, I. *Angewandte Chemie International Edition* **1999,** 38, (24), 3641-3644.

Table of Contents

Friday, May 14, 2021

Chapter 7

Summary and Future work

7.1. Summary

In the present thesis, emerging phosphors based on alkaline earth borophosphate, barium cerate and lithium aluminate hosts are synthesized and characterized for potential applications spanning from UV-*B*, UV-*A*, red, deep red-NIR LEDs to radiation dosimetry. The synthesis and extensive optical characterization of $MBPO_5$: Ce/Eu/Gd, $BaCeO_3$: Eu and $LiAl_5O_8$: Eu/Cr/Fe phosphors are explored in detail. A brief chapter wise summary of the thesis along with the scope for future study is outlined as follows.

A brief literature review about the importance of synthesis routes, host materials, luminescent centers, the structural and optical properties, and the challenging issues are presented in chapter 1. The motivation and objective of the research work are also briefed in this chapter.

The experimental techniques carried out for material synthesis and characterization are briefly outlined in chapter 2, with the basic principle of operation and major components of the instruments. The synthesis of $MBPO_5$: Ce/Eu/Gd phosphors through a modified SSR route while $BaCeO_3$: Eu and $LiAl_5O_8$: Eu/Cr/Fe phosphors through the SCS route are presented.

In chapter 3, the structure, morphology, band gap and luminescence properties of $MBPO_5$: Ce phosphors are investigated. PL of Ce^{3+} exhibits intense UV-Blue (320-420 nm) emission with nanosecond lifetime (10-36 ns) whose utility is exploited in security industry, fluorescent sensing levels and scintillators. PL lifetime and TRES measurements confirm the presence of Ce^{3+} in two different sites in $MBPO_5$ hosts. PALS study suggests two types of defects present in undoped and Ce doped SBP that influence its luminescence properties. The mechanism of the TSL glow curve of γ-irradiated SBP: Ce phosphor is established from its TSL emission spectrum. A comparative luminescence study of Ce^{3+} among $SrBPO_5$, $CaBPO_5$ and $BaBPO_5$ hosts is also presented.

Chapter 4 focuses on the optical properties of Gd doped and Eu-Gd codoped $MBPO_5$ phosphors. Gd^{3+} exhibits intense and narrow UV-*B* emission at 313 nm in $MBPO_5$: $Gd_{0.075}$ phosphors. Here, the effect of Gd codoping on the PL and TSL properties of $SrBPO_5$: Eu phosphors is explored. In the Eu-Gd codoped $MBPO_5$, Eu^{3+} luminescence gets significantly enhanced due to the energy transfer from Gd^{3+} to Eu^{3+}. In addition to the energy transfer, surprisingly, Gd^{3+} facilitates the valency conversion from Eu^{2+} to Eu^{3+} which enhances the efficiency of Eu^{3+} luminescence furthermore. This has not been reported so far to the best of our knowledge and is addressed in the present work. The comparative study shows intense orange-red emission from Eu^{3+} in $CaBPO_5$: $Eu_{0.01}$, $Gd_{0.10}$, $SrBPO_5$: $Eu_{0.01}$, $Gd_{0.075}$ and $BaBPO_5$: $Eu_{0.01}$, $Gd_{0.05}$ with 97%, 94% and 97% color purity suggesting them as potential candidates for SSL applications. This study is relevant towards making efficient orange-red (Eu^{3+}), blue (Eu^{2+}) and UV-B (Gd^{3+}) LEDs. In addition to PL, TSL investigations on SBP: Eu/Gd are reported in detail for the first time. The mechanism of TSL and calculation of trap parameters in SBP: Eu, SBP: Gd and SBP: Eu, Gd phosphors are presented. The chapter highlights the favorable TSL characteristics of SBP: Eu, Gd phosphor that has shown a linear dose-response covering two orders of magnitude in the dose range of 100 mGy to 10Gy and useful trap parameters for radiation dosimetry.

Chapter 5 presents the PL and TSL properties of perovskite structured $BaCeO_3$: Eu prepared through the SCS route. The SEM image analysis ascertains high agglomeration above 1200 °C. Optimization of calcination temperature (1000-1300 °C) and Eu-concentration (1-10 mol%) reveal intense red color from $BaCeO_3$: $Eu_{0.09}$ phosphors calcined at 1200 °C. PL study corroborates that the asymmetric ratio of Eu^{3+} is as a function of dopant concentration, excitation wavelength and temperature. The color purity of Eu^{3+} in $BaCeO_3$:

$Eu_{0.09}$ is found to be 100% with excellent color coordinate suggesting it as a suitable candidate for red phosphor. PL lifetime and TRES analysis confirm two site occupancies for Eu^{3+} in this host. The defect studies using PALS reveal the presence of oxygen vacancy and barium-oxygen vacancy complex in this host for the first time. TSL glow curves of γ-irradiated $BaCeO_3$: Eu exhibit multiple traps and a linear dose-response in the range of 0-1000 Gy suggesting it as a high-energy radiation dosimetry phosphor.

Chapter 6 presents the single-step synthesis of in $LiAl_5O_8$: $Fe^{3+}/Cr^{3+}/Eu^{3+}$ nano phosphors through the SCS route at 600 °C. The powder XRD patterns confirm the single phase and inverse spinel structured cubic lattice of $LiAl_5O_8$. The morphology of synthesized phosphors shows the formation of spherical and compacted nano particles with an average size of 60 nm. The XAS investigations reveal the exact local coordination environment of dopants for the first time. The study confirms the presence of Eu^{3+} in Li^+-O_h site whereas Fe^{3+} in Li^+-O_h, Al^{3+}-O_h and Al^{3+}-T_d sites with a reduction in coordination number. The reduction in the coordination number indicates a lower symmetry and the presence of oxygen vacancy around the activators in this host resulting in intense deep red-NIR emission. The cause of the observed unusual broad emission of Fe^{3+} (620-830 nm) is due to its presence in multiple sites experiencing a different magnitude of CFS. TRES studies also corroborate the site occupancy of Fe^{3+} showing a blue-shift in different time domains. PL of $LiAl_5O_8$: Eu (0.5 mol%), $LiAl_5O_8$: Fe (500 ppm) and $LiAl_5O_8$: Cr (100 ppm) exhibits intense deep red-NIR emission with 100% color purity and improved color coordinates than that of the National Television Standard Committee recommendations suggesting them as potential nano phosphors for SSL, laser and biomedical applications.

7.2. Future work

In the future, the following work can be carried out.

- Quantification of Eu^{2+} to Eu^{3+} conversion

- Leaching studies with respect to different site occupancy
- Field study of $SrBPO_5$: Gd, Eu and $BaCeO_3$: Eu phosphors for radiation dosimetry applications
- Development of LEDs based on $SrBPO_5$, $BaCeO_3$ and $LiAl_5O_8$ phosphors for solid-state lighting and biomedical applications
- Development of nano phosphors for optical thermometry and long afterglow phosphors for noninvasive temperature sensing and emergency security applications.

Homi Bhabha National Institute

SYNOPSIS OF Ph. D. THESIS

1. Name of the Student: Sitakanta Panda

2. Name of the Constituent Institution: Indira Gandhi Centre for Atomic Research

3. Enrolment No.: CHEM02201504006

4. Title of the Thesis: Lanthanide and transition metal ions activated advanced phosphors for optical and radiation dosimetry applications

5. Board of Studies: Chemical Sciences

SYNOPSIS

Solid-state luminescent materials, commonly called phosphors, have drawn the attention of researches owing to their wide applications in solid-state lighting (SSL), biomedical imaging and radiation dosimetry [1-3]. Many of such phosphors have borate, phosphate, borophosphate, oxides of silicate and aluminate, and oxysulfide as host materials. Most importantly, phosphors based on oxysulfide, halide, phosphate and borate [4-7] hosts have not been paid much attention owing to their hygroscopic nature, poor chemical and thermal stability. In this context, the silicate hosts [8-10] pose excellent thermochemical stability and non-hygroscopicity, though they require a very high calcination temperature (≥1250 °C) for their synthesis. However, the alkaline earth borophosphate ($MBPO_5$; M=Ca/Sr/Ba) hosts possess good thermochemical stability as well as non-hygroscopicity [5]. Unlike silicates, $MBPO_5$ can be prepared by the conventional solid-state reaction (SSR) route at lower calcination temperature (900-1000 °C). Synthesis at low temperature effectively reduces the volatilization of the structural component and thereby, the defects formation is reduced leading to efficient luminescence from the phosphor. Moreover, an advanced phosphor must have multi photonic applications with improved color quality, high longevity, non-hygroscopicity, high radiation stability, environmental sustainability and low cost. In addition to these properties, the phosphor must have a large band gap (>3.2 eV), as in semiconductors and insulators, so as to avoid the absorption and emission from the host [11]. To keep pace with the recent demand for advanced lighting technology, synthesis of lanthanide and transition metal ions doped phosphors is in active research to develop highly efficient phosphors that meet the industrial standards. An efficient phosphor must have a befitting combination of activator(s) and host. In this context, lanthanide and transition metal ions doped stillwellite structured $MBPO_5$, perovskite structured $BaCeO_3$ and cubic structured $LiAl_5O_8$ phosphors are important due to their favorable structural and optical properties.

In $MBPO_5$, the M^{2+} ion is well connected by the tetrahedral borate (BO_4^{5-}) and phosphate (PO_4^{3-}) units forming a tortuous 3-dimensional rigid network. Hence, borophosphates possess very high physiochemical stability. Additionally, the ionic size of the M^{2+} ions is comparable with that of the lanthanide ions [12], allowing them to easily get incorporated into the host lattice with the least distortion in the host lattice up to a few atomic mole percentages of the activator concentration. In $MBPO_5$: Eu phosphors, europium exhibits both +2 and +3 oxidation states even though the phosphor is prepared in air atmosphere [13, 14]. Also, there are several hosts such as borates [7, 15], phosphates [16], silicates [17, 18], aluminates [19], sulfates [20] where the coexistence of Eu^{2+} and Eu^{3+} is observed. The coexistence of Eu^{2+} curtails the color quality of Eu^{3+} luminescence and remains a challenge that is yet to be addressed. Many researchers have reported prospective applications of

$MBPO_5$: Ln (Ln=Ce^{3+}, Eu^{3+} and Eu^{2+}) phosphors in X-ray imaging, neutron storage and display devices [2, 21-24]. These emerging applications urge to synthesize high-quality lanthanide activated $MBPO_5$ phosphors. Based on a detailed literature survey, it is found that there exists a vast scope for improving the luminosity by taking various activator combinations. For example, the optical properties of gadolinium doped and gadolinium-europium codoped phosphors are not yet studied in $MBPO_5$. Also, there is no detailed comparative study of Ce^{3+}, Gd^{3+}, Eu^{3+} and Eu^{2+} dopants in $MBPO_5$ hosts. Further, there is a lack of study on the effect of γ-radiation and the influence of defect centers on the luminescence properties of Gd/Eu activated $MBPO_5$. Also, there are no studies in $MBPO_5$ hosts where enhancement of Eu^{3+} luminescence is addressed. This motivated us to carry out a thorough investigation of the optical properties of Ce^{3+}, Gd^{3+}, Eu^{3+} and Eu^{2+} in $MBPO_5$.

Similarly, the perovskite structured MNO_3 (M=divalent and N=tetravalent cations) hosts have been of research interests due to their intriguing properties in industrial applications. MNO_3 is made up of cuboctahedral MO_{12} and octahedral NO_6 units forming a stable network. The perovskite hosts are known to have wide applications as hydrogen gas sensor [25], catalyst electrodes in a solid oxide fuel cell [26], hydrogen permeable membranes [27], reactors for ammonia synthesis [28], desulfurization of natural fuel [29] and dehydrogenation of alkane to alkene [30]. The perovskite hosts are also preferred for field emission display and plasma display panel devices [31, 32]. Intense luminescence in the blue-red region has been reported in many cerate hosts such as Sr_2CeO_4, $SrCeO_3$ and $BaCeO_3$ [33-35]. Among the cerates, $BaCeO_3$ also has high thermal stability (m.p. =1743 °C) and diverse applications [36]. Lanthanides activated $BaCeO_3$ have high protonic and oxygen conductivity [37, 38] due to the extrinsic oxygen vacancies that are generated following the aliovalent substitution of dopants [39]. The ionic conductivity of orthorhombic $BaCeO_3$ doped with Y, Nd or

Gd has been addressed [34]. However, a detailed investigation of lanthanide luminescence in this host is yet to be made [34, 40]. The role of defects present in the microenvironment of the dopant that influences the luminescence properties is not reported yet. The radiation dosimetry properties of lanthanide doped $BaCeO_3$ has not been studied so far to the best of our knowledge. Among the lanthanides, Eu^{3+} acts as an excellent structural probe revealing any change in the site symmetry in the host lattice as the site symmetry strongly influences its absorption and emission properties. However, there is no report explaining the influence of the site symmetry on the luminescence properties of orange-red emitting Eu^{3+} in this host. A few researchers have synthesized $BaCeO_3$ through the SSR route calcining at very high temperatures (1300-1600 °C) and long durations (12-24 h) [36, 41, 42]. Synthesis of phosphors at elevated temperatures for long durations is often accompanied by poor crystallinity, high agglomerations, volatilization of structural components, nonuniformity and bigger microcrystalline particles that ultimately lead to inefficient luminescence. To circumvent these drawbacks, investigation of alternate synthesis routes involving lower calcination temperature and reduced calcination duration gains significance.

Extensive research has been carried out on lithium aluminium oxide host (Li_2O-Al_2O_3 system) doped with lanthanide and transition metal ions. Among various Li_2O-Al_2O_3 systems, $LiAlO_2$ and $LiAl_5O_8$ hosts have been extensively investigated due to their excellent thermochemical and irradiation stability. They have potential applications in molten carbonate fuel cells and nuclear reactors as radiation shield [43-45]. $LiAlO_2$ and $LiAl_5O_8$ hosts can be synthesized via the solution combustion synthesis (SCS) route with single phase purity [46]. The host $LiAlO_2$ exists in different allotropic forms (α, β and γ) depending upon the calcination temperature (600-1000 °C) in the post-combustion treatment. The most stable allotropic form of $LiAlO_2$ is its γ-phase that requires high calcination temperature and long duration whereas $LiAl_5O_8$ is formed in a single-step of the combustion process when ignited at 500-600 °C in a couple of minutes and does not need any post-combustion treatment. In addition, the $LiAl_5O_8$ (LAO) has a higher melting point (1915 °C) than that of γ-$LiAlO_2$ (1785 °C) [47]. Therefore, LAO has gained much attention owing to its ease of synthesis, high thermochemical stability and excellent optical properties [48, 49]. The importance of red-emitting Eu^{3+}, blue-emitting Ce^{3+} and green-emitting Tb^{3+} doped LAO phosphors in functional photonic devices have been well documented [50-52]. Also, intense green-emitting LAO: Mn^{2+} phosphor has been reported [53]. The narrow and deep red LAO: Cr^{3+} phosphor has shown promising characteristics of lasing material and photoluminescence thermometry [48, 54]. Similarly, LAO: Fe^{3+} phosphor has been found to be biocompatible and has broad emission in the deep red-NIR region suggesting its applications in the in-vivo temperature sensing and luminescence guided surgery [55, 56].

Interestingly, the pristine LAO samples are known to contain Cr^{3+} and Fe^{3+} as intrinsic impurities [57]. The origin of these impurities is from the aluminum precursor [58]. However, the quantification of these impurities and their effect on luminescence from this phosphor are yet to be reported. It may be noted that the synthesis via the SCS route proceeds without high calcination temperature to minimize the defect generation due to the possible volatilization of Li_2O [59]. An explicit study of the luminescence characteristics including the decay time of LAO phosphor synthesized through the SCS route, is yet to be reported. The uniqueness of the LAO host is that it belongs to a cubic lattice with an inverse spinel crystal system where the trivalent cation (Al^{3+}) is positioned two-fifths at the tetrahedral (Td) and three-fifths at octahedral (Oh) sites and all the monovalent cation (Li^+) resides at Oh site. However, there has been an ambiguity regarding the site occupancy of the dopants at the available Li^+-Oh, Al^{3+}-Oh and Al^{3+}-Td cationic sites in this host [60-62]. Hence, there is a necessity to probe the site speciation of the dopants in the inverse spinel LAO to understand their luminescence behavior.

In the present thesis, emerging phosphors based on alkaline earth borophosphate, barium cerate and lithium aluminate hosts have been synthesized and characterized for potential applications spanning from UV-B, UV-A, red, deep red-NIR LEDs to radiation dosimetry. Luminescence properties of UV-B emitting Gd^{3+}, UV-A to blue-emitting Eu^{2+} and Ce^{3+}, and orange-red emitting Eu^{3+} in $MBPO_5$ are studied in detail. Also, the optical properties of an intense red-emitting $BaCeO_3$: Eu^{3+}phosphor prepared through the facile SCS route is reported for red LEDs and w-LEDs applications. Single-step solution combustion synthesized $LiAl_5O_8$: $Eu^{3+}/Cr^{3+}/Fe^{3+}$ nano phosphors that have biomedical and LEDs applications are investigated systematically.

The present thesis comprises of seven chapters and the outline of each chapter is as follows:

Chapter 1 introduces the classification, principle and nature of luminescence. The optical properties of the 4*f*-4*f* and 4*f*-5*d* transitions of lanthanides, and the 3d-3d transitions of transition metal ions reported in the literature are surveyed. This chapter also explains the energy transfer mechanism in photoluminescence and thermally stimulated luminescence processes, the desired characteristics of a good host material and the problems that are yet to be addressed based on an exhaustive literature survey.

Chapter 2 reports a detailed description of the synthesis routes followed for the preparation of phosphors and the characterization techniques used for investigating the synthesized materials. $MBPO_5$: Ce and $MBPO_5$: Eu/Gd phosphors have been prepared through the SSR route while $BaCeO_3$: Eu and $LiAl_5O_8$: Eu/Cr/Fe phosphors have been prepared through the SCS route. The various characterization techniques used to investigate the structural and optical properties include X-ray diffraction (XRD), X-ray absorption spectroscopy (XAS), scanning electron microscopy

(SEM), diffuse reflectance spectroscopy (DRS), spectrophotometry photoluminescence (PL), PL lifetime, time-resolved emission spectroscopy (TRES), thermally stimulated luminescence spectroscopy (TSL) and positron annihilation lifetime spectroscopy (PALS).

Chapter 3 presents the characterization and optical properties of Ce^{3+} in $SrBPO_5$ host prepared through the SSR route in air atmosphere. The structure, morphology, band gap and luminescence properties of the phosphors are investigated. Ce^{3+} doped phosphors are of interest as they give UV-A (320-400 nm) emission whose utility is exploited in security industry, sensing fluorescent levels and scintillators. The chapter deals with the study on the nature of defects, site occupancy of Ce^{3+} and dosimetry properties of SBP: Ce phosphors using PALS, TRES and TSL, respectively. The mechanism of TSL glow curve of γ-irradiated SBP: Ce phosphor is established from its TSL emission spectrum. A comparative luminescence study of Ce^{3+} among $SrBPO_5$, $CaBPO_5$ and $BaBPO_5$ hosts is also presented.

Chapter 4 focuses on the optical properties of Gd^{3+} activated phosphors that give narrow UV-B emission at 313 nm. Here, the luminescence of Gd^{3+} in $SrBPO_5$ is optimized with respect to Gd-concentration. The effect of Gd codoping on the PL and TSL properties of $SrBPO_5$: Eu phosphors is explored. The basis for choosing Gd^{3+} as codopant is to explore the possibility of the energy transfer from Gd^{3+} to Eu^{3+}. In addition to the energy transfer, surprisingly, Gd^{3+} facilitates the valency conversion from Eu^{2+} to Eu^{3+} that has not been reported so far to the best of our knowledge and is addressed in the present work. A comparative study of the luminescence properties of Gd^{3+}, Eu^{3+} and Eu^{2+} in $MBPO_5$ hosts is investigated in order to arrive at a potential LED phosphor that gives maximum luminescence. The observed efficient energy transfer ($Gd^{3+} \rightarrow Eu^{3+}$) and a plausible mechanism for the valency conversion ($Eu^{2+} \rightarrow Eu^{3+}$) in the presence of Gd^{3+} are explained in detail. This study is relevant towards making efficient orange-red (Eu^{3+}), blue (Eu^{2+}) and UV-B (Gd^{3+}) LEDs. In addition to PL, TSL investigations on SBP: Eu/Gd are reported in detail for the first time. The mechanism of TSL and calculation of trap parameters in SBP: Eu, SBP: Gd and SBP: Eu, Gd phosphors are presented. The chapter highlights the favorable TSL characteristics of SBP: Eu, Gd phosphor that has shown a linear dose-response covering two orders of magnitude in the dose range of 100 mGy to 10Gy and useful trap parameters for radiation dosimetry. Moreover, the local coordination environment of Eu^{3+} has been investigated in $SrBPO_5$ host lattice using the XAS.

Chapter 5 presents the PL and TSL properties of perovskite structured $BaCeO_3$: Eu prepared through the SCS route. Influence of calcination temperature on (1000-1300 °C) on the morphology and particle size, the observed difference in PL spectra of $BaCeO_3$: Eu samples at 77 and 300 K, the variation of asymmetric ratio as a function of dopant concentration, excitation wavelength and temperature are explained in detail. The color purity of Eu^{3+} in $BaCeO_3$ has been optimized with respect to Eu-concentration and calcination temperature, resulting in an intense red emission with a higher color rendering index than the readily available red phosphors, suggesting it as a suitable candidate for red phosphor. TRES is recorded to find out the site occupancy of Eu^{3+} in the host. The presence of metal-oxygen vacancy defects is explored using PALS. TSL studies of γ-irradiated $BaCeO_3$: Eu exhibit multiple traps and a linear dose-response in the range of 0-1000 Gy suggesting it as a high-dose radiation dosimetry phosphor.

Chapter 6 presents the results obtained on the optical properties of Fe^{3+}, Cr^{3+} and Eu^{3+} in $LiAl_5O_8$ nano phosphors consisting of spherical particles with an average size of 60 nm. The samples are prepared at 600 °C forming single phased cubic lattice $LiAl_5O_8$. The study reports about the exact local coordination environment of dopants as determined by XAS studies for the first time. Eu^{3+} doped $LiAl_5O_8$ is also investigated as a structural probe and compared its emission characteristics with those of Cr^{3+} and Fe^{3+} as all the three dopants strongly emit in the red region. The influences of activator concentration and excitation wavelength for all the three ions doped in $LiAl_5O_8$ have been investigated. The site symmetry information is obtained by probing Eu^{3+} edge using XAS. The cause of the observed unusual broad emission of Fe^{3+} and the sharp emission of Cr^{3+} in the deep red-NIR region are also discussed in detail. The pristine $LiAl_5O_8$ contains Cr^{3+} and Fe^{3+} as trace impurities and an effort is made to estimate Fe-concentration in it. The activators in this host exhibit intense red-NIR emission with 100% color purity suggesting them as potential phosphors for SSL, laser and biomedical applications.

Chapter 7 concludes the major findings of the present work and scope for future work in the following directions.

- Quantification of Eu^{2+} to Eu^{3+} conversion
- Leaching studies with respect to different site occupancy
- Field study of $SrBPO_5$: Gd, Eu and $BaCeO_3$: Eu phosphors for radiation dosimetry applications
- Development of LEDs based on $SrBPO_5$, $BaCeO_3$ and $LiAl_5O_8$ phosphors for solid-state lighting and biomedical applications

References

1. Huang, X.; Guo, H.; Li, B. *J. Alloys Compd.* **2017,** 720, 29-38.
2. Nakamura, T.; Takeyama, T.; Takahashi, N.; Jagannathan, R.; Karthikeyani, A.; Smith, G.; Riedi, P. *J. Lumin.* **2003,** 102, 369-372.
3. Matthews, R.; Stoebe, T. *J. Phys. C: Solid State Phys.* **1982,** 15, (30), 6271.
4. Park, S.; Mho, S.; Kim, C.; Jeong, B.; Park, H. *Solid State Commun.* **1992,** 83, (1), 47-52.
5. Karthikeyani, A.; Jagannathan, R. *J. Lumin.* **2000,** 86, (1), 79-85.
6. Reis, S.; Karabulut, M.; Day, D. *J. Non-Cryst. Solids* **2001,** 292, 1, (3), 150-157.
7. Pei, Z.; Su, Q.; Zhang, J. *J. Alloys Compd.* **1993,** 198, 1, 2, 51-53.

8. Baginskiy, I.; Liu, R.; Wang, C.; Lin, R.; Yao, Y. *J. Electrochem. Soc.* **2011,** 158, (10), 118-121.
9. Kim, J. S.; Park, Y. H.; Kim, S. M.; Choi, J. C.; Park, H. L. *Solid State Commun.* **2005,** 133, (7), 445-448.
10. Ming, Z.; Qiao, J.; Molokeev, M. S.; Zhao, J.; Swart, H. C.; Xia, Z. *Inorg. Chem.* **2020,** *59, (2), 1405-1413*.
11. Das, A.; Saha, S.; Panigrahi, K.; Ghorai, U. K.; Chattopadhyay, K. K. *Microsc. Microanal.* **2019**, 25, (6), 1422-1430.
12. Shannon, R. D. *Acta Crystallogr. Sect. A* **1976,** 32, (5), 751-767.
13. Kharabe, V.; Oza, A. H.; Dhoble, S. *Optik* **2015,** 126, (23), 4544-4547.
14. Su, Q.; Liang, H.; Hu, T.; Tao, Y.; Liu, T. *J. Alloys Compd.* **2002,** 344, 1, (2), 132-136.
15. Zhou, X.; Yang, X.; Wang, Y.; Zhao, X.; Li, L.; Li, Q. *J. Alloys Compd.* **2014,** 608, 25-29.
16. Tāle, I.; Kūlis, P.; Kronghauz, V. *J. Lumin.* **1979,** 20, (4), 343-347.
17. Peng, M.; Pei, Z.; Hong, G.; Su, Q. *J. Mater. Chem.* **2003,** 13, (5), 1202-1205.
18. Dai, W.; Lei, Y.; Yu, T.; Peng, M.; Zhang, Q. *Mater. Res. Bull.* **2015,** 67, 176-184.
19. Peng, M.; Pei, Z.; Hong, G.; Su, Q. *Chem. Phys. Lett.* **2003,** 371, 1, (2), 1-6.
20. Madhusoodanan, U.; Jose, M.; Lakshmanan, A. *Radiat. Meas.* **1999,** 30, (1), 65-72.
21. Blasse, G.; Bril, A.; De Vries, J. *J. Inorg. Nucl. Chem.* **1969,** 31, (2), 568-570.
22. Sakasai, K.; Katagiri, M.; Toh, K.; Takahashi, H.; Nakazawa, M.; Kondo, Y. *Appl. Phys. A* **2002,** 74, (1), 1589-1591.
23. Liang, H.; Su, Q.; Lu, S.; Tao, Y.; Hu, T.; Liu, T. *Mater. Res. Bull.* **2002,** 37, (12), 1981-1989.
24. Sakasai, K.; Katagiri, M.; Matsubayashi, M.; Nakamura, T.; Kondo, Y. *Nucl. Instrum. Methods Phys. Res. Sec. A* **2004,** 529, (1-3), 378-383.
25. Taniguchi, N.; Kuroha, T.; Nishimura, C.; Iijima, K. *Solid State Ionics* **2005,** 176, 39, (40), 2979-2983.
26. Kulkarni, A.; Ciacchi, F.; Giddey, S.; Munnings, C.; Badwal, S.; Kimpton, J.; Fini, D. *Int. J. Hydrogen Energy* **2012,** 37, (24), 19092-19102.
27. Tao, Z.; Yan, L.; Qiao, J.; Wang, B.; Zhang, L.; Zhang, J. *Prog. Mater. Sci.* **2015,** 74, 1-50.

28. Yin, J.; Wang, X.; Xu, J.; Wang, H.; Zhang, F.; Ma, G. *Solid State Ionics* **2011,** 185, (1), 6-10.
29. Li, J.; Luo, J.-L.; Chuang, K. T.; Sanger, A. R. *Electrochim. Acta* **2008,** 53, (10), 3701-3707.
30. Fu, X.-Z.; Luo, J.-L.; Sanger, A. R.; Luo, N.; Chuang, K. T. *J. Power Sources* **2010,** 195, (9), 2659-2663.
31. Stranks, S. D.; Snaith, H. J. *Nat. Nanotechnol.* **2015,** 10, (5), 391.
32. Gupta, S. K.; Pathak, N.; Kadam, R. *J. Lumin.* **2016,** 169, 106-114.
33. Van Pieterson, L.; Soverna, S.; Meijerink, A. *J. Electrochem. Soc.* **2000,** 147, (12), 4688-4691.
34. Melekh, B.-T.; Egorov, V.; Baikov, Y. M.; Kartenko, N.; Filin, Y. N.; Kompan, M.; Novak, I.; Venus, G.; Kulik, V. *Solid State Ionics* **1997,** 97, 1, (4), 465-470.
35. Zhang, C.; Jiang, W.; Yang, X.; Han, Q.; Hao, Q.; Wang, X. *J. Alloys Compd.* **2009,** 474, 1, (2), 287-291.
36. Yamanaka, S.; Fujikane, M.; Hamaguchi, T.; Muta, H.; Oyama, T.; Matsuda, T.; Kobayashi, S.-i.; Kurosaki, K. *J. Alloys Compd.* **2003,** 359, 1, (2), 109-113.
37. Katahira, K.; Kohchi, Y.; Shimura, T.; Iwahara, H. *Solid State Ionics* **2000,** 138, 1, (2), 91-98.
38. Medvedev, D.; Gorbova, E.; Demin, A.; Tsiakaras, P. *Int. J. Hydrogen Energy* **2014,** 39, (36), 21547-21552.
39. Knight, K. *Solid State Commun.* **1999,** 112, (2), 73-78.
40. Kompan, M.; Baikov, Y. M.; Melekh, B.-T.; Volchek, B. *Solid State Ionics* **2003,** 162, 1-5.
41. Giannici, F.; Longo, A.; Balerna, A.; Martorana, A. *Chem. Mater.* **2009,** 21, (4), 597-603.
42. Gorbova, E.; Maragou, V.; Medvedev, D.; Demin, A.; Tsiakaras, P. *J. Power Sources* **2008,** 181, (2), 207-213.
43. Jimenez-Becerril, J.; Bosch, P.; Bulbulian, S. *J. Nucl. Mater.* **1991,** 185, (3), 304-307.
44. Terada, S.; Nagashima, I.; Higaki, K.; Ito, Y. *J. Power Sources* **1998,** 75, (2), 223-229.
45. Kawamura, Y.; Nishikawa, M.; Tanaka, K.; Matsumoto, H. *J. Nucl. Sci. Technol.* **1992,** 29, (5), 436-444.

46. Suriyamurthy, N.; Panigrahi, B.; Natarajan, A. *Mater. Sci. Eng. A* **2005,** 403, 1, (2), 182-185.
47. Kale, M.; Joshi, C.; Moharil, S. *Int. J. Self-Propag. High-Temp Synth.* **2012,** 21, (1), 19-24.
48. Singh, V.; Chakradhar, R.; Rao, J.; Kwak, H.-Y. *Solid State Sci.* **2009,** 11, (4), 870-874.
49. de Sousa, O. M. *Comput. Theor. Chem.* **2018,** 1123, 96-101.
50. Silva, A. J.; Nascimento, P. A.; Andrade, A. B.; Sampaio, D. V.; Moulton, B. J.; Silva, R. S.; Rezende, M. V. d. S. *J. Lumin.* **2018,** 199, 298-301.
51. Pitale, S. S.; Kumar, V.; Nagpure, I.; Ntwaeaborwa, O.; Swart, H. *Curr. Appl. Phys.* **2011,** 11, (3), 341-345.
52. Mohapatra, M.; Seshadri, M.; Naik, Y.; Meena, G.; Kadam, R.; Singh, V. *J. Mater. Sci.: Mater. Electron.* **2018,** 29, (9), 7778-7784.
53. Singh, V.; Chakradhar, R.; Rao, J.; Kim, D.-K. *Mater. Chem. Phys.* **2008,** 110, (1), 43-51.
54. Li, X.; Jiang, G.; Zhou, S.; Wei, X.; Chen, Y.; Duan, C. K.; Yin, M. *Sens. Actuators B: Chem.* **2014,** 202, 1065-1069.
55. Kniec, K.; Tikhomirov, M.; Pozniak, B.; Ledwa, K.; Marciniak, L. J. *Nanomater.* **2020,** 10, (2), 189-200.
56. Shu, W.; Qiang, R.; Xiao, S.; Yang, X.; Ding, J. *J. Alloys Compd.* **2011,** 509, (9), 3886-3888.
57. Li, Z.; Zhang, Y.; Wu, X.; Wu, X.; Maudgal, R.; Zhang, H.; Han, G. *Adv. Sci.* **2015,** 2, 1500001-1500006.
58. Hashimoto, S.; Hattori, K.; Inoue, K.; Nakahashi, A.; Honda, S.; Iwamoto, Y. *Mater. Res. Bull.* **2009,** 44, (1), 70-73.
59. Singh, V.; Rao, T. G. *J. Solid State Chem.* **2008,** 181, (6), 1387-1392.
60. Bhargava, S. *J. Phys. C: Solid State Phys.* **1986,** 19, (35), 7045-7070.
61. Kobayashi, R.; Tamura, H.; Kamada, Y.; Kakihana, M.; Matsushima, Y. *ECS Trans.* **2018,** 88, (1), 225-236.
62. Teixeira, V.; Silva, A.; Manali, I.; Gallo, T.; Galante, D.; Ferreira, N.; Andrade, A.; Rezende, M. D. S. *Opt. Mater.* **2019,** 94, 160-165.

Publications in Refereed Journals:

a. Published

1. Probing the optical properties and luminescence mechanism of a UV-emitting $SrBPO_5$: Ce^{3+} phosphor. **Sitakanta Panda**, P. Vinodkumar, U. Madhusoodanan, B.S. Panigrahi. *Luminecence*, **2019**, 1-8.

2. Synthesis, characterization and optical properties of $BaCeO_3$: Eu – An efficient red phosphor for w-LED applications. **Sitakanta Panda**, P. Vinodkumara, U. Madhusoodanan, Renjith Ramachandran, V. Sridharan, B.S. Panigrahi. *J. Lumin.* **2019**, 214, 116538-116545.

3. Effect of gadolinium on europium luminescence and its in-situ valence conversion in $SrBPO_5$ host. **Sitakanta Panda**, P. Vinodkumar, Satendra Kumar, B.S. Panigrahi. *J. Lumin.* **2020**, 225, 117349-117357.

b. Under Preparation:

1. Probing the Site Occupancy of Dopants in Deep Red-NIR Emitting $LiAl_5O_8$: Eu^{3+}, Cr^{3+} and Fe^{3+} Nano Phosphors through Photoluminescence and X-ray Absorption Spectroscopy Studies. **Sitakanta Panda**, P. Vinodkumar, Madhusmita Sahoo, U. Madhusoodanan, B.S Panigrahi. (Communicated).

2. A comparative study of Ce^{3+} luminescence in $CaBPO_5$, $SrBPO_5$ and $BaBPO_5$ hosts. **Sitakanta Panda**, P. Vinodkumar, U. Madhusoodanan, B.S Panigrahi.

3. A comparative study of Gd^{3+}, Eu^{3+} and Eu^{2+} luminescence in $MBPO_5$ (M: Ca, Sr, Ba) hosts. **Sitakanta Panda**, P. Vinodkumar, U. Madhusoodanan, B.S Panigrahi.

Other Publications:

a. Published

1. Thermoluminescence properties of strontium borophosphate doped with praseodymium and enhancement with uranyl codoping. P. Vinodkumar, **Sitakanta Panda**, U. Madhusoodanan, B.S Panigrahi. *Radiat. Phys. Chem.* **2020**, 174, 108914-108920.

2. Structural and optical properties of Ce-doped strontium borophosphate glasses. P Ramakrishna, **Sitakanta Panda**, P Vinod Kumar, D K Mohapatra, Hrudananda Jena, BS Panigrahi, ***Indian J. Phys.*** **(Accepted)**.

b. Conference Presentations

1. Photoluminescence study of Europium and Samarium doped $SrBPO_5$. **Sitakanta Panda,** U. Madhusoodanan, Annapurna Rout, B.S Panigrahi; National conference on Luminescence and its Application (NCLA), CSIR-IICT, Hyderabad, India, 2017 (January 9-11): Poster Presentation.

2. $SrBPO_5$: Eu, Gd as a new TL material for radiation dosimetry. **Sitakanta Panda,** P. Vinodkumar, U. Madhusoodanan, B.S Panigrahi; National Conference on Thermophysical Properties (NCTP), IGCAR, Kalpakkam, India, 2017 (November 6-8): Oral Presentation (**Young Scientist Award for Outstanding Presentation**).

3. Optical properties of $SrBPO_5$: Ln^{3+} [Dy^{3+}/Sm^{3+}/Gd^{3+}] nano phosphors. **Sitakanta Panda,** P. Vinodkumar, U. Madhusoodanan, B.S Panigrahi; National conference on Luminescence and Application (NCLA), CSIR-NIIST, Trivandrum, India, 2018 (February 14-16): Poster Presentation (**Best Poster Presentation**).

4. Luminescence properties of $BaCeO_3$: Eu^{3+} phosphors. **Sitakanta Panda,** P. Vinodkumar, U. Madhusoodanan, B.S Panigrahi; International Conference on Luminescence and its Applications (ICLA), PRS University, Raipur, India, 2019 (January 7-10): Oral Presentation.

5. Lanthanide-activated $CaBPO_5$ phosphors for phototherapy and LEDs applications. **Sitakanta Panda,** P. Vinodkumar, P. Ramakrishna, U. Madhusoodanan, B.S Panigrahi; National Conference on Advanced Materials & Environmental Science, (NCAMES), Kalinga University, Naya Raipur, India, 2019 (October 14-15): Oral Presentation.

Signature of Student: Sitakanta Panda.

Date: 02.09.2020

Doctoral Committee:

S. No.	Name	Designation	Signature	Date
1.	Dr. K. Ananthasivan	Chairman		02.09.2020
2.	Dr. B. S. Panigrahi	Guide & Convener	Panigrahi	02.09.2020
3.	Dr. T. R. Ravindran	Member	Ravindran	2.9.2020
4.	Dr. K. I. Gnanasekar	Member	Gnanasekar	2/9/2020

N. Sivaraman
14.9.2020

Prof: N. SIVARAMAN
Dean-Academic
Chemical Sciences
HBNI-IGCAR
Kalpakkam-603102

Received: 19 December 2018 | Revised: 13 May 2019 | Accepted: 1 July 2019
DOI: 10.1002/bio.3687

RESEARCH ARTICLE

WILEY LUMINESCENCE
The Journal of Biological and Chemical Luminescence

Probing the optical properties and luminescence mechanism of a UV-emitting $SrBPO_5:Ce^{3+}$ phosphor

Sitakanta Panda[1] | **P. Vinodkumar**[1] | **U. Madhusoodanan**[2] | **B.S. Panigrahi**[1]

[1] Health Safety & Environment Group, Indira Gandhi Centre for Atomic Research, Homi Bhabha National Institute, Kalpakkam 603102, Tamil Nadu, India

[2] Health Safety & Environment Group, Indira Gandhi Centre for Atomic Research, Kalpakkam 603102, Tamil Nadu, India

Correspondence
B. S. Panigrahi, Health Safety & Environment Group, Indira Gandhi Centre for Atomic Research, Homi Bhabha National Institute, Kalpakkam-603102, Tamil Nadu, India
Email: bsp@igcar.gov.in

Abstract

Ce-doped (1×10^{-5} to 3.0 mol%) $SrBPO_5$ phosphors were synthesized using a conventional solid-state reaction route at 1273 K in an air atmosphere. Phase and morphology of the samples were studied from powder X-ray diffraction (XRD) patterns and scanning electron microscope (SEM) micrographs, respectively. The band gap energies of the pure and Ce-doped $SrBPO_5$ phosphors were calculated from the recorded diffuse reflectance spectra. Photoluminescence (PL) and Ce^{3+} lifetime were recorded at 300 and 77 K. Photoluminescence lifetime measurements revealed two-lifetime values for Ce^{3+} at both 300 K (17 and 36 nsec) and 77 K (12 and 30 nsec), suggesting the presence of two different environments around Ce^{3+}. Time-resolved emission spectroscopy (TRES) studies confirmed the presence of Ce^{3+} in two different environments. In addition, $SrBPO_5$:Ce exhibited intense UV emission, signifying its possible use as an efficient sensitizer for solid-state lighting applications. The effect of γ-irradiation on PL was also determined. Thermally stimulated luminescence (TSL) glow curves of the γ-irradiated phosphor, along with trap parameters, dose–response, and the possible TSL mechanism were also investigated. Positron annihilation lifetime spectroscopy was carried out to probe defects present in undoped and Ce-doped $SrBPO_5$.

KEYWORDS

band gap, Ce-doped strontium borophosphate, photoluminescence, positron annihilation, thermally stimulated luminescence, trap parameters

1 | INTRODUCTION

Rare earth-doped solid-state phosphors have been given much attention due to their practical applications in various fields such as the lighting industry, biomedical fields for imaging, and the nuclear industry for scintillation and dosimetry, etc.[1–3] Ce^{3+} with electronic configuration $4f^1 5d^0 6s^0$ displays unique optical properties as an activator.[4,5] Ce^{3+} emits in the UV–visible region, and the position of its lowest 5d band strongly depends on many factors such as host lattices, synthesis route, calcination temperature, and size of phosphors particles.[6–10] Unlike trivalent lanthanide ions, Ce^{3+} 4f→5d transitions are parity allowed and show intense, broad luminescence that often sensitizes other Ln^{3+} ions, enhancing their luminescence efficiency. Since the last decade, researchers have tried to synthesize an efficient green phosphor for multiple applications such as green lasers, silicon-based detectors, solar cells, fluorescence lamps, cathode ray tubes, and plasma display panels.[5,11–14] In particular, the efficiency of green emitting Tb^{3+}-doped phosphors can be remarkably enhanced by co-doping with Ce^{3+} in suitable hosts due to efficient energy transfer between Ce^{3+} and Tb^{3+} and leading to tricolour lamp

---

Abbreviations used: CB, conduction band; DRS, diffuse reflectance spectroscopy; $e^-–h^+$, electron–hole; E_g, band gap energy; E_r, recombination energy; GC, glow curve; K–M, Kubelka–Munk; PALS, positron annihilation lifetime spectroscopy; PL, photoluminescence; SEM, scanning electron microscopy; TRES, time-resolved emission spectroscopy; TSL, thermally stimulated luminescence; VB, valence band; w-LED, white light-emitting diode; XRD, X-ray diffraction; Z_{eff}, effective nuclear charge.

Journal of Luminescence 214 (2019) 116538

Contents lists available at ScienceDirect

Journal of Luminescence

journal homepage: www.elsevier.com/locate/jlumin

Synthesis, characterization and optical properties of $BaCeO_3$: Eu - An efficient red phosphor for w-LED applications

Sitakanta Panda[a], P. Vinodkumar[a], U. Madhusoodanan[b], Renjith Ramachandran[c], V. Sridharan[c], B.S. Panigrahi[a,b,*]

[a] Health Safety & Environment Group, Indira Gandhi Centre for Atomic Research, Homi Bhabha National Institute, Kalpakkam, 603102, Tamil Nadu, India
[b] Health Safety & Environment Group, Indira Gandhi Centre for Atomic Research, Kalpakkam, 603102, Tamil Nadu, India
[c] Materials Science Group, Indira Gandhi Centre for Atomic Research, Homi Bhabha National Institute, Kalpakkam, 603102, Tamil Nadu, India

ARTICLE INFO

Keywords:
Barium cerate
Europium
Asymmetry ratio
Time-resolved emission
Thermally stimulated luminescence
Positron annihilation

ABSTRACT

Single phase perovskite structured barium cerate ($BaCeO_3$) doped with europium phosphors were prepared through solution combustion route followed by calcination in air atmosphere. The morphology of the phosphor was analyzed from scanning electron micrograph. Diffuse reflectance spectra were recorded to determine the band gap energy of both undoped and Eu-doped $BaCeO_3$ using the Kubelka-Munk method. Eu^{3+} exhibited intense red emission with high color purity and varied with Eu-concentration. The asymmetry ratio of Eu^{3+} varied for different excitation wavelength and Eu-concentration. The environment around Eu^{3+} was found to be more symmetric at 77 K unlike at 300 K. PL lifetime decay measurements of Eu^{3+} luminescence revealed two different sites for it in this host. Time-resolved emission spectroscopy confirmed the presence of two different sites for Eu^{3+} occupancy, exhibiting two different emission profiles. Thermally stimulated luminescence indicated multiple trap sites, and the intensity was linear with γ-dose in the range of 0–1000 Gy suggesting the possibility of using this material as a dosimetry phosphor. Positron annihilation lifetime spectroscopic studies indicated the presence of oxygen and barium vacancy-related defects.

1. Introduction

Perovskite materials have been gaining attention due to their intriguing properties from both science and technological point of view. They are known to have potential applications as hydrogen gas sensor, catalyst electrodes in a solid oxide fuel cell, hydrogen permeable membranes, reactors for ammonia synthesis, desulfurization of natural fuel, decomposer of alkane to alkene and steam electrolysis [1–7]. The perovskite hosts being sufficiently conductive to release accumulated charges on the surface of the phosphors can be used for field emission display (FED) and plasma display panel (PDP) devices [8,9]. Among several perovskites, $BaCeO_3$ has manifold applications due to its high thermal stability (m.p. = 1743 °C) [10]. This host doped with lanthanides acts as a high protonic and oxygen conductor [11–16]. Doping of rare earth (RE) ions introduce extrinsic oxygen vacancy in $BaCeO_3$ host due to aliovalent substitution leading to improved conductivity [17]. The energy states of RE ions in the host lattice are significantly influenced by the crystal field, local symmetry, covalency, and positioning in the host, etc. Information regarding the local symmetry can easily be obtained by doping Eu^{3+} ions that act as an excellent probe because the site symmetry strongly influences its absorption and emission spectra. The symmetry and crystal structure of $BaCeO_3$ changes with different dopant at different concentration. For instance, the orthorhombicity of $BaCeO_3$ is kept for Gd, Nd, and Y at 20%, 10%, and 5% doping, respectively [18]. The ionic conductivity of $BaCeO_3$ doped with different lanthanide ions has been widely studied, whereas the lanthanide luminescence in this host is sparsely investigated. Ce^{3+} and Eu^{3+} luminescence though reported from this host [18,19], a detail discussion about the luminescence spectrum is yet to be made. Luminescence efficiency of phosphors is greatly influenced by many factors such as size, shape, and homogeneity, etc. Therefore, the method of synthesis plays an important role in tuning luminescence efficiency. Conventional solid-state synthesis typically encounters elevated calcination temperature, poor homogeneity, microcrystalline sized particles, and agglomeration [20]. So, the wet chemical routes like solution combustion synthesis are preferred due to its lower synthesis temperature and better homogeneity leading to efficient luminescence.

In this study, we have synthesized Eu-doped barium cerate through

---

[*] Corresponding author. Health Safety & Environment Group, Indira Gandhi Centre for Atomic Research, Homi Bhabha National Institute, Kalpakkam, 603102, Tamil Nadu, India.

E-mail address: bsp@igcar.gov.in (B.S. Panigrahi).

https://doi.org/10.1016/j.jlumin.2019.116538
Received 1 March 2019; Received in revised form 4 June 2019; Accepted 4 June 2019

Journal of Luminescence 225 (2020) 117349

Contents lists available at ScienceDirect

Journal of Luminescence

journal homepage: http://www.elsevier.com/locate/jlumin

Effect of gadolinium on europium luminescence and its in-situ valence conversion in $SrBPO_5$ host

Sitakanta Panda [a,b], P. Vinodkumar [a,b], Satendra Kumar [c], U. Madhusoodanan [b], N. Suriyamurthy [d], B.S. Panigrahi [a,b,*]

[a] *Homi Bhabha National Institute, Mumbai, India*
[b] *Safety Quality & Resource Management Group, Indira Gandhi Centre for Atomic Research, Kalpakkam, 603102, Tamil Nadu, India*
[c] *Material Chemistry and Metal Fuel Cycle Group, Indira Gandhi Centre for Atomic Research, Kalpakkam, 603102, Tamil Nadu, India*
[d] *Health Physics Unit, Prototype Fast Breeder Reactor, BHAVINI, Kalpakkam, 603102, Tamil Nadu, India*

ARTICLE INFO

Keywords:
Strontium borophosphate
Europium
Gadolinium
Energy transfer
Valence conversion
TSL

ABSTRACT

Gadolinium/europium-activated strontium borophosphate ($SrBPO_5$) phosphors were synthesized through solid-state reaction route in air atmosphere. Morphology and particle size were analyzed using scanning electron microscopy (SEM). Both europium and gadolinium were observed to emit strongly in this host. Interestingly, photoluminescence (PL) of both Eu^{2+} and Eu^{3+} was also observed. In the co-activated $SrBPO_5$: Eu, Gd phosphors, the PL intensity of Eu^{3+} was enhanced significantly with simultaneous quenching of Eu^{2+} luminescence. The excitation and emission profiles of europium indicated the valence conversion (VC) of Eu^{2+} to Eu^{3+} in the presence of gadolinium. In addition to the VC, the luminescence of Eu^{3+} was also enhanced due to the energy transfer (ET) from Gd^{3+} to Eu^{3+}. The ET was maximum for $SrBPO_5$: $Eu_{0.01}$, $Gd_{0.075}$ phosphor at a critical distance of 2.76 Å. The co-activated phosphors exhibited a high color rendering index for Eu^{3+}, suggesting it to be an efficient orange-red phosphor. PL lifetime decay studies suggested a single site occupancy for Eu^{2+} though the number of sites for Gd^{3+} and Eu^{3+} varied depending on their concentrations. The time-resolved emission spectroscopy (TRES) revealed different emission profiles for Eu^{3+} in varying time domains corroborating its different site occupancies. Strong thermoluminescence (TSL) was observed from these phosphors, though Eu^{2+} and Eu^{3+} PL were quenched following γ-irradiation. The calculated trap parameters and dose-response of γ-irradiated Eu, Gd-coactivated phosphor, suggested it to be a good thermoluminescent phosphor.

1. Introduction

Lanthanides (Ln) luminescence is widely studied due to their interesting spectral characteristics and significant applications. Ln ions show narrow emission, long lifetime, large Stokes shift and low photobleaching effect. The emission peak positions of these ions (except Ce^{3+} and Eu^{2+}) do not change significantly irrespective of different hosts due to the shielding effect. Divalent europium is of significant importance as it was reported to emit in blue, green or red regions depending on the hosts due to its 4f-5d transitions. Anthony et al. reported the tunability Eu^{2+} emission by changing the coordination number (CN) at the activator site [1]. In some hosts, Eu^{2+} with CN > 2 displayed emission from UV to red region, suggesting a large Stokes shift. The red emission from Eu^{2+} with CN = 8, 9 was reported in $LiBa_2B_5O_{10}$ and $Ba_2MgB_2O_6$ hosts, respectively [2,3]. However, Blasse and Nakamura et al. observed intense blue emission from Eu^{2+} with higher CN in $MBPO_5$ (M: Ca, Sr, Ba) suggesting these phosphors as better candidates for X-ray imaging [4–6]. Karthikeyani et al. mentioned the more intense blue emission from Eu^{2+} in non-hygroscopic $SrBPO_5$ host than in hygroscopic BaFBr with UV and X-ray excitations [7]. Based on this, they suggested $SrBPO_5$: Eu^{2+} to be a better phosphor than BaFBr: Eu^{2+} for X-ray imaging. Sakasai et al. also suggested $SrBPO_5$: Eu^{2+} as an excellent neutron imaging phosphor [8].

The choice of a suitable host plays an important role, considering the wide applications of solid-state lanthanide luminescence. The phosphate-based phosphors are good luminescent materials, but the hygroscopic nature is the reason for their poor chemical stability [9]. Ln doped borate hosts, though exhibit strong luminescence, have a low melting point indicating low thermal stability [10]. Borophosphate hosts have been of significant interest for their non-hygroscopicity,

---

* Corresponding author. Homi Bhabha National Institute, Mumbai, India.
E-mail address: bsp@igcar.gov.in (B.S. Panigrahi).

https://doi.org/10.1016/j.jlumin.2020.117349
Received 27 January 2020; Received in revised form 20 April 2020; Accepted 5 May 2020

KALINGA
UNIVERSITY

National Conference on

Advanced Materials & Environmental Sciences

(NCAMES 2019), October 14-15, 2019
Organized by
Department of Physics, Kalinga University, Naya, Raipur (C.G.) - 492101
Sponsored By
Council of Scientific and Industrial Research (CSIR), New Delhi

Certificate of Participation

This is to certify that Prof./Dr./Mr./Ms. Sitakanta Panda *from* Homi Bhaba National Institute, Kalpakkam *has participated in the National Conference on Advanced Materials and Environmental Sciences - 2019 (NCAMES - 2019) held at Department of Physics, Kalinga University Raipur, during 14-15 October 2019 and presented an Invited talk/Contributory talk/Poster Presentation entitled* Lanthanide-activated $CaBPO_5$ phosphors for phototherapy and LEDs applications.

Dr. R. P. Patel
Convener

Dr. A. K. Diwakar
Convener

Aloke Verma
Organizing Secretary

Anita Verma
Joint Secretary

Dr. Sandeep Gandhi
Registrar

International Conference on Luminescence and its Applications

(ICLA-2019), January 7-10, 2019

Organized by

School of Studies in Physics and Astrophysics, Pt. Ravishankar Shukla University
Raipur-492010, Chhattisgarh, INDIA
& Luminescence Society of India (LSI) Regd. No. Guj. / 1156 Baroda, September, 1995

Co-Organizers

Department of Physics, NIT, Raipur
Department of Physics, Govt. N S College, Raipur

CERTIFICATE

This is to certify that Prof./Dr/[✓ Mr.]/Ms SITAKANTA PANDA

is a registered participant of ICLA-2019. He/ ~~She~~ presented an [✓ Oral] / ~~Poster~~ presentation

entitled Luminescence properties of $BaCeO_3 : Eu^{3+}$ phosphor.

Prof. N. Brahme
Convener, ICLA-2019

Prof. D. P. Bisen
Secretary, LSI

Dr. K. V. R. Murthy
President, LSI , Chair, ICLA-2019

National Conference on Luminescence and Applications [NCLA-17]

9-11th January, 2017

Organized by

CSIR- Indian Institute of Chemical Technology [IICT] Hyderabad

Mahatma Gandhi National Institute of Research & Social Action (MGNIRSA), Hyderabad

Luminescence Society of India, Regd. No. Guj. / 1156 Baroda

Certificate

This is to certify that ~~Prof.~~/~~Dr~~/Mr./~~Ms~~ SITAKANTA PANDA

is a registered participant of NCLA-2017 He/ She presented an Invited Talk/ Invited Technical Talk entitled Photoluminescence study of Europium and Samarium doped $SrBPO_5$.

11/1/17

Dr. V Jayathirtha Rao
Chairmen,
NCLA-2017

Hyderabad, 11-1-2017

Dr. K. V. R. Murthy
President, LSI,
Chair, NCLA-2017

THERMOPHYSICAL SOCIETY OF INDIA (TPSI)

NCTP -2017

(November 06-08, 2017)

TPSI Founder President's Award

This is to certify that S I T A KANTA PANDA, H.B.N.I, Kalpakkam (TN) participated in 9th National Conference on Thermophysical Properties, NCTP-2017, held from Nov. 06-08, 2017 in the Indira Gandhi Centre for Atomic Research, Kalpakkam, Tamil Nadu.

His/Her Oral presentation entitled Luminescence studies in Lithium Fluoride

is hereby awarded cash of Rs. 7000/- as Young Scientist Award for Outstanding Presentation.

N.V. Chandra Sh
(N. V. Chandra Shekar)
Convener, NCTP-2017

Kanan bala
(Kananbala Sharma)
Secretary, TPSI

(N.S. Saxena)
President, TPSI

9th National Conference on Thermophysical Properties
(NCTP - 2017)
Participation Certificate

This is to certify that Prof./Dr./Mr./Ms. Sitakanta Panda

has participated and presented Oral/Poster paper titled $SrBPO_5$: Eu, Gd as a new TL material for radiation dosimetry

at 9th National Conference on Thermophysical Properties CNCTP-2017) held during November 6-8, 2017 at Indira Gandhi Centre for Atomic Research, Kalpakkam, Tamilnadu.

G. Amarendra
(G. Amarendra)
Chairperson

N.V. Chandra Shekar
(N.V. Chandra Shekar)
Convener

Awadhesh Mani
(Awadhesh Mani)
Organizing Secretary

National Conference on Luminescence and its Applications
NCLA-2018

Organized by

CSIR - National Institute of Interdisciplinary Science and Technology, Thiruvananthapuram &
Luminescence Society of India (LSI)

BEST POSTER AWARD

This is to certify that Dr. /Mr. /Ms. /Mrs. SITAKANTA PANDA

affiliated to IGCAR, Tamil Nadu

has been awarded the ~~First~~ / ~~Second~~ / Third position for his /her poster entitled "Optical Properties of $SrBPO_5:Ln^{3+}(Dy^{3+}/Sm^{3+}/Gd^{3+})$ Nanophosphor." *in the National Conference on Luminescence and its Applications, NCLA-2018 held at CSIR-National Institute of Interdisciplinary Science and Technology, Thiruvananthapuram during 14-16 February, 2018.*

Dr. P. Prabhakar Rao
CSIR-NIIST, Chairman, NCLA-2018

Dr. K. V. R. Murthy
President, LSI, Patron, NCLA-2018

NATIONAL CONFERENCE ON LUMINESCENCE AND APPLICATIONS

NCLA-18, 14-16th FEBRUARY 2018

ORGANIZED BY

CSIR- NATIONAL INSTITUTE FOR INTERDISCIPLINARY SCIENCE AND TECHNOLOGY, TRIVANDRUM

AND

LUMINESCENCE SOCIETY OF INDIA

(Regd. No. Guj./1156 Baroda, September, 1995)

CERTIFICATE

This is to certify that

Prof./Dr./Mr./Ms. SITAKANTA PANDA is a registered participant of NCLA-2018 and has given an oral/[✓ poster] presentation on the topic entitled Optical Properties of $SrBPO_5: Ln^{3+}$ [$Dy^{3+}/Sm^{3+}/Gd^{3+}$] Nanophosphors

Dr. P. Prabhakara Rao
Chairman, NCLA-2018

Dr. K. V. R. Murthy
President, LSI, Chair, NCLA-2018

Trivandrum, 16 February 2018

Thesis Highlight

Name of the Student: Sitakanta Panda
Name of CI: Indira Gandhi Centre for Atomic Research **Enrolment No.:** CHEM 02 2015 04 006
Thesis Title: Lanthanide and transition metal ions activated advanced phosphors for optical and radiation dosimetry applications
Discipline: Chemical Sciences
Sub-Area of Discipline: Spectroscopy, Material Science, Luminescent Materials, Radiation Dosimetry
Date of viva voce: 07/05/2021

* UV-Blue emitting stillwellite-structured $MBPO_5$: Ce^{3+} (M=Ca, Sr, Ba) phosphors are synthesized. Time-resolved emission spectroscopy (TRES) reveals the Ce^{3+} occupancy in two sites with short lifetimes (<50 ns). The UV-Blue emitting $SrBPO_5$: Ce^{3+} phosphor may be exploited in LEDs devices, fluorescent sensing levels and scintillators. (Fig. 1)

* Synthesized $MBPO_5$: Gd^{3+} phosphor exhibits intense and narrow UV-*B* emission (313 nm) suggesting its application in phototherapy. Gd^{3+} sensitizes Eu^{3+} luminescence in $MBPO_5$: Eu, Gd via energy transfer (ET), $Gd^{3+}\rightarrow Eu^{3+}$ (Fig. 2, left). In addition to ET, for the first time, in-situ valency conversion (VC) of $Eu^{2+}\rightarrow Eu^{3+}$ is explored in air-fired $MBPO_5$: Eu, Gd (Fig. 2, right). The ET and VC processes significantly enhance Eu^{3+} luminescence with ultra-high color purity (94-97%) (Fig. 3, left) in $MBPO_5$: Eu, Gd phosphors indicating candidacy for orange-red LEDs.

Furthermore, γ-irradiated SBP: Eu, Gd phosphor shows favorable TSL properties with linear dose-response (100 mGy-10Gy) highlighting its potency for radiation dosimetry field (Fig. 3, right).

* Solution combustion synthesized perovskite-structured $BaCeO_3$: Eu^{3+} (9 mol%) emits intense red emission with 100% color purity making it as a potential candidate for red LEDs and W-LEDs devices. Notably, $BaCeO_3$: Eu^{3+} displays predominantly red emission when recorded at room temperature whereas predominant orange emission at 77 K (Fig. 4, left) suggesting its utility in cryogenic preservation of biological samples and is the need of the hour. PL lifetime and TRES analyses confirm two site occupancies for Eu^{3+} in $BaCeO_3$. PALS studies reveal oxygen vacancy and barium-oxygen vacancy complex in this host.

TSL of γ-irradiated $BaCeO_3$: Eu exhibit multiple traps and a linear dose-response in the range of 0-1000 Gy suggesting it as a high-energy radiation dosimetry phosphor (Fig. 4, right).

* Single-step and single-phase cubic (Fig. 5, left) $LiAl_5O_8$: $Fe^{3+}/Cr^{3+}/Eu^{3+}$ nano phosphors (60 nm) are fabricated via combustion synthesis. X-ray absorption spectroscopy (XAS) investigations confirms the presence of Eu^{3+} at Li^+-O_h site only whereas Fe^{3+} at Li^+-O_h, Al^{3+}-O_h and Al^{3+}-T_d sites with reduced coordination number (CN). The reduction in CN indicates a lowered symmetry, oxygen vacancy and intense emission. Fe^{3+} exhibits unusual broad (620-830 nm) emission (Fig. 5, right) which is established by TRES and XAS studies. Cr^{3+} (100 ppm) displays narrow (fwhm=2.22 nm) emission at 713 nm (Fig. 6, left). PL of $LiAl_5O_8$: (a) Eu (0.5 mol%) (b) Cr (100 ppm) and (c) Fe (500 ppm) exhibits intense deep red-NIR emission with 100% color purity (Fig. 6, right) and improved color coordinates than that of the NTSC recommendations suggesting them as potential candidates for SSL, laser and biomedical applications.

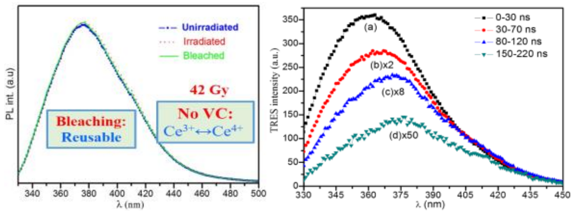

Fig. 1 PL emission spectra of unirradiated, γ-irradiated and bleached $SrBPO_5$: Ce^{3+} phosphor (Left), and TRES of Ce^{3+} (right).

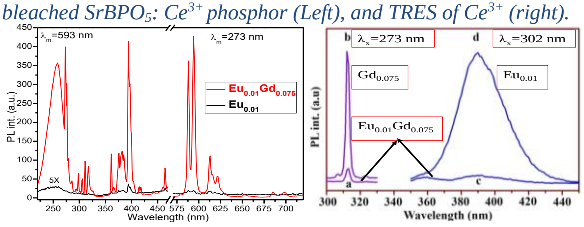

Fig. 2 PL excitation and emission spectra of Eu^{3+} in $SrBPO_5$: Eu, Gd (Left). PL emission spectra of Gd^{3+} and Eu^{2+} in $SrBPO_5$ (right).

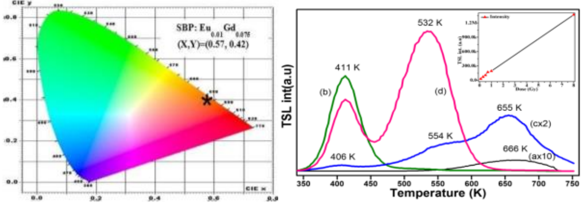

Fig. 3 Color coordinates for $SrBPO_5$:$Eu_{0.01}$, $Gd_{0.075}$ (left). TSL glow curves of (a) undoped (b) $Eu_{0.01}$ (c) $Gd_{0.01}$ and (d) $Eu_{0.01}$, $Gd_{0.01}$, and inset shows the dose-response of $SrBPO_5$:$Eu_{0.01}$, $Gd_{0.01}$ (right).

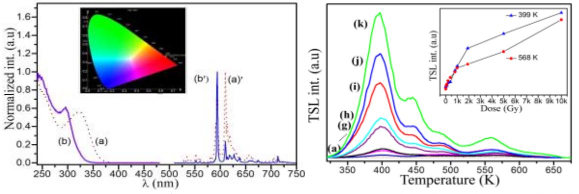

Fig. 4 PL spectra of $BaCeO_3$: $Eu_{0.01}$ at 300 K (a,a') and 77 K (b,b'), and inset shows its color coordinates (Left). TSL of (a-k) $BaCeO_3$: $Eu_{0.01}$ (0-10 kGy) and inset shows the dose-response of (right).

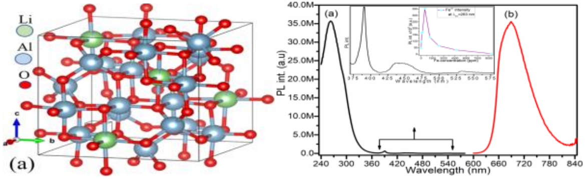

Fig. 5 Structure of $LiAl_5O_8$ (left). PL spectra of Fe^{3+}(500 ppm), and inset shows the zoomed spectra and PL intensity vs. [Fe^{3+}] (right).

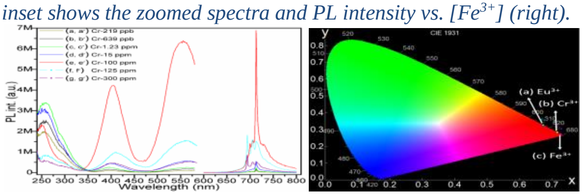

Fig. 6 PL spectra of Cr^{3+} (left). Inset shows the color coordinates for (a) Eu^{3+}(0.5 mol%) (b) Cr^{3+}(100 ppm) & (c) Fe^{3+}(500 ppm) (right).